

THE FORMATION AND EARLY EVOLUTION OF BINARIES
AND THEIR ENVIRONMENTS

by

Rachel Ann Smullen

Copyright © Rachel Ann Smullen 2020

A Dissertation Submitted to the Faculty of the

DEPARTMENT OF ASTRONOMY

In Partial Fulfillment of the Requirements
For the Degree of

DOCTOR OF PHILOSOPHY
WITH A MAJOR IN ASTRONOMY AND ASTROPHYSICS

In the Graduate College

THE UNIVERSITY OF ARIZONA

2020

THE UNIVERSITY OF ARIZONA
GRADUATE COLLEGE

As members of the Dissertation Committee, we certify that we have read the dissertation
prepared by: Rachel Ann Smullen

titled: The Formation and Early Evolution of Binaries and Their Environments

and recommend that it be accepted as fulfilling the dissertation requirement for the Degree of
Doctor of Philosophy.



Kaitlin Kratter

Date: Jul 17, 2020



Yancy Shirley

Date: Jul 20, 2020



Nathan Smith

Date: Jul 17, 2020



Renu Malhotra

Date: Jul 17, 2020



Joan Najita

Date: Jul 17, 2020

Final approval and acceptance of this dissertation is contingent upon the candidate's submission
of the final copies of the dissertation to the Graduate College.

I hereby certify that I have read this dissertation prepared under my direction and recommend
that it be accepted as fulfilling the dissertation requirement.



Kaitlin Kratter

Astronomy

Date: Jul 17, 2020

ACKNOWLEDGEMENTS

And so this chapter of my life comes to a close. The last year has been surreal, as I've been encouraged to confront both the past and the future; it's been a time of reflection on what I've done (and the people who helped me along the way) and where I hope to be during the next stages of my life. Mostly, I've been thinking about how truly fortunate I've been in my life to be surrounded by friends, family, and teachers who have always held me up so I can reach for the stars. Forgive me while I wax a bit nostalgic about the huge number of people who have touched my life and contributed to my success.

I want to begin by thanking those people at the University of Wyoming that gave me a strong foundation from which I could grow. Chip, Danny, Travis, Nicole, Lynn, Shauna, Brad, Earl, Rudi, Cameron, Charles, Nick, Adam, Nathan, Morgan, and everyone else I met at UW: you likely won't ever read this, but your advice, friendship, and support during my time in Laramie meant everything to me as I started learning about the person I am now. You probably don't know the impact you had on my life, but it mattered. And Chip, thank you especially for opening my eyes to the wonder of binary stars and encouraging me to pursue all of this. Did you know when you first took me to the telescope a decade ago that I'd be here and still obsessed with binaries?

Next, I want to thank all of the staff and administrators that have made my time here at Arizona possible. Michelle, you are the glue that holds our graduate program together; thank you for the incredible amount of work and care you put in to our success. Chris Reidy, thank you so much for your unwavering help in debugging and demystifying HPC. I am so grateful for Debbie, Treva, Kristi, and all of the other people who have helped me navigate paperwork and policy. Buell, Xiaohui, Marcia, Dan, and the other people who have guided the department during my tenure here: thank you for everything you do. I respect you all so much, and I am certain that you don't get told enough how much of a positive influence you have on everyone around you, especially the grad students.

Then, there are all of the faculty who have made my time here at UA a joy. Of course, my committee members Renu, Joan, Yancy, and Nathan: thank you for always being interested in and supportive of my work (even before you had to as committee members). Andrew, George, Ann, Gurtina, Tom, Phil P., Feryal, Serena, and many others, thank you for the time you took to chat or check in, even if it was just a comment here or there. You made sure I never got lost in the background.

My collaborators have been the foundation of my accomplishments. Stella, thank you for the incredible amount of time and care you have invested in me. You are an amazing mentor, and I look forward to working with you more in the years to come. Kat, thank you for the gossip about dynamics, cats, and everything else. Aaron, thanks for all of the random questions answered and all of the random advice given.

I also need to give profusive thanks to my past and present peers at Steward that filled my years here with fun and science. Christine and Ekta, thank you for being my best friends and partners in crime. I couldn't have done it without you. Together, we conquered grad school, and I hope that we continue to conquer life as close friends. Christine: we definitely need to meet back in Tucson to go on all of the adventures the current state of the world put on pause! Then, there's my star and planet theory cronies, Rixin, Adam, Michael, and Sarah. I owe many important conversations about both life and science to y'all. I also owe a lot of my sanity to the other grad students who've made such an impact on my time here, including the rest of my cohort—Yifan, Eckhart, Mengtao, and Jianwei—and the older and younger grad students who touched my life, including Jennifer, Carolyn, Erin, Raga, Alex, Jeremy, Jordan, Evan, Justin, JT, Junhan, Brian, and everyone else not named (because there are waaay too many of us now to list individually).

Thank you to my family for providing love and support over the course of my life. Grandma, Nana, Aunt Dee, Uncle Steve, Christy, Dan, Heidi, Clara, and the rest of my family both old and new: thank you for the joy you bring to my life every time we talk or see each other.

Finally, the individuals that I think contributed the most to my current success.

Kaitlin, I know I gave you a "World's Best Advisor" glass several years ago now, but I want you to know that I think it is even more true today than it was then. You have been a truly incredible advisor, mentor, teacher, and supporter for the past six years. Thank you for pushing me when I needed it, and for letting me stand on my own when I could. I look up to you so much, and I can only hope to become a fraction of the amazing scientist and woman you are.

Mom and Dad, thank you for your unwavering belief in me over the past twenty-eight years. You'll probably never know just how much I love and appreciate you. Thank you for encouraging me to become a strong, confident adult while always knowing I have the safety of my parents behind me. Dad—thank you for being so invested in my personal and professional achievement, and for making sure I always have the tools for success. Mom—thank you for always being there and helping me. From cooking dinners when I'm overwhelmed, to listening to me ramble about everything, to swapping books and talking art (and for my 100+ pairs of earrings), I rely so much on you. I know that both of you will be there whenever I need you.

Last, but absolutely not least, my husband Gary. Thank you for working up the courage to kiss me eight years ago, moving away from your home to stay with me six years ago, and saying "I do" two years ago. You have been my rock, my sanity, my cheerleader, and my heart through some of the highest highs and lowest lows in my life. I know with certainty that I would not have been successful without you standing beside me. I look forward to all of our future adventures together: new jobs, new cities, new expeditions, and yes—more death marches around all of the fantastical places I want to visit in the world. I love you the mostest.

DEDICATION

To all the people out there who will triumph because they do not know they can't.

TABLE OF CONTENTS

LIST OF FIGURES	9
LIST OF TABLES	11
ABSTRACT	12
CHAPTER 1 Introduction	14
1.1 Dynamics	16
1.1.1 Dynamical Stability in N-body Systems	16
1.1.2 Binary-influenced Dynamics	17
1.1.3 Resonant Dynamics	21
1.2 The Role of Binaries at Different Scales	23
1.2.1 The Kuiper Belt and Planetesimal Binaries	23
1.2.2 Stellar Binaries	26
1.3 Overview of This Work	29
CHAPTER 2 The Fate of Debris in the Pluto-Charon System	31
2.1 Introduction	32
2.1.1 Pluto's Moons	33
2.1.2 The Kuiper Belt and Collisional Families	34
2.2 Circumbinary Dynamics in the Pluto System	36
2.3 Methods	37
2.3.1 Pluto-Charon System	39
2.3.2 Solar System	42
2.3.3 Migration	43
2.4 Fate of Debris: Collisions with Charon	45
2.4.1 Relevant Time-scales	45
2.4.2 Collisions and the Disk	47
2.4.3 Craters on Charon's Surface	48
2.4.4 Internal Heating and Charon's Surface	53
2.5 Fate of Debris: Ejections into the Solar System	55
2.5.1 Ejections and the Disk	55
2.5.2 Debris in the Solar System	57
2.6 Conclusions and Discussion	61

TABLE OF CONTENTS – *Continued*

CHAPTER 3	Machine Learning Classification of Kuiper Belt Populations . .	67
3.1	Introduction	68
3.1.1	The Kuiper Belt	68
3.1.2	Machine Learning Classification in Astronomy	69
3.2	Data and Methods	70
3.2.1	Kuiper Belt Observations and Classification	71
3.2.2	Classifier Selection and Training	73
3.3	Results	79
3.3.1	Object Classification and Feature Importance	79
3.3.2	Probability of Class Membership	81
3.3.3	Object Clone Classification	86
3.4	Discussion	91
3.4.1	Reasons for Misclassification	91
3.4.2	Classification of DECam Objects	99
3.4.3	Improvements to the Classifier	101
3.5	Conclusions	105
CHAPTER 4	Planet Scattering Around Binaries: Ejections, Not Collisions .	108
4.1	Introduction	109
4.2	Planetary Stability	111
4.3	Methods	113
4.3.1	Integrator	113
4.3.2	Planetary Initial Conditions	116
4.3.3	Integration Parameters	118
4.4	Results	120
4.4.1	Differences Between Single and Binary Planet Populations . .	121
4.4.2	Differences Between Planet Populations	125
4.4.3	Impact on Stellar Binary Orbit	128
4.5	Discussion	129
4.5.1	Stability of Resultant Planetary Populations	129
4.5.2	Absence of Stellar Collisions in Circumbinary Systems	130
4.5.3	Extent of Binary Influence	136
4.5.4	Role of Giant Planets in Planet Multiplicity	138
4.5.5	Observables	139
4.6	Conclusions	142
CHAPTER 5	The Highly Variable Time Evolution of Star-forming Cores Iden- tified with Dendrograms	145
5.1	Introduction	146

TABLE OF CONTENTS – *Continued*

5.2	Methodology	149
5.2.1	A Note on Nomenclature	149
5.2.2	Simulations	150
5.2.3	Structure Identification	152
5.2.4	Linking Structures Through Time	157
5.3	Parameter Variations	162
5.3.1	Background cutoff	163
5.3.2	Density Increment	163
5.3.3	Resolution	164
5.3.4	Linking Distance	169
5.4	Results: Core Properties and Evolution	171
5.4.1	Core Property Distributions vs. Individual Core History . . .	171
5.4.2	Isolated, Starless Cores	176
5.4.3	Virial Evolution of Cores	176
5.4.4	Short-lived Overdensities	178
5.4.5	Core Mass Function	182
5.5	Results: Insights from Methodology	183
5.6	Discussion	188
5.6.1	Interpreting the IMF from the CMF	188
5.6.2	Other Ways to Identify Cores	191
5.6.3	Implications of Core Identification	194
5.7	Conclusions	195
CHAPTER 6	Summary and Future Directions	198
6.1	Summary	198
6.2	Future Directions	202
REFERENCES	205

LIST OF FIGURES

1.1	Zero Velocity Surfaces for Two Binary Mass Ratios	20
1.2	Kuiper Belt Populations	25
1.3	Known Planets in Binaries	27
2.1	Pluto-Charon Instability Boundary	38
2.2	Outcomes of Solar System Migration	46
2.3	Debris Collisional Fractions with Charon	49
2.4	Crater Numbers as a Function of Particle Size and Disk Surface Density	52
2.5	Tidal Heating on Charon	56
2.6	Debris Fraction Ejected from Pluto-Charon Binary	58
2.7	Eccentricity vs. Semi-major Axis in Kuiper Belt for Debris Ejected from Pluto-Charon Binary	62
3.1	Classifier Accuracy as a Function of Simulation Length	78
3.2	Identified Classes of KBOs	82
3.3	Importance of the Top Ten Classifier Features	83
3.4	Top Two Feature Correlation	84
3.5	Top Four Feature Correlation	85
3.6	Cumulative Probability of Class Membership	87
3.7	Probabilities of Class Membership for Each Object	88
3.8	Eccentricity vs. Semi-major Axis for Clone Classifications	92
3.9	Minimum and Maximum Clone Class Comparison	93
3.10	Ensemble Clone Class Comparison	94
3.11	Time Evolution of Misclassified Object	97
3.12	Cumulative Probabilities of Combined Sample	100
3.13	DECam KBO Classification	102
3.14	Cumulative Probabilities of DECam Classes	103
4.1	LM Planet Mass Probability Distribution	119
4.2	Average Multiplicity as a Function of Time	122
4.3	Fractional Outcomes of Planet Scattering in Different Populations . .	125
4.4	Initial vs. Final Distributions of Planet Populations	127
4.5	Zero Velocity Contours and Jacobi Constants for Circumbinary Planets	134
4.6	Distance and Jacobi Constant Evolution for an Example Planetary System	135
4.7	Minimum Pericenter Distance of Ejected Planets	137

LIST OF FIGURES – *Continued*

4.8	Most Massive Planet as a Function of Multiplicity	140
4.9	Orbital Element Distributions for Systems Having or Lacking Massive Planets	141
5.1	Time Evolution of Dense Gas	153
5.2	Example Dendrogram with Fiducial Initialization	157
5.3	Possible Linking Outcomes	160
5.4	Two Avenues of Leaf Linking Behavior	161
5.5	Comparison of Dendrograms with Different Minimum Increment . . .	165
5.6	Leaf Contour Comparison at Different Resolution	167
5.7	Derived Parameters at Different Resolution	168
5.8	Comparison of Linking Distance	170
5.9	Core Mass Distribution and Individual Evolution	174
5.10	Time Evolution of Isolated Cores	177
5.11	Virial Parameter Distribution and Evolution	179
5.12	Densities of Temporary Cores	181
5.13	Core Mass Function Comparison	184
5.14	Core Mass Function for Different Core Definitions	185
5.15	Comparison of Structure in Consecutive Timesteps	187
5.16	Cartoon Explanation Algorithmic Structure Variation	189
5.17	Leaf Mass vs. Sink Mass	192

LIST OF TABLES

2.1	Initial Conditions for Solar System Migration	44
2.2	Fate of Particles Ejected from the Pluto-Charon Binary	61
2.3	Fraction of Debris in Resonance	63
3.1	Overview of Observed KBO Catalog	73
3.2	Hyperparameter Search Range	77
3.3	Best-fit Hyperparameters for Classifier	79
4.1	Simulation Overview and Outcomes	126
4.2	Number of Orbit Crossings at 10 Myr	130
4.3	Transit Expectations	142
5.1	Coefficient of Variance for Core Properties	175
5.2	Coefficient of Variance for Isolated Cores	178

ABSTRACT

Binaries—two bodies of comparable mass that orbit a common center—influence the evolution of gas and planets in their vicinity and are ubiquitous in star and planet formation. And yet, because of the complexity binaries add to already complex problems, they have often been excluded from consideration in theoretical and observational work. In this dissertation, I present an exploration of the formation and early evolution of binaries and their environments in four contexts: debris in the Pluto-Charon system, dynamics in the Kuiper Belt of our Solar System, planetary systems around binary stars, and variability in star-forming cores.

First, I explore the fate of debris that could have resulted from the giant impact origin of the Pluto-Charon dwarf planet binary to look for observational signatures of its formation that may persist to this day. Using N-body simulations, I estimate the cratering rates on Charon’s surface that would result from collisions of small debris from the post-formation debris disk, and I also make predictions for the presence of a Pluto-Charon disk collisional family of debris that were ejected from the binary that may still be orbiting in the Kuiper Belt today. Second, I develop a machine learning algorithm to quickly and accurately classify the dynamical population membership of observed Kuiper Belt objects. Current classification methodologies require substantial human intervention, and with imminent surveys expected to increase the number of known Kuiper Belt objects by an order of magnitude, automated methods are required. I find good accuracy in my method and characterize the reasons the algorithm can fail, including object rarity and the inherent ambiguity of classification in a time-dependent system. Third, I simulate the dynamical evolution of the planet populations around both single and binary stars to understand the influence of a close central binary on planetary system architecture. I find that a central binary only changes the planet loss mechanism: planets around

a binary are much more likely to suffer a catastrophic interaction with the binary and be ejected from the system rather than undergoing a more gentle scattering that can lead to collisions. Instead, the system architecture is primarily driven by the most massive planet in the system regardless of the central object. Finally, I study the time evolution of dense, star-forming cores using magnetohydrodynamical simulations. I create an algorithm to link cores through time, and I find that the structures we identify can have large variability in extracted quantities (such as mass) in time despite the distributions of those quantities remaining stable. I postulate that a large fraction of the variability could come from the structure identification algorithms, which rely upon relative measures of structure that can change in time.

CHAPTER 1

Introduction

Observational capabilities in the astronomical community are advancing rapidly; the data collected are more detailed and numerous than ever before. Because of these advances, it is imperative that computational astrophysics strives to match (or even anticipate) observations so that we can better understand the universe around us. To motivate the content of this dissertation, I will discuss four of the recent key observatories that inspire the questions explored herein.

The *Kepler* satellite transformed exoplanet science with its first science release in 2010. *Kepler* discovered over 2,700 transiting exoplanets in its ~ 10 year mission lifetime and helped increase the number of known planets by nearly an order of magnitude.¹ It made possible the discovery of small, rocky planets; it is now understood that small planets are the most common type of planet, and the pre-*Kepler* observations of exclusively massive planets represent only a small fraction of the exoplanet demographics (e.g., Tabachnik and Tremaine, 2002; Batalha et al., 2013). Observations also revealed that planetary architectures are far more varied and dynamic than we might expect in our own Solar System: as an example, systems of tightly-packed inner planets (STIPS) like Kepler-11 host multiple rocky planets at distances interior to the orbit of Mercury (Lissauer et al., 2011a). Previously-unseen planet types like Kepler-16, the first “Tatooine” planet—a planet orbiting a binary star—were also found (Doyle et al., 2011). *Kepler* has completely shifted the paradigm of exoplanets and has left a huge and vibrant field in its wake.

The Atacama Large Millimeter/submillimeter Array (ALMA) is another telescope that has revolutionized many fields of astronomy beginning with first light in 2011. It provides an unparalleled sensitivity and resolution for many astronomical objects, especially in star and planet formation. ALMA observed the HL Tau

¹Data from exoplanetarchive.ipac.caltech.edu/docs/counts_detail.html

circumstellar disk at a resolution of only 3.5 AU, revealing a multitude of gaps and rings that could be indications of planet formation (ALMA Partnership et al., 2015). Observations by ALMA have since shown that structure in protoplanetary disks (asymmetries, gaps, rings) is nearly ubiquitous (e.g., Andrews et al., 2018; Long et al., 2019). It has also provided important information on the chemical and kinematic structure of protostellar cores and disks that are helping to unveil the micro- and macro-physics that govern star and planet formation.

In 2015, the *New Horizons* spacecraft visited Pluto and made history as the first flyby of a dwarf planet. The encounter revealed that Pluto and Charon were far more complicated than anticipated. Pluto possesses a diverse geology, including craters, mountains, glaciers, and valley networks, and was even observed to have a complex layered atmosphere (Stern et al., 2018). Charon revealed a tantalizing lack of small craters, which places tension on models of the Kuiper Belt (Singer et al., 2016). *New Horizons* then flew by the cold classical contact binary Arrokoth in 2019; this encounter, too, places strong constraints on the understanding of planetesimal formation in our Solar System. *New Horizons*, with its high resolution view of minor bodies, forced a reevaluation of our understanding of the outer Solar System.

Finally, the Vera Rubin Observatory and its Legacy Survey of Space and Time (LSST) is expected to begin science operations in 2022. This survey will cover the sky every ~ 4 nights for at least 10 years and produce > 500 PB of images and catalogs (Ivezić et al., 2019). Among other goals, LSST is expected to greatly increase the census of small objects in the Solar System by about an order of magnitude: it is projected to find one hundred thousands near Earth objects, 5 million asteroids, and more than ten thousand Kuiper Belt objects. Bodies like asteroids and Kuiper Belt objects provide insight into the formation and early evolution of our own planetary system. They are a fossil record of chemical and dynamical processes in the Solar System, and therefore, a thorough accounting of minor bodies will help inform detailed planet formation models.

Each of these observatories challenged (or will challenge) the state of the art in astronomical data analysis and interpretation. In the rest of this chapter, I give an

overview of physical, observational, and theoretical results that further motivate my research into the Kuiper Belt, planetary dynamics, and star formation.

1.1 Dynamics

In this section, I summarize some of the important, recurring physical concepts that provide intuition and physical insight for the work presented later in this dissertation. To be explicit in the definition of binarity used throughout this work, I consider two objects orbiting a common center of gravity a “binary” if the mass ratio m_2/m_1 is $> 10\%$. I will use the term “primary” to refer to the more massive component of a binary and “secondary” to refer to the less massive component, and I use “host” for the body which a planet or disk orbits and “companion” for the remaining component of the binary.

1.1.1 Dynamical Stability in N-body Systems

Dynamical stability, or the ability of systems to resist large orbital variations, is a critical factor when considering the long-term evolution of planetary systems, including our own Solar System. Mutual perturbations between bodies must be small enough that the orbits are not catastrophically changed. Instability can be defined in several ways. Most obviously, a system is unstable if planets are ejected from the system (if they become gravitationally unbound), or if planets collide with each other or a star. Many numerical works have chosen the somewhat more restrictive definition of instability as the “Hill stability” criterion in which planets cannot have close encounters (orbit crossing). Gladman (1993) explored Hill stability for a system of two low mass planets and found that systems are stable as long as they are separated by at least $\Delta > 2.4((m_1 + m_2)/M)^{1/3}$, where Δ is the scaled spacing between the two bodies, m_1 and m_2 are the masses of the planets, and M is the mass of the central star. For more complicated systems, it becomes useful to

define dimensionless planet spacing β in units of mutual Hill radii ($R_{H,m}$) such that

$$R_{H,m} = \left(\frac{m_1 + m_2}{3M} \right)^{\frac{1}{3}} \frac{a_1 + a_2}{2} \quad (1.1)$$

and

$$\beta = \frac{a_2 - a_1}{R_{H,m}} \quad (1.2)$$

Here, a_1 and a_2 are the semi-major axes of the planets. The dimensionless spacing correlates well with the time to instability: systems that are more widely spaced in β will have longer lifetimes. Gyr stability in systems with at least three planets has been found to require initial $\beta > 10$ (Chambers et al., 1996; Smith and Lissauer, 2009; Pu and Wu, 2015).

One can also flip the idea of stability to constrain physical properties of systems. For instance, mass is a difficult quantity to measure in systems with limited dynamical information like the *Kepler* exoplanetary systems or for the Pluto-Charon circumbinary moons. By requiring orbital stability for Solar System timescales, Youdin et al. (2012) was able to constrain the upper limit of masses for Nix and Hydra years before the bodies were observed in detail by the *New Horizons* spacecraft. Fang and Margot (2012b) used dynamical spacing arguments to predict the likelihood of unseen planets in *Kepler* two planet systems.

1.1.2 Binary-influenced Dynamics

Orbits are only integrable in generic systems containing at most two bodies. Thus, a problem involving a binary and other bodies has no formally predictable solution for all time. All bodies in the system are free to exchange angular momentum and energy, thereby changing their orbital elements such as eccentricity or inclination. However, there are approximations that can provide significant insight into the expected dynamics of bodies in the presence of a binary. Specifically, the circular restricted three-body problem (CR3BP) makes the approximation of a massless particle (frequently called a test particle) orbiting under the influence of two massive bodies (a binary, for this purpose) that orbit each other with no eccentricity. In this

system, there is only one conserved quantity: the Jacobi constant C_J , which is also called the integral of relative motion.

$$C_J = 2U - v^2 \quad (1.3)$$

Here, U is a scalar pseudo-potential that contains both the centrifugal potential (accounting for the Coriolis force) and the gravitational potential; v^2 relates to the kinetic energy. C_J in the synodic (rotating) frame can be expressed as

$$C_J = n^2(x^2 + y^2) + 2 \left(\frac{\mu_1}{r_1} + \frac{\mu_2}{r_2} \right) - (\dot{x}^2 + \dot{y}^2 + \dot{z}^2) \quad (1.4)$$

or in the sidereal (inertial) frame as

$$C_J = 2n(\chi\dot{\phi} - \phi\dot{\chi}) + 2 \left(\frac{\mu_1}{r_1} + \frac{\mu_2}{r_2} \right) - (\dot{\chi}^2 + \dot{\phi}^2 + \dot{\omega}^2) \quad (1.5)$$

In equations 1.4 and 1.5, n is the mean motion of the binary ($n = 2\pi/P$ with P being the binary period), μ is the mass ratio of the stars such that $\mu = 1 = \mu_1 + \mu_2 = G(m_1 + m_2)$, and r is the position of the planet measured relative to each star. The coordinates and velocities (x, y, z) and $(\dot{x}, \dot{y}, \dot{z})$ are measured in the rotating frame, and (χ, ϕ, ω) and $(\dot{\chi}, \dot{\phi}, \dot{\omega})$ are measured in the inertial frame. In both of these equations, the first term represents the rotational component, the second shows the gravitational component, and the last shows the kinetic component of the relative energy integral.

It is important to note that C_J in the CR3BP does not say anything about predictable future trajectories (a body is not forced to remain in a static orbit); rather, it constrains the region of space in which a test particle is allowed to orbit. By removing the kinetic component of the particle's orbit, a “zero-velocity” surface shows these allowed regions. I present two examples of these zero-velocity surfaces in Figure 1.1. In the equal mass case on the left, a particle with $C_J = 4$ can only orbit around either individual star or outside the binary altogether. However, a particle with $C_J = 3$ is essentially unconstrained except for two small islands and can therefore change its trajectory to orbit either star, the binary, or some combination thereof.

There are three consequences I would like to highlight.

1. A body exterior to the binary can be forbidden from ever interacting directly with the components of the binary as long as there is no outside influence. Similarly, a body orbiting one of the stars can be forbidden from changing its host (e.g., orbiting the other star or the binary center of mass).
2. On the other hand, for a select range of C_J a planet has the ability to move freely between orbiting the primary and the secondary as is shown by the contour for 3.55 in the right panel of Figure 1.1. This idea has been explored in works such as Moeckel and Veras (2012) and Kratter and Perets (2012).
3. The zero-velocity surface “opens” to the exterior of the less massive component of the binary before it opens to the exterior of the primary. This means that more material that is initially exterior to the binary will have the opportunity to interact with the secondary (e.g., collisions) before it reaches the primary

Holman and Wiegert (1999) explored the long-term (10^4 binary orbits) stability of planetary orbits in binary systems using a large number of N-body simulations and derived empirical formulae for the critical radius of stability (a_c) for both bodies orbiting one component of the binary and bodies orbiting the binary center of mass.² In this work, a_c will be referred to as the binary instability limit. Because of their simple dependence upon binary mass ratio, eccentricity, and semi-major axis, these relations have been widely used in the literature despite updated and/or more complete published relations (e.g., Quarles et al., 2020). For S-type orbits, Holman and Wiegert (1999) report a critical semi-major axis for stability in their equation 1 of

$$\frac{a_c}{a_b} = 0.464 - 0.380\mu - 0.631e + 0.586\mu e + 0.150e^2 - 0.198\mu e^2 \quad (1.6)$$

where a_b is the binary semi-major axis, $\mu = m_{\text{companion}}/(m_{\text{host}} + m_{\text{companion}})$ is the binary mass ratio, and e is the binary eccentricity. For an equal mass ($\mu = 0.5$),

²In this and other works, orbits in binaries are often classified as *S* or *satellite* type for bodies orbiting one component of the binary (circum-primary or circum-secondary; the Sun-Earth-Moon system), or *P* or *planetary* type for bodies orbiting the binary barycenter (circumbinary; the moons of the Pluto-Charon binary).

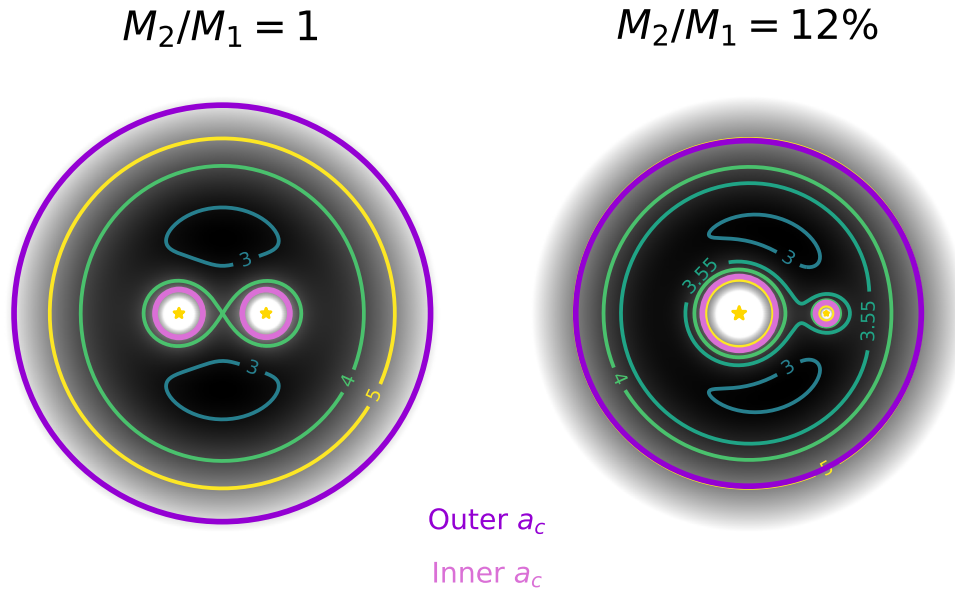


Figure 1.1: Zero velocity surfaces and empirical binary stability limits a_c at the same scale for two binary mass ratios: an equal mass binary (left) and a binary with a mass ratio similar to Pluto-Charon (right). The gray gradient and the contours show the Jacobi constant, C_J that is the only conserved quantity in the circular restricted three body problem; particles orbiting the star(s) cannot cross the contour indicated by its unique value of C_J . The pink (purple) circles delineate the region interior (exterior) to which planets have been found to have stable orbits by Holman and Wiegert (1999).

circular ($e = 0$) binary, this equation reduces to $a_c = 0.27a_b$. For P-type orbits, they find in equation 3 a critical semi-major axis of

$$\frac{a_c}{a_b} = 1.60 + 4.12\mu + 5.10e - 4.27\mu e - 5.09\mu^2 - 2.22e^2 + 4.61\mu^2 e^2 \quad (1.7)$$

An equal mass, circular binary then has $a_c = 2.4a_b$.³ The locations of these instability boundaries is shown by the pink (inner a_c) and purple (outer a_c) lines in Figure 1.1. The instability boundaries move slightly closer to (for circumstellar orbits) or further from (for circumbinary orbits) the reported location with longer integrations due to longer-term dynamical perturbations. This time dependence of the instability boundary has been attributed to mean motion resonance overlap with the binary (Mudryk and Wu, 2006; Sutherland and Kratter, 2019). The location of the instability boundary can also change if other orbital characteristics are included such as the inclination between the binary orbital planet and the particle's orbit or the initial mean longitude of the binary relative to the planet (Quarles et al., 2020).

1.1.3 Resonant Dynamics

Resonance—the commensurability of frequencies such as spin or orbit—is found in many astronomical systems. It is prevalent in the Solar System, including the well known examples of the Galilean moons of Jupiter (e.g., Sinclair, 1975), Kirkwood gaps in the asteroid belt (e.g., Ferraz-Mello, 1994), resonant populations in the Kuiper Belt (e.g., Chiang and Jordan, 2002; Chiang et al., 2003), and the near-resonant orbits of the Pluto-Charon circumbinary moons (e.g., Showalter and Hamilton, 2015). Resonance has also been seen in exoplanetary systems, such as the well-publicized seven planet resonant chain in the TRAPPIST-1 system (Luger et al., 2017). In this section, I briefly explain the basic intuition behind simple mean motion resonances that are important in later chapters of this dissertation.

Mean motion resonance can be most simply described as a period ratio between

³In equation 5 of Holman and Wiegert (1999), the authors report the somewhat different relation $a_c = 2.3a_b$.

two bodies that can be described as a ratio of integers, or

$$\frac{P_1}{P_2} = \frac{p}{p+q} \quad (1.8)$$

P is the orbital period of a body, and p and q are integers with $p > q > 0$ for the exterior resonances considered in this dissertation.⁴ The variable q is sometimes called the “order” of the resonance. For instance, the 3:2 resonance in the Kuiper Belt is a first-order resonance that captures the Pluto-Charon binary into a stable configuration with Neptune despite the fact that the binary’s orbit crosses that of Neptune. Neptune orbits three times for every time Pluto-Charon orbits twice, and the resonant perturbations in the system protect Pluto-Charon from collisions with Neptune.

A body is found to be in resonance if it librates around some resonant angle ϕ . This means that the time evolution of ϕ is bounded to some oscillation amplitude $\Delta\phi$ instead of circulating (going through the full range $0 - 2\pi$ in time). The resonant angle is defined as

$$\phi = p\lambda_1 - q\lambda_2 - r_1\varpi_1 - r_2\varpi_2 - s_1\Omega_1 - s_2\Omega_2 \quad (1.9)$$

In this equation, λ is the mean longitude (a mean orbital position), ϖ is the longitude of perihelion (the angle at which an object comes closest to the central star), and Ω is the longitude of the ascending node (the angle at which an object crosses from below the reference plane to above), and r_1, r_2, s_1 , and s_2 are integers that satisfy the constraint $p - q - r_1 - r_2 - s_1 - s_2 = 0$.⁵

Libration often manifests itself in the orbital elements as periodic variations in orbital semi-major axis and eccentricity. Different resonances, therefore, will have an associated resonance width in semi-major axis that depends on the planet-star mass ratio and the eccentricity. These resonant widths can overlap, thereby pumping the eccentricity of the object in resonance and causing chaos; this is a major driver of

⁴Equation 1.8 is often written in terms of the mean motion $n = 2\pi/P$.

⁵Formally, $\lambda = \Omega + \omega + M$ and $\varpi = \Omega + \omega$, where ω is the argument of perihelion and M is the mean anomaly.

dynamical instability (e.g., Malhotra, 1996; Morrison and Kratter, 2016; Sutherland and Kratter, 2019).

1.2 The Role of Binaries at Different Scales

Binarity is a critical, but frequently overlooked, underpinning of the star and planet formation process. Binaries are ubiquitous at scales from planetesimals (~ 10 km) to stellar systems ($\sim 10^4$ AU). I discuss the importance of binaries in three regimes (the Kuiper Belt, planetary systems, and star formation) below.

1.2.1 The Kuiper Belt and Planetesimal Binaries

The Kuiper Belt is the collection of small bodies (Kuiper Belt objects, KBOs) that lie beyond Neptune in our Solar System and encodes a record of early chemical and dynamical evolution in the planet formation process.⁶ There are over 2,000 observed KBOs ranging in size from $\sim 1 - 10^4$ km (Bannister et al., 2018; Arimatsu et al., 2019). Broadly, the Kuiper Belt hosts four dynamical populations (with distinctions differing between different works, e.g. Gladman et al., 2008; Malhotra, 2019). KBOs are either classified as resonant (swept into mean motion resonances with Neptune during migration), classical (relatively dynamically untouched), scattering or scattered (having past, present, or future substantial changes in orbital properties), and scattered disk/detached (objects beyond the classical Kuiper Belt with semi-major axes $a \gtrsim 50$ AU that have minimal dynamical connection with Neptune). I show a selection of close ($a < 70$ AU) Kuiper Belt objects colored by their Gladman et al. (2008) population in Figure 1.2. The resonant structure of the Kuiper Belt and relative population of different resonances is directly linked to the dynamical evolution and early migration of the giant planets (e.g., Nesvorný, 2015; Chen et al., 2019b; Lawler et al., 2019).

The classical Kuiper Belt additionally preserves a wealth of information about

⁶More generally, objects with semi-major axes larger than that of Neptune are called trans-Neptunian objects, or TNOs.

planetesimal formation. Colors and composition of KBOs constrain early gaseous disk composition and sedimentation mechanisms (e.g., Stern et al., 2019; Young et al., 2020). The size distribution and binary fraction of KBOs also provide strong limits on the formation mechanisms of planetesimals. Fraser et al. (2017) postulates that a majority of classical KBOs were created in binaries, and Grundy et al. (2019) show that the resolved Kuiper Belt binaries prefer binary orbits that are prograde with respect to the orbit around the Sun. There is also now evidence of binary formation channels all the way down to small scales with the *New Horizons* visit to the cold classical contact binary Arrokoth (2014 MU₆₉; Porter et al. 2019). By leveraging these observational realities of KBOs, one can then limit formation mechanisms to those that can reproduce all characteristics of the size distribution, compositional variations, and binary properties. For instance, Nesvorný et al. (2019a) show how the streaming instability planetesimal formation channel can produce a majority of planetesimals that are binary and prograde with a size distribution consistent with the observed Kuiper Belt.

Pluto-Charon

Arguably the most famous of the Kuiper Belt binaries, Pluto-Charon is a binary dwarf planet and a member of the 3:2 resonant “Plutino” population of Kuiper Belt objects.⁷ Pluto is the largest observed KBO⁸ with a radius of 1,200 km, and it has a mass about one one-thousandth that of Earth; its binary companion Charon has a radius of 600 km and is 12% of Pluto’s mass (Stern et al., 2018). The binary barycenter lies one Pluto-radius outside Pluto’s surface, and the binary orbits on a nearly circular orbit with a period of about 6.4 days. Charon is thought to have formed via giant impact in the early Solar System and tidally migrated to its current location (Canup, 2005).

⁷Although it disappoints many, including the author’s father, Pluto-Charon is far cooler as the preeminent binary dwarf planet than as the runt of the Solar System planets.

⁸Pluto is not, however, the most *massive* KBO: Eris is $\sim 25\%$ more massive than Pluto (Brown and Schaller, 2007).

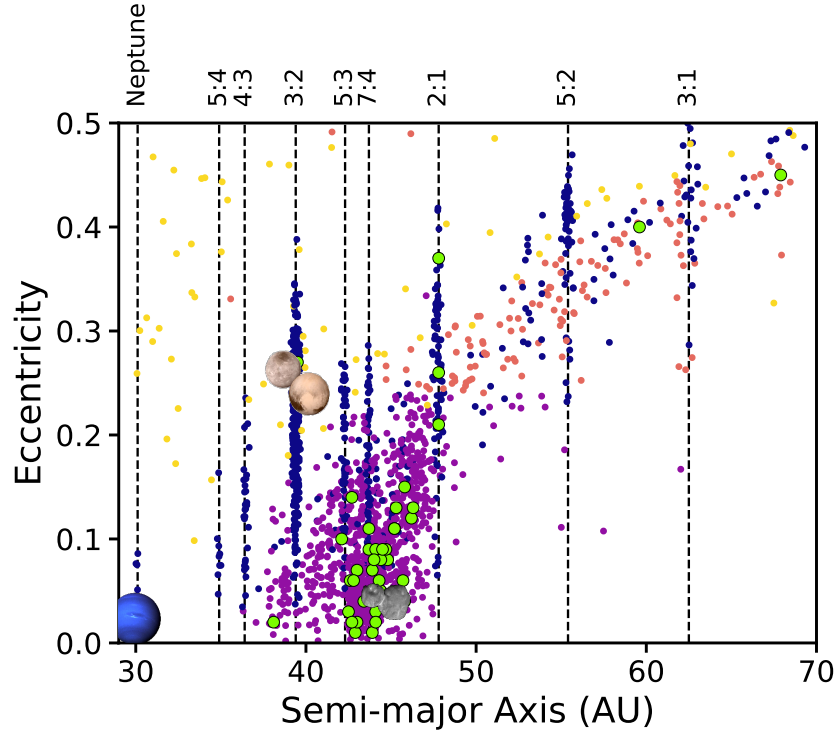


Figure 1.2: Eccentricity vs. semi-major axis for the sample of Kuiper Belt objects used in Smullen and Volk (2020) and 3. The colors indicate the dynamical population: dark blue are resonant KBOs, purple are classical KBOs, orange are detached KBOs, and yellow are scattering KBOs. Vertical dashed lines show the location of well-populated resonances. The green circles show the Kuiper Belt binaries from Table 19 of Grundy et al. (2019). The well-know outer Solar System objects Neptune, Pluto-Charon, and Arrokoth are shown in images at their present locations.

Four, icy circumbinary moons—Styx, Nix, Kerberos, and Hydra—orbit the Pluto-Charon binary in circular ($e < 0.006$), coplanar ($i < 1^\circ$) orbits. These moons are near, but not exactly in, mean motion resonances with the binary in 1:3:4:5:6 period ratios (Showalter and Hamilton, 2015). However, the formation of the circumbinary moons still proves elusive: the composition and delicate orbital configuration suggest that the objects were not captured from the Kuiper Belt, but the Charon-forming impact and subsequent tidal migration makes the bodies difficult to form in situ (Ward and Canup, 2006; Lithwick and Wu, 2008b; Canup, 2011; Kenyon and Bromley, 2014; Cheng et al., 2014b; Walsh and Levison, 2015; Woo and Lee, 2018).

1.2.2 Stellar Binaries

Nearly half of all Sun-like stars reside in binaries (Raghavan et al., 2010; Moe et al., 2019). Binarity is found to increase with stellar mass from $\sim 25\%$ in M stars to $> 80\%$ in O stars, with O stars even having a slight preference for more than one companion star (Duchêne and Kraus, 2013). Thus, the universality of stellar binarity has far-reaching impacts on astrophysical topics, including star and planet formation (discussed below), supernova rates and types (Kochanek, 2009; Sana et al., 2012), gravitational wave progenitors (Abbott et al., 2017), and cosmic reionization (Madau and Fragos, 2017; Götberg et al., 2020).

Planets in Binaries

As shown in Section 1.1.2, the presence of a binary companion places strict limitations on the dynamically stable orbits of planets. Despite this, planets have been observed in a wide variety of stellar multiples in both circumstellar (S-type) and circumbinary (P-type) orbits as shown in Figure 1.3. The host binaries from Schwarz et al. (2016) span the full range of mass ratios ($q \sim 0.1 - 1$), have primary masses from $0.1 - 1.5 M_{\odot}$, and have binary semi-major axes from $0.03 - 0.3$ AU for the circumbinary planets and 5 AU to more than 10^3 AU for the circum-primary/circum-secondary planets.

Circumbinary planets have primarily been discovered via transits by the *Kepler* satellite. Because of irregular transit signals due to the motion of both planet and binary, these planets have most frequently been discovered without automated methods. There are roughly one dozen known circumbinary planets (Schwarz et al., 2016), including the three planet circumbinary system Kepler-47 (Orosz et al., 2012, 2019). Circumbinary planet formation likely follows slightly different channels than “traditional” planet formation. The inner gaseous/planetesimal disk around a binary experiences a forced eccentricity from the binary, leading to higher collisional velocities between planetesimals that may inhibit planetary growth (Marzari et al., 2013; Silsbee and Rafikov, 2015). Planets may form more efficiently in the outer

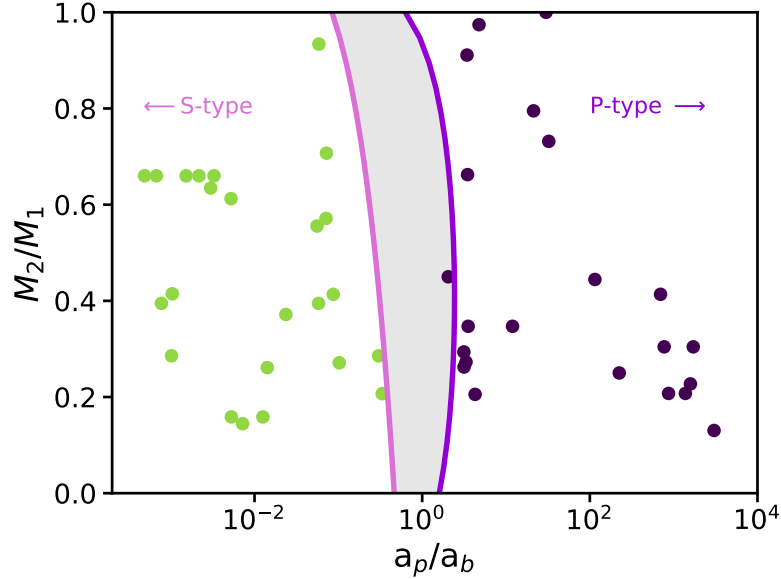


Figure 1.3: A census of known planets in binaries with semi-major axis $a_b < 100$ AU using the updated catalog from Schwarz et al. (2016). The horizontal axis shows the planet-binary semi-major axis ratio, and the vertical axis shows the binary star mass ratio. Green points show S-type (circum-primary or circum-secondary) planets, while purple points show P-type (circumbinary) planets. The pink and violet lines show the Holman and Wiegert (1999) empirical stability limits for a zero eccentricity binary. Planets with circular binaries cannot have stable orbits in the grey shaded region.

disk and migrate inward towards the circumbinary instability limit while gaining moderate eccentricity (Pierens and Nelson, 2013) or outwards, thereby becoming more difficult to observe (Pierens and Nelson, 2008). Additionally, circumbinary planets may experience an increase in inclination (misalignment) due to the central binary or an outer tertiary companion (Fabrycky and Tremaine, 2007; Muñoz and Lai, 2015; Hamers et al., 2016). Coupled with the fact that the asymmetric potential of the central binary will always induce nodal precession in circumbinary planet orbits, transiting circumbinary planets are rare and transient: circumbinary planets only transit $\sim 10 - 50\%$ of their orbits (Martin, 2017). For example, Kepler-453 b has precessed out of transit (Welsh et al. 2015); however, *because* of precession, most circumbinary planets will transit given sufficient observational time (Martin

and Triaud, 2015).

Binaries also play an important role in the formation and architecture of circumprimary and circum-secondary systems. For instance, Moe and Kratter (2019) show that binaries up to ~ 100 AU suppress circumstellar planet formation (with a roughly linearly increasing suppression as binary orbits shrink). In some ways, this is not surprising as an outer companion will truncate or regulate the amount of material available to the planet-forming disk. Despite the proposed starving of circumstellar disks, planets are still able to form: Kepler-444A hosts five rocky planets (total mass $\approx 1.5 M_{\oplus}$) within 0.08 AU despite the presence of an outer M-dwarf binary with perihelion of 5 AU Dupuy et al. (2016). Outer companions can also influence the dynamical evolution of formed planetary systems. The eccentric Kozai-Lidov effect, which sees an outer companion exciting eccentricity and inclination variations in a planet, has been proposed as a mechanism by which wide giant planets can experience tidal dissipation and become hot Jupiters (e.g., Naoz et al., 2012).⁹

Protostellar Binaries

Binarity is an important component of the star formation process. It has been shown that many protostars form in binaries, and some companions are lost by the time the stars reach the main sequence; Tobin et al. (2016) find a Class 0 multiplicity fraction of $\sim 60\%$ and a Class I multiplicity fraction of $\sim 25\%$. Additionally, the protostellar binary separation distribution is found to be bimodal with peaks at 75 and 3000 AU (Tobin et al., 2016). This suggests two primary formation mechanisms for binaries: disk instability (gravitational fragmentation) for the close binaries (e.g., Machida et al., 2008; Kratter et al., 2010) and core instability (such as turbulent fragmentation) for the wide binaries (e.g., Offner et al., 2010).

Binary companions can significantly impact the structure and extent of disks at all timescales, which then greatly impacts the efficacy of planet formation. Outer companions can incite warps and misalignments; for instance, they can incite dy-

⁹Moe and Kratter (2019) suggest that there is no evidence of an excess of observed wide companions to hot Jupiter hosts.

namical Kozai-Lidov cycles in the circumstellar disk causing the disk to become inclined or eccentric (Martin et al., 2014). The presence of a binary companion can hasten the dispersal of circumstellar disks (Kraus et al., 2011). Lee et al. (2019) show that wide binaries can undergo orbital decay from $> 10^4$ AU to < 100 AU on \sim Myr timescales due to dynamical friction. Outer companions have also been shown to induce structure in older circumstellar disks: Wagner et al. (2018) observe that the 10 Myr-old HD 100453 protoplanetary disk is sculpted by a wide companion at ~ 100 AU that incites spiral arms.

1.3 Overview of This Work

The above sections demonstrate why binarity is such an important consideration at multiple scales, from the Kuiper Belt, to planetary systems, to star-forming cores. Therefore, this dissertation utilizes a wide variety of numerical techniques and analyses to explore the formation and early evolution of binaries and their environments at different scales. I begin with the smallest scales: Chapter 2 presents an investigation of the dynamics of debris around the Pluto-Charon binary that would have resulted from Charon’s formation. By combining numerical simulations of a debris disk around the binary with models of the debris disk, I posit expectations for cratering rates on Charon’s surface due to the colliding debris, and I make predictions for the characteristics of a family of bodies in the Kuiper Belt that were ejected from the post-formation debris disk. In Chapter 3, I create a machine learning classifier to classify the observational populations in the Kuiper Belt. This type of automated, high accuracy scheme is critical for upcoming survey missions that will increase the number of known Kuiper Belt objects by at least an order of magnitude. Moving to full planetary systems, Chapter 4 explores the dynamical interactions of planets around tight binary stars like the observed *Kepler* circumbinary planets and compares the evolution of those planetary systems to the evolution of planetary systems around single stars. At the largest scales, Chapter 5 investigates the time evolution of star-forming cores identified with a hierarchical structure identification algorithm

to understand the interpretation and evolution of physical quantities observed in star-forming regions. Finally, Chapter 6 summarizes this work and presents future continuations of these important research questions.

CHAPTER 2

The Fate of Debris in the Pluto-Charon System

This chapter has been previously published as Smullen R. A., Kratter K. M., 2017, MNRAS, 466, 4480 (DOI: 10.1093/mnras/stw3386)

Abstract

The Pluto-Charon system has come into sharper focus following the fly by of *New Horizons*. We use N -body simulations to probe the unique dynamical history of this binary dwarf planet system. We follow the evolution of the debris disk that might have formed during the Charon-forming giant impact. First, we note that in-situ formation of the four circumbinary moons is extremely difficult if Charon undergoes eccentric tidal evolution. We track collisions of disk debris with Charon, estimating that hundreds to hundreds of thousands of visible craters might arise from 0.3–5 km radius bodies. *New Horizons* data suggesting a dearth of these small craters may place constraints on the disk properties. While tidal heating will erase some of the cratering history, both tidal and radiogenic heating may also make it possible to differentiate disk debris craters from Kuiper belt object craters. We also track the debris ejected from the Pluto-Charon system into the Solar System; while most of this debris is ultimately lost from the Solar System, a few tens of 10–30 km radius bodies could survive as a Pluto-Charon collisional family. Most are plutinos in the 3:2 resonance with Neptune, while a small number populate nearby resonances. We show that migration of the giant planets early in the Solar System’s history would not destroy this collisional family. Finally, we suggest that identification of such a family would likely need to be based on composition as they show minimal clustering in relevant orbital parameters.

2.1 Introduction

New Horizon's arrival at Pluto has brought a new spotlight to the Solar System's largest Kuiper belt dwarf planet and most well-known binary. Pluto and its largest moon, Charon, have a mass ratio of about 0.12 (Brozovic et al., 2015). Thus, the barycenter of the system lies between the two objects, and the regime of binary dynamics is most applicable. Four circumbinary moons, Styx, Nix, Kerberos, and Hydra, have also been identified. With the better characterisation of the Pluto-Charon system stemming from the high-resolution view of *New Horizons*, we can gain deeper insight into this system. This work aims to investigate two tracers of Pluto and Charon's formation: craters on the surface of Charon and debris that escaped into the Kuiper belt.

McKinnon (1989), Canup (2005, 2011), and others have proposed and refined a giant impact origin for the Pluto-Charon binary. Canup (2011) studied a variety of collisions between Pluto and an impactor. The bodies can be either differentiated or non-differentiated; different incoming trajectories are simulated to understand the variations in the resultant system. A giant collision of this type will typically form a moon, a disk, or both. This study finds that a body one third to half the mass of the primordial Pluto will form Charon when it collides, although the newly formed moon tends to form with high eccentricity and a pericenter close to Pluto (within a few Pluto radii). If the impactor is differentiated, a disk is very likely and will have mass anywhere from 0.001% of Pluto's mass to Charon's mass. A post-collision disk may extend out to about 30 Pluto radii. After the Charon forming impact, Charon is thought to migrate to its current position via tidal evolution. This tidal evolution can either be eccentric (Cheng et al., 2014a) or circular (Dobrovolskis, 1989; Dobrovolskis et al., 1997; Peale, 1999) and should take at most a few million years. Charon concludes its migration tidally locked to Pluto with a 6.4 day period (semi-major axis of roughly 17 Pluto radii) and has eccentricity $\leq 5 \times 10^{-5}$.

2.1.1 Pluto’s Moons

Despite a compelling explanation for the formation of Charon, a theory for the emplacement of the four small circumbinary moons remains elusive. Many works, such as Ward and Canup (2006), Lithwick and Wu (2008b,a), Canup (2011), Cheng et al. (2014b), Kenyon and Bromley (2014), and Walsh and Levison (2015), have tried to explain the location of the small moons. Dynamical stability studies by Youdin et al. (2012) predicted low masses and high albedos for the moons, which were confirmed by Brozovic et al. (2015), and *New Horizons* (Stern et al., 2015). They find that the moons have masses of about $< 1 \times 10^{-6}$, 3.1×10^{-6} , 1.1×10^{-6} , and 3.3×10^{-6} relative to Pluto for Styx, Nix, Kerberos, and Hydra, respectively. These limits suggest that the circumbinary moons are icy, consistent with an origin in the disk from the Charon-forming impact. Nevertheless, many features of these moons remain difficult to explain when accounting for the tidal history of Charon. Specifically, the migration of Charon would easily destroy the extreme coplanarity ($< 0.5^\circ$), low eccentricity (< 0.006), and the nearness to resonance (nearly 3:1, 4:1, 5:1, and 6:1 with Charon) (Brozovic et al., 2015).

The dynamical properties of the moons listed above are most consistent with in-situ disk formation, yet the disks in the Canup (2011) simulations simply do not have enough material at the moons’ current locations to form them. Many proposed solutions have invoked resonant transport from the inner disk (where bodies form) to the outer disk, but these methods often pump the eccentricities and/or inclinations of the small moons well above the observed values. The corotation resonance from Ward and Canup (2006) would not excite eccentricities, but this method requires different Charon eccentricities to transport each moon. Thus, Lithwick and Wu (2008b) and Cheng et al. (2014b) suggest that this mechanism is unlikely. Cheng et al. (2014b) show a method to capture and transport disk material outward in a low (albeit non-zero) eccentricity orbit through capture into multiple Lindblad resonances while Charon is tidally evolving; however, they are unable to migrate material at the 3:1 and 4:1 commensurability with Charon (the locations of Styx

and Nix). Pires dos Santos et al. (2012) suggests that the current moons could come from collisions of other bodies near Pluto in the Kuiper belt, but the collision time-scales for massive enough objects are too long. Walsh and Levison (2015) suggest that the moons could form from disruption of an existing satellite in the system. This would provide a secondary disk, possibly at larger orbital radii, from which the moons can form, but still struggles to account for the wide range of circumbinary moon semi-major axes.

2.1.2 The Kuiper Belt and Collisional Families

The history of the Pluto-Charon system is tied to the history of the Kuiper belt and Kuiper belt objects (KBOs). A plethora of works beginning from Malhotra (1995b,a) have explored the early history of the Solar System and the sculpting of the Kuiper belt via giant planet migration. In these scenarios, Neptune and Pluto begin closer to the Sun than they are today. Neptune then migrates outward to its current orbit and Pluto is captured into the 3:2 resonance. During this process, Pluto’s orbit gains both eccentricity and inclination.

It is likely that the Charon-forming collision occurred early in the history of the Solar System because the density of planetesimals was higher and thus collisional time-scales shorter. Additionally, works such as Levison et al. (2008) propose that there may be large numbers of larger objects (Pluto-sized) in the primordial Kuiper belt, which means that the cross section for giant impacts was larger. Therefore, Pluto and Charon have likely existed in their current state for most of the Kuiper belt’s history and should record information about the surrounding population of KBOs through cratering. Greenstreet et al. (2015) simulates the expected crater size distribution on the surfaces of Pluto and Charon for both “divot” (discontinuous double power law, e.g. Shankman et al., 2016) and “knee” (broken power law, e.g. Bernstein et al., 2004; Fraser et al., 2014) Kuiper belt populations. The true size distribution is still uncertain due to small samples and the likely presence of multiple populations.

Another interesting feature of massive KBOs is the presence of collisional fam-

ilies. Many KBOs, including the Pluto-Charon system, show evidence of giant impacts that would produce a collisional family. The Haumea collisional family originally reported by Brown et al. (2007) is the only identified collisional family in the Kuiper belt. This family consists of roughly a dozen objects with similar compositions and orbits to the dwarf planet Haumea. In Haumea’s case, the collisional family was easily identified because the members share a striking spectral feature and because the velocity dispersion of family members is about an order of magnitude lower than expected (Schlichting and Sari, 2009). The typical collisional family, however, should have velocity dispersions closer to the escape velocity from the parent system, which is closer to one km s^{-1} . Marcus et al. (2011) find that collisional families in the Kuiper belt are difficult to distinguish using the same method of low velocity dispersion used to find the Haumea family, but these families may be possible to pick out using other methods, such as clustering in inclination. They also estimate that there should be, at most, a handful of collisional families from massive collisions and a few tens of families from progenitors of 150 km in size. The Haumea collisional family is suggested to be old (from less than 1 Gyr after Solar System formation) and therefore may be primordial (Ragozzine and Brown, 2007). Thus, the majority of collisional families might stem from a time when the Kuiper belt was more dense, before dynamical stirring by Neptune. Leinhardt et al. (2010) note that collisional families in the Kuiper belt and the main asteroid belt have different characteristics due to Kuiper belt giant collisions tending to be slower and more massive.

In this work, we investigate the evolution of a debris disk resulting from the Charon-forming collision. We look at collisions onto Charon’s surface that might leave visible craters. This crater population may contaminate measurements of the KBO size distribution. We also look at the population of debris ejected into the Solar System that might manifest as a Pluto collisional family in the Kuiper Belt. In Section 2.2, we discuss the circumbinary dynamics in the Pluto-Charon system. Section 2.3 presents our simulation methodology. Section 2.4 presents results for collisions onto Charon’s surface, while Section 2.5 shows the properties of ejected

particles.

2.2 Circumbinary Dynamics in the Pluto System

The origin of Pluto’s four circumbinary moons still remains a mystery. The destabilizing influence of the binary almost certainly rules out in-situ formation if Charon undergoes eccentric tidal evolution. As noted by Kenyon and Bromley (2014), Walsh and Levison (2015), and Bromley and Kenyon (2015), the Holman and Wiegert (1999) binary instability boundary provides strict limitations on the stable locations of particles around the Pluto-Charon binary. The location of this empirical boundary, a_{crit} , is a function of both binary eccentricity and mass ratio ($\mu = M_C/(M_P + M_C)$), as shown in equation 2.1. The overwhelming majority of particles that cross inside this boundary will go unstable in less than 10^4 orbital periods and either eject from the system or collide with another body.

$$a_{\text{crit}}/a_{\text{PC}} = 1.60 + 5.10e - 2.22e^2 + 4.12\mu - 4.27e\mu - 5.09\mu^2 + 4.61e^2\mu^2 \quad (2.1)$$

Simulations of Charon’s formation suggest that it may have formed with an initial eccentricity as high as $e = 0.8$. Subsequently, Charon must undergo outward tidal evolution to reach its current semi-major axis and low eccentricity. Tidal evolution models such as Cheng et al. (2014a) require that Charon remain eccentric for nearly the entire outward migration. If we apply the binary instability boundary in equation 2.1 to the Cheng models (both the semi-major axis and eccentricity evolution), we find that one or more of the circumbinary moons would be unstable for any tidal evolution model except one with zero eccentricity. This is shown in Figure 2.1, where we plot the location of the instability boundary against time for different tidal evolution models. The colored lines show different initial eccentricities for the constant Δt model (solid) and constant Q model (dashed) (see Cheng et al. 2014a Sections 2.1 and 2.2 for a description of the Δt model and constant Q model, respectively). The semi-major axis evolution of Charon is shown in black, and the present-day locations of the four moons are shown in red. Debris or moons interior to

(below) any of these curves cannot survive the tidal evolution of Charon because the instability time-scale is much shorter than the migration time-scale. For instance, at the location of Hydra, the period is 38 days; 10^4 orbital periods is just over 1000 years and is much shorter than the Myr migration time-scale for Charon. Thus in situ moon formation from the initial debris disk is inconsistent with these eccentric tidal evolution models. It is possible to form the moons in situ if Charon’s orbit is initially circular or if the eccentricity is damped early in the tidal evolution history.

Particles in the debris disk will encounter the instability boundary as it sweeps outward with the migration of Charon. The debris that interacts with the instability boundary will likely be ejected from the system or collide with Charon. Smullen et al. (2016) find that circumbinary planets initially exterior to the instability boundary will preferentially be ejected from the system when scattered toward the central binary by other bodies. Compared to systems with a single central object, collisions are much more rare (by up to an order of magnitude) in a binary system. Those objects that collide will more often collide with the less massive body as shown by Sutherland and Fabrycky (2015). This behaviour can be understood from simple three-body dynamical arguments discussed in Section 5.2 of Smullen et al. (2016). Thus, as Charon migrates outward, the instability boundary sweeps across the previously unperturbed disk and causes new waves of particle loss.

2.3 Methods

We investigate the fates of debris in a disk from the formation of Charon. First, we simulate the interaction of the Pluto-Charon system with a disk of test particles in isolation and track the final outcomes of particles. In these simulations, we examine the impact of collisions onto the surface of Charon. We also record all ejected particles at Pluto’s Hill sphere, and then we inject these ejected particles into the Solar System and integrate to understand the long-term behaviour of this population of Pluto ejecta.

We utilise integrators in the Chambers and Migliorini (1997) N -body integra-

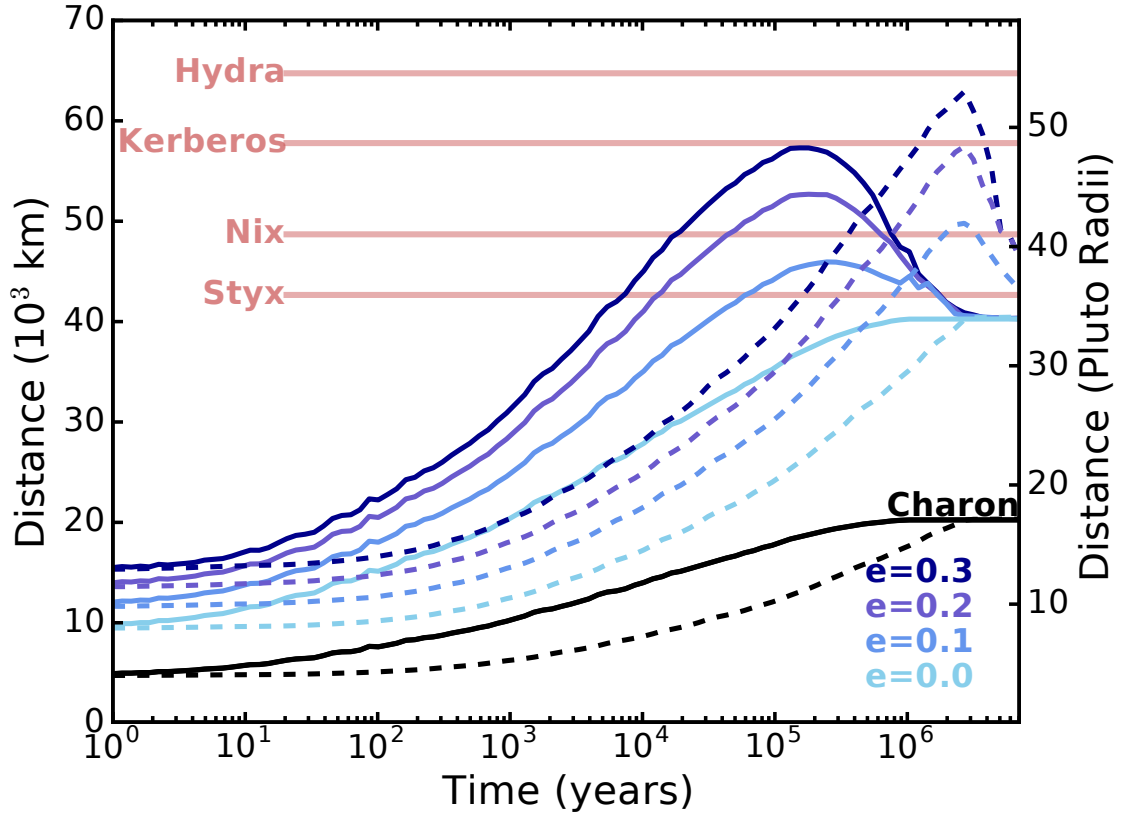


Figure 2.1: The location of the binary instability boundary as a function of time for different tidal evolution models. The solid lines show the constant Δt model and the dashed lines show the constant Q model from Cheng et al. (2014a). The color denotes initial eccentricity. The black line shows the semi-major axis evolution of Charon, and the red lines show the current locations of the four circumbinary moons. In every case but the $e = 0$ model, the instability boundary sweeps over a present-day location of one or more of the moons. Bodies that cross the instability boundary will be driven unstable on short time-scales (less than 1000 years), so the moons cannot have been formed in situ if Charon undergoes the tidal evolution presented here.

tor MERCURY. For integrations of the Pluto-Charon system itself, which has two massive bodies, we use the Gauss-Radau variable time step integrator *Radau* in the modified version of MERCURY presented in Smullen et al. (2016). We use the Bulirsch-Stoer integrator *BS* for the forced migration simulations of the Pluto-Charon system. For integrations of particles in the Solar System, we use the *Hybrid* integrator from the unmodified version of MERCURY, which uses a Bulirsch-Stoer integrator for close encounters and a symplectic integrator for all other time steps.

Both the isolated Pluto-Charon and the Solar System integrations have been effectively parallelized by running smaller sets of test particles with the same sets of massive bodies. This means, though, that our simulations do not finish with identical ending conditions for the massive bodies because we allow close encounters with test particles. When MERCURY uses an adaptive time step method, such as the Bulirsch-Stoer or *Radau* integrators, the time step of the simulation changes. In the Solar System integrations, the overall time of the simulation returns to the symplectic time step after the close encounter has passed, but an imprint of the change remains. Minute variations in the orbits during adaptive stepping routines act as a source of “chaos” in the system, leading to significant variations in the final conditions after long time scales. Because of the many massive bodies and long time-scales in the Solar System these variations manifest themselves in all orbital elements. In the Pluto-Charon system, where there are only two massive bodies, the variations tend to manifest as differences in final mean anomaly.

2.3.1 Pluto-Charon System

To reach its current position, the Pluto-Charon binary must have migrated, but the details of this migration are unknown. To this end, we implement three unevolving Pluto-Charon orbits representing different stages of eccentric tidal evolution, and we also implement a circular migration model.

For the constant orbit integrations, our initial conditions are motivated by the Cheng et al. (2014a) tidal evolution models for Charon: we initialise Charon at binary semi-major axis $a = 5 r_{\text{P}}$ and eccentricity $e = 0.3$, $a = 17 r_{\text{P}}$ and $e = 0.3$,

and $a = 17 r_P$ and $e = 0.0$. Thus, we cover a set of Pluto-Charon orbits that span the most compact to the widest at a plausible range of eccentricities.

Each integration begins with Charon at a mean anomaly M of 90° and is integrated to 10^7 days, or roughly 1.5 million Pluto-Charon orbits at $a = 17 r_P$. The disk has 27060 test particles that range in barycentric distance from 0–65000 km with eccentricities randomly drawn from a uniform distribution from 0 to 0.01 and inclinations randomly drawn from a uniform distribution from 0 to 0.5° . Walsh and Levison (2015) find that a stable ring around the Pluto-Charon binary should collisionally circularize in about a decade, meaning that any free eccentricity in the debris’ orbit set from the progenitor collision should damp within a few decades. While the disk will not be perfectly circular due to a forced eccentricity from the binary, in the regions under consideration, the forced eccentricity will be less generally much less than 0.3 using the formulation from Leung and Lee (2013). Mudryk and Wu (2006) note that the instability of circumbinary material is not a strong function of initial eccentricity, so an initial lack of forced eccentricity will not impact our results. The disk is then evolved under the influence of the binary, so within very few orbital periods, the inner edge of the disk (just exterior to the binary instability boundary) becomes slightly eccentric due to the forced eccentricity from the central binary. The test particles are drawn such that the average spacing between any two particles is constant; this is achieved by initialising the same number of test particles in 132 annular rings where the area of each ring is constant. Consequently, the innermost rings have widths of several hundred to a few thousand km, while outer rings will only be a few km in width. Our disk is unphysically large for the Canup (2011) models of Pluto-Charon formation, but such a large simulated disk allows us to convolve any physical disk model in post-processing. While our disk is initialised around the Pluto-Charon barycenter, we tested a model with a Pluto-centered disk and found little change in particle fates.

We also implement the migration model described below in Section 2.3.3 in the Pluto-Charon system to understand the differences in particle fates caused by an evolving orbit. Charon migrates through the disk (which is the same as above) from

$5 r_P$ to $17 r_P$. We run the simulations for 10^5 yr (about three times longer than the constant orbit simulations).

We set the sizes of Pluto and Charon using spherical shapes and densities of 1.88 g cm^{-3} and 1.65 g cm^{-3} , respectively. Particles are tracked to the surface of the massive bodies by setting the massive body close encounter radius to one physical radius, thereby ensuring that there are no extrapolation errors introduced into collision rates. Particles are considered to be ejected when they reach a distance equivalent to Pluto’s modern-day Hill sphere of about 0.06 AU (about 140 times the initial disk extent in the simulations). We track Pluto-barycentric positions and velocities at the ejected time step to use in our Solar System integrations.

As a test, we also integrated the present Pluto-Charon system with the four circumbinary moons and the test particle disk. The presence of extra massive bodies in the system results in extra particle loss, as the circumbinary moons help scatter debris inwards. Most of these losses are through ejections instead of collisions. Additionally, significant structure appears in the disk, such as co-orbital debris near the small moons and shepherded rings between the moons. We choose to not analyse these simulations in detail because we are concerned with the impact of the Pluto-Charon binary alone. Additionally, due to the uncertain nature of the origin of the circumbinary moons, there is no way to estimate the appearance of the system at our different Pluto-Charon configurations.

At 10^7 days, our constant orbit simulations show median energy conservation of $\Delta E/E = 1 \times 10^{-11}$ and median angular momentum conservation of $\Delta L/L = 1 \times 10^{-11}$.

We integrate the Pluto-Charon system in isolation despite the potentially significant perturbations from the Sun on long time-scales. There are two major effects the Sun could have on debris in the outer parts of Pluto’s Hill sphere: an induced harmonic oscillation in specific angular momentum due to solar torques and secular perturbations causing Kozai oscillations. Following the example of Benner and McKinnon (1995) and Goldreich et al. (1989), the Sun should drive a change in the specific angular momenta of disk particles with a period equal to half of Pluto’s

heliocentric orbital period, or about 124 years. The change in the mean specific angular momentum simplifies to

$$\frac{\delta h}{\bar{h}} = \frac{15}{8} \frac{P_{\text{particle}}}{P_{\text{Pluto}}} \frac{e_{\text{particle}}^2}{\sqrt{1 - e_{\text{particle}}^2}} \quad (2.2)$$

where P_{particle} denotes the period of the particle in the disk, P_{Pluto} is the heliocentric period of Pluto, and e is the eccentricity of the disk particle. For a disk particle with $e = 0.9$ at 1000 Pluto radii from the barycenter (an orbital period of ~ 8 years), this constitutes only a 10% change in the angular momentum every century; for a disk particle with the same eccentricity at 100 Pluto radii, the difference is less than 0.5%. Our simulations do not produce a population of high apocenter bodies that remain in the simulation for more than about 200 years because things are scattered out of the system very quickly. Thus, this induced oscillation from solar torques is unlikely to impact our results. Similarly, Kozai oscillations induced by the Sun will not affect the outcomes of our simulations. The Kozai timescale for Pluto-Charon and a test particle as the inner binary and the Sun as the outer component, is a few to a few thousand times Pluto’s heliocentric orbital period, depending on the period of the test particle (Fabrycky and Tremaine, 2007). For the average disk particle, the Kozai timescale will be longer than the length of our simulations. While both of these effects will change the orbits of any debris that remains in the system over long time-spans, the fates of particles quantified in this work should not be strongly influenced by the Sun prior to leaving the Pluto-Charon Hill Sphere.

2.3.2 Solar System

We inject particles ejected from Pluto-Charon into the Solar System at three different points in the Pluto-Charon heliocentric orbit: $M_P = 180^\circ$ (apocenter), $M_P = 90^\circ$, and $M_P = 0^\circ$ (pericenter). We also simulate test particles in an evolving Solar System using the migration model described below in Section 2.3.3. We use a Solar System model comprised of the Sun (with mass increased by the masses of the four terrestrial planets), the four giant planets, and Pluto. The positions and

velocities of the planets and Pluto are taken from the JPL HORIZONS catalogue.¹ We randomly sample 16000 test particles, distributed over 100 individual simulations, from the full set of particles ejected from the simulation in which Charon has $a = 17 r_P$ and $e = 0.3$. The test particles are boosted into the Solar System frame from the isolated Pluto-Charon system by adding the Pluto-Charon barycenter position and velocity at the start of the simulation. We run two orientations of the Pluto-Charon disk with respect to the Pluto-Charon heliocentric orbit. The first set is aligned with Pluto’s heliocentric orbit, while the second set is aligned with the present-day Pluto-Charon orbit, having $i = 96.3^\circ$, $\Omega = 223.0^\circ$, and $\omega = 172.6^\circ$ with respect to Pluto’s heliocentric orbit.² We set the time step of the simulations to be 200 days, and the hybrid changeover is set to 3 Hill radii. Planetary radii are calculated using spheres with densities 1.33, 0.70, 1.30, 1.76, and 1.88 g cm⁻³ for Jupiter, Saturn, Uranus, Neptune, and Pluto, respectively. The ejection radius is set to 2000 AU. We integrate the simulations for 1.5 Gyr, or about 6 million heliocentric Pluto orbits.

At 1.5 Gyr, our median energy conservation is $\Delta E/E = 1 \times 10^{-6}$ and our median angular momentum conservation is $\Delta L/L = 4 \times 10^{-12}$.

2.3.3 Migration

We implement the Malhotra (1995a) migration model in both the isolated Pluto-Charon system and the Solar System. In the model, migration is considered a drag force. This drag acceleration takes the form

$$\mathbf{a}_{\text{migration}} = -\frac{\hat{\mathbf{v}}}{\tau} \left[\sqrt{\frac{GM_\odot}{a_{\text{final}}}} - \sqrt{\frac{GM_\odot}{a_{\text{init}}}} \right] \exp\left(-\frac{t}{\tau}\right). \quad (2.3)$$

In the Solar System integrations, the acceleration is applied to each of the giant planets (Pluto is allowed to migrate naturally under the influence of Neptune). We choose $\tau = 2 \times 10^6$ years our migration time-scale, and we use the initial positions,

¹Apocenter in the HORIZONS catalogue occurs on 2114 Feb 22, $M = 90^\circ$ is on 2051 Dec 5, and pericenter is on 1990 Jan 29.

²These angles are taken from the JPL HORIZONS catalogue.

Table 2.1: Initial conditions for migration: we show the initial semi-major axis, prescribed change in semi-major axis, and initial eccentricity for the massive bodies in our simulations. Pluto has no Δa because it is allowed to naturally be captured into the 3:2 resonance.

Planet	a_{init} (AU)	Δa (AU)	e_{init}
Jupiter	5.4	−0.2	0.048
Saturn	8.7	0.9	0.056
Uranus	16.3	2.9	0.046
Neptune	23.2	6.9	0.009
Pluto	32.0	—	0.050

eccentricities, and migration distances ($\Delta a \equiv a_{\text{final}} - a_{\text{init}}$) given in Table 2.1. The orbital angles for the giant planets are the same as in the pericenter simulations, and inclinations are set to the modern-day values. Pluto’s inclination is set to 0° relative to the plane of the Solar System. These values are all consistent with those used in Malhotra (1995a). While this migration model is not as involved as those in more modern works (e.g., Levison et al., 2008), it is adequate to explore some of the impact of a dynamically evolving Solar System on the orbits of Pluto ejecta. We use only this migration model as it is simple to implement; a more complicated migration model is beyond the scope of this chapter.

We use the same hybrid integrator as we did for our non-migrating Solar System simulations, and we adopt the same orbital angles for the giant planets and Pluto in the migration simulations as we do in the pericenter run above in Section 2.3.2. We again use 16000 initial test particles distributed over 100 simulations and run for 1.5 Gyr. The first 100 Myr of each simulation are run with a time step of 100 days, and the final 1.4 Gyr are run with a time step of 200 days. Figure 2.2 shows the final semi-major axes and eccentricities of the massive bodies (the four giant planets and Pluto) in the simulations at the end of 1.5 Gyr. The expected values are shown by the large black squares, and the initial values are shown by the colored squares outlined in black. 60 of 100 runs with the disk aligned with Pluto’s orbit and 66 of 100 runs with the disk aligned with the modern Pluto-Charon orientation finished

successfully with Pluto in the 3:2 resonance; these are the only ones presented in Figure 2.2 and considered for the rest of the analysis. Most of the unsuccessful runs saw Pluto ejected from the Solar System. All semi-major axes for the massive bodies are within 1% of the expected semi-major axes. The eccentricities vary much more, but do match the ranges encompassed by other Solar System migration models, such as those presented in Tsiganis et al. (2005). The final inclinations are also very close to modern-day values.

In the isolated Pluto-Charon system, the only body to which the migration drag force is applied is Charon. The migration time-scale is set to $\tau = 10^4$ yr. We use the Bulirsch-Stoer integrator in the modified MERCURY and integrate for 10^5 yr. A migration time-scale of 10^4 years is short for proposed tidal evolution models for Charon, but, due to computational limitations, we choose a shorter time. However, the dynamics will scale similarly with longer tidal evolution time-scales because the dynamical time-scale of test particles in these regions is very short compared to the speed with which Charon moves radially outward. Particles inside the binary instability boundary will be removed within about 10^4 orbital periods; at the instability boundary of the initial Pluto-Charon orbit, this is around 100 yr, which is much shorter than the time it takes for Charon to migrate through the region.

2.4 Fate of Debris: Collisions with Charon

2.4.1 Relevant Time-scales

The tidal evolution of Charon should take on the order of 1 Myr (Dobrovolskis, 1989; Cheng et al., 2014a). Collisions can occur at any time during or shortly after the migration as the binary instability boundary excites disk material. Observations from *New Horizons* presented in Singer et al. (2016) suggest that Charon’s surface age is upwards of 4 Gyr and could stem from shortly after formation, so these collisions should be preserved.

Because Charon is formed via a violent collision, the surface should not be solid

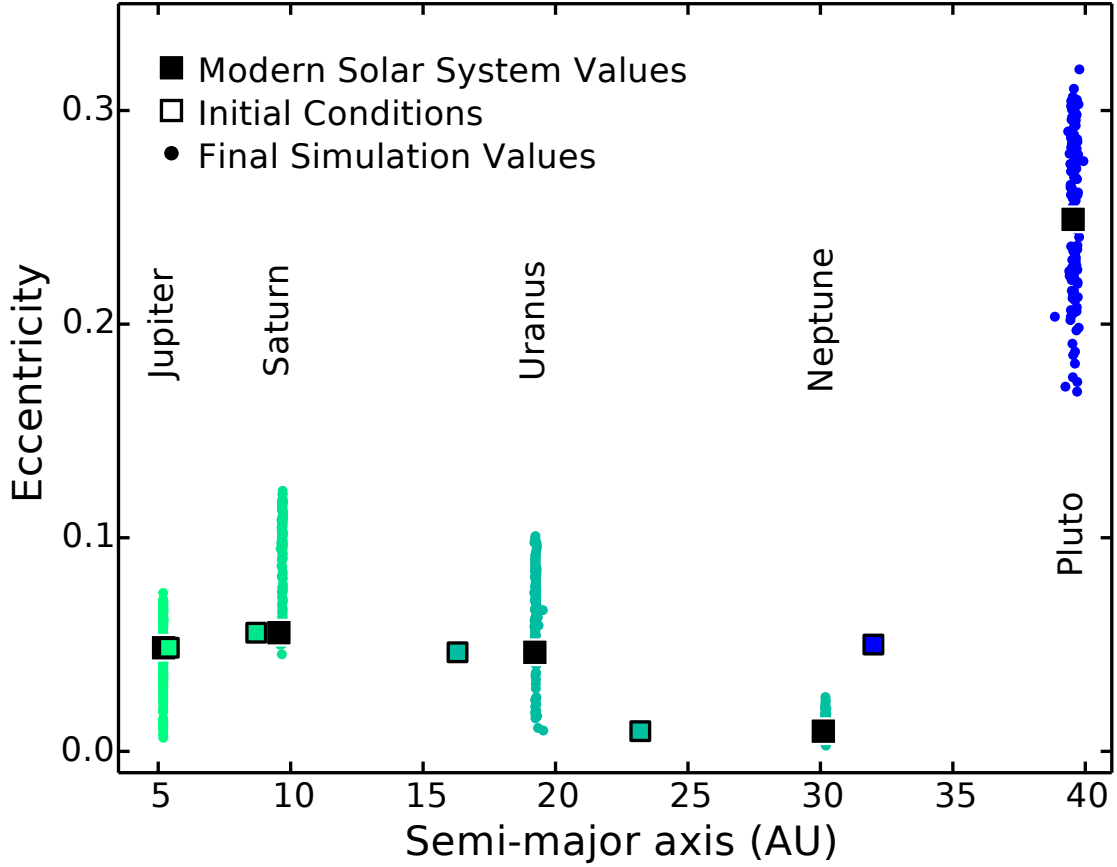


Figure 2.2: The combined final eccentricities vs. semi-major axis for the giant planets and Pluto after 1.5 Gyr in the two sets of simulations that include migration. The color denotes the body, and the large black squares show the modern-day values for each body. The colored square outlined in black shows the initial conditions in our simulations and can also be found in Table 2.1. Pluto migrates under Neptune's influence to its proper semi-major axis and eccentricity. The mean semi-major axis for all simulated bodies is less than 1% different from the actual values. The eccentricities have larger scatter but are consistent with other Solar System migration models, as are the inclinations.

early in the binary’s history. Collisions would therefore not be preserved in this era. Thus, we must estimate a time at which collisions would be recorded. If we turn to the surface cooling time-scales of non-tidally heated bodies in the Solar System, such as an estimated 10^3 years for an atmosphereless Mars from Monteux et al. (2015) or 10^4 – 10^6 years for Earth from Spohn and Schubert (1991), Tonks and Melosh (1993), and others, we can make a rough estimate that the much smaller and icier Charon cooled on time-scales of a few hundred to a few thousand years in the absence of other effects. The surface cooling time-scale is therefore much smaller than the tidal evolution time-scale. Accordingly, a significant fraction of the disk may be unperturbed when Charon solidifies and the continued accretion of disk material should be imprinted on the surface. Note that this cooling time-scale does not account for sources of internal heating, which we discuss in Section 2.4.4.

2.4.2 Collisions and the Disk

Figure 2.3 shows the colliding fraction as a function of barycentric distance for four Pluto-Charon orbits: $a_{\text{PC}} = 5 r_{\text{P}}$ and $e = 0.3$, $a_{\text{PC}} = 17 r_{\text{P}}$ and $e = 0.3$, $a_{\text{PC}} = 17 r_{\text{P}}$ and $e = 0$, and a migrating Charon from $a_{\text{PC}} = 5$ – $17 r_{\text{P}}$ on a circular orbit. The first three are representative of three phases of a proposed tidal evolution model for Charon from Cheng et al. (2014a), while the last actually moves Charon through the disk. The most compact configuration is similar to the orbit at ~ 100 years after impact. The wide, eccentric configuration is most similar to what is expected around 10^4 – 10^5 years after impact and is where we see the most disk disruption take place. Finally, the wide, circular case is similar to the Pluto-Charon system seen today. The semi-regular decreases in colliding fractions in the circular case (third panel) arise where low-order mean motion resonances (such as the 3:2, 2:1, 5:2, and 3:1) cause preferential ejection of material. This circular case is least realistic, as the wide, eccentric Charon would have previously cleared out all of the debris able to interact with a wide, circular Charon.

While the bulk of collisions should occur early, there will be craters from disk debris throughout the migration. Both the most compact case (top) and the migrat-

ing case (bottom) show a sharp decrease in collisions outwards of about 13000 km; the collisions interior occur on time-scales of a few to a few hundred years, which is comparable to the solidification time of Charon. Thus, neither of the collision populations interior to 13000 km would be visible on the surface of Charon. However, in both cases, a significant quantity of disk material remains exterior and interacts with the evolving binary at a later time.

2.4.3 Craters on Charon’s Surface

We can estimate the number of craters visible on the surface of Charon for a given disk profile and size distribution of disk particles. We calculate cratering for two Pluto-Charon configurations: the $a = 5 r_P$ and $e = 0.3$ disk, as this is the stage with the most dynamical evolution of the disk, and the migration model. Additionally, we only take the material exterior to Charon’s orbit (outside the purple region in Figure 2.3) for the constant orbit model because the binary instability boundary would reach this location at roughly 1000 years in the Cheng et al. (2014a) constant Δt model (see Figure 2.1); 1000 years is approximately the estimate for Charon’s surface cooling time-scale. We only consider collisions originating outside of 14000 km in the migration model because the instability boundary will take about 1000 years to move to this location. Typical collision speeds should be roughly the escape velocity from Charon added in quadrature with the relative velocity of the collider and Charon, or about $0.5\text{--}1 \text{ km s}^{-1}$. This velocity of about 0.5 km s^{-1} is about a quarter of the expected velocities of $1\text{--}2 \text{ km s}^{-1}$ for KBOs impacting Pluto and Charon quoted in Greenstreet et al. (2015). We use an impactor-to-crater size ratio of 5, which is a small but consistent value calculated using Charon’s escape velocity in Greenstreet’s equation 5. *New Horizons* has a resolution of $1\text{--}1.5 \text{ km}$ on the surface of Charon for the largest data sets (Moore et al., 2016), so we take “observable” craters to be those larger than 3 km , implying an impactor at least 600 m in diameter.

Canup (2011) finds that a debris disk from a Charon-forming impact can extend up to 30 Pluto radii and will range in mass from $10^{20}\text{--}10^{24} \text{ g}$. We adopt a disk with

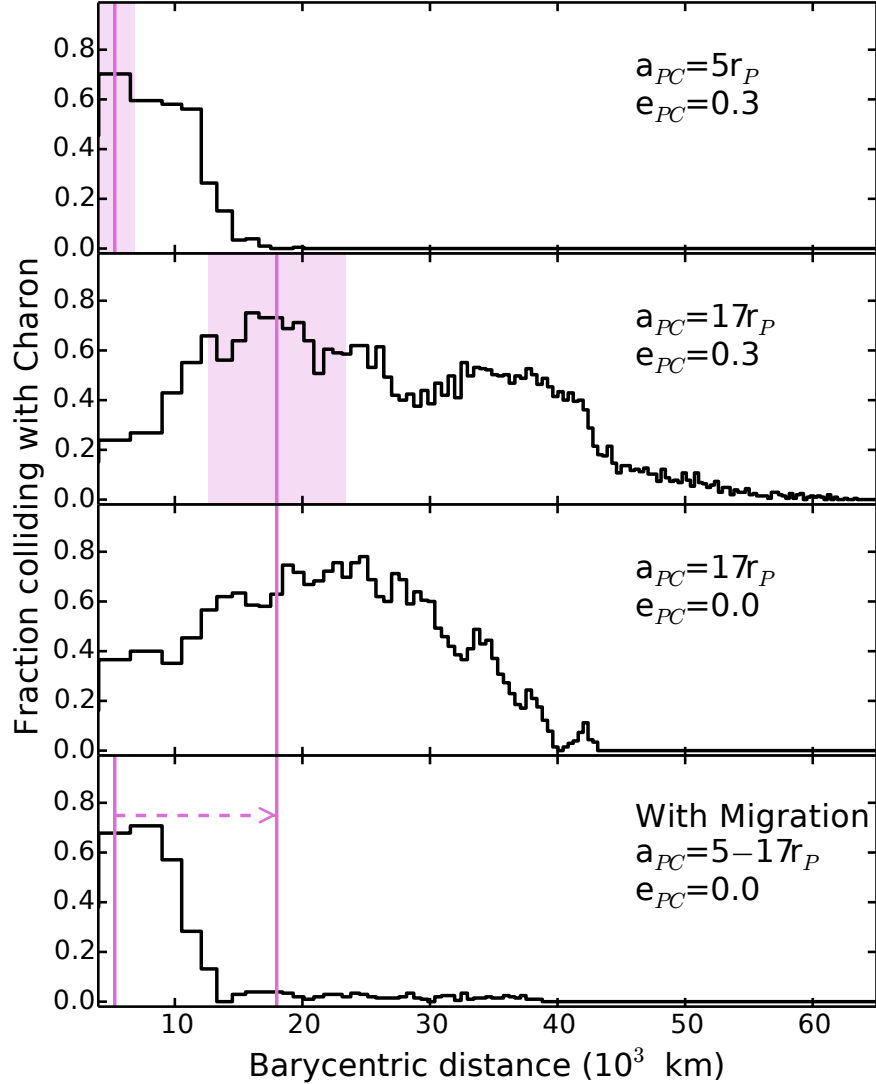


Figure 2.3: The fraction of disk particles colliding with Charon per radial bin as a function of barycentric distance. The four panels show different Pluto-Charon orbits: $a = 5r_P$ and $e = 0.3$, $a = 17r_P$ and $e = 0.3$, $a = 17r_P$ and $e = 0$, and a migration from $5-17r_P$ with zero eccentricity. The purple line shows the semi-major axis of Charon, and the purple rectangle shows the radial extent of Charon's orbit (pericenter to apocenter). In some regions, upwards of 50% of material collides with Charon. The outer edge of collisions is governed by the instability boundary; exterior to this boundary, material is unperturbed.

radial extent of 30 Pluto radii and mass 10^{22} g for our analysis, an optimistic but not unrealistic disk. We convolve this disk model with the constant density, large radius test particle disk in our N -body simulations. We then can calculate a disk surface density parametrized by the disk surface density index β and radial extent r over a Pluto radius r_P such that

$$\Sigma(r) = \Sigma_0 \left(\frac{r}{r_P} \right)^{-\beta}. \quad (2.4)$$

Σ_0 is a normalisation factor calculated by equating the disk mass and the integrated surface density. By multiplying the surface density profile from the giant impact-motivated disk with our collision fractions from our simulated disk, we can calculate a colliding mass per radial bin. Then, we must assume a particle size distribution to find a number of colliders. We take this to be a power law parametrized by particle size index q . Thus

$$N(s) = N_0 (2s)^{-q}, \quad (2.5)$$

where s is the particle radius and N_0 is found by assuming that each body is a sphere with density $\rho = 1 \text{ g cm}^{-3}$, an icy composition, and that our particles range in size from 1 cm to 5 km. We choose the upper limit of $s = 5$ km so that our debris is equal in size or smaller than the existing moons. Decreasing either the upper or lower size limit increases the number of visible craters, while increasing either limit decreases visible craters because more of the fixed mass goes into larger bodies, dropping the total number of colliders. Finally, we sum the number of colliders in all radial bins as a function of size and calculate the number with radii greater than 300 m. These are the impacts from the disk that would be visible on the surface of Charon with *New Horizons* imaging.

Our estimates for the number of colliders as function of the particle size index q and disk surface density index β are shown in Figure 2.4 for two of the Pluto-Charon orbits we simulate. We take the $a = 17 r_P$ and $e = 0.3$ simulation as the most optimistic case (most collisions) and the migration model as the least optimistic (fewest collisions) for simulations in which Charon is near its current orbit. We show typical values of β for protoplanetary disks (which normally range from 0.5–

1.5) and proto-lunar disks (e.g., Charnoz and Michaut, 2015). The value of $q = 3$ labelled KBO is taken from crater size measurement on Charon from Singer et al. (2016). At this value of q , we estimate that there may be hundreds to hundreds of thousands of craters on the surface of Charon that stem from the Charon-forming disk. We expect the craters to be evenly distributed across Charon’s surface because Charon was not initially tidally locked to Pluto and the height of the disk at the instability boundary (where the colliders typically originate) is comparable to the size of Charon. However, these craters from the disk would be among the oldest on the surface and among the smallest with the range of allowed particle sizes we have chosen. Singer et al. (2016) note that there appears to be a lack of small craters on Charon’s surface, which suggests fewer impacts originating from the disk itself. The real disk is therefore likely comprised of smaller debris (less than a few km in radius), smaller in radial extent, or has a steeper surface density index.

If it is possible to identify and date craters on Charon as stemming from the disk, clues as to Charon’s tidal evolution outward can be inferred. Encounter velocities tend to be lower when Charon is in an eccentric orbit because the encounters are more likely to occur in the outer part of the orbit where orbital velocities are slower. Thus, if we can assume a similar size of impactors through all stages of the tidal evolution, epochs of an eccentric Charon would show smaller craters relative to a circular Charon.

Note that we do not consider collisions with Pluto for two important reasons: first, collisions with the more massive component of a binary are intrinsically rarer. We see a factor of 3–4 reduction in the number of collisions with Pluto compared to collisions with Charon. Secondly, the resurfacing time-scale of Pluto (specifically, Sputnik Planum) has been estimated to be less than 10 Myr by Moore et al. (2016) and Trilling (2016). The surface is therefore expected to be much younger than Charon, although some regions may be much older and thus susceptible to disk cratering. Any craters originating from disk debris in young areas would be erased by recent or previous resurfacings.

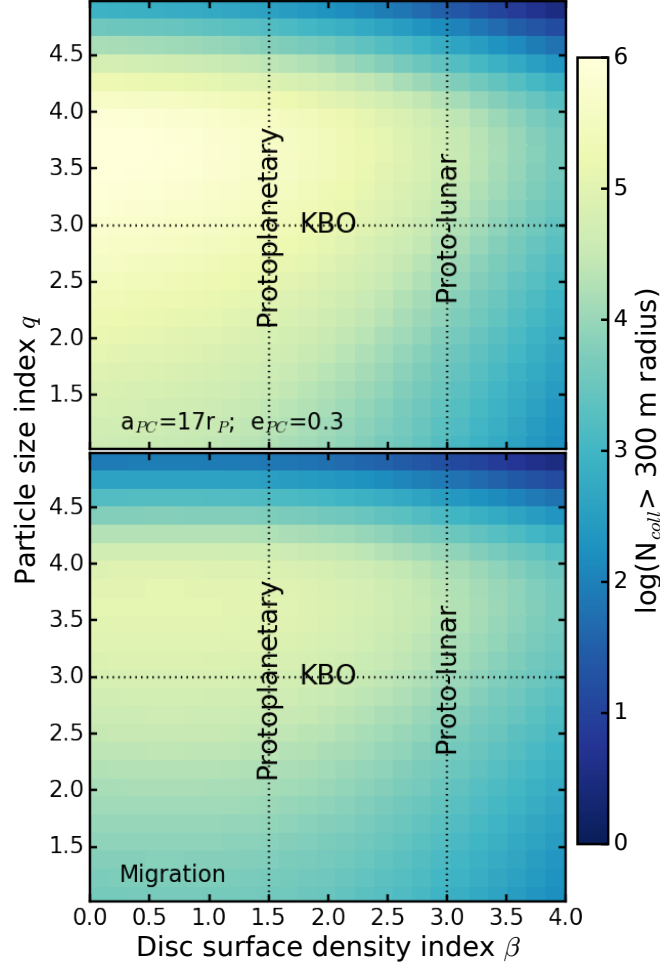


Figure 2.4: The number of colliders that would leave visible craters as a function of particle size index q and disk surface density index β . The parent disk extends to $30 r_P$ and had a mass of 10^{22} g. The top panel shows the number of colliders for Charon with static orbit $a = 17 r_P$ and $e = 0.3$ and the bottom panel shows the same for the migrating Charon. Only bodies external to the maximum extent of Charon’s orbit are considered in the eccentric case and external to the instability boundary at 1000 years, located at 14000 km, in the migrating case (see the second and fourth panels of Figure 2.3, respectively). Colliders are taken to be observable if they are greater than 600 m in diameter, which should correspond to a crater at least 3 km in diameter (3 km is twice the resolution of *New Horizons*). Also labelled are typical values of β for protoplanetary and proto-lunar disks. The q value for Kuiper belt objects is taken from crater size measurements on the surface of Charon from Singer et al. (2016). For reasonable values of q and β , there should be hundreds to a few tens of thousand craters on Charon’s surface from the Charon-forming disk.

2.4.4 Internal Heating and Charon's Surface

In the previous sections, we did not account for the effects of internal heating, either through tidal or radiogenic processes. These two effects might prolong the era of a liquid surface on Charon or cause slow resurfacing.

Jackson et al. (2008) parametrize the tidal heating rate per surface area (their equation 3) as

$$h = \left(\frac{63}{16\pi} \right) \frac{(GM_P)^{3/2} M_P R_C^3}{Q'_C} a^{-15/2} e^2. \quad (2.6)$$

Here, P denotes Pluto and C denotes Charon, which have been changed from Jackson's S (star) and P (planet), respectively. Q' is the tidal dissipation parameter and is given as $Q' = 3Q/(2k_2)$. Q is the tidal dissipation function (taken here to be 100), and k_2 is the Love number. In the analysis, Jackson et al. (2008) consider anything with $h > 2$ to be highly volcanic, $2 > h > 0.04$ to have enough heating for tectonic activity, and anything less than this to have too little internal heating to promote activity (what we refer to as dead). For reference, Jupiter's moon Io has $h \sim 2 - 3$ W/m², while Europa may have tidal heating as high as $h \sim 0.2$ W/m². Earth's heating, which comes from radiogenic sources and the heat of formation, is about 0.08 W/m². We do not expect a surface in the volcanic regime to retain any craters as resurfacing is very fast. Craters may be retained if the body is tectonic, although relaxation of the surface material may make the craters smooth out or fill in over time. Craters on dead bodies should not undergo significant evolution without outside influence.

Figure 2.5 presents h vs a for an eccentric Charon. We adopt the constant Δt semi-major axis evolution from Cheng et al. (2014a) (the solid black line in Figure 2.1) and a constant eccentricity of 0.3. The two lines denote different values of the Love number k_2 . Blue shows an estimate of Charon's Love number from Murray and Dermott (1999) Table 4.1, who estimate $k_2 = 0.006$, and red shows a rocky, Earth-like Love number of 0.3. We color regions based on the Jackson et al. (2008) demarcations: yellow shows the volcanic region where tidal heating causes violent and fast resurfacing, green shows the tectonic region where a solid surface

may be slowly changed over time, and blue shows geologically dead bodies. We also plot reference values for Io, Europa, and Earth. The factor of 50 difference between the two Love numbers has a large impact on the expected observability of craters from the disk. With a large Love number, Charon spends the majority of the early evolution firmly in the volcanic region. It is therefore unlikely that the surface would retain any craters as constant resurfacing is probable. With the lower, and likely more appropriate, Love number, the time spent undergoing violent tidal heating is less than our estimated cooling time-scale in Section 2.4.1. Thus, craters should be imprinted as soon as the surface cools from formation.

For any craters to be visible, the surface needs to be solid and slowly changing (for our purpose, in the tectonic regime) before the binary instability boundary reaches the outer edge of the disk. Assuming the same disk extent of $30 r_{\text{Pused}}$ above and using the $e = 0.3$ binary instability boundary in Figure 2.1, the surface of Charon needs to solidify by, generously, about 5000 years after formation to retain any craters from the debris disk. We can change the time spent in the volcanic state most easily through k_2 , as shown above, or through eccentricity. If Charon begins with a lower eccentricity, the time that Charon spends in the volcanic regime is much shorter because tidal heating scales as e^2 . For $e = 0.1$ and $k_2 = 0.3$, Charon moves into the tectonic regime by about 800 years after formation. For a circular migration scenario, Charon undergoes no tidal heating.

In the tectonic regime, craters may last on the surface for thousands to millions of years. Moore et al. (1998) find that craters on the surface of Europa may last for up to 10^8 years. Because Charon should be absolutely cold by the end of the tidal evolution at $\sim 10^6$ years, craters from the tectonic regime may still be visible. They may show similar features to impact craters on Europa noted by Moore et al. (1998, 2001) such as shallow basins or relaxed crater walls. In extreme cases, the craters may resemble more of a circular ridge than a true crater. This may be a way to distinguish craters from the debris disk from KBO craters: as debris craters will be among the oldest and may stem from a time when Charon had different surface properties, the physical appearances of the two crater populations may be

very different.

The other important source of internal energy, radiogenic heating, is orders of magnitude smaller but may have an impact on Charon’s surface a few Gyr after formation. Desch et al. (2009) run a full radiogenic heating model for Charon and find that the heat flux through Charon’s surface peaks at 5 mW/m^2 at 0.5-1.5 Gyr after formation. This is enough heat flux to differentiate the interior of Charon but cannot melt the crust, which is expected to be 60–85 km thick (Rubin et al., 2014). Thus, once the surface of Charon has solidified, further heating should not completely resurface the moon; this is consistent with surface age measurements from Singer et al. (2016). Radiogenic heating is enough to make the surface malleable and allow long-term relaxation of craters. Additionally, radiogenic heating may drive cryovolcanism on Charon. Cryovolcanism could contribute to minor resurfacing by filling in craters and causing erosion. Desch et al. (2009) estimate that around 120 m of ice will be deposited uniformly on the surface through cryovolcanism over the past 3.5 Gyr, although later studies such as Neveu et al. (2015) suggest that this may be an overestimate of the cryovolcanic activity because the surface may be difficult to crack. While the few tens of meters of cryovolcanic residue is not enough ice to completely remove kilometre-sized craters from the surface, when coupled with more extreme relaxation early in Charon’s history, the oldest craters are likely to be very eroded and difficult to find.

2.5 Fate of Debris: Ejections into the Solar System

2.5.1 Ejections and the Disk

As the binary instability boundary sweeps out through the disk with Charon’s migration, debris is more likely to be ejected from the system than collide with either member of the binary. We show the ejecting fraction per radial bin in Figure 2.6 for the four Pluto-Charon orbits described in Section 2.4.2. In the three non-migrating orbits, ejections increase with radial distance in the disk. When migration is included, ejections constitute a high fraction of particle loss from the outer edge of

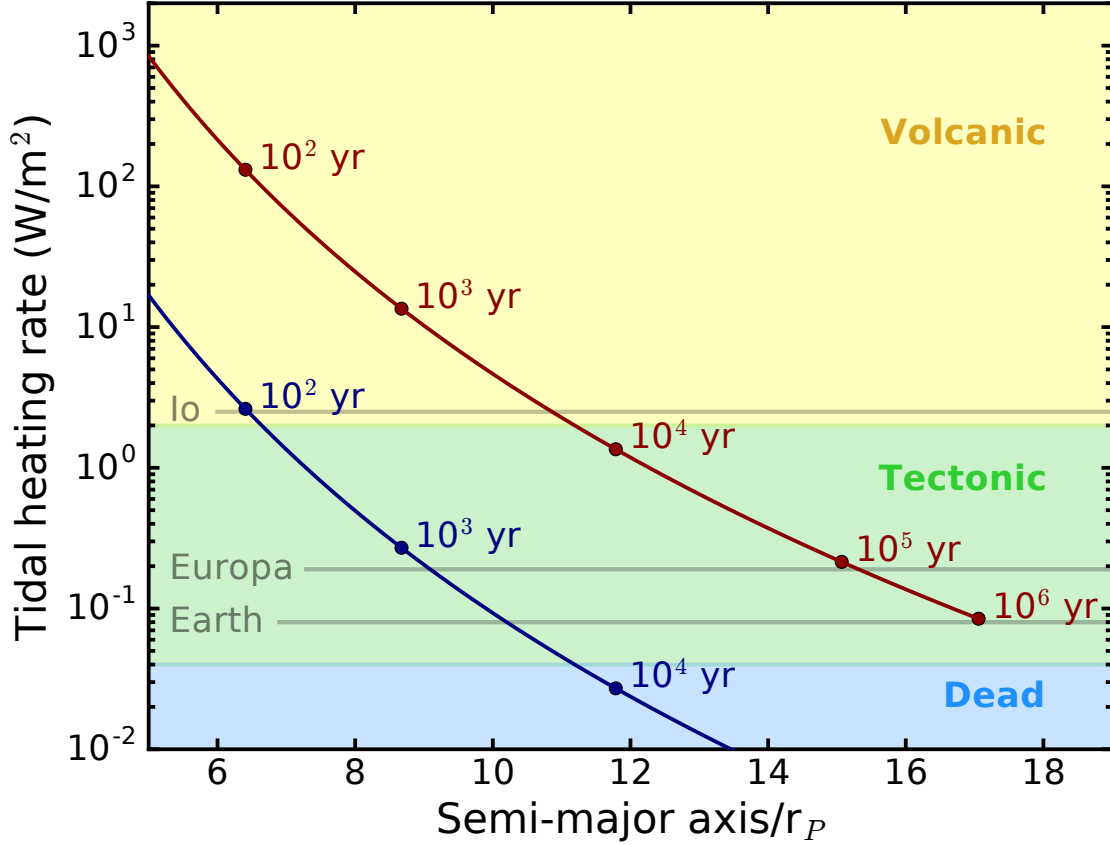


Figure 2.5: The tidal heating rate per unit surface area for Charon’s tidal evolution history. We apply the Cheng et al. (2014a) constant Δt semi-major axis evolution at constant $e = 0.3$ to equation 2.6. The blue line shows the tidal heating rate for Charon with $k_2 = 0.006$ from Murray and Dermott (1999) Table 4.1, and the dark red line shows the tidal heating rate for a Charon with an Earth-like Love number of $k_2 = 0.3$. The yellow region shows what Jackson et al. (2008) consider volcanic, or violently disturbed from tidal heating, green shows the tectonic regime where there may be some surface activity, and blue shows heating rates that lead to a geologically dead body. Io, Europa, and Earth have been labelled for reference. For the rocky Love number, Charon’s surface would not cool enough to retain craters (cross the volcanic-tectonic boundary) until nearly 10^4 years after formation. As the binary instability boundary reaches the outer extent of the debris disk at around 5000 years after formation, we would not expect to see any craters from the debris disk. With the icy Love number, Charon should not experience significant tidal heating after a few hundred years, so craters from the debris disk should be preserved.

the initial instability boundary to the final instability boundary. The slight decrease in ejection fraction as a function of radius occurs because particles are either put on semi-stable eccentric or inclined orbits or have not yet been destructively perturbed (put on an orbit that leads to loss). We do not include collisional damping of disk particles, which Walsh and Levison (2015) show can help stabilise debris, especially in orbits close to the instability boundary. Collisional damping time-scales are on the order of a few tens to a few hundred years (about an order of magnitude shorter than the instability time-scale), so this could have significant implications for the survival of a ring near the instability boundary.

We record the positions and velocities of all ejected test particles with respect to the Pluto-Charon barycenter when the test particles reach our ejection radius of 0.06 AU, roughly Pluto’s Hill radius at 40 AU. The particles are ejected at 1–15+ times Pluto’s escape velocity at the Hill sphere. Charon’s eccentricity is the main factor in the ejection velocity; because encounter velocities are typically lower in the eccentric case, ejection velocities are correspondingly lower (typically by a factor of 2–3). This effect is invariant of Charon’s semi-major axis. The majority of ejections in the eccentric case have velocities between 1–5 times escape velocity, while the circular case tends to have ejections with velocities 3–10 times escape velocity.

2.5.2 Debris in the Solar System

We release the ejected test particles from the isolated Pluto-Charon simulation with orbit $a = 17 r_P$ and $e = 0.3$ into the Solar System so that we can track the evolution of the Pluto-Charon disk debris. We simulate three configurations of the modern-day Solar System (with Pluto at $M = 0, 90, \text{ and } 180^\circ$, respectively) and one with the migration model presented in Malhotra (1995a); we orient the Pluto-Charon disk in two ways, labeled “Aligned with P-C heliocentric orbit” and “Misaligned with P-C heliocentric orbit”, as described in Section 2.3.2. The fates of these disk-ejected test particles after 1.5 Gyr are shown in Table 2.2. The integration including migration retains the largest number of test particles, and the integrations with a misaligned disk retain more test particles in all four initial Solar System configurations. The

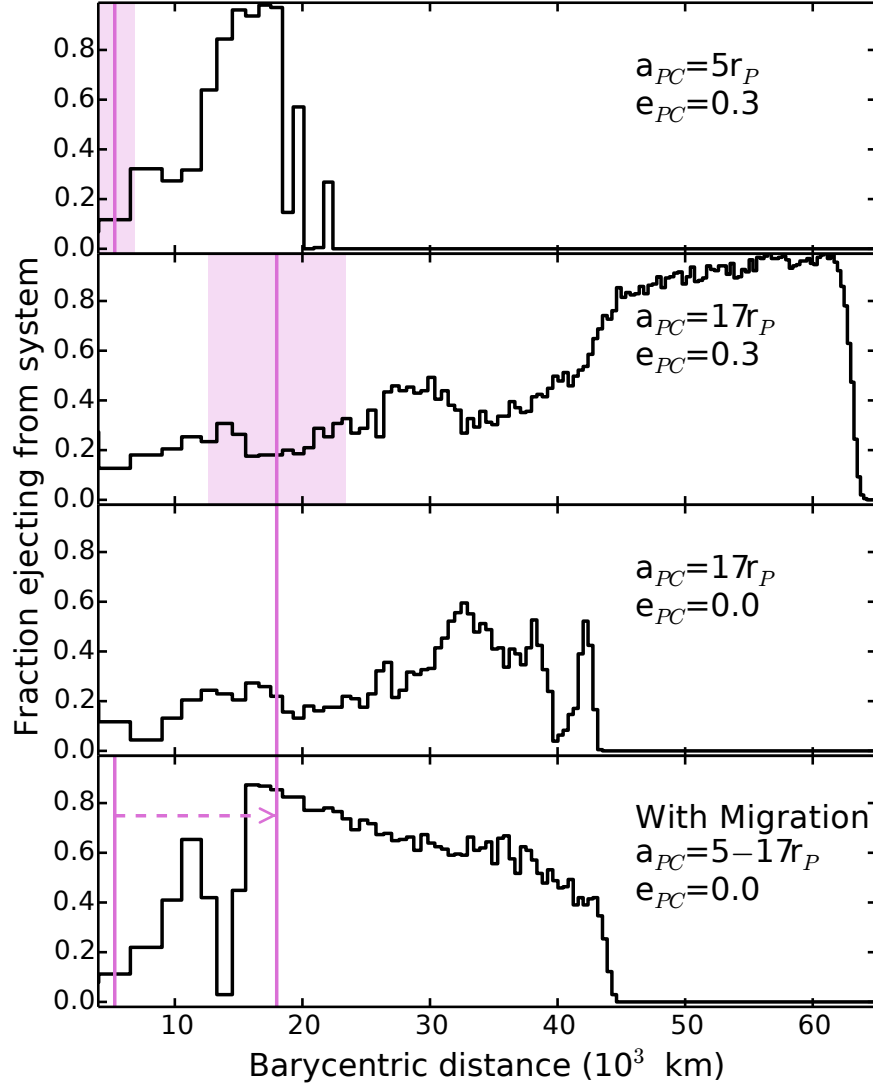


Figure 2.6: The fraction of disk particles ejected from the Pluto-Charon system per radial bin as a function of barycentric distance. The figure follows the same style as Figure 2.3. Ejections become more common in the outer parts of the disk. In the migration case, the sharp increase in ejections outwards of 12000 km occurs because the outer edge of the instability region sweeps through the disk and perturbs bodies such that they eject instead of collide. Ejections are nonexistent outside the instability boundary because the disk has not been perturbed.

number of collisions is roughly constant throughout; the most common collisions by far are with Jupiter, which account for nearly 50% of all collisions. Nearly equal numbers of collisions occur with Neptune and Saturn at 10–20% each, while collisions with the Sun and Uranus are rare (less than 10% each in most cases). Collisions with Pluto are non-existent.

The semi-major axes and eccentricities of the remaining particles are shown in Figure 2.7. In all cases, the majority of the remaining particles populate the 3:2 resonance alongside Pluto. Nearby resonances can also be populated. Specifically, we see resonant populations around the 5:4, 4:3, 5:3, and 7:4 resonances with Neptune; some other higher-order resonances may also be populated in between those listed. We show the fraction of test particles in each resonance in Table 2.3. In the simulations with a non-migrating Solar System, test particles with high initial velocities are more likely to escape the 3:2. High velocity test particles are lost more frequently in the misaligned disk, leaving a more dominant population in the 3:2. The majority of bodies that end a simulation in a resonance other than the 3:2 are near their initial resonance at the beginning of the simulation due to the additional velocity from ejection modifying the orbital elements. For instance, a body ejected at Pluto’s heliocentric apocenter with 10 times Pluto’s escape velocity at the Hill sphere (meaning an addition of 140 m/s to Pluto’s orbital velocity of 3.7 km/s) will have a new semi-major axis of 41.4 AU compared with Pluto’s semi-major axis of 39.5 AU. This places the body just interior to the 5:3 resonance. The occupation of other resonances is more common for release near apocenter in the aligned simulations because a small velocity change in the particle can cause a larger change in the semi-major axis at apocenter. We see this trend disappear in the misaligned disk because the high velocity particles are put onto unstable orbits when ejected from the disk. In the migrating case, though, there does not appear to be a preference with initial velocity. Particles in all five resonances are consistent with libration around the center of $\phi_{\text{res}} = 180^\circ$. Those in the 3:2 specifically tend to librate with a higher amplitude than Pluto’s $\Delta\phi_{\text{res}} = \pm 82^\circ$: the amplitude of the libration of the resonant angle is closer to 120° .

In the eight simulations presented here, a population of debris ejected from the Pluto-Charon disk always remains in the Solar System. These bodies would constitute a Pluto-Charon collisional family. Using the same methodology as presented above to determine the number of craters on Charon’s surface, we can estimate the properties of members of the family. We use the same disk mass and extent as before, but we relax the size constraints to allow the debris to grow to 30 km in radius. This is about the size of Hydra. The inner cutoffs of the disk are maintained, as it would take time for debris to coagulate into large sizes observable in the Kuiper belt. We take “large” debris that could be observed by future surveys and constitute a collisional family to be greater than 10 km in radius. For the Pluto-Charon orbit with $a = 17 r_P$ and $e = 0.3$, we calculate that there would be a maximum of 70 objects ejected from the disk larger than 10 km. For the migrating Pluto-Charon, a maximum of 200 objects larger than 10 km would be ejected. Only 7–21% of these bodies survive to 1.5 Gyr with either disk orientation. We therefore estimate that there could be 5–15 large KBOs stemming from the Pluto disk that gives the most collisions, while the disk that gives the most ejections seeds the Kuiper belt with 14–42 bodies.

While we have used a smooth migration model in this work, it is possible that the early history of the Solar System was more chaotic (e.g., the Nice model from Tsiganis et al., 2005; Levison et al., 2008, among others). As long as a Solar System migration model can place Pluto in the correct orbit, our results should be relatively unaffected. Because the debris ejected from the Pluto-Charon system is very dynamically similar to other Kuiper belt populations, there should be similar dynamical evolution between ejected debris and the resonant Kuiper belt objects.

These members of a Pluto collisional family would be difficult to distinguish from other KBOs. The particles in our simulations do not have any obvious association in physical space or orbital angles with Pluto at the end of the simulations (perhaps a slight clustering in both ω , the argument of pericenter, and Ω , the longitude of ascending node). The most promising method to identify KBOs as members of a Pluto family is through composition; they should have a composition similar to

Table 2.2: Fate of particles in Solar System integrations: The first column shows the orientation of the debris disk at the start of the simulation, the second column shows the starting position of Pluto, the third shows the number of particles in the sample, and the final three columns show the percentage of particles that remain in the simulation, are ejected, or collide with massive bodies or the Sun.

	Integration	N_{tot} $\times 10^3$	Remain %	Eject %	Collide %
<i>Aligned</i>	Apocenter ($M = 180$)	16	13.1	85.5	1.4
<i>with P-C</i>	$M = 90$	16	8.7	89.9	1.5
<i>heliocentric</i>	Pericenter ($M = 0$)	16	6.7	92.0	1.3
<i>orbit</i>	With Migration	9.6	20.7	78.2	1.1
<i>Misaligned</i>	Apocenter ($M = 180$)	16	14.4	81.2	1.4
<i>with P-C</i>	$M = 90$	16	8.9	89.4	1.7
<i>heliocentric</i>	Pericenter ($M = 0$)	16	11.4	87.3	1.3
<i>orbit</i>	With Migration	10.56	17.3	81.4	1.3

Pluto’s icy moons. Additionally, following the method of Brown et al. (2007) in calculating the velocity dispersion of the collisional family, the plutino members of our remaining debris have a low velocity dispersion of order 100–200 m/s.

2.6 Conclusions and Discussion

This work aims to investigate the impact of a debris disk from the Charon-forming giant impact in both the Pluto-Charon system and in the Kuiper belt. We present N -body simulations of the isolated Pluto-Charon binary to follow the fates (collisions and ejections) of debris in the disk, and we also present simulations of the evolution of this debris in the Solar System. We find the following:

1. The current circumbinary moons, Styx, Nix, Kerberos, and Hydra, did not form in situ if Charon has an eccentric tidal evolution history. The Holman and Wiegert (1999) instability boundary crosses at least one of the moons’ current positions if Charon has $e > 0.048$ at its current semi-major axis; many realisations of the Charon-forming impacts from Canup (2005, 2011) have the moon forming with eccentricity from 0.1–0.8. Thus, circumbinary moon formation mechanisms must either invoke a circular tidal evolution for

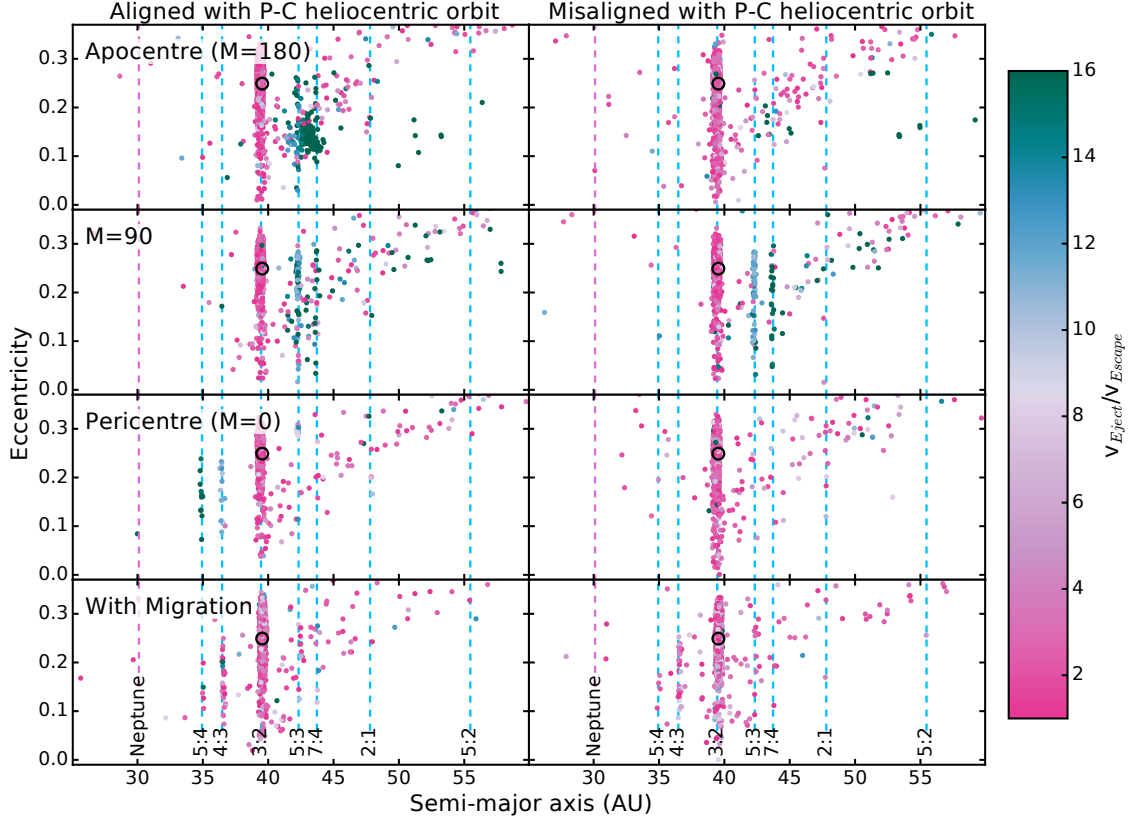


Figure 2.7: Eccentricity vs. semi-major axis after 1.5 Gyr for wight sets of simulations in which ejected debris from Pluto is released into the Solar System. The panels, from top to bottom, show debris initially released when Pluto is at apocenter, $M = 90^\circ$, pericenter, and in a Solar System with migration. The columns show the results for different initial orientations of the Pluto-Charon disk. color denotes the initial velocity of the particle (when it leaves Pluto’s Hill sphere) relative to the escape velocity from Pluto. The black open circles show the current location of Pluto. The dashed line on the left shows the location of Neptune, while the blue dashed lines show the locations of first, second, and third order resonances. While most of the particles are ejected, 60–80% of those that remain are trapped in the 3:2 as a population of plutinos. The majority of other remaining particles, which also tend to be the initially higher velocity particles, are captured into nearby resonances.

Table 2.3: Fraction of remaining particles in resonances: The first column shows the orientation of the debris disk at the start of the simulation, the second shows the starting position of Pluto, the third shows the number of particles that remain in the simulations after 1.5 Gyr, and the last five columns show the percentage of remaining particles that fall into the listed first, second, and third order resonances.

	Integration	N _{rem}	3:2 %	5:4 %	4:3 %	5:3 %	7:4 %
<i>Aligned</i>	Apocenter	2112	67.1	0.1	0.1	6.3	6.3
<i>with P-C</i>	$M = 90$	1423	61.6	0.1	0.1	6.7	2.2
<i>heliocentric</i>	Pericenter	1065	60.2	1.0	1.4	3.2	0.9
<i>orbit</i>	With Migration	2040	79.6	0.3	1.5	1.0	0.6
<i>Misaligned</i>	Apocenter	2793	81.2	0.1	0.2	0.5	0.7
<i>with P-C</i>	$M = 90$	1437	65.6	0.1	0.1	4.7	1.8
<i>heliocentric</i>	Pericenter	1824	74.0	0.2	0.1	0.7	0.4
<i>orbit</i>	With Migration	2259	83.3	0.3	1.6	0.9	0.3

Charon (or one that leaves Charon on a circular orbit long before it reaches its current semi-major axis) or involve forming the moons after Charon reached its current orbit (through capture, disruption of other bodies, or some other mechanism).

2. The predominant loss mechanisms in a debris disk around Pluto-Charon are collisions with Charon and ejections. The amount of clearing is a strong function of Charon’s eccentricity. Collisions are most common from particles that begin close to Charon, while ejections begin to dominate in the outer disk. Including migration in the simulations causes ejections to increase dramatically because the binary instability boundary interacts with previously unperturbed disk material as the Pluto-Charon orbit expands. Walsh and Levison (2015) find that including collisional evolution in the disk may stabilise material on shorter time-scales, but interactions with the instability boundary will always cause particle loss.
3. Collisions with Charon are most common for a wide orbit, eccentric Charon, such as may have existed near the end of the tidal evolution process. Collisions with Charon are the least common if migration is included. Ejections dominate

exterior to Charon’s orbit in the wide, eccentric case when Charon undergoes eccentric tidal evolution because the instability boundary is large. Ejections dominate the majority of the disk in the migration case because of the moving instability boundary.

4. Assuming a reasonable, realistic (albeit optimistic) disk from Canup (2011) and accounting for a surface solidification time-scale of a few hundred to a few thousand years, we predict hundreds to thousands of craters visible by *New Horizons* on the surface of Charon that stem from the disk and not incident KBO collisions. It would be difficult to disentangle these populations from size alone as crater-to-impactor size ratios (collisional velocities) are similar. It is probable that the debris has a different size distribution than KBOs, in addition to a different average impact velocity, so the presence of two distinct crater populations on the surface of Charon might give insight into the disk. The apparent lack of small craters on Charon noted by Singer et al. (2016) already has implications on the extent or composition of a debris disk.
5. Violent tidal heating during the early tidal evolution of Charon may prevent craters from forming on the surface. If the surface solidifies while tidal heating is still warming the interior, craters should form but may relax. Radiogenic heating later in the system’s history (Gyrs after formation) may contribute to more surface relaxation and/or cryovolcanic resurfacing. While neither process should cause the oldest craters to disappear, old craters, such as those originating from the debris disk, may appear to be filled in or have indistinct crater walls. The physical appearance of old craters may help distinguish craters from the disk and craters from KBOs.
6. About 80–90% of material ejected into the Solar System is lost within 1.5 Gyr, regardless of initial Pluto position or inclusion of migration. The material that remains tends to reside in the 3:2 resonance with Neptune, thereby maintaining a similar orbit to Pluto. Some material populates nearby resonances, especially the 5:4, 4:3, 5:3, and 7:4 resonances. The material that remains does not show

any strong correlation at the end of the simulations with the initial position of Pluto or the other planets. The objects in resonances, especially in the 3:2, have resonant angles consistent with librating orbits.

7. Using the same methodology that was used to calculate crater numbers and the most optimistic ejection profile, we estimate anywhere from 14–42 icy bodies greater than 10 km in radius could be produced through ejections from the Pluto-Charon disk, forming a “Pluto disk collisional family.” Larger, more easily observable members of a Pluto collisional family may originate from the Charon-forming impact itself, such as is seen with the Haumea collisional family. Members of the collisional family should have similar icy composition to the original disk and a low velocity dispersion. We find no evidence that a collisional family will be disrupted by the migration of the giant planets in the early Solar System, nor will it be disrupted through secular or resonant effects over Gyr time-scales.

The formation of the Pluto-Charon binary and its moons remains both a fascinating and frustrating problem, especially with the enhanced view of the system provided by the *New Horizons* flyby in July 2015. Through potentially observable tracers such as craters from the debris disk on the surface of Charon or the presence of a Pluto collisional family, we might be able to better constrain the formation and early evolution of this intriguing system.

Acknowledgements

Our gratitude to our anonymous referee for insightful comments that improved this manuscript. Sincere thanks to Alex Parker, Renu Malhotra, Kathryn Volk, Andrew Shannon, and Matija Ćuk for helpful discussions pertaining to this work. RAS is supported by the National Science Foundation under Grant No. AST-1410174 and Grant No. DGE-1143953. KMK is supported by the National Science Foundation under Grant No. AST-1410174. The numerical simulations presented herein were

run on the El Gato supercomputer, which is supported by the National Science Foundation under Grant No. 1228509.

CHAPTER 3

Machine Learning Classification of Kuiper Belt Populations

*This chapter has been accepted to MNRAS as Smullen, R. A. and Volk, K. 2020
(DOI: 10.1093/mnras/staa1935)*

Abstract

In the outer solar system, the Kuiper Belt contains dynamical sub-populations sculpted by a combination of planet formation and migration and gravitational perturbations from the present-day giant planet configuration. The subdivision of observed Kuiper Belt objects (KBOs) into different dynamical classes is based on their current orbital evolution in numerical integrations of their orbits. Here we demonstrate that machine learning algorithms are a promising tool for reducing both the computational time and human effort required for this classification. Using a Gradient Boosting Classifier, a type of machine learning regression tree classifier trained on features derived from short numerical simulations, we sort observed KBOs into four broad, dynamically distinct populations—classical, resonant, detached, and scattering—with a >97 per cent accuracy for the testing set of 542 securely classified KBOs. Over 80 per cent of these objects have a $> 3\sigma$ probability of class membership, indicating that the machine learning method is classifying based on the fundamental dynamical features of each population. We also demonstrate how, by using computational savings over traditional methods, we can quickly derive a distribution of class membership by examining an ensemble of object clones drawn from the observational errors. We find two major reasons for misclassification: inherent ambiguity in the orbit of the object—for instance, an object that is on the edge of resonance—and a lack of representative examples in the training set. This work provides a promising avenue to explore for fast and accurate classification of

the thousands of new KBOs expected to be found by surveys in the coming decade.

3.1 Introduction

3.1.1 The Kuiper Belt

The Kuiper Belt consists of many sub-populations of small bodies in the outer solar system. The orbital distribution of Kuiper Belt objects (KBOs) records the complex early dynamical history of the solar system’s giant planets as well as a variety of current dynamical processes (see, e.g., Morbidelli et al., 2008; Dones et al., 2015). In order to use observations of KBOs to constrain processes in the current and early solar system, they must be classified into different dynamical groups. The classification of these populations is a critical first step towards identifying distinct compositional classes in the Kuiper Belt that might be indicative of formation processes (e.g., Pike et al., 2017) and constraining models of the early dynamical evolution of the solar system by making direct comparisons between models and observations (e.g., Nesvorný, 2015; Nesvorný et al., 2019a,b; Chen et al., 2019a).

Different classification schemes exist for the Kuiper Belt, but here we will use Gladman et al. (2008)’s scheme. Briefly, this scheme divides KBOs into classical belt objects, scattering objects, resonant objects, and detached objects, the detailed definitions of which are described in more detail in Section 3.2.1. Classical belt objects are a mixture of dynamically cold and dynamically excited KBOs mostly in the semi-major axis range $a \sim 36 - 50$ au; identifying these objects in an observational sample is important because the dynamically cold sample of classical objects are generally thought to have formed in situ and to represent a remnant of the original planetesimal disc (see, for example, the recent results about the primordial origins of the classical KBO Arrokoth McKinnon et al. 2020). Resonant objects are those in mean motion resonances with Neptune. Resonant objects are of particular importance for constraining the dynamical history of the outer solar system; while some KBOs are merely temporarily resonant (see, e.g., Lykawka and Mukai, 2007; Yu et al., 2018), the large number of KBOs in resonance with Neptune

is best understood to be a result of resonant capture during the epoch of planetary migration in the early solar system (see, e.g. Morbidelli et al., 2008; Malhotra, 2019). Detached objects are those KBOs that (on the 10 Myr dynamical time-scale of the Gladman et al. (2008) scheme) do not appear to experience significant orbital evolution, i.e., they are dynamically ‘detached’ from the giant planets. These objects are important to identify because their current orbits are difficult to obtain through interactions with the currently known planetary system. Truly detached objects must have been dynamically perturbed on to their current orbits either by large bodies or by processes in the early solar system that are not longer extant (e.g., rogue planets Gladman and Chan 2006, close stellar flybys Kaib et al. 2011, interactions within the sun’s birth cluster Brasser et al. 2012, resonant drop-out while Neptune migrates Lawler et al. 2019). Scattering objects are those that are currently being strongly dynamically perturbed by direct gravitational interactions with Neptune, thus reflecting current solar system conditions.

3.1.2 Machine Learning Classification in Astronomy

Astronomy has long been an ideal field for applications of machine learning—statistical methods that learn to recognize data based on patterns and inference—due to the large data volume and wide range of problem complexity. Beginning with simple clustering and neural network applications for galaxy classification (e.g. Adorf and Meurs, 1988; Storrie-Lombardi et al., 1992), astronomers have been adopting more varied and sophisticated machine learning methodologies to utilize the full spectrum of information contained in both observations and simulations. Indeed, the importance of machine learning integration in future astronomy programs has been discussed in many works, such as Nord et al. (2019).

Several recent investigations in astronomical machine learning use time-dependent features from the outputs of numerical simulations for classification. For instance, Tamayo et al. (2016) use a standard machine learning classifier and features derived from semi-major axis and eccentricity in short N-body simulations to predict the orbital stability of three planet systems. McLeod et al. (2017) use cos-

mological simulations and a neural network to predict the mass of the Local Group. Lam and Kipping (2018) train a deep neural network to predict the stability of circumbinary planetary systems using only four dynamical features derived from N-body simulations. Choudhary et al. (2019) shows how machine learning methods (in this case, a Hamiltonian neural network) can even learn to predict orbital dynamics (such as long-term chaotic or non-chaotic orbits) without the need for numerical simulations. For dynamically-evolving systems, a single snapshot in time is insufficient for classification and thus, it is critical to incorporate more complex, time-dependent data for a complete prediction.

A methodology to quickly and accurately classify new objects in dynamical populations is especially critical for solar system purposes. The Vera Rubin Observatory’s Legacy Survey of Space and Time (LSST) is expected to find millions of solar system objects, including a few tens of thousands of new KBOs (see, e.g., Schwamb et al., 2018; Ivezić et al., 2019). Traditional classification procedures for the Kuiper Belt, particularly, require some level of human intervention/verification for nearly every object, which quickly becomes unsustainable with ballooning data size. A more efficient tool for dynamical classification of KBOs detected by LSST will be needed (Schwamb et al., 2019).

Thus, in this chapter, we demonstrate the efficacy of a machine learning classification algorithm on separating observed KBOs into their component dynamical populations. This method allows for fast and accurate classification while substantially reducing the need for human intervention. We describe the data and machine learning algorithm in Section 3.2. We then show the results of our classifier on the testing data, including the robustness of our results, in Section 3.3. Finally, in Section 3.4, we discuss the implications of our investigation and explore improvements to the methodology shown herein.

3.2 Data and Methods

The goal of a classification scheme is to take the observed orbits of KBOs, run

numerical integrations of their evolution, and then classify the objects into dynamical categories based on these integrations. In Section 3.2.1, we describe the set of KBOs used as the training and testing data for the machine learning classifier; these KBOs have been previously classified according to the Gladman et al. (2008) scheme. Section 3.2.2 then describes the training and refinement of the machine learning algorithm for classifying the KBOs.

3.2.1 Kuiper Belt Observations and Classification

Here we describe the data set of observed KBOs used in this chapter, which is the set of KBOs that was examined in Volk et al. (2017) (all multi-opposition objects beyond Neptune available in the Minor Planet Center¹ database as of late 2016) combined with the set of classified objects from the Outer Solar System Origins Survey reported by Bannister et al. (2018). The classifications of these ~ 2300 KBOs were produced following the procedures detailed in Gladman et al. (2008). Briefly, an orbit is fit to the observations of each object using the Bernstein and Khushalani (2000) orbit-fitting code. Then, the uncertainty in that orbit fit is estimated by finding the largest deviations in semi-major axis on either side of the best-fitting orbit that does not produce observational residuals that are more than 1.5 times worse than the residuals from the best-fitting orbit. This produces three versions, or ‘clones’ of the observed KBO that are integrated forward in time under the gravitational influence of the Sun and the four giant planets (using SWIFT; Levison and Duncan 1994) for 10 Myr.

For objects with semi-major axes beyond Neptune, the dynamical evolution of each clone (as determined by the time evolution of barycentric orbital elements) is then classified into the following categories.

1. Resonant objects show libration of a mean motion resonance argument for more than 50 per cent of the 10 Myr span. Mean motion resonances occur when a KBO’s orbital period is commensurate with Neptune’s orbital period,

¹www.minorplanetcenter.net

which results in the libration (rather than circulation) of some combination of the KBO's mean longitude λ_{KBO} , Neptune's mean longitude λ_N , and the KBO's longitude of perihelion ϖ_{KBO} and/or longitude of ascending node Ω_{KBO} (see Murray and Dermott 1999 for a complete description of mean motion resonances); an example is Neptune's 3:2 resonance in which Pluto-Charon resides, for which the angle $\phi = 3\lambda_{\text{KBO}} - 2\lambda_N - \varpi_{\text{KBO}}$ librates around $\phi = 180^\circ$.

2. Scattering objects are objects whose semi-major axes a change by more than 1.5 au over the course of the 10 Myr integration. This is a result of gravitational interactions with Neptune that change the energy (and therefore semi-major axis) of the objects' orbit. In practice, most scattering objects have perihelion distances $q \lesssim 37 - 38$ au, the rough boundary where strong direct interactions with Neptune are possible at perihelion (e.g., Gladman et al., 2002).
3. Detached objects are objects with large eccentricities ($e > 0.24$) but that do not experience significant changes in semi-major axis ($\Delta a < 1.5$ au) over 10 Myr. This indicates a lack of strong interactions with Neptune; detached objects typically have semi-major axes $a \gtrsim 50$ au and large perihelion distances.
4. Finally, classical objects are KBOs that do not fall into any of the above categories. Objects in the 'main' classical belt have semi-major axes between the 3:2 and 2:1 resonances with Neptune ($39 \text{ au} < a < 48 \text{ au}$); 'inner' classical objects fall interior to the 3:2, and 'outer' classical objects are exterior to the 2:1. (See Gladman et al. 2008 for full discussion of the motivations for these classification boundaries).

These classifications are determined by a combination of simple time-series analysis and visual inspection of the orbital evolution.

Table 3.1 breaks down how our ~ 2300 KBO data set is divided between these four categories. The table is divided into secure and insecure classifications; secure classifications are those objects for which all three clones behave similarly during

Table 3.1: Overview of Observed KBO Catalog

Population	Secure	Insecure
All	1805	500
Resonant	642	184
3:2	333	14
2:1	71	6
7:4	51	31
5:2	48	7
5:3	45	11
4:3	26	3
3:1	11	9
Classical	998	151
Main	941	139
Inner	43	6
Outer	14	5
Detached	74	90
Scattering	91	75

the 10 Myr integrations while insecure objects are those with differing classifications between clones of the same object. Insecure classifications are often the result of large uncertainties in the orbit of a KBO, although sometimes it reflects an object with a very well-determined orbit being near the boundary of dynamical classes (often being very near the edge of one of Neptune’s mean motion resonances). We use only the ~ 1800 securely classified objects in our training and initial assessment of machine learning algorithms (Section 3.2.2 and Section 3.3); we discuss how the classifier performs on the insecure objects in Section 3.4.1.

3.2.2 Classifier Selection and Training

A supervised machine learning classifier, such as we use here, must have labelled (pre-classified) data to train and test upon so that we can calculate a method accuracy.² *Thus, we make the critical assumption that the Gladman et al. (2008) 10 Myr classification of KBOs described above represent the ‘true’ class of the object for*

²The data features for all best fit orbits in the sample and the classifier developed in this article can be found at https://github.com/rsmullen/KBO_Classifier.

our chosen classification scheme. There are other possible classification schemes for observed objects (e.g., Elliot et al., 2005); the approach we take here should, in principle, be generalizable to any classification methodology.

Data Features

A machine learning classifier is trained on *features*, or properties of an object. For this classification problem, we compute various statistics of the numerical integrations generated for the classification procedure described in Section 3.2.1; these statistics are then used by the classifier to identify the true KBO population that an object belongs to. The simulations output barycentric semi-major axis a , eccentricity e , inclination i , argument of pericentre ω , longitude of the ascending node Ω , and mean anomaly M at fixed time intervals (which, for the fiducial simulations, occur every thousand years). For the purposes of this chapter, we discard M because this angle (for a fixed orbit) simply varies linearly in time and its evolution depends only on semi-major axis. We take subsamples of the data from time $t = 0$ to a range of final times and record the initial, final, minimum, maximum, mean, standard deviation, and maximum deviation of the remaining five osculating orbital elements. We also take step-wise time derivatives at each simulation output and calculate the minimum, maximum, mean, and maximum deviation of the time derivatives. We do not normalize any of the features. In total, we compute 11 features for each of the five orbital elements, leading to a total of 55 features per object used in our classification. To be explicit, every clone of an observed KBO (e.g., best fit orbit, minimum or maximum orbit from observed errors) is treated as an independent object. While many of the features may be highly correlated, the nature of the classifier used herein (described in Section 3.2.2) reduces the risk of overfitting due to these correlations.

The simulations used for the current classification methodology run to 10 Myr. However, many of the dynamical signatures indicative of class membership can be seen on shorter time-scales (for example, single libration cycles for many of Neptune’s mean motion resonances are $\sim 10^4$ years). Thus, we explore classi-

fication accuracy along the time axis. We output features with final times of $5 \times 10^3, 10^4, 5 \times 10^4, 10^5, 5 \times 10^5, 10^6, 5 \times 10^6$, and 10^7 years. If shorter numerical integrations are sufficient to securely classify the majority of objects, then it would be possible to leverage the same computational power per object to more thoroughly explore the uncertainty range in the orbit fits. Because of the evolving nature of KBO orbits, the 10 Myr classification may not actually describe the orbital behavior passed to the classifier. We discuss this further in Section 3.4.1.

Choosing and Refining a Classifier

Machine learning classification algorithms have been developed and optimized for a multitude of purposes. Each has a type of data that it will classify most accurately. Thus, it is important to test a variety of classifiers to find the best tool for these data. We therefore test 15 of the multi-class classifiers available in `scikit-learn` (Pedregosa et al., 2011) with default parameters.³ First, we test the support vector machine classifiers: Support Vector Classifier (SVC) and Linear Support Vector Classifier (LSVC). Support vector machines try to create classes that are as well separated as possible in the multi-dimensional feature space; these classifiers work best when classes are more discrete rather than more continuous. The next ensemble of classifiers are the tree classifiers, which include Gradient Boosting Classifier (GBC), Random Forest Classifier (RFC), AdaBoost Classifier (ABC), Extra Trees Classifier (ETC), and Decision Tree Classifier (DTC). Tree classifiers use many layers of binary classifications based on features to sort data into classes and are commonly the choice for the type of multi-class classification problem explored herein. We also test linear model classifiers, which classify based on a linear combination of features, include Logistic Regression (LR), Passive Aggressive Classifier (PAC), Ridge Classifier (RC), and SGD Classifier (SGDC); Quadratic Discriminant Analysis (QDA) is a similar classifier that uses a quadratic instead of linear decision function (the function that returns a binary true or false classification for an object). The last few

³For transparency and reproducibility, we use a seed of 30 for all instances of a random number generator.

classifiers tested are Gaussian NB (GNB; based on Bayes' theorem), K-Neighbors Classifier (KNC; computing classes based on clustering in high-dimensional feature space), Gaussian Process Classifier (GPC; based on Laplace approximation), and Multi-layer Perceptron classifier (MLPC; a simple neural network classifier).

We show the accuracy of the different classifiers in Figure 3.1. The left panels show the accuracy of classifiers trained on a 30 per cent hold-out, meaning that a random 30 per cent of the data are reserved for testing the accuracy of the method trained on the other 70 per cent of the data. While objects in the 30 per cent hold-out testing set are randomly selected from the full ensemble of data, we use the same testing set throughout this work. The right panels of Figure 3.1 show the classifier accuracy in a 5-fold cross validation, meaning that the data are split into 5 subsections. New initializations of the classifier are trained on four subsections and tested on the fifth for all combinations of the subsections. The reported accuracy is then the average accuracy of the 5 different iterations of the classifier. Two of the classification methods, LSVC and LR, did not converge (the required accuracy was not reached in a reasonable number of iterations) and are therefore not shown in the figure. The poorest performing algorithm shown is GPC; GPC is susceptible to overfitting (fitting specific features in the training set instead of the broad populations) in multi-class classification when different classes occupy similar parameter spaces and therefore shows poor accuracy with the testing set. Most of the tree classifiers performed exceedingly well across all time slices, achieving > 90 per cent accuracy without further refinement.

Based on these results, we choose the Gradient Boosting Classifier (GBC) as the algorithm used for classification throughout the rest of this chapter. We also choose an integration length of 100 kyr as our fiducial choice: this time subset reaches high accuracy in the classifier (> 97 per cent without additional refinement), represents more than 100 orbital periods for most distant objects, and requires a very computationally inexpensive simulation.

The next step is to maximize the accuracy of the Gradient Boosting Classifier by optimizing the hyperparameters of the classifier, which are the parameters that

Table 3.2: Hyperparameter search ranges to optimize method accuracy

Parameter	Default	Search Range
Loss ^a	Deviance	{Deviance, Exponential}
Learning Rate ^b	0.1	{0.1–1} with step 0.05
$N_{\text{estimators}}$ ^c	100	{10–500} with step 10
Maximum Depth ^d	3	{1–6} with step size 1
Maximum Features ^e	None	{None, Auto, Sqrt, Log2}

^a The function used to quantify the accuracy of the method.

^b The scale of the step length in the gradient descent, which controls overfitting.

^c The number of regression trees in the classifier.

^d The height of the regression tree.

^e The size of the subset of features considered when splitting a node.

control how the classifier learns. A basic description of these parameters and the impact they have on GBC is given in the scikit-learn user guide⁴ For the purposes of reproducibility, we show the five hyperparameters we tested and the range searched in Table 3.2; using all combinations of these variables, we search for the most accurate and efficient combination to use for the rest of this work. The hyperparameters are validated using a 5-fold cross validation technique. This is a similar approach for hyperparameter optimization as taken in, for example, Tamayo et al. (2016). The top five most accurate combinations of hyperparameters are then given in Table 3.3. The chosen classifier hyperparameters are given in the bottom line of the table; they create the classifier that has the best combination of speed and accuracy, achieving an average ~ 98 per cent accuracy on our data with a 5-fold cross validation (with a maximum accuracy of 99.2 per cent on any individual fold), and a 98.5 per cent accuracy with the same 30 per cent hold-out split we use for Figure 3.1. The choice of a small learning rate (which dampens fluctuations in the algorithm training process) leads to a classifier that should be fairly robust against overfitting.

⁴scikit-learn.org/stable/modules/ensemble.html.

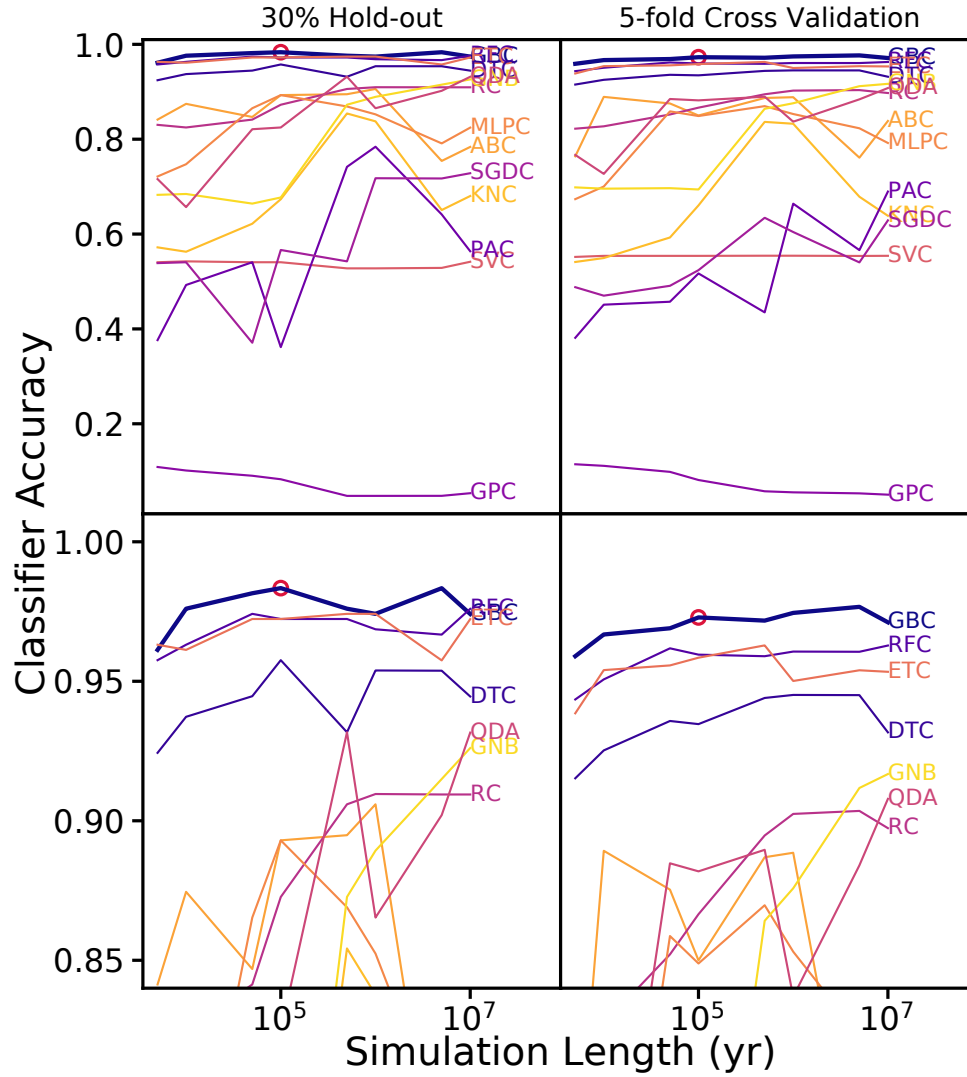


Figure 3.1: The accuracy of different machine learning classifiers as a function of simulation length. The bottom panels zoom in on the upper 15 per cent of the upper panels. The left panels show accuracy when a random 30 per cent of the data are held out for testing, while the right panels show the accuracy for 5-fold cross validation, in which a random 20 per cent of the data is held out for each of 5 iterations and the final accuracy is the averaged accuracy of all iterations. Every line is labelled with the acronym provided in the text. The best combination of accuracy and simulation length is achieved with the Gradient Boosting Classifier (GBC; thick blue line) at 10^5 yr, which is marked with a small red circle in each panel.

Table 3.3: Highest accuracy hyperparameter combinations

Rank	Loss Function	Learning Rate	$N_{\text{estimators}}$	Max Depth	Max Features	Accuracy
1	Deviance	0.2	140–500 ^a	3	Log2	97.9 ± 0.9
2	Deviance	0.1	130	3	Log2	97.9 ± 1.1
3	Deviance	0.15	360	1	Log2	97.9 ± 1.3
4	Deviance	0.3	320	1	Sqrt	97.9 ± 1.4
5	Deviance	0.15	500	1	Log2	97.8 ± 1.3
Best	^b Deviance	0.1	130	3	Log2	97.9 ± 1.1

^a All classifiers in this range of estimators gave identical results

^b The best classifier was chosen based on a combination of speed and accuracy.

3.3 Results

In this section, we describe the characteristics of our machine learning classifier tested on the fiducial data set (100 kyr simulations of the ~ 1800 securely classified KBOs) with the features described above. We explore the data features that lead to a good classification, study the probabilities of class membership to determine how well our algorithm might perform on unknown data, and investigate the performance of our algorithm on error-space clones of KBOs used in the classifier. We then explore the performance of the algorithm on other types of objects, such as the insecurely classified observed KBOs, in Section 3.4.

3.3.1 Object Classification and Feature Importance

The performance of the best-fitting classifier is shown in Figure 3.2. Of the 542 objects in the testing set, only eight were misclassified. To dissect the physical intuition behind the classifier, we show the most important features that drive classification in Figure 3.3. The two most important features for classification are the standard deviation in semi-major axis (σ_a) and the maximum time derivative of the argument of pericentre ($\max \dot{\omega}$). We show how objects occupy the parameter space for these two features in Figure 3.4. Other parameters, including the spread of eccentricities and the changes in inclination, become important for further refinement of classes.

As Figure 3.4 shows, the misclassified objects (identified by red boxes) typically lie along the boundary of multiple classes in feature space. Some of these objects are also near the boundaries between classes apparent in Figure 3.2; in several cases, the misclassified objects undergo late-simulation orbital evolution that changes the population the object belongs to in the 10 Myr simulations. Generally, the classifier performs quite well on the majority of resonant objects despite the lack of semi-major axis normalization in the feature creation. In addition, the classifier is able to distinguish detached objects from classical KBOs despite the lack of a strong differentiation between the populations in terms of their orbital evolution (which is quite stable in both classes).

Figure 3.4 shows that, typically, classical objects have the smallest deviation in semi-major axis between the classes. The resonant objects have a much larger σ_a because they undergo periodic changes in a and e as they librate in their resonances. Detached objects lie somewhere between classical and resonant. Scattering objects have the largest σ_a because of Neptune’s influence on their orbital evolution. Classical objects tend to have a large, positive $\max \dot{\omega}$, while detached and resonant objects have a smaller value (or even negative value, for ~ 20 resonant KBOs). The longitude of perihelion, ϖ , is a sum of the argument of perihelion ω and the longitude of ascending node Ω . For KBOs that are not strongly influenced by mean motion or secular resonances, ϖ precesses and Ω regresses at rates determined by the net gravitational influence of the time-averaged orbits of the giant planets (see the discussion of secular theory in Murray and Dermott 1999). These rates generally decrease with increasing semi-major axis with the exception of a sparsely populated region $a = 40 - 42$ au in the classical belt where there are secular resonances (see, e.g., Chiang and Choi, 2008). Thus it makes sense that the relatively small range of semi-major axes for the classical KBOs translates into a relatively well-defined range of $\max \dot{\omega}$ in Figure 3.4, and the more distant detached objects generally have lower values of $\max \dot{\omega}$. For the resonant objects, the evolution of ω is influenced by resonant dynamics; the very small or negative values of $\max \dot{\omega}$ for some objects likely reflect so-called ‘Kozai’ libration within mean motion resonances (e.g. Mor-

bidelli and Moons, 1993), where $\dot{\Omega}$ and $\dot{\varpi}$ cancel, leading to libration of ω . For scattering objects, $\max \dot{\omega}$ varies broadly, reflecting their wider range of semi-major axes and that their orbits undergo significant changes. Reassuringly, all of the misclassified objects lie upon a boundary between populations in Figure 3.4, indicating that there is a physical ambiguity in the object’s orbital evolution that the classifier is picking out.

We show distributions of and correlations between the top four features (σ_a , $\max \dot{\omega}$, $\Delta \dot{a}$, and σ_e) in Figure 3.5. Again, in most of these parameter spaces, the misclassified objects fall along a boundary between different classes. Similarly, the misclassified objects are never absolute extrema; rather, they tend to have middling values. None of the distributions for different classes are well-separated in any individual features, and the ordering of the peaks changes. This demonstrates that a two-parameter correlation is unable to uniquely separate the four classes, but a highly-multidimensional classification, such as is constructed by the classifier, is able to pick out nuances that lead to accurate classifications.

3.3.2 Probability of Class Membership

For an automated method of object classification to be viable, a majority of objects should have a high probability of correct class membership, and ideally all of the misclassified objects will have low class membership probabilities. In the classification algorithm, each object is assigned a probability of membership for each of the classes such that the sum of all individual probabilities is one, and the assigned class is that with the highest probability. We show the probabilities of class membership for the four populations of correctly classified objects and the misclassified set in Figure 3.6. Most objects, especially the common resonant and classical KBOs, have high probabilities of membership. Over 80 per cent of the testing set has a greater than 3σ probability of class membership: 79 per cent of resonant KBOs, 88 per cent of classical KBOs, 11 per cent of detached, and 75 per cent of scattering objects have very high probabilities of belonging to the correct population. The detached objects have lower probabilities when compared to the other classes because there

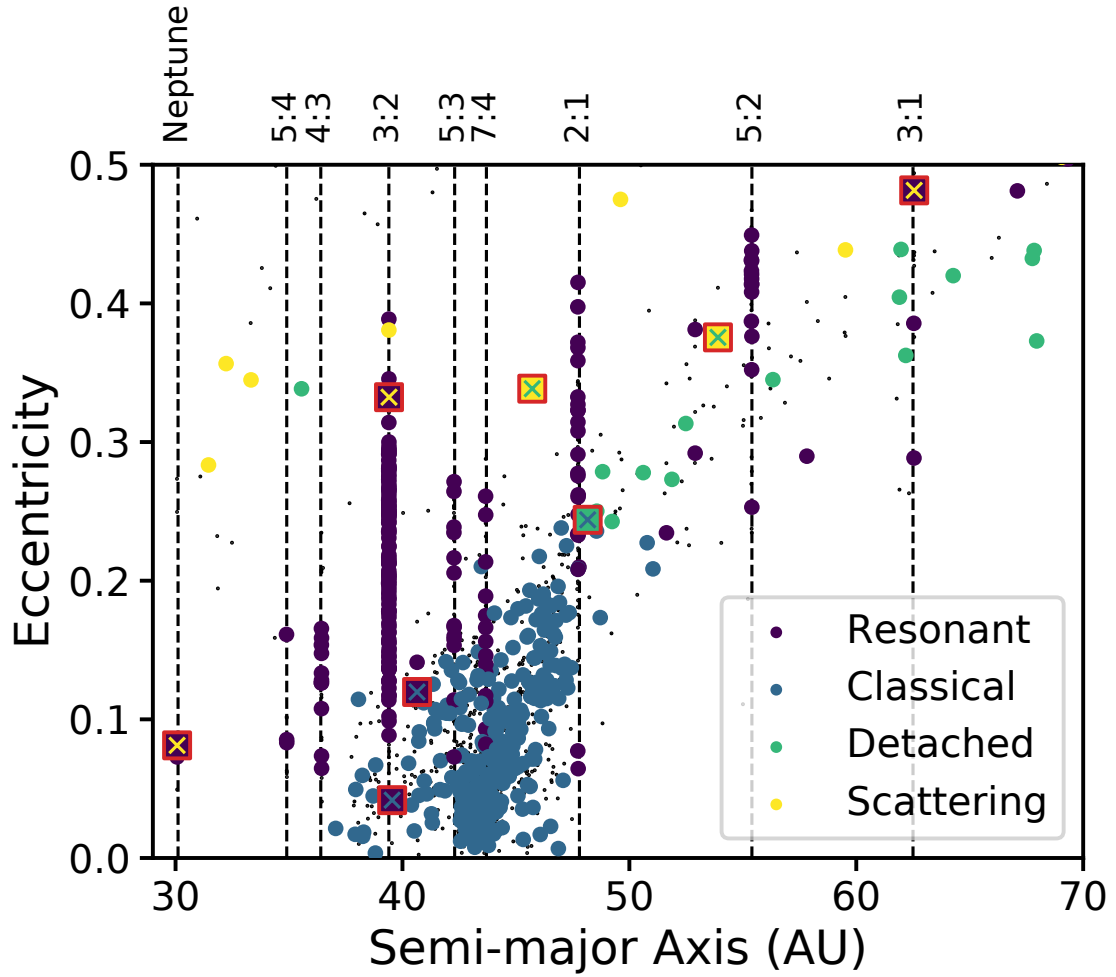


Figure 3.2: The classes of objects identified, plotted in the standard orbital plot of eccentricity vs. semi-major axis. The training data are identified as small black points in the background, while the testing data are shown by the larger coloured points. Misclassified objects are identified by red squares, where the background colour in the square shows the true class and the 'x' shows the computed class. We achieve a 98 per cent accuracy in our classifier using the 542 objects in our testing set.

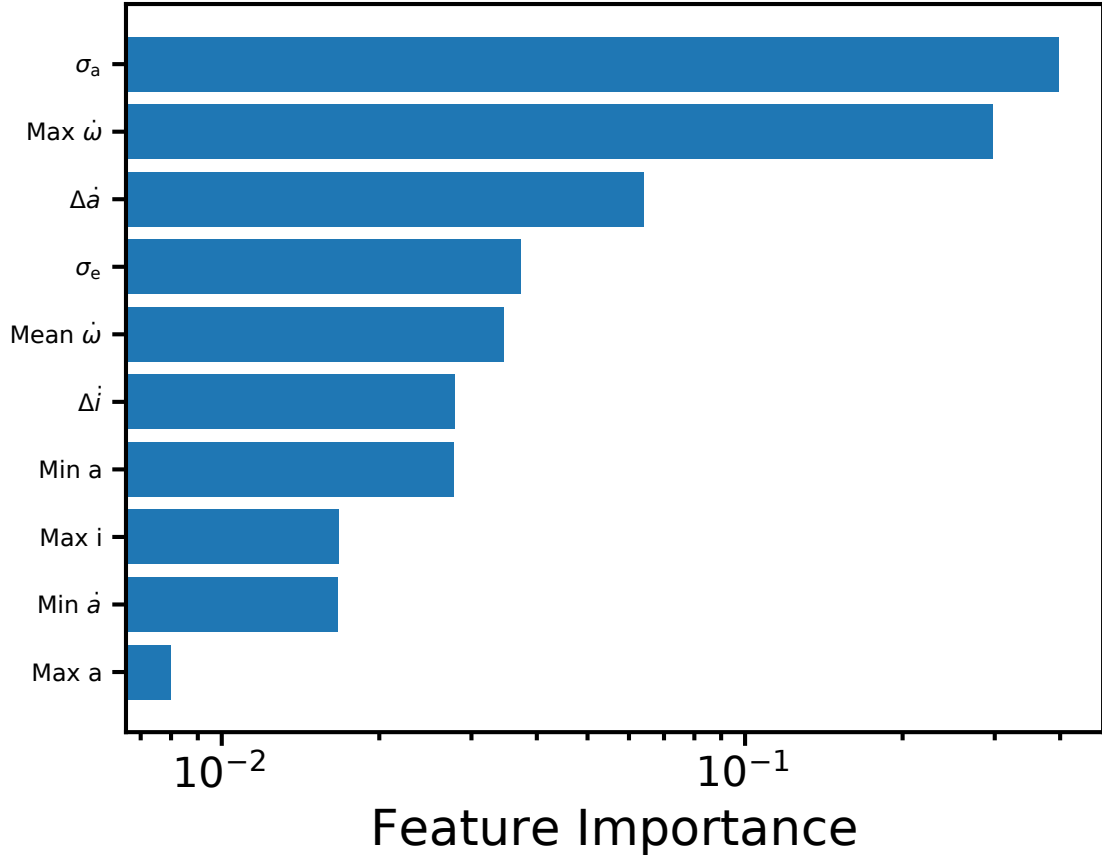


Figure 3.3: Relative importance of the top ten features (from top to bottom: most to least important) used by the classifier to sort objects into their populations. The sum of all feature importances adds to one. As can be seen, the most important orbital features for classification are the standard deviation of semi-major axis (which will be indicative of scattering or libration) and the maximum rate of change of the argument of pericentre.

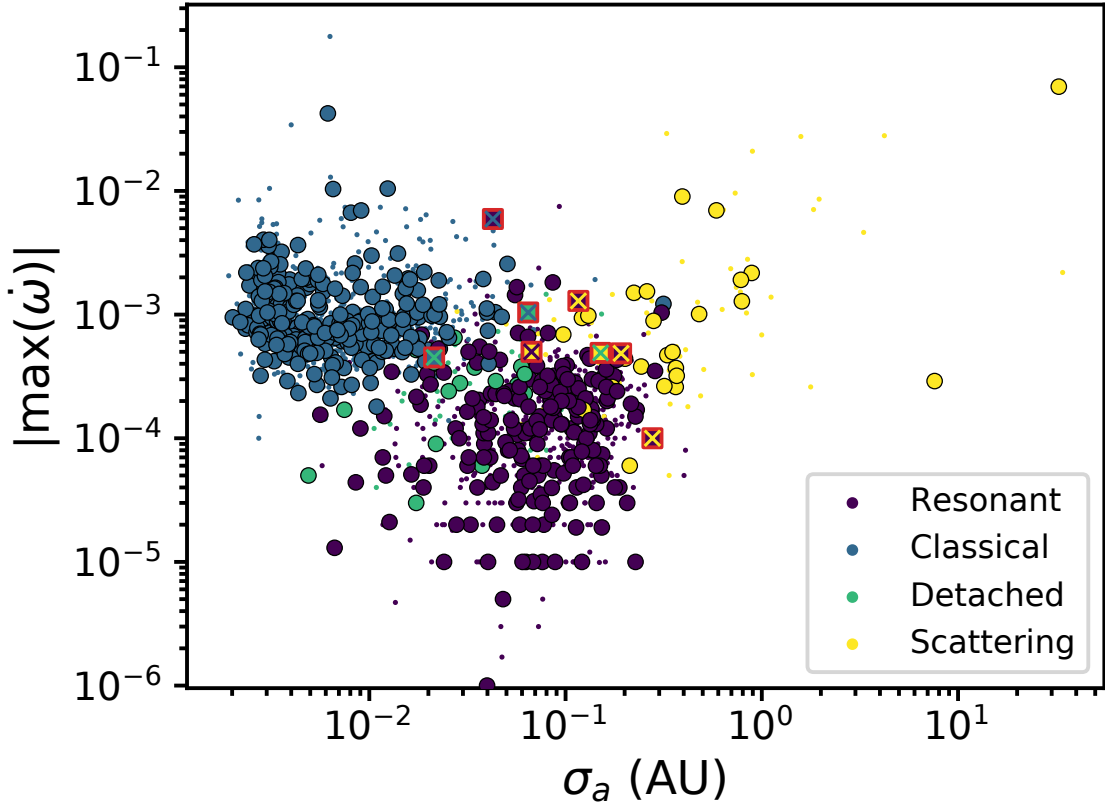


Figure 3.4: The parameter space defined by the two most important features, σ_a and $\max \dot{\omega}$. Small points show objects from the training set, outlined circles depict objects from the testing set, and squares outlined in red show the misclassified objects with the same convention as Figure 3.2. All of the misclassified objects lie along boundaries between classes.

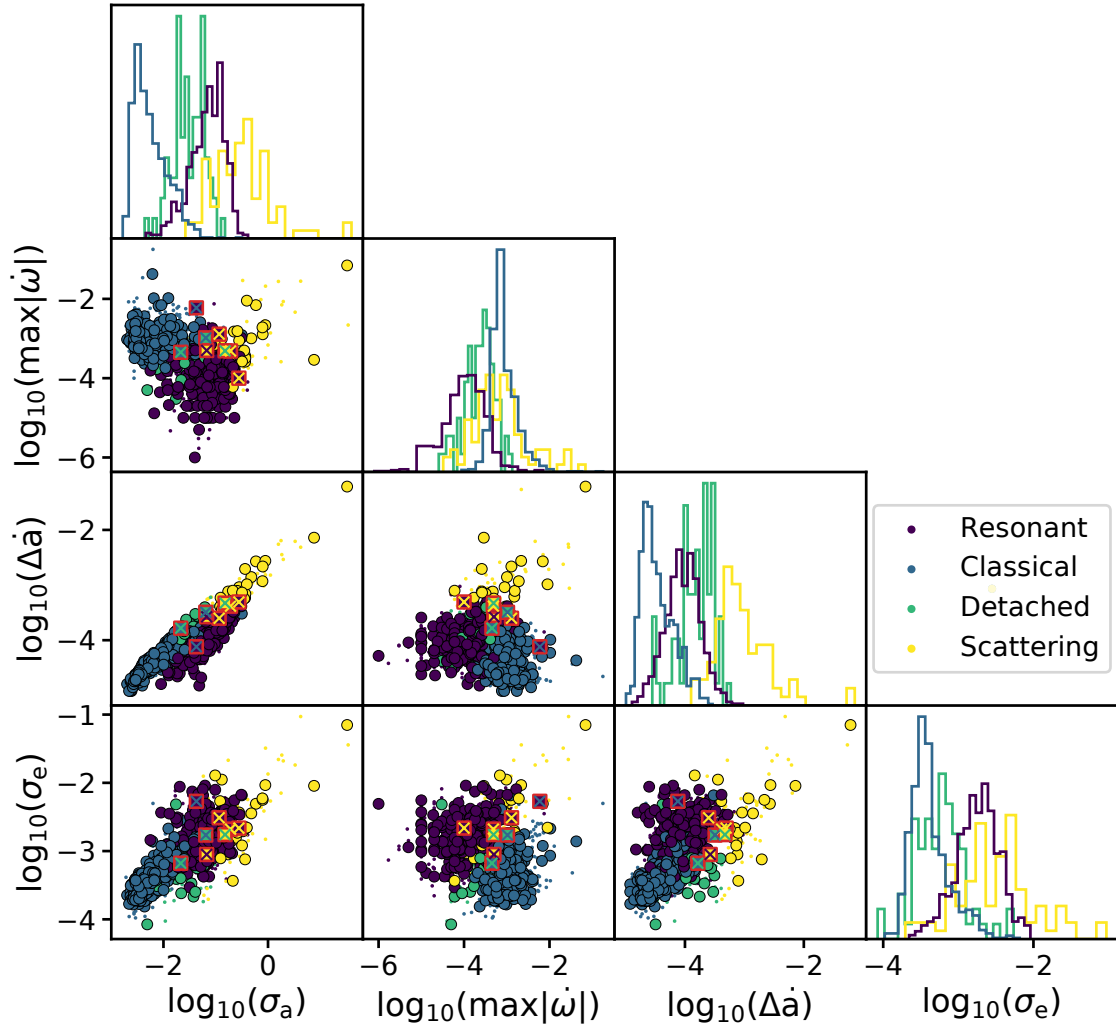


Figure 3.5: Correlation plot for the four most important features in the classification algorithm. The plotting convention follows that of Figure 3.4. Plots along the diagonal show normalized histograms of objects in the four classes.

are relatively few detached objects with secure classifications, so they are under-represented in the training set. Many of the observed ‘detached’ objects are either near the edges of mean motion resonances with Neptune or have orbit-fit uncertainties that encompass these resonances, thereby leading to lower class membership probabilities. None of the misclassified objects has a probability greater than 2σ . By using even a conservative probability of membership cutoff of $3\sigma \approx 99.7$ per cent, we may be able to reduce the burden of human intervention substantially should a method like this be incorporated into a KBO classification pipeline. We explore this further in Section 3.4.

We can also examine the distribution of class probabilities for each object, which we show in Figure 3.7. The misclassified objects have a spread of class probabilities that is much smaller than other objects. Additionally, the class with the second highest preference is typically, but not always, the correct class, meaning that the classifier did pick up on some of the features associated with the correct classification. Most of the test set objects have well-stratified probabilities, indicating that one class is highly favored. Figure 3.7 shows that the classical KBOs typically are very dominant in preference for their true class, with resonant classification being consistently the next highest (though still low) probability. Classicals have a much lower probability of being detached or scattering. Resonant, and scattering objects have little preference for the class with the second highest probability. There is a mild preference amongst the detached objects for a resonant classification being the next most probable. This is likely a reflection of the fact that the observed detached KBOs do tend to fall relatively close to resonances with Neptune.

3.3.3 Object Clone Classification

The machine learning classifier presented above provides a more automated and computationally less expensive method to classify individual objects. As such, one particularly useful application of this type of algorithm is to make a more reliable classification pipeline with an expanded consideration of the orbit-fit uncertainties for each observed KBO. A machine learning classifier could be used to classify ‘error

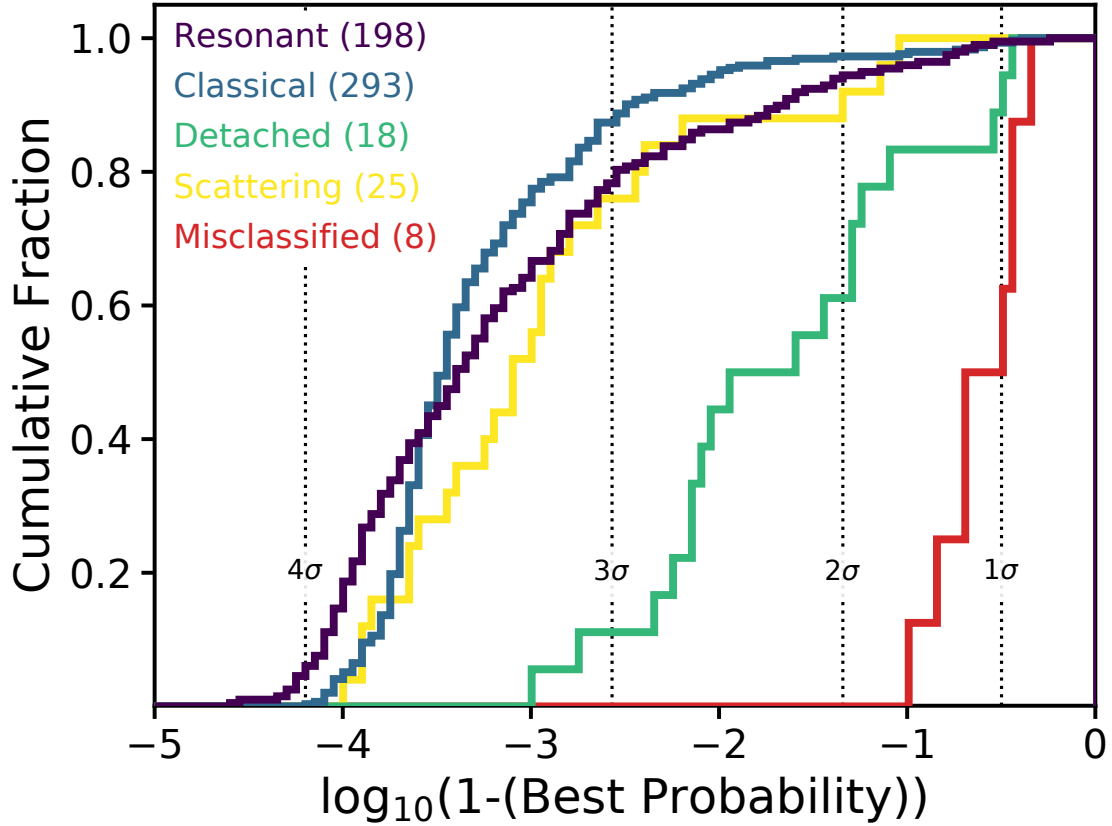


Figure 3.6: Cumulative distribution of the probability of class membership for objects correctly identified in the four classes and for the misclassified objects. Vertical lines denote traditional confidence intervals. Over 80 per cent of objects boast a $> 3\sigma$ probability of class membership, and all of the misclassified objects have a low probability of membership compared to others. This means that only a small fraction of objects could require human intervention for correct classification.

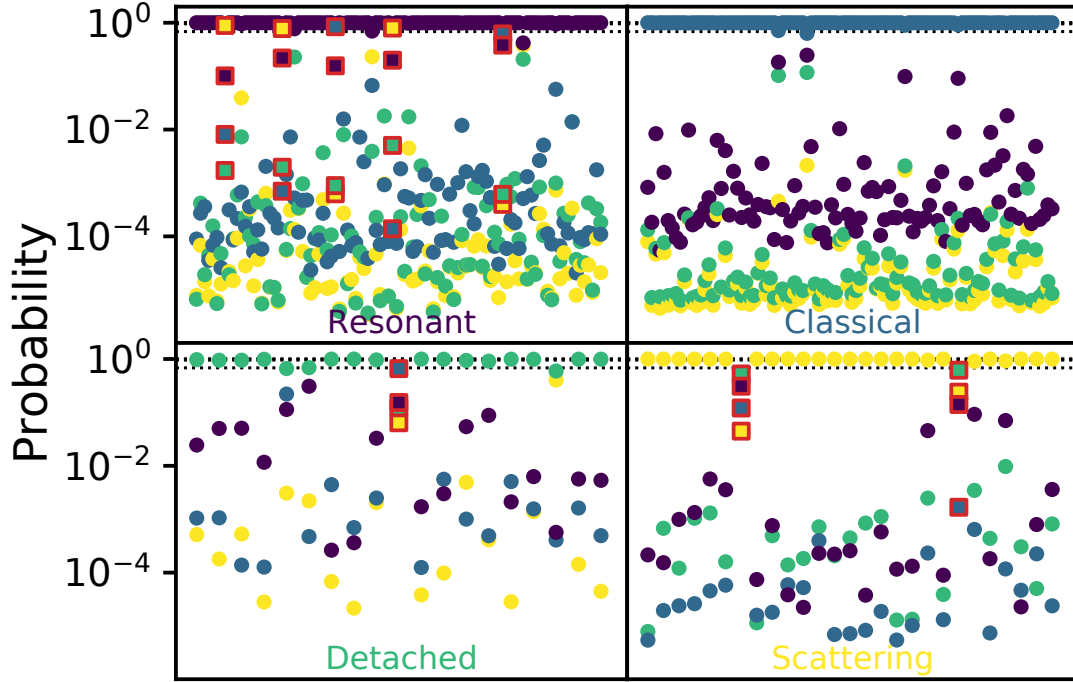


Figure 3.7: Probability of membership in all four classes for each object, with objects separated into quadrants based on their true class. Each location along the horizontal axis in a panel shows a different object. An object’s probability of membership for each of the four classes are shown as colour-coded dots (which sum to one) along that vertical line. Objects that were misclassified are identified by red squares. The number of correctly classified objects shown in the resonant and classical panels has been reduced to one hundred for visual clarity. From this, we can see that resonant objects and classical KBOs typically resemble each other the most due to the stratification of class probabilities, while detached and scattering objects don’t have an obvious trend for the ordering of other class probabilities.

clones’ of an observed object that are initialized with perturbations in orbital elements drawn from the observational error space of the KBO. Because we have used shorter numerical integrations (100 kyr) in our classification scheme, we can run ~ 100 simulations of error clones for the same computational cost as the traditional 10 Myr integration. Additionally, the inclusion of error clones in the classification provides better leverage on the probability of class membership: if the clones agree with the classification of the best fit, the object’s classification can be better trusted.

We first investigate the classifications of the minimum and maximum error clones for each object in the testing set (drawn following the methodology of Gladman et al. (2008) and described in Section 3.2.1). We call the collection of the independently classified minimum, best fit, and maximum clones for each observed KBO a ‘clone set’ that we can analyse as an ensemble. Because our training and testing data draw only from the securely classified KBOs, these clones have the same true classifications as the best-fitting clones. The error clones were classified using the fiducial GBC classification algorithm trained on original training set of securely classified, best fit KBOs. The classification of these objects is shown in Figure 3.8. The majority of clones agreed with both the true class and the best fit class: 98 per cent of clones agreed with the best fit, and 97 per cent of clones agreed with the true value. There is no preferential population or area of parameter space in which the clone classification under-performs.

The 17 misclassified clone sets (out of 541 in the testing set) are explored further in Figure 3.9. Six of the sets had all clones agree with each other (meaning that the best fit and error clones were systematically misclassified), and 15 had at least one clone agree with the best fit. There is no preference for the type of clone disagreement seen: we find all populations mixed among the clones and true values.

To better understand the behavior of clones in the full error space, we select six clone sets that agreed with both each other and the true classification and six clone sets that disagreed and ran simulations for an additional 250 clones randomly sampled from the observational uncertainties. To do this, we use the orbit uncertainties and corresponding covariance matrix calculated in the Bernstein and Khushalani

(2000) orbit-fitting procedure to generate clones. This samples an uncertainty range somewhat different from the Gladman et al. (2008) minimum and maximum clones because the covariance matrix does not account for potential systematic uncertainties in the astrometry reported for the objects. The classifications of these clones are shown in Figure 3.10.

For illustrative purposes, we now discuss the individual behavior of the rightmost six objects from Figure 3.10. We find that, in most instances, only the extreme maximum and minimum error clones, or clones close to the extrema, differ from the best fit value. Four of six clone sets agree with the best fit value entirely. The clone ensembles also have very similar probabilities of class membership with one another (less than 0.2 dex for the examples shown here except for K14B64W⁵, which has a spread of nearly two orders of magnitude) and have similarly stratified probabilities in all classes (meaning that the probability ordering of one object’s clones frequently does not change across the error space).

K11Uf2Q only has three differing clones, which agree with the classification of the maximum error clone, and the best fit agrees with the ‘true’ classification. Similarly, K14Wp0S’s clones agree with both the best fit value and the true classification, and only the minimum error clone disagrees with all other clones. Both of these cases show the power of using a large ensemble of clones: the machine learning method correctly identifies that the dynamical behavior of the vast majority of the ensemble is consistent, with only a few clones at the edges of the uncertainty range showing different physical evolution. This provides a strong constraint on the true classification of the observed object.

The error clone classifications of K15RR7W, K15VG7P, and l1152 all consistently disagree with the ‘true’ classifications of the objects. K15VG7P is in a mixed-argument resonance, and the classifier incorrectly identifies it as a classical object. K15RR7W is a Neptune Trojan (in the 1:1 mean motion resonance with Neptune). The classifier did not perform well at identifying low eccentricity Trojans as resonant

⁵We refer to individual objects by their packed designations; see <https://www.minorplanetcenter.net/iau/info/PackedDes.html>

objects. We discuss the underlying reasons for these kinds of misclassifications in Section 3.4.1. KBO 11152 is a weakly (~ 2 au) scattering object on longer time-scales (~ 0.5 Myr), but has a very stable semi-major axis on the short time-scale integration used by the classifier; therefore, the classifier correctly identified the population based on the information used but failed relative to the full 10 Myr integration. These three objects highlight the fact that these kinds of errors in the machine learning classifier will need to be addressed and/or characterized to be able to see the full benefits of error clone analysis. We discuss possible avenues of improvement in Section 3.4.3.

Only one object, K14B64W has substantial disagreement in clone classification across the clone ensemble. K14B64W’s clones are classified as 36 per cent resonant, 57 per cent detached, and 8 per cent scattering. There is no obvious patterning of clone classification in semi-major axis, eccentricity, or inclination space; the identified class appears to be randomly distributed. However, visual examination of the clones show variable dynamical evolution. This object intermittently librates in a high-order resonance. Thus, the ambiguity in the machine learning classification of clones reflects the diversity of dynamical evolution across the uncertainty range for this observed orbit.

3.4 Discussion

Here we discuss in more detail the dominant reasons for errors in the machine learning classifier, both in the data set classified above and in two additional data sets to which we have applied the trained classifier. We suggest some future improvements that could be made to increase the accuracy of machine learning as applied to dynamical classification in the outer solar system.

3.4.1 Reasons for Misclassification

We examined in detail many of the cases of misclassification by the GBC classifier to get a sense of the dominant reasons for misclassification. Some of the misclassi-

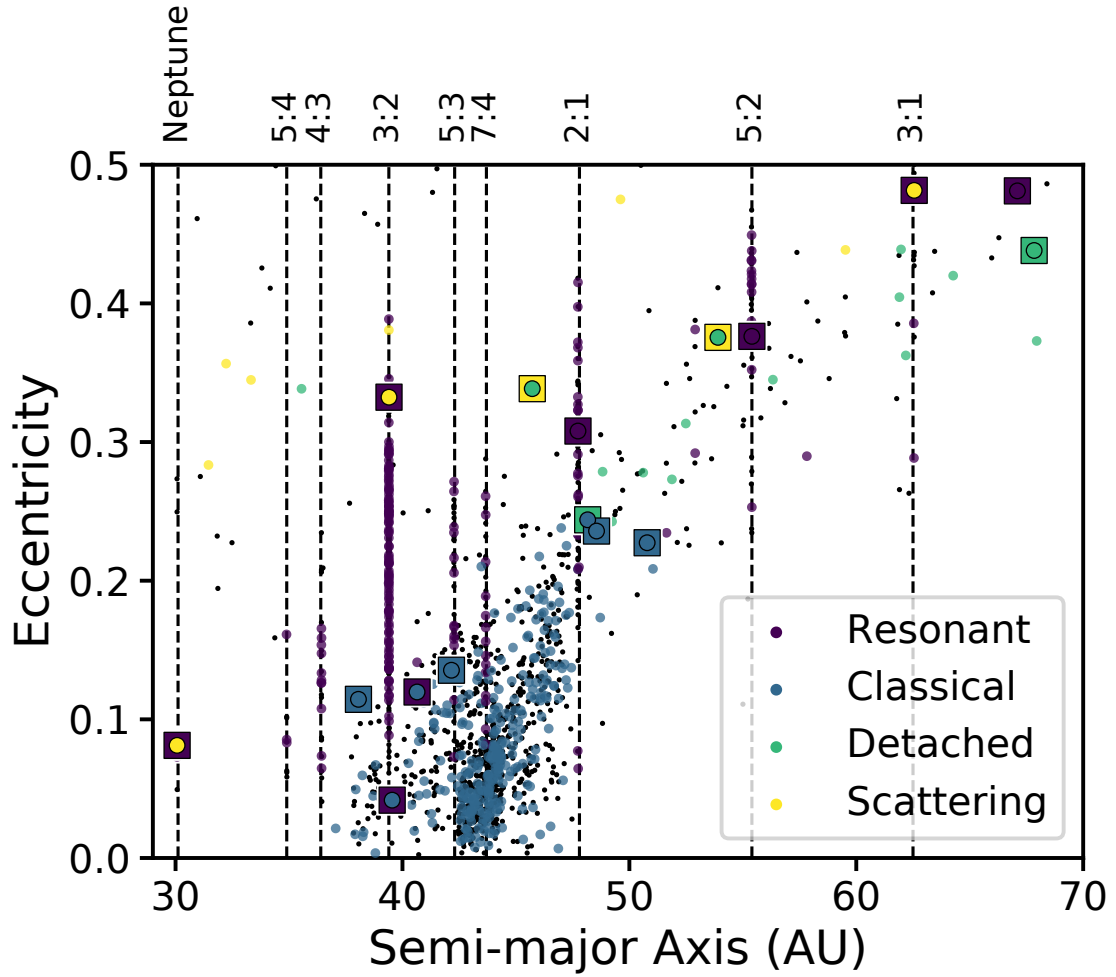


Figure 3.8: Eccentricity vs. semi-major axis for clones of secure objects. Small black points in the background show the training data, while the small points show the clones where all three objects had the same classification and were correctly sorted into the true class. Squares show KBOs in which at least one of the clones was not assigned the ‘true’ class (~ 3 per cent of the testing data). The background colour of the square depicts the true class, while the coloured circle in the middle shows the class of the best-fitting orbit.

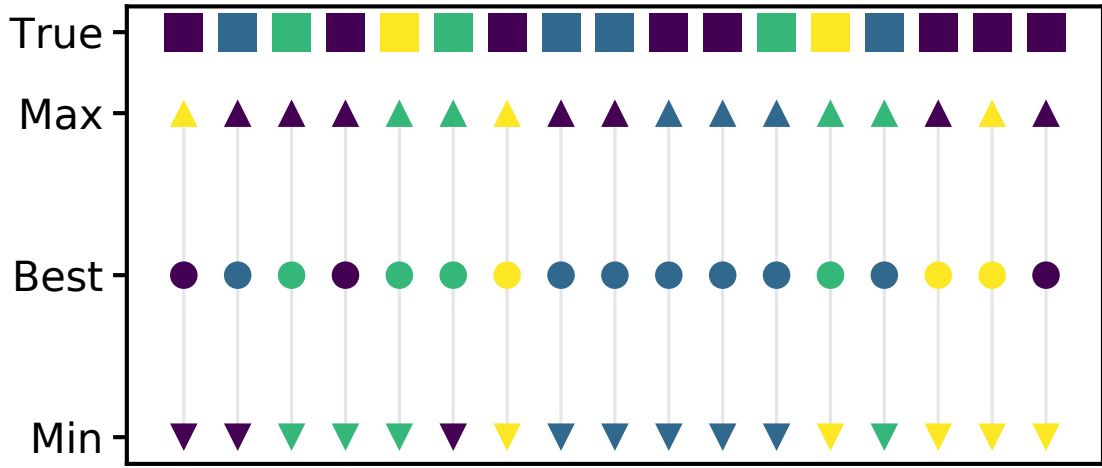


Figure 3.9: Comparison of the classification of the clones that did not agree with each other and/or the true value. Each column shows the true class (square), maximum error clone (up triangle), best fit orbit (circle), and minimum error clone (down triangle) for one object, with colours corresponding to the same classes used in previous plots, such as Figure 3.8. We find objects where all three clones agree with each other but disagree with the true value (e.g., second set from the right), and we find instances in which at least two clones disagree with each other (e.g., left-most example).

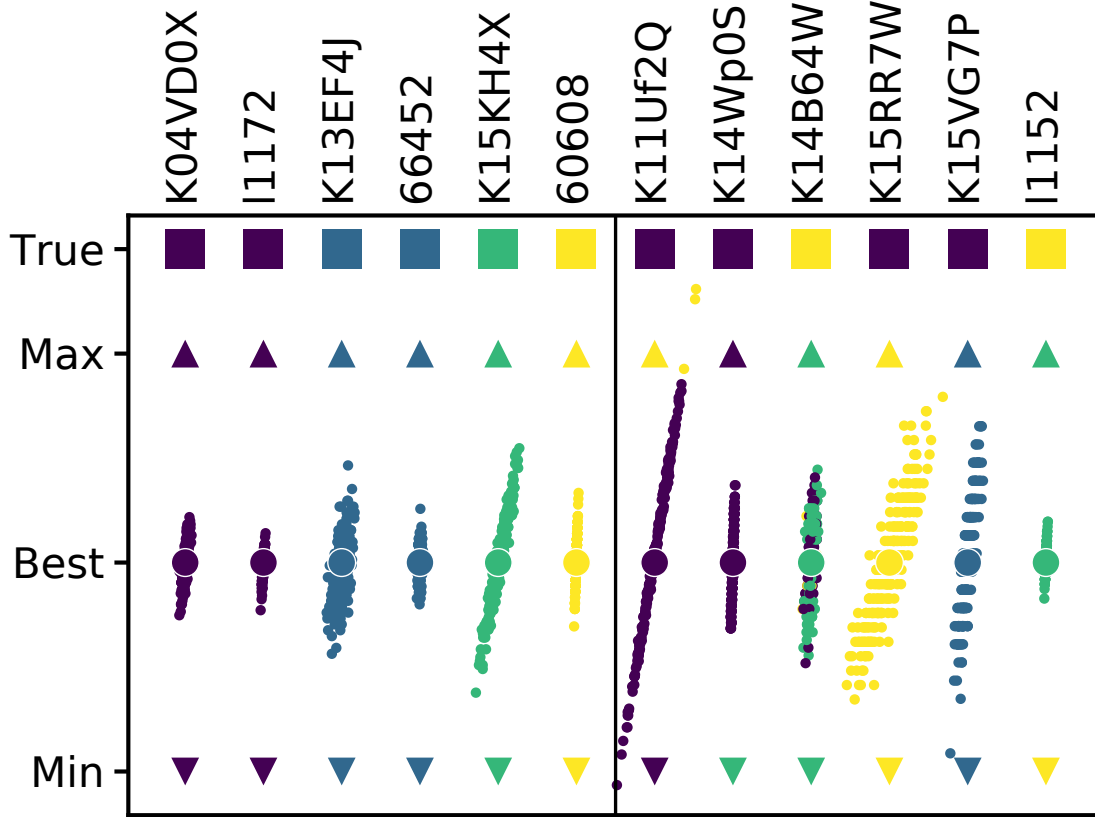


Figure 3.10: Clone classification for 250 clones drawn from the error space of the observations. The six objects on the left have secure classifications, where all clones agree with each other and the true classification, and the six objects on the right have clones that disagree with either each other or the true classification. The triangles, squares, and large circles are the same as in Figure 3.9. The small points show the classification of individual clones. The vertical position of the point denotes the semi-major axis relative to the maximum and minimum error clones (triangles). The horizontal spread shows the eccentricity relative to the eccentricity of the best fit orbit (circle). Most of the objects on the right have a majority of clones agree with each other; K14B64W is the only object that has substantial disagreement between clones.

fied objects are KBOs whose orbital evolution is just inherently ambiguous. These include cases where a judgement call was made to determine the ‘true’ classification; examples of this include objects on the border between scattering and detached (i.e., semi-major axis variations very close to the empirical limit of 1.5 au determined by Gladman et al. 2008). In other ambiguous cases, the true classification is resonant because an object’s resonant angle librates for the majority of the 10 Myr simulation, but that libration is intermittent. Some of these intermittently resonant objects are not librating at the very start of the integrations, so the machine learning classifier is not wrong, strictly speaking, when it classifies those as non-resonant based on short integrations; Figure 3.11 shows an example of this kind of ‘misclassification’. We see a few similar instances of misclassification of true scattering objects as detached where the object’s short-term orbital evolution is quite stable, but longer integrations show it will scatter on 10 Myr time-scales. In these cases, the use of the shorter integration time-scale results in a different classification than for longer integrations because the dynamical behavior changes significantly over time. There are other instances, however, when the short-time-scale behavior can predict the classification on longer time-scales, even if the short-time-scale behavior does not meet the Gladman et al. (2008) definitions; an example of this is when the machine learning classifier correctly identifies a scattering object even though its semimajor axis does not undergo significant changes in the 100 kyr integrations. While the classifications based on shorter integrations perform well overall compared to the 10 Myr integrations in the Gladman et al. (2008) scheme, this kind of behavior does highlight that classifications can be time-dependent.

Other cases of misclassification are likely due to limitations of the training set. For instance, the algorithm is not always able to distinguish between classical and detached objects. This is likely partly because there are relatively few detached objects in the data set on which to train and partly because the boundary between classical and detached in the Gladman et al. (2008) scheme is slightly arbitrary at smaller semi-major axes where these two populations share similar current orbital evolution.

In the misclassifications described above, the classifier tends to assign more equal probabilities to two or more classes, and the wrong ‘best’ class is typically not strongly favored. The one instance we find in our data set where the classifier assigns a high probability to the wrong class membership is for resonant objects librating in mixed eccentricity and inclination type resonances. The vast majority of resonant KBOs discovered to date librate in eccentricity-type mean motion resonances, meaning that the resonant angle involves the KBO’s longitude of perihelion and the libration causes coupled variations in the KBO’s semi-major axis and eccentricity. However, there are a few (~ 10) resonant KBOs that have librating resonant angles that involve both the KBO’s longitude of perihelion and the longitude of ascending node. These mixed-type resonances are generally weaker than the eccentricity-type resonances, so the variations in semi-major axis and eccentricity are less pronounced; there are also variations in inclination not seen in eccentricity-type resonances. The classifier, which is essentially trained only on eccentricity-type resonances, therefore does not have the statistical power to recognize this alternative form of resonance. The dominance of eccentricity-type resonances in the training set likely also contributes to the classifier’s poor performance identifying low-eccentricity Neptune Trojans. The 1:1 resonant argument does not involve the longitude of perihelion, so it does not produce strongly coupled variations in a and e like most of the resonant population. We discuss how these insights could lead to improved machine learning classifiers in Section 3.4.3.

Classification of Insecure Objects

In the analysis presented above, we only show the classification of securely classified KBOs. We now investigate the performance of the fiducial classifier (trained on the secure objects) on the best-fitting orbits of the 500 KBOs from Table 3.1 with insecure classifications according to the Gladman et al. (2008) scheme. The overall accuracy for this data set was unsurprisingly lower than for the secure objects at 75 per cent. Additionally, the probabilities of class membership were somewhat lower. Only about 70 per cent of correctly classified classical KBOs had more than a 3σ

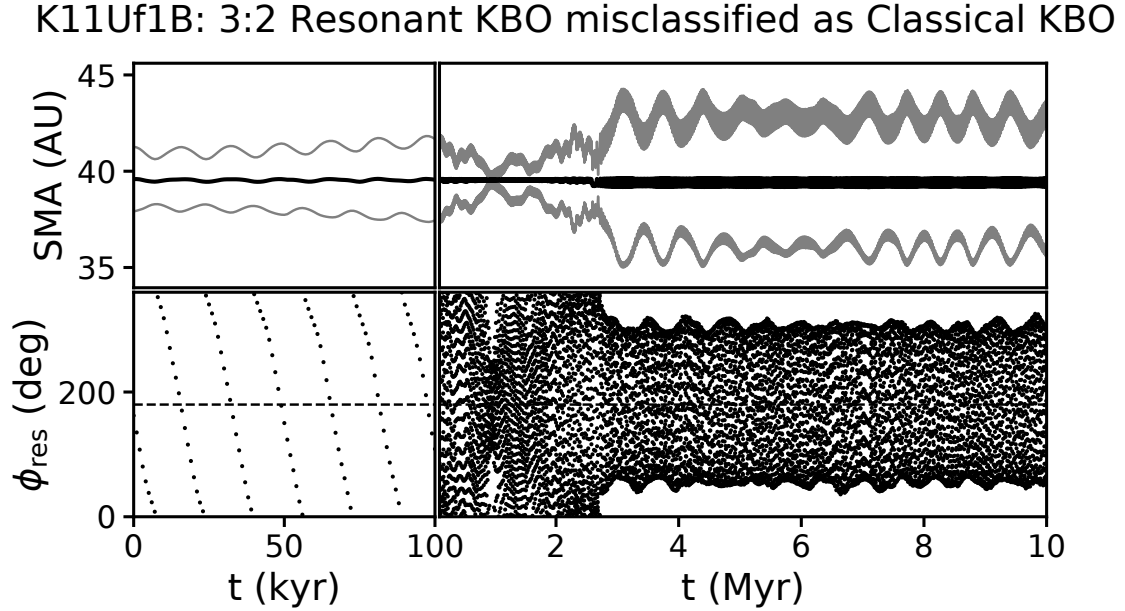


Figure 3.11: Semi-major axis and resonant angle as a function of time for a misclassified object. In the top panels, the black line shows the semi-major axis and the grey lines show the pericentre and apocentre distance. The bottom panels show the resonant angle (assuming libration in the 3:2 resonance) with the centre of libration (180°) indicated by the horizontal dashed line. The left panels show the simulation used in the classifier (10^5 yr), while the right panel shows the simulation used to compute the true class (10^7 yr). This object shows one of the major reasons for misclassification: a dynamical event happens past the time of the simulation fed to the classifier (in this case, the object scatters into the 3:2 resonance at around 3 Myr). The classifier correctly identified this object as a classical KBO given the short simulation it was given, but the long-term dynamical behavior clearly indicates that the object exists in the 3:2 resonance.

probability of class membership, and the other three classes contained < 40 per cent correctly classified objects with high probability.

A reasonable fraction (~ 15 per cent) of misclassified insecure KBOs possessed a high (3σ) probability of class membership. Of the incorrect classifications, we closely examined the 50 KBOs (about 40 per cent of misclassified objects) with (incorrect) classification probabilities at > 95 per cent confidence. Of these, 6 are KBOs whose orbital evolution dances along the borders between classes; for the integration provided to the classifier, the algorithm made a reasonable choice. Another 7 are mixed-argument resonant objects that were incorrectly deemed classical due to the lack of representative objects in the training sample. There are 13 resonant KBOs that are only intermittently resonant and are not librating over the 100 kyr time-scale integrations and were thus misclassified. Finally, 7 KBOs had ‘true’ classifications that differ from the behavior of the best-fitting orbit: the Gladman et al. (2008) procedure assigns classifications based on the minimum and maximum clones in cases where those both agree even if they *disagree* with the best-fitting orbit, meaning that the GBC classifier correctly identified the class of the best-fitting orbit. Thus, we have only 17 KBOs that were unambiguously misclassified. Most of those 17 KBOs have true classifications that place them in high-order resonances (which are inherently more rare in the training data set) and/or have libration at very large amplitude within their resonances (meaning they are nearly non-resonant). Overall this is consistent with the reasons for misclassification found in the main data set.

A typical observed set of KBOs will have a mix of secure and insecure classifications, so we can estimate the expected probability distribution for our classifier by mixing insecure objects into our test set. Our overall set of KBOs has ~ 20 per cent insecure classifications (see Table 3.1), so adding a randomly chosen set of 135 insecurely classified KBOs to our testing set of 542 securely classified objects results in a typical mix of secure and insecure objects. The expected combined probability distributions from the machine learning classifier for this set of KBOs is shown in Figure 3.12. The features we noted in Section 3.3.2—a large fraction of high probabilities for correctly classified objects and a large fraction of low probabilities for

misclassified objects—still hold true, which bodes well for the future applicability of this methodology. About 75 per cent of correctly classified objects have $> 3\sigma$ probability of class membership, while more than 70 per cent of misclassified objects have probabilities less than 2σ . The small tail of high probability misclassifications results from objects suffering from classification time-scale ambiguity as described above.

3.4.2 Classification of DECam Objects

The recent publication of observations of 131 new KBOs discovered using the Cerro Tololo-DECam (Wasserman et al., 2020) provides an independent set of objects on which to test the trained machine learning algorithm. Using the astrometry provided by the Minor Planet Center, we followed the Gladman et al. (2008) procedure described in Section 3.2.1 to determine the ‘true’ classifications of these new KBOs. From this procedure, we find 54 classical, 52 resonant, 18 detached, and 7 scattering KBOs in this data set.

We then classify all of the DECam data using the GBC classifier developed above (which uses the same training set of objects as the classifier in Section 3.3). We do not remove objects with insecure classifications from the data set, as we aim to characterize the performance of the classifier on ‘unknown’ data with a fairly typical mix of secure and insecurely classifiable objects, as would happen if this methodology was folded into a blind pipeline analysis. Without any modifications to the algorithm, the machine learning classifications agreed with the true classifications 92.4 per cent of the time, as shown in Figure 3.13. We have 10 objects that do not agree with the true classification, and seven of those are objects that have an insecure true classification. The misclassifications in this data set occupy a similar parameter space to misclassifications in our fiducial testing set: the classifier finds ambiguity in a few low eccentricity resonant objects and an object that is close to the classical–detached boundary.

We show the best-fitting class probability in Figure 3.14. In this figure, we do not differentiate between the correct classifications and misclassified objects in an

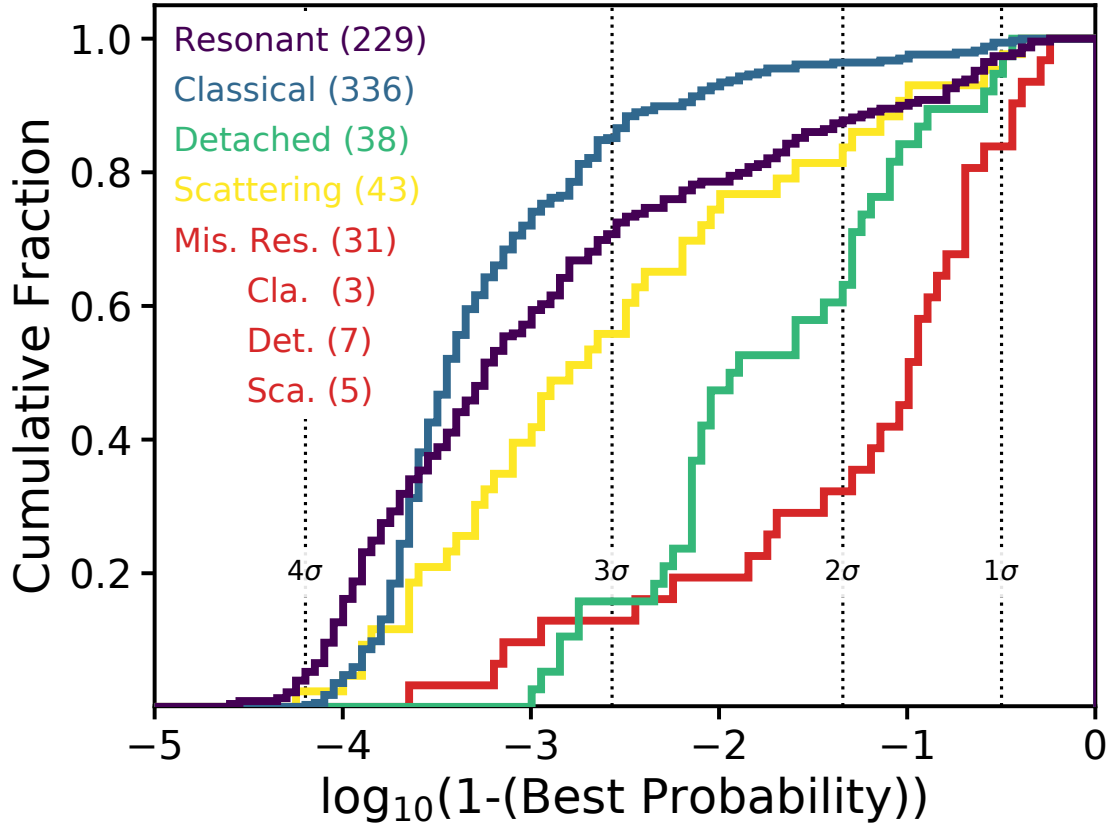


Figure 3.12: Cumulative probability distributions for the combined secure and insecure sample (representing 30 per cent of our overall KBO sample, with ~ 80 per cent secure and ~ 20 per cent insecure). The plot follows the conventions of Figure 3.6. Many of the misclassified objects with high probability are misclassified due to the differences in time-scales between the 10 Myr Gladman et al. (2008) classification scheme and the 100 kyr method presented herein: the dynamics observed on shorter time-scales are consistent with a different class than the dynamics seen on longer time-scales.

effort to simulate the distribution that might be expected from a blind classification of unknown data. Similarly to the fiducial data set and the joint secure/insecure analysis in Section 3.4.1, a majority of classical (63 per cent) and resonant (62 per cent) objects have best-fitting probabilities of $> 3\sigma$. Only one of the ten misclassified objects (K13RC4O, a true resonant classified as a classical) is a ‘false positive’ with a best-fitting probability of 3.00σ ; this object is in a mixed-argument resonance, and the true classification is insecure.

Because this data set is very manageable in size, we visually examined the dynamical evolution of each clone of the 131 new KBOs to determine exactly how well the machine learning algorithm did and to identify features of the objects classified incorrectly or classified at low probability. We find that every false classification made at > 90 per cent confidence was the result of the true classification being a mixed-argument resonance. The majority of both the misclassifications and true classifications made at lower probabilities are either resonant objects with low eccentricities or very small semi-major axis libration or are objects whose ‘correct’ classifications are a judgment call because they are on the border between different dynamical classes. The algorithm generally gives lower probabilities to the detached classifications. An examination of the ‘true’ detached KBOs in this data set reveals that they are mostly insecure classifications; 15 of the 18 detached KBOs are close to the boundaries of resonances with Neptune, and an additional 2 nearly have enough semi-major axis mobility on 10 Myr time-scales to be classified as scattering rather than detached. Thus, the lower probabilities for class membership are appropriate.

3.4.3 Improvements to the Classifier

Alternate Features

In this work, we have used only the features that are simplest to directly extract from the numerical simulations in the machine learning classifiers. However, one could imagine that more dynamically-motivated features, such as pericentre distance, could improve classifications, especially of objects like the Neptune Trojans

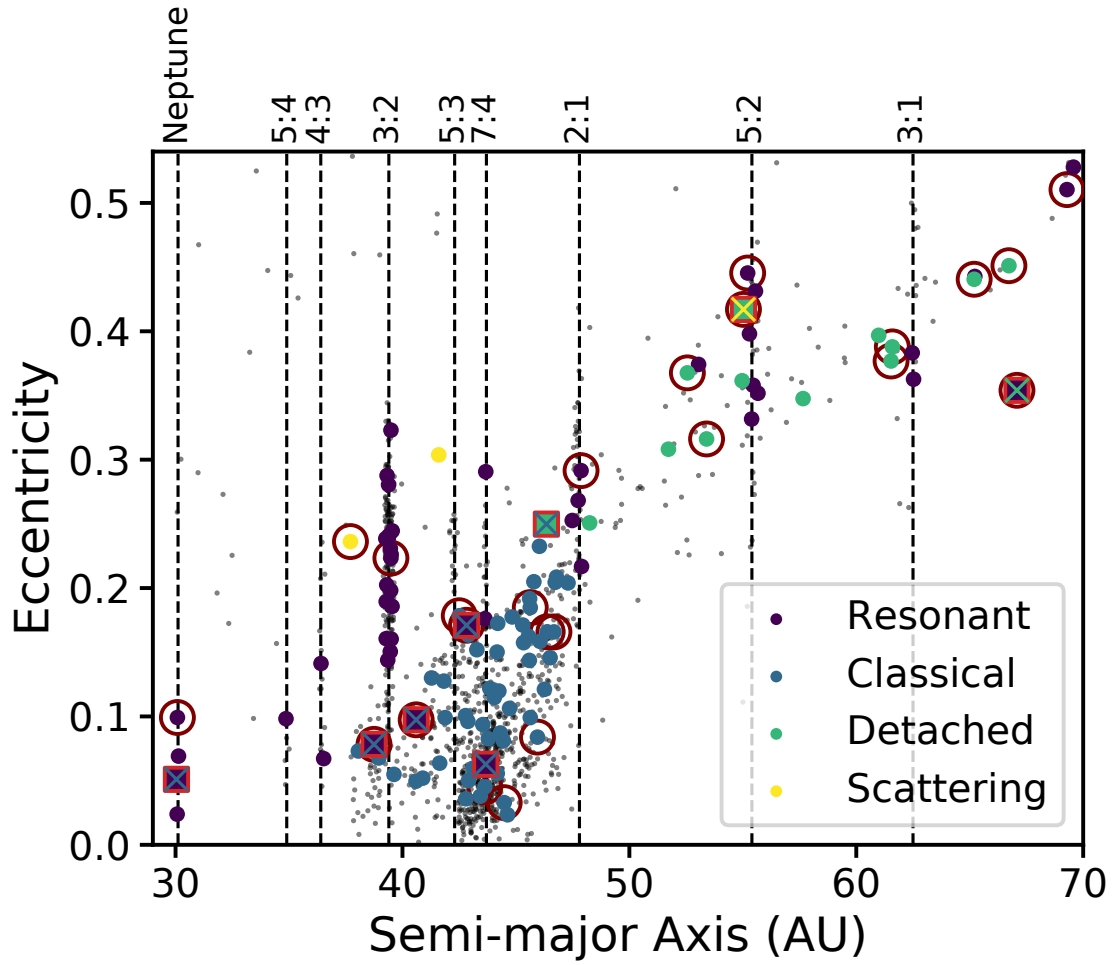


Figure 3.13: Eccentricity vs. semi-major axis for the DECAM objects following the colouring conventions of Figure 3.2. Maroon circles surround objects that have an insecure classification by the traditional method of classification (8 of the insecure objects are outside the plot limits). Of the 131 DECAM objects classified here, 10 disagreed with the labelled class (92.4 per cent accuracy) despite 33 of those labelled classifications being insecure.

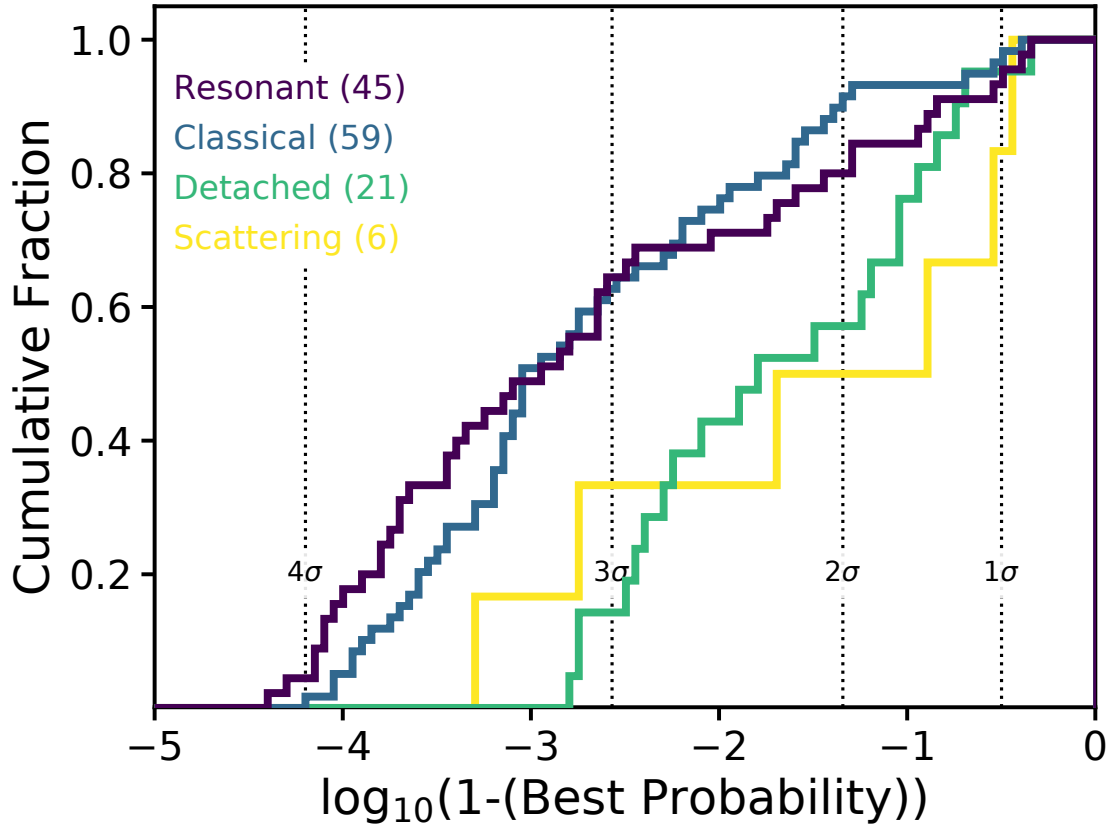


Figure 3.14: The cumulative probabilities of class membership for the DECam objects based on the class assigned by the GBC machine learning classifier. Over 50 per cent of objects have a $> 3\sigma$ probability of class membership despite the relatively large error of the observed orbits that act as inputs to this method.

(objects in the 1:1 resonance) or scattering objects that cross Neptune’s orbit. To test if new features improves the classification, we compute the pericentre distance for all objects at each simulation step and extract the same set of features described in Section 3.2.2 (mean, standard deviation, time derivative, etc.) to add to the feature ensemble used to train the classifier. We also add some additional features for the orbital angle evolution: we include the total slope of ω and Ω , which are intended to be less sensitive to short time-scale variations than $\dot{\omega}$. Using the same set of objects in the training and testing sets, albeit with the new features, we achieve the same accuracy as found for the fiducial data. The best-fitting probability distributions are nearly identical; the cumulative fractions vary by less than 0.07 across all bins for all classes. The ordering and relative influence of feature importances are the only change resulting from the addition of new features. The second most important feature in the fiducial data, $\max \dot{\omega}$, is replaced by the slope of ω , and the initial pericentre distance becomes the third most important feature. However, because pericentre is a higher-dimensional combination of features that already exist in the data, little *new* information is added to the classifier, leading to no better accuracy in object classification.

Synthetic Kuiper Belt Catalogs

The classifier developed herein has the most difficulty classifying less common objects, such as objects in mixed-argument resonances. The dominant factor in the classifier’s struggle with these types of objects is low number statistics. Because only a few examples are known across the entire Kuiper Belt, there aren’t sufficient numbers in the training set for the classifier to extract a strong set of features that characterizes the population well. To alleviate this issue, one could create a more balanced data set (meaning that there are more equal numbers in different populations) using simulated objects. The benefits of a synthetic catalog include an extremely well-characterized input sample and the ability to include large numbers of objects in every population class. The larger number of objects in a synthetic data set would also allow separation of some classes into sub-components. This

would be particularly useful for identifying different kinds of resonant behavior. If the mixed-argument resonant objects, which have different characteristic a , e , and i evolution compared to the eccentricity-type resonant objects, were included in the classifier as an independent class, the classifier would likely achieve a better and more accurate classification for this population. This approach might also help with classifying intermittently resonant objects; feeding the classifier a labelled set of objects that are not librating during the 100 kyr integrations but that will librate for the majority of a 10 Myr integration might help it identify features associated with being on the boundary of a resonance. Just as with an observed data set, a synthetic data set runs the risk that any type of object not included in the synthetic data set (such as a type of resonance not yet seen) may not be properly classified; but conversely, in a synthetic data set, one could include theoretically hypothesized or predicted populations of objects not yet observed. A synthetic catalog might also be more useful for sub-classifying resonant objects into their specific resonances rather than into one bulk class of resonant objects. This idea will be explored in a future paper.

3.5 Conclusions

In this chapter, we successfully demonstrate that very short (~ 100 kyr) numerical integrations can be used to classify observed KBOs into their dynamical populations (resonant, classical, detached, and scattering) with high accuracy (> 90 per cent). We use 1805 KBOs that have secure classifications as the fiducial data set and take the traditional 10 Myr classification as the ‘true’ classification; the data consist of 642 resonant, 998 classical, 74 detached, and 91 scattering KBOs. We find the following.

1. A gradient boosting tree classifier, which is a multi-class machine learning classifier that uses several initializations and layers of sorting trees for classification, achieves a 98 per cent accuracy on the fiducial testing set of 542 securely classified KBOs. We find that the most important data features for

classification are the standard deviation of semi-major axis (σ_a) and the maximum time derivative of the argument of pericentre ($\max \dot{\omega}$).

2. we find that ~ 80 per cent of our fiducial testing set has a $> 3\sigma$ probability of belonging to the correct class. Misclassified objects typically have a much lower probability of class membership ($< 2\sigma$), making them easy to differentiate. Almost all of the objects assigned higher probabilities of incorrect classifications (i.e., potential false positives) are objects that are in mixed-argument mean motion resonances with Neptune; this is an uncommon type of resonance inadequately sampled in our training set.
3. Misclassified objects tend to lie along the boundaries between populations in feature space, indicating that the classifier is picking up on ambiguity between dynamical populations. Many of these objects have orbital evolution that makes their true classifications difficult to determine.
4. Objects drawn from the observed error space of known KBOs typically have the same classification and probability of class membership as the best fit. Because the machine learning algorithm operates on a shorter integration time-scale than the fiducial 10 Myr classifications, a promising avenue for future classification pipelines is to use those computational savings to better explore the uncertainty range of the observed KBOs' orbit fits. We demonstrate how a large ensemble of clones can be used to better verify population membership for an object and to provide insight into the intrinsic physical variability of an orbit's observed error distribution.
5. we test our algorithm on a completely new data set of 131 KBOs recently released from a DECam survey (Wasserman et al., 2020) and find a 92 per cent agreement with the 'true' classifications despite only 75 per cent of the objects having a secure true classification. This successful performance on an unknown data set with a mix of secure and insecure 'true' classifications that is typical for surveys indicates that a machine learning classifier will be

viable for any new observed KBOs.

We have shown that a simple machine learning classifier will be a viable and valuable tool for classifying KBOs in the LSST era. We are able to substantially reduce both the computational and human resources needed to label observed KBOs into their dynamical populations, which will be critical as the number of objects grows by an order of magnitude in the next several years. Methods like this have also recently been proven successful for asteroid family members (Carruba et al., 2020). There are a number of improvements to the work presented here that would enable this methodology to be more reliable for expected large survey observations. Most importantly, a large synthetic training set should be created; such a training set would allow for more accurate classification of rarely-observed dynamical types, prepare for classification of as-yet unobserved object types, and perhaps enable for a more detailed division of dynamical classes (e.g., classifying into individual resonances). Being able to accurately and efficiently classify Kuiper Belt observations will enable science by allowing for detailed comparisons of planet formation and evolution models with the Kuiper Belt today.

Acknowledgements

We thank our reviewer Jean-Marc Petit for his thoughtful analysis of our work. We thank Leon Palafox for input on an early iteration of this project, and we thank Kaitlin Kratter for helpful comments on this manuscript. RAS acknowledges support from the National Science Foundation under Grant No. DGE-1143953. KV acknowledges support from NSF grant AST-1824869 and NASA grants NNX14AG93G, NNX15AH59G, and 80NSSC19K0785.

CHAPTER 4

Planet Scattering Around Binaries: Ejections, Not Collisions

This chapter has been previously published as Smullen R. A., Kratter K. M., Shannon A., 2016, MNRAS, 461, 1288 (DOI: 10.1093/mnras/stw1347)

Abstract

Transiting circumbinary planets discovered by *Kepler* provide unique insight into binary star and planet formation. Several features of this new found population, for example the apparent pile-up of planets near the innermost stable orbit, may distinguish between formation theories. In this work, we determine how planet-planet scattering shapes planetary systems around binaries as compared to single stars. In particular, we look for signatures that arise due to differences in dynamical evolution in binary systems. We carry out a parameter study of N -body scattering simulations for four distinct planet populations around both binary and single stars. While binarity has little influence on the final system multiplicity or orbital distribution, the presence of a binary dramatically effects the means by which planets are lost from the system. Most circumbinary planets are lost due to ejections rather than planet-planet or planet-star collisions. The most massive planet in the system tends to control the evolution. Systems similar to the only observed multi-planet circumbinary system, Kepler-47, can arise from much more tightly packed, unstable systems. Only extreme initial conditions introduce differences in the final planet populations. Thus, we suggest that any intrinsic differences in the populations are imprinted by formation.

4.1 Introduction

In the early part of this decade, a long-awaited discovery was made: the first transiting circumbinary planet from *Kepler*. This planet, Kepler-16, was reported by Doyle et al. (2011). Since then, another eleven circumbinary planets (CBPs) have been found, including the only known circumbinary multi-planet system, Kepler-47 (Orosz et al., 2012). While the sample of planets is still small, a few unique characteristics have emerged. Welsh et al. (2014) observe that there are no very massive, close-in planets, and the known planets tend to reside close to the stability limit of the binary. Although these trends might arise coincidentally due to the small sample size, if real, they hint at differences in the formation and evolution of planets around binary and single stars. In this work, we aim to tease out whether circumbinary disks might preferentially form lower mass planets near the stability boundary, or if dynamical processes sculpt the systems into what we observe.

Transiting CBPs provide important insight into planet formation and planetary dynamics because we can investigate the interplay and timeline of binary star formation and planet formation. Most simply, formation “in-situ” around the binary is strongly favored. Armstrong et al. (2014) find that the observed CBP population is consistent with formation in a co-planar disk, unless the formation efficiency for CBPs drastically exceeds that for single stars. This similarity aside, the formation mechanisms for CBPs may be somewhat different than those posited for planets around single stars. Circumprimary/secondary protoplanetary disks are often truncated or less massive in close binaries, leaving less planet-forming material, while circumbinary disks can be as massive as a single-star disk (Harris et al., 2012). In contrast, the population of the debris disks around binaries do not show flux deficits, as might be expected given the reduced mass in the parent population (Rodríguez et al., 2015). Martin et al. (2013) propose that CBP formation might happen more efficiently in dead zones (quiescent regions in the disk mid-plane), which could produce gas giants easily. On the other hand, the binary can excite substantial eccentricity in the protoplanetary disk, inhibiting planet formation near the binary.

The eccentric disk gives rise to eccentric planetesimals which suffer high velocity collisions that lead to erosion instead of growth, pushing planet formation to larger radii (Marzari et al. (2013), Silsbee and Rafikov (2015)). If a planet instead forms in the outer disk and migrates inward due to tidal interactions with the disk, one might still expect planets to exist close to the stars, which Bromley and Kenyon (2015) posit to be the likely scenario. Pierens and Nelson (2013) find that a planet forming in the outer disk can migrate toward the stability limit but will probably be pumped to moderate eccentricity along the way. Additionally, Pierens and Nelson (2008) find that massive planets, if they exist around binaries, are probably found at larger radii because tidal torques from the binary cause outward migration.

We must also consider planet formation in the presence of binary evolution. There is a lack of observed planets around short period binaries (periods less than about 7 days; Armstrong et al. (2014), Martin and Triaud (2014)). Models proposed in Mazeh and Shaham (1979) and Fabrycky and Tremaine (2007) suggest that these binaries form on wider orbits and then migrate due to tidal circularization stemming from Kozai oscillations induced by a tertiary companion. Martin et al. (2015) suggest that this is prohibitive for CBP existence around a tight binary, while Muñoz and Lai (2015) and Hamers et al. (2016) posit that CBPs may just become very misaligned. Both of these scenarios would provide a dearth of transiting CBPs around close binaries.

Formation alone, however, does not explain the present-day orbits in planetary systems around single stars. Previous works, such as Chambers et al. (1996), Faber and Quillen (2007), Jurić and Tremaine (2008), Chatterjee et al. (2008), Smith and Lissauer (2009), Raymond et al. (2010), Lissauer et al. (2011b), and Pu and Wu (2015) have looked at the impact of planet scattering on planet populations around single stars. Mustill et al. (2014) and Veras and Gansicke (2014) have extended this to understand dynamical evolution over the full stellar lifetime. Specifically, Jurić and Tremaine (2008), Chatterjee et al. (2008), and Pu and Wu (2015) have found that the observed exoplanet sample is consistent with significant sculpting by dynamical evolution. This naturally raises the question of how scattering is modified

around binaries.

The addition of a second massive body substantially changes stability very close to the binary. Holman and Wiegert (1999) have shown empirically that orbits within about two times the binary semi-major axis are unstable on very short timescales, suggesting that neither planets nor the natal disk should exist in this region. However, it is unclear how significantly planets on wider orbits will be impacted except at special locations such as mean motion resonances with the binary. One possible avenue of further evolution is the modest eccentricity excitation at semi-major axis 2-10 times the binary semi-major axis, which may fundamentally change the course of planet-planet scattering and thereby change the resultant population. In this work we aim to understand the impact of the binary on planet populations sculpted by planet-planet scattering. By isolating the role of the binary in any differential evolution due to scattering, we can determine which differences are imprinted by formation.

To address the interplay between the formation and dynamical evolution of circumbinary planets, we perform N-body integrations of planets around single and binary stars. We study the binary’s impact on a wide range of different planet populations, investigate the changes in orbital properties as a result of dynamical processes, and compare the resultant populations around single and binary stars. We first review previous work in Section 4.2. In Section 4.3, we discuss the methods used to carry out our study and explain our choice of systems and planet populations. Section 4.4 details the differences we see between the various planet populations and between planetary systems around single and binary stars. Section 4.5 discusses the physical intuition for the reduction of collisions, the role of giant planets in system evolution, and the observable properties of our systems.

4.2 Planetary Stability

While any system of three or more bodies may be chaotic, there are several limiting cases where orbits are well behaved. The simplest case is that of two planets around a

single star that are Hill stable, which means that they cannot suffer close encounters. Gladman (1993) explored Hill stability for low mass, low eccentricity, co-planar bodies and found that systems of two planets are Hill stable for orbital separations greater than $\Delta > 2.4((m_1 + m_2)/M_*)^{1/3}$ where m_1 and m_2 are the masses of the planets and M_* is the mass of the central star; here, the orbital radius of the inner planet is taken to be 1.

Multi-planet stability is often referenced to the two-planet Hill stability limit by measuring planet spacing in terms of a mutual Hill radius:

$$R_{\text{H,m}} = \left(\frac{m_1 + m_2}{3M_*} \right)^{\frac{1}{3}} \frac{a_1 + a_2}{2} \quad (4.1)$$

where a_1 and a_2 are the semi-major axes of the planets. We define the dimensionless spacing of planets in terms of mutual Hill radii as:

$$\beta = \frac{a_2 - a_1}{R_{\text{H,m}}} \quad (4.2)$$

Note that in some regimes, β may not provide the best metric for planetary stability (see Morrison and Kratter (2016)). Previous works such as Chambers et al. (1996), Faber and Quillen (2007), Smith and Lissauer (2009), Shikita et al. (2010), Lissauer et al. (2011b), and Pu and Wu (2015) have studied the impact of β on the dynamical “lifetime,” meaning the timescale for planets to enter crossing orbits, for systems of three or more equal mass planets around a single star. They find that the lifetime of a system decreases with increasing planet mass, planet eccentricity (e), and system multiplicity, and increases with the initial spacing measured by β . Chambers et al. (1996) suggested that Gyr stability requires $\beta > 10$ for > 3 planet systems and Smith and Lissauer (2009) found that a spacing of $\beta > 8$ is required for Myr stability in systems with five or more equal mass planets. Kratter and Shannon (2014) investigated two-planet circumbinary systems and found that they are long-term stable (10^8 binary orbits) with $\beta > 7$. Because we are interested in CBPs of higher multiplicity and non-constant mass, we therefore might expect our planet distributions to require larger spacing than this in order to be stable for tens to hundreds of millions of binary orbits.

4.3 Methods

4.3.1 Integrator

Our integrations are carried out with a Gauss-Radau variable timestep integrator in a modified version of the N -body orbital integration package MERCURY from Chambers and Migliorini (1997). The standard variable time step orbit integrators included in the code such as Bulirsch-Stoer and Gauss-Radau are agnostic about the number of massive bodies or hierarchy of the system, and therefore are well suited to planet-binary integrations in general (Youdin et al., 2012; Kratter and Shannon, 2014; Sutherland and Fabrycky, 2015). While binary symplectic integrators exist (Chambers et al., 2002; Beust, 2003), these still require switching to a B-S style integration to resolve close encounters. If encounters are common, the integrator will be forced to use B-S integration schemes for a significant fraction of the integration.

Because of MERCURY’s origins as a planetary system integration package, most calculations are carried out in heliocentric coordinates. While this poses no challenge for the main N -body integration for some integrators, any part of the code which relies on assumptions of Keplerian orbits about a central body requires modification, such as the close encounter checks. The changes to MERCURY described herein remove this assumption when the user sets a flag for a central binary in one of the input files. This new version of the code is available for download online.¹ We briefly describe the main modifications below. All of our integrations were carried out with the Everhart (1985) Radau integrator, although the modifications should work with other adaptive time step methods.

- For circumbinary systems, we treat close encounters between any two bodies in the same way, in contrast to the standard MERCURY practice of treating encounters with the central star separately. For any pair of bodies, the code searches for close encounters based on the current Cartesian state vectors. For the Radau integrator, interactions flagged as close encounters do not effect

¹https://github.com/rsmullen/mercury6_binary

the overall time stepping in the code. This is in contrast to hybrid symplectic integrators that use a close encounter flag to choose interactions to further resolve. For the Radau integrator, the variable time step ensures that interactions down to the close encounter radius of a particle are well resolved. For planet encounters, we use $1 R_{\text{Hill}}$ as the close encounter radius, following previous work (Jurić and Tremaine, 2008). For stars, we use the empirical stellar mass-radius relationship from Demircan and Kahraman (1991) to determine the radii as a function of mass. We set the close encounter radius to three stellar radii for our fiducial runs. Note that the central body radius and second star’s radius are set in the subroutine “`mfo_user_centralradius`,” which can be easily modified to incorporate any prescription.

- Collisions, like close encounters, are also calculated for every pair of bodies based on Cartesian state vectors. They are calculated based on extrapolation from the close encounter radius over a time step. We use MERCURY’s third order interpolation scheme for all bodies, which ignores the gravitational contributions of all other bodies during the encounter. For planet-planet encounters, the choice of close encounter radius between $1/4$ and $1 R_{\text{Hill}}$ does not change the number of planet-planet collisions, so we have chosen the default of $1 R_{\text{Hill}}$ to avoid the computational cost of very small time steps. For star-planet encounters, where ignoring the gravitational accelerations from one of the stars is most severe, the time step is always sufficiently short compared to the orbital period that the star moves of order 1 stellar radius during the extrapolated encounter. The time step is guaranteed to be small, $1/1000$ th of an orbital period, because the small close encounter radius for stars forces very high time resolution during close approaches. To achieve even better accuracy for stellar collisions, one can set the close encounter radius equal to the collision radius to force the integrator to resolve all collisions explicitly. We find that the number of stellar collisions for an equal mass binary is exactly the same for close encounter radii from 1 to 3 stellar radii; however, because of

the inherent chaos of the systems and the different time resolutions, the time of collision, and the binary component that suffered a collision, may change.

- The standard MERCURY routines for calculating Jacobi coordinates and planetary Hill radii must also be modified to account for both re-ordering of planets and the offset between the system center of mass and the central body. We include a new Jacobi coordinate routine that employs a bubble sort algorithm to re-order bodies by distance before performing a coordinate transform from heliocentric coordinates. Hill radii for close encounters are calculated using the distance from the system center of mass, rather than semi-major axis, and incorporate the enclosed mass instead of the mass from a single central body.
- Finally, we apply the bug fix reported in De Souza Torres and Anderson (2008) that fixes a status initialization problem, although this is not used in the current study.

Using this modified version of MERCURY, we obtain an average energy conservation of about 10^{-5} over our 10 Myr (3×10^8 binary orbits) integration time, with ranges from 10^{-7} to 10^{-5} . Our angular momentum conservation is of order 10^{-5} . Jurić and Tremaine (2008), who also used a custom version of MERCURY found an energy error of up to 10^{-4} using their hybrid symplectic/Bulirsch-Stoer scheme.

We have also performed a code comparison with another publicly available integrator, REBOUND, (Rein and Liu, 2012). We employ their 15th order integration scheme which is similar to Radau, but conserves energy significantly better (Rein and Spiegel, 2014). The trade off is of course a dramatic (order of magnitude) increase in run time, which made it unfeasible for use in this parameter study. While REBOUND automatically treats encounters between any pair of bodies equivalently and operates in barycentric coordinates, one must modify collision routines and ensure that the system does not drift out of the box by frequently resetting the system back to the center of mass. For integrations of identical initial conditions drawn from our fiducial sample we achieved very good agreement between the two integrators (0.1% difference for planet-planet and planet-star collisions and 1.7% difference

in ejections and remaining planets when the systems are run to 10^5 years). Note that, due to the highly chaotic nature of the orbits, numerical errors introduced by the different integration algorithm are expected to produce small changes in orbit outcomes for a given planet. Additionally, the ejection algorithms, in particular, are different (MERCURY ejects from a sphere, while REBOUND ejects from a cube), so we expect small differences in the outcomes from these effects, as well.

4.3.2 Planetary Initial Conditions

There are two major influences on the long term evolution of CBPs: the properties of the binary system and the structure of the planetary system. Because the primordial conditions of circumbinary systems are uncertain, we consider a range of planet populations and binary configurations to investigate the dependence upon initial conditions. We do not use the observed planetary statistics for our populations because observed systems may already be sculpted by scattering.

Our systems are initialized with ten planets that have been randomly drawn from the planet populations described below. Our fiducial binary is equal mass and circular with components of $0.5 M_{\odot}$ separated by 0.1 AU, which gives a 10 day period. We make no assumptions about stability other than re-sampling any planet that falls within the Holman and Wiegert (1999) circumbinary stability limit of $a_{\text{pl}} < (2.278 + 3.824e_b - 1.71e_b^2)a_b$ (equation 5 in their text) where a_{pl} is the planet semi-major axis computed from the system barycenter and a_b and e_b are the semi-major axis and eccentricity of the binary. This resampling forbids initial conditions interior to the probable disk truncation edge. Planets are unlikely to have formed or even migrated into this region and may contribute to overall system destabilization, thus polluting our statistics. We apply the same initial semi-major axis cutoff for planets around a single star as we do for the binary to ensure consistency between our populations, although no such restrictions exist around single stars. Thus, very short period planets are initially forbidden around single stars but can be scattered inward during the simulation.

Each distribution is integrated with both our fiducial binary and a single star

with a mass of $1 M_{\odot}$ making the effective central mass in both cases the same. For a subset of planet populations, we vary the binary eccentricity and/or mass ratio (we define mass ratio as $\mu = M_2/M_1$); these variations are listed in Table 4.1. Although we only study one binary orbital period herein, our results are mostly scalable to wider periods, as we discuss in Section 4.5.3.

For all populations, we assume the eccentricity and inclination (i) distributions of Jurić and Tremaine (2008), who used a Rayleigh distribution with scale parameter $e = 0.1$ and $i = 5.73^\circ$. Inclinations are somewhat uncertain, so we remain with the low inclination distribution to represent a mostly flat disk formation scenario, such as suggested in Fang and Margot (2012a). The eccentricity we use is roughly consistent with the observations of Van Eylen and Albrecht (2015), who find that observed planets follow a Rayleigh distribution with scale parameter $e = 0.05$.

Our mass and semi-major axis distributions are described below. All orbital elements henceforth are described with respect to the system barycenter.

JT08 This distribution serves as our reference sample and is taken directly from the Jurić and Tremaine (2008) “c10s10” ensemble to compare CBPs to previous simulations around single stars. Planet masses are drawn from a log uniform sample ranging from 0.1 to $10 M_J$ and semi-major axes are drawn from a log uniform sample between 0.1 and 100 AU.

MMHR The MMHR (matched mutual Hill radius) distribution matches the initial planet-planet spacing of JT08, as measured by the mutual Hill radius spacing, but with lower mass planets and smaller semi-major axes. The planets are drawn from a log uniform distribution spanning 1 to $160 M_{\oplus}$ in mass and log uniform from 0.1 to 1.7 AU in semi-major axis. We choose this population to highlight the impact of binary-planet perturbations. The dynamical spacing of planets (a measure of the strength of inter-planet perturbations) is the same as in JT08, but binary perturbations will be stronger because of the compact nature of the population.

Mordasini This planet population is modeled after the population synthesis models

of Mordasini et al. (2009a,b). The semi-major axes span a range from 0.1 to 15 AU with a peak at 3 AU. The masses span $1\text{--}10^4 M_{\oplus}$, with a dominant peak at low mass and small peaks around $1 M_{\text{Neptune}}$ and $1 M_J$. The Mordasini data from which our distributions are taken do have a correlation in mass-semi-major axis space; however, our randomly drawn planets do not take this two-dimensional density into account.

LM In order to capture the properties of observed exoplanets around single stars, even though the present-day distribution may not be primordial, we create the LM (low mass) planet population. We apply the empirical planetary mass-radius relations from Weiss and Marcy (2014), Lissauer et al. (2011b), and Wolfgang and Laughlin (2012) to observed radii distributions from Morton and Swift (2014), Fressin et al. (2013), and Lissauer et al. (2011b) to create an average mass distribution for exoplanets. We then match an analytic expression for the probability distribution function using an exponential with flat probabilities at $m < 3 M_{\oplus}$ and $m > 40 M_{\oplus}$, as shown in equation 4.3.

$$P(m) = \begin{cases} 1; & m < 3 M_{\oplus} \\ (2.758 \times m^{-0.745} - 0.133) / 1.083; & 3 M_{\oplus} < m < 40 M_{\oplus} \\ (2.758 \times 40^{-0.745} - 0.133) = 0.043; & m > 40 M_{\oplus} \end{cases} \quad (4.3)$$

Figure 4.1 shows the average mass distribution in the thick black line and the analytic fit used for the LM distribution in the thick magenta line. We draw masses from $1\text{--}10^4 M_{\oplus}$; most planets have masses less than $20 M_{\oplus}$. The semi-major axes are drawn from a gamma distribution with mean 4.5 AU and range approximately 0.1–15 AU.

4.3.3 Integration Parameters

We integrate 100 different realizations for each system architecture for 10 Myr. Each system begins with 10 planets. A planet is considered ejected if it travels more

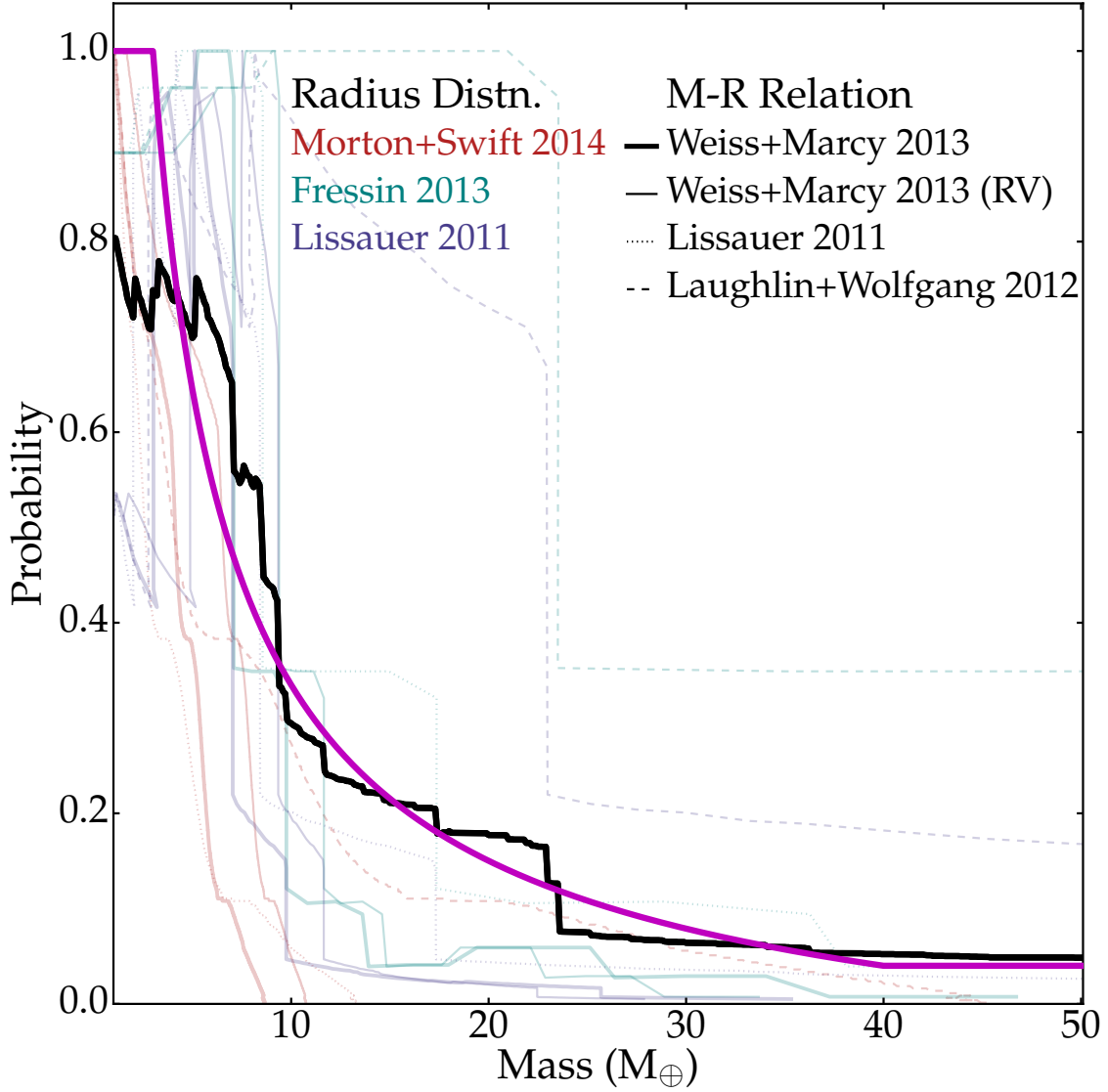


Figure 4.1: The derived probability distribution for planet masses in the LM planet sample. Each line indicates a probability distribution of planet mass in Earth masses. Each of the three colors (red, teal, and blue) represents a different completeness-corrected radius distribution derived from the *Kepler* planet sample. The different line styles denote the mass-radius relation applied to each observed radius distribution. The thick black line is the average of all of the red, blue, and teal lines. The magenta line shows our analytic expression for the probability distribution using an exponential function with flat probabilities at $M < 3 M_{\oplus}$ and $M > 40 M_{\oplus}$ as shown in equation 3. We use this mass distribution to produce an observationally motivated planet sample.

than 1000 AU from the primary star.² Note that, for the widely spaced planet populations, there is a small subset of high eccentricity, high semi-major axis planets that are removed from the system while still bound. However, these planets are a minority and would likely not contribute greatly to the further dynamical evolution of the system. Collisions between all objects are allowed in a mass and momentum conserving form (we do not allow collisional erosion or tidal dissipation).

Planetary radii are calculated using mass and an assumed density of $\rho = 1\text{g/cm}^3$. This assumed density best describes a normal giant planet, such as Jupiter. For the range of densities of known *Kepler* systems, we underestimate the radius by at most a factor of two for the least dense planet and overestimate by a factor of three for the most dense planet. Our assumption of a constant density should have negligible impact on planetary collisions; in fact, because most of our planets are smaller than Jupiter, we should more frequently overestimate the radii and therefore overestimate collisions.

It is important to note that this problem is scale free aside from collisions, which of course set an absolute radius. Otherwise, binary and planetary orbits can be scaled up or down, with the timescale adjusted accordingly. Because we find that collisions of any kind are relatively rare for most distributions, the trends presented here should be applicable to wider circumbinary systems. In these systems one would expect collisions to occur even less frequently due to increased distances between objects.

4.4 Results

The primary difference we observe between planetary systems around single and binary stars is the loss mechanism of unstable planets. Circumbinary planets are lost almost exclusively by ejections, whereas single star planetary systems undergo a substantial number of planet-planet and planet-star collisions. The evolution at

²We do not account for the offset of the primary from the system center of mass, as this distance is negligible in comparison to the ejection radius.

10 Myr has reached a near steady state; most systems have non-crossing planetary orbits that have changed little over the last few Myr. Figure 4.2 shows the average number of planets remaining in the system as a function of time. Figure 4.3 shows the outcomes for planets in the four populations. Despite the differences in outcome, single stars and binaries asymptote towards similar orbital distributions, except for the most compact, packed initial populations.

Though the final distributions of orbital elements for each planet population are relatively invariant with central object, each planet population retains a “memory” of its original state, which can be seen in Figure 4.4; the shapes of the final distributions vary significantly between different initial populations.

Scattering does not appear to account for the pileup of observed planets near the stability limit, nor do binaries preferentially lose massive planets close to the binary. Scattering thus does not reproduce these noticeable features of the observed CBP population. However, the fate of planets that begin or are scattered close to the binary star (within $\sim 10a_b$) is different from those that never enter this region, as we explore in Section 4.5.3. We discuss in Section 4.5.4 that the presence or absence of a giant planet has greater impact on the dynamical evolution of a system than the central object.

4.4.1 Differences Between Single and Binary Planet Populations

The four planet distributions around the fiducial binary show a factor of ~ 20 – 30 reduction in planet-star collisions. Planet-planet collisions are reduced by 1–2 times, and ejections are enhanced by factors of 1.5–2.5. We provide a physical explanation for these differences in Section 4.5.2. The average number of planets remaining in a system as a function of time is generally similar between the single star and the binary case. Systems reach 10 Myr with 2–4 planets remaining, on average. Figure 4.2 shows the time evolution of the number of planets in the system.

JT08 The JT08 set of initial conditions is the only one in which we have a direct comparison to previous work. We present the results of the Jurić and Tremaine

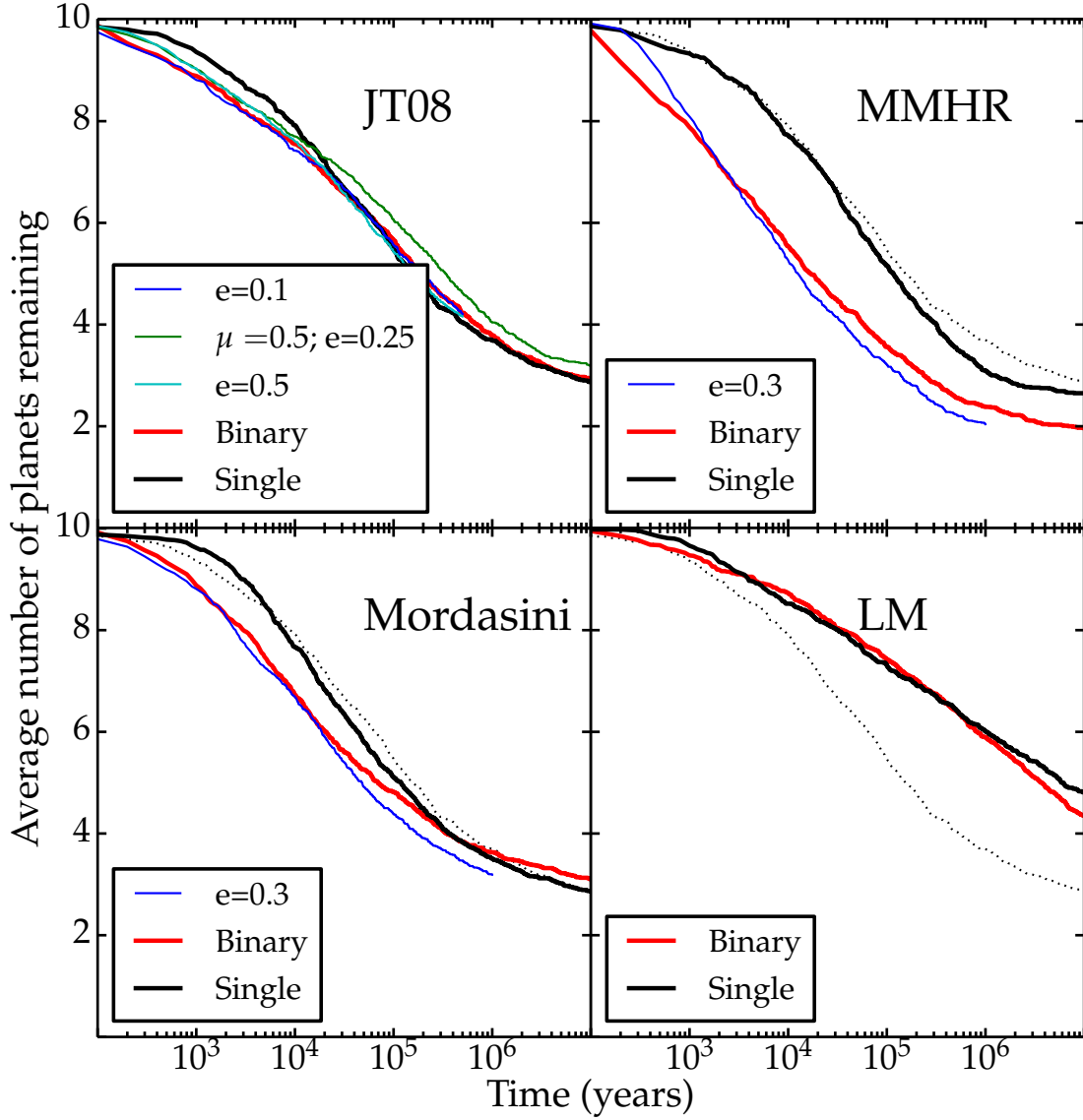


Figure 4.2: The average number of planets remaining per system as a function of time for each planet distribution. Red lines show the fiducial equal-mass, circular binary planetary systems and black lines show the single star planetary systems. Other colors show variations of the central binary (in e or μ). The dotted black line shows the JT08 single star case as a reference. In every case but MMHR, the single and binary systems lose very similar numbers of planets. However, the rate of loss can vary, with the binary systems tending to lose planets faster at early times. In contrast to the other distributions, the LM planet population is still dynamically evolving at 10 Myr because low mass planet-planet encounters rarely lead to ejections.

(2008) “c10s10” integration alongside our own in Table 4.1 and see that the single star integrations are consistent.

Over our 1000 planet sample for each of the binary and single star tests, we found a nearly equal number of remaining planets, an enhancement of 1.3 in ejection rates for the binary case, a reduction of 17.6 times in the number of planet-star collisions, and a factor of 2.1 reduction in planet-planet collisions. The loss mechanism is shown graphically in the first column of Figure 4.3, which depicts the fractional distribution of planet outcomes at 10 Myr. The average number of planets remaining at the end of the integration times is also shown in Table 4.1, which lists both the fiducial binary ($e = 0; \mu = 1$) and variations on binary eccentricity and mass ratio. Because we don’t run all variations on the binary to 10 Myr, we include data from the fiducial binary at the shorter times for comparison. We find that the differences between planet populations around different binaries are small.

MMHR In the binary population, we found a reduction of 1.4 times in the number of planets remaining, an increase of 2.4 times the ejection rate, and reductions of 25.8 and 2.2 in planet-star and planet-planet collisions relative to the single star case. The large increase in ejections in the binary case can be attributed to the compactness of the population (the median MMHR semi-major ax is ~ 0.6 AU or $6a_b$, as opposed to $49a_b$, $20a_b$ and $22a_b$ for JT08, Mordasini, and LM, respectively). The fractional loss rates for this set of initial conditions can be seen in the second column of Figure 4.3, and the average number of planets remaining in the system can be seen in Table 4.1.

Mordasini Despite having wildly different planet mass and semi-major axis distributions, the Mordasini population behaves most similarly to the JT08 population. On average, each Mordasini system will have one giant planet ($M > M_J$), which leads to the similarities in evolution (see Section 4.5.4). Comparing the binary and single star planet populations, there is no significant change in the number of planets remaining, a factor of 1.3 more ejections for CBPs, and

reductions of 28.6 and 1.6 in planet-star and planet-planet collisions, respectively. The outcomes of planets in this integration are shown in the third column of Figure 4.3 and in Table 4.1.

LM This is our least active sample due to the wide initial spacing in mutual Hill radii and low average planet mass. The results for this planet population should be interpreted with caution because about 50% of systems are still undergoing significant dynamical evolution at 10 Myr. We show the comparison of binary and single outcomes in the fourth column of Figure 4.3 and in Table 4.1.

Figure 4.4 compares the initial and final distributions of single and circumbinary planetary systems for the four planet populations. The semi-major axis distributions are broadened as planets are scattered to larger distances (or smaller, in the single star case, albeit rarely). The peaks of the final eccentricity distributions are similar to the initial distributions, but with a tail at high eccentricities. Lower mass planets are preferentially lost, leaving dominant populations of higher mass planets. The inclination distributions (in the binary case, as measured relative to the binary’s angular momentum axis) also develop a small tail at higher inclinations, but the majority of planets follow the initial distributions. Finally, the β distributions narrow and shift to higher values, peaking between 10 and 30 $R_{H,m}$. This is similar to the observed packing of *Kepler* single star systems reported in Fang and Margot (2013) and Malhotra (2015).

The MMHR planet population has the most variation between the single and binary cases, with the semi-major axis, eccentricity, and inclination all having an Anderson-Darling p-value less than 1%. Thus, an initially compact and packed planetary system evolves differently around a binary. Although both binary and single star systems are initialized without very close-in planets, single stars accumulate a sizable population of short period planets. Independent of central object, the MMHR planets show significant mass accretion due to collisions; the final population has a maximum mass two times higher than the initial maximum mass. JT08

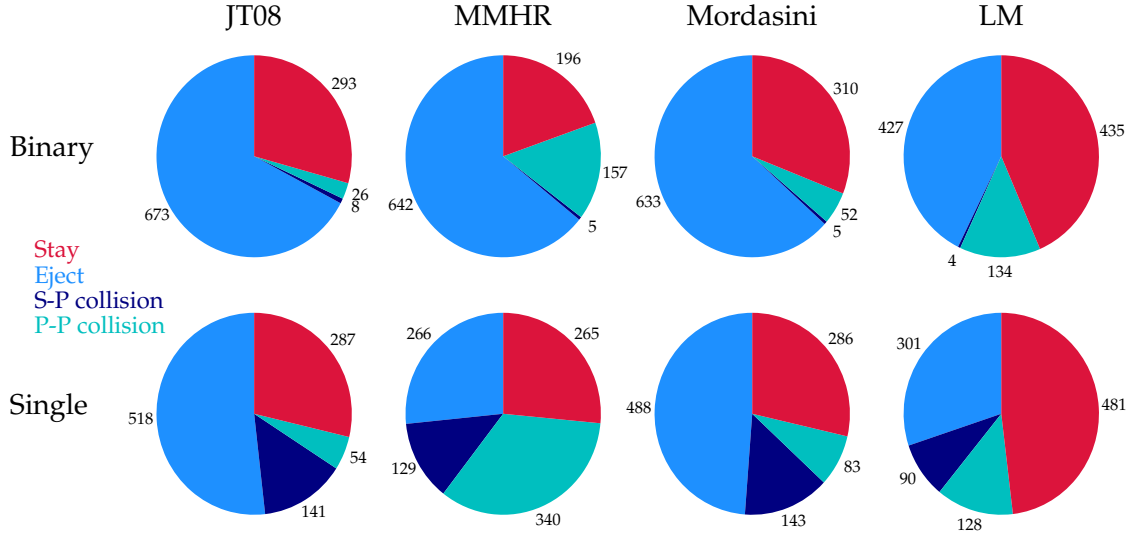


Figure 4.3: Pie charts showing the fate of planets in each distribution at 10 Myr for both binary (top row) and single (bottom row) stars. The columns correspond to the JT08, MMHR, Mordasini, and LM planet populations from left to right. Going counterclockwise, red shows the fraction of planet remaining in each system. Blue, navy, and cyan indicate the fraction of planets lost by ejections, stellar collisions and planet-planet collisions, respectively. Although the number of remaining planets is roughly constant between single and binary systems, the loss mechanism is very different. The planets around binaries suffer far fewer collisions in exchange for far more ejections.

and LM have different eccentricity distributions between single and binary (tending to lower eccentricities in the binary case), and Mordasini and LM have different inclination distributions (tending to lower inclinations in the binary case). For all populations, the mass and β distributions are similar between the single and binary cases. In both cases, the typical separation in β is a significantly larger than the minimal value for stability in idealized calculations (Smith and Lissauer, 2009; Kratter and Shannon, 2014).

4.4.2 Differences Between Planet Populations

We find that planet-star collisions remain roughly constant across all distributions, planet-planet collisions increase with decreased initial semi-major axis range, the number of remaining planets increases with increasing initial mutual Hill radius

Table 4.1: Outcome Fractions: The first column denotes the central object in the system. The second column shows the integration time in Myr. The next columns show the percentage of the initial planet populations that remained in the system, were ejected, or suffered planet-star or planet-planet collisions. The percentages here denote fraction of the total population, which will only be impacted by Poisson noise (32 planets, for our 1000 planet ensemble).

System	Int. Time Myr	Stay %	Eject %	Planet-Star %	Planet-Planet %
JT08					
Jurić and Tremaine (2008) c10s10	100	26	48	18	8
Single	10	28.7	51.8	14.1	5.4
Binary	10	29.3	67.3	0.8	2.6
Binary	0.5	42.3	54.3	0.8	2.6
Binary; $\mu = 1$; e=0.1	0.5	42.0	54.0	1.5	2.5
Binary; $\mu = 1$; e=0.5	0.5	41.6	56.5	0.7	1.2
Binary; $\mu = 0.5$; e=0.25	0.5	46.2	50.7	0.5	2.6
MMHR					
Single	10	26.5	26.6	12.9	34.0
Binary	10	19.6	64.2	0.5	15.7
Mordasini					
Single	10	28.6	48.8	14.3	8.3
Binary	10	31.0	63.3	0.5	5.2
Binary	1	36.3	59.0	0.5	4.2
Binary; $\mu = 1$; e=0.3	1	31.9	63.3	1.2	3.6
LM					
Single	10	48.1	30.1	9.0	12.8
Binary	10	43.5	42.7	0.4	13.4

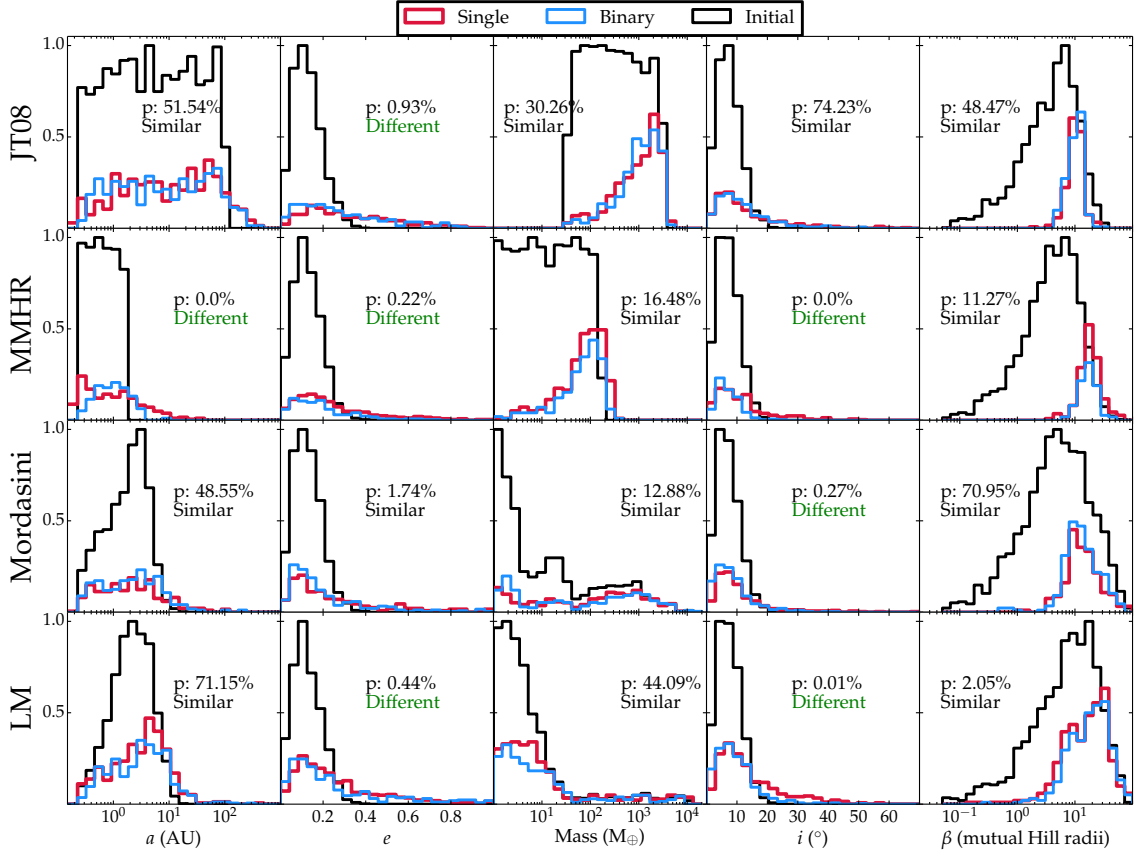


Figure 4.4: Histograms showing the initial and final distributions of orbital elements for the four planet populations. From top to bottom, the rows depict the JT08, MMHR, Mordasini, and LM populations. The columns, from left to right, show the a , e , mass, i , and β distributions. The black histogram shows the initial distribution and is created by combining the initial elements for both the binary and single cases. The single star systems are represented by the thick red line and circumbinary planets are shown in blue. Final distributions show the populations at 10 Myr. Each panel is independently normalized by the black initial distribution. We use the Anderson-Darling test to compare the single and binary distributions in each panel. Most of the properties of the planet distributions are minimally affected by the presence of the binary; however, we do see that the CBPs tend to be lower in eccentricity and inclination and that the tighter the initial a distribution, the more different the single and binary populations become (for instance, MMHR).

spacing, and ejections seem to increase with increased average planet mass and planetary compactness, consistent with Morrison and Malhotra (2015). Despite all systems beginning with 10 planets, there are significant differences in the typical number of planets remaining in a system around the fiducial binary at the end of 10 Myr. The LM population keeps the most planets (about 4, although half of systems still have planets on crossing orbits). Mordasini and JT08 each retain about 3, and MMHR systems are left with only 2 on average. In JT08, a massive, widely spaced distribution, the binary plays little role in the rate of planet loss. The MMHR planets are much more impacted by the binary because of the small semi-major axes: the binary clears out planets very fast. The Mordasini population behaves very similarly to JT08, which is likely due to the presence of a massive planet in most systems (later discussed in Section 4.5.4). Finally, the LM planets have a wider initial spacing in mutual Hill radii, so planet-planet perturbations are weaker, leading to longer instability times. Additionally, because the planets are mostly low mass, an average planet-planet close encounter will not be able to overcome the system escape velocity. Thus, to be removed from the system, a planet must interact with a rare giant planet or star, or wait for a relatively rare planet-planet collision. This leads to the “long-term” (several tens of millions of years) survival of planets from this population; note that this is still short compared to the main sequence lifetime of the central stars. There is little difference between the final inclination and eccentricity distributions, although there is a small population of high eccentricity, high inclination planets around binaries for all populations.

4.4.3 Impact on Stellar Binary Orbit

The binary’s orbital parameters are impacted very little by the dynamical evolution of the planets; most experienced less than a 1% change in their orbital characteristics. The most significant changes are seen in the JT08 binary, but even those changes are small. For instance, binary inclinations (measured with respect to the total angular momentum vector of the system) never reach greater than 20° in the most extreme case, the maximum final stellar eccentricity in initially circular

systems is 0.11, and the semi-major axis never changed by more than 0.005 AU (5%).

4.5 Discussion

4.5.1 Stability of Resultant Planetary Populations

We have conducted our above analysis after only 10 Myr of evolution. While long term evolution will still occur, the rate of planet loss (shown in Figure 4.2) appears to level off for all populations but LM. A small number of systems in the other populations still have orbit crossings, a sign of ongoing dynamical evolution. The number of orbit crossings for each of the four distributions in the single and binary cases are shown in Table 4.2. We find that, at 10 Myr, the binary systems tend to have fewer orbit crossings as compared to the single star systems. Additionally, as seen in Figure 4.2, the binary systems lose planets faster. The more rapid onset of planet ejections in the binary case is likely responsible for the reduction in any other kind of collision. Unstable, high eccentricity planets are ejected before they can interact with other planets. All of these effects combined may cause the binary planet populations to be dynamically colder after 10 Myr. If we apply the planet-packing metrics used by Kratter and Shannon (2014), we find that our final systems are consistent with being minimally packed, rather than sparse, meaning that the addition of planets in between existing pairs would likely trigger instability.

Some systems with high numbers of orbit crossings remain stable for nearly the length of the integration, especially for the LM planet population. In these instances, the kick velocities of the planet-planet encounters are much less than the escape velocity from the system. These planets will likely remain in the system until a planet-planet collision or a planet-star encounter occurs. When we extend the full complement of single-star LM integrations to 10^8 years, we find that the rate of planet loss remains constant at about 1 planet per decade of logarithmic time with no sign of reaching a constant number of planets in the system.

We find similar multiplicities to previous N -body integrations from Jurić and

Table 4.2: Orbit Crossings at 10 Myr: The number of systems with orbit crossings at 10 Myr for both single and binary systems. The first column shows the distribution. The next three columns show the number of binary systems having no, one, or two or more orbit crossings at 10 Myr. The final three columns show the same information for the single star systems.

Dist.	Binary			Single		
	0	1	2+	0	1	2+
JT08	82	16	2	73	26	1
MMHR	87	12	1	62	28	10
Mordasini	77	10	13	79	10	11
LM	49	6	45	41	15	44

Tremaine (2008), Chatterjee et al. (2008), and Raymond et al. (2010), despite all of these studies being carried out around single stars and with very different initial planet populations and initial multiplicities of 10+, 3, and 3, respectively. All assume massive planet populations, which is consistent with our finding that initial planet mass has the largest influence on the final system multiplicity, which is discussed in more detail in Section 4.5.4.

4.5.2 Absence of Stellar Collisions in Circumbinary Systems

For all circumbinary populations, the dominant form of planet loss is ejection. Indeed, ejections begin to dominate earlier in the CBP case than in the single star case. These rapid ejections are triggered when planets cross into the instability region of the binary described in Section 4.3.2. As planets get pumped to higher eccentricities by planet-planet interactions, the pericenter will enter the unstable region around the binary. Consistent with Holman and Wiegert (1999), ejections typically occur on timescales of tens to hundreds of planetary orbits after the initial crossing into the instability region. For all sets of initial conditions, over 70% of the planets that had a recorded distance less than $2.23a_b$ (the empirical Holman and Wiegert (1999) instability boundary) are ejected. 70% is a rough estimate due to coarse output timesteps in our data that may not record every planet that crossed the instability boundary. In a high-cadence output test of JT08 CBPs integrated to

100 kyr, more planets are recorded within the instability region, as expected.

The reduction of planet-star collisions can be understood using intuition gained from the circular restricted three-body problem (CR3BP). The CR3BP is a well known solution to the three-body problem in which a test particle orbits in the gravitational potential of two massive bodies on a circular orbit. While our systems inherently violate the assumptions of the CR3BP due to planets having mass and interacting with one another, we can still gain insight from approximating our systems as multiple instantaneous CR3BPs with each planet as a test particle orbiting the binary, similar to Moeckel and Veras (2012) and Kratter and Perets (2012). One can constrain the allowed orbits of test particles in a binary using the constant of motion, the Jacobi constant, shown in equation 4.4. Here, n is the mean motion of the binary ($n = 2\pi/T$ with T being the period, which is unity for our circular binary), μ is the mass ratio of the stars such that $\mu = 1 = \mu_1 + \mu_2 = GM$ and $\mu_1 = \mu_2 = 0.5$ for our equal mass binary, and r is the position of the planet measured relative to each star. The coordinates and velocities (x, y, z) and $(\dot{x}, \dot{y}, \dot{z})$ are measured in the inertial frame.

$$C_J = 2n(xy\dot{y} - y\dot{x}) + 2\left(\frac{\mu_1}{r_1} + \frac{\mu_2}{r_2}\right) - \dot{x}^2 - \dot{y}^2 - \dot{z}^2 \quad (4.4)$$

The CR3BP allows us to calculate zero velocity curves for test particle orbits with a given C_J , which denote regions in phase space where a given test particle can and cannot orbit. These are shown in the top row of Figure 4.5, where the dashed circle in all panels depicts the Holman and Wiegert (1999) instability boundary for the binary shown. The bottom row of Figure 4.5 shows value of the Jacobi constant for a particle on a circular Keplerian orbit at a particular (x, y) location. A planet with a given Jacobi constant cannot cross a zero velocity contour of the same value.

Comparing the plots in the first column of Figure 4.5, we see that a planet with $C_J = 6$ can reside on a circular orbit outside the instability boundary, but can also just penetrate the unstable region. If this happens, the planet will be strongly perturbed by the binary and its orbit will become chaotic. However, a planet with $C_J = 6$ cannot collide with either star because the zero velocity contour

completely surrounds both stars. Thus a small perturbation from another planet might easily trigger an ejection by sending the planet into unstable region around the binary. However, a small kick would not result in a planet-star collision, because without a substantial change in energy, orbits intersecting the stars are prohibited. Alternatively, a very strong planet-planet encounter causing C_J to decrease to ~ 3 would open up the orbital phase space to allow a collision with either star because the zero velocity contours are completely open on both sides. Because all of the planets in our simulations begin outside the instability boundary, with $C_J > 4$, they cannot collide with the binary unless an outside perturbation changes the constant of motion. Since most planets have much larger values of C_J , very strong planet-planet kicks are necessary to cause collisions. Note that Szebehely and McKenzie (1981) effectively predicted the empirical Holman and Wiegert (1999) boundary based on zero velocity curves.

In a high-cadence test, most planets that cross into the instability region do not have a C_J such that a stellar collision is possible, yet every planet that does collide has an external interaction that changes the energy in the system such that a collision *is* allowed according to the instantaneous value of C_J . This suggests that despite the inherent simplifications in the above model, C_J provides a useful constraint on available orbital phase space. A large fraction of planetary orbits achieve a C_J that allows them to penetrate the instability region without ever being able to collide with a star. These planets can easily be ejected from the system on short timescales, before they are likely to suffer another planetary encounter that can further decrease C_J . This leads to the > 20 times decrease in planet-star collisions and can account for some of the increase in ejections. It is also important to note that a planet with $C_J \leq 3.46$ is not guaranteed to collide; this value of the Jacobi constant allows a planet to slip through the zero velocity surface at just the right phase and interact with the stars. There are still large regions of space that disallow collisions altogether. Direct interactions with the stars are only unconstrained in space for $C_J < 3$.

Our analysis is consistent with the findings of Sutherland and Fabrycky (2015);

they find that ejections are the most common fate of unstable test particles around binaries, and that collisions are primarily with the secondary star (in the second column of Figure 4.5, the critical contour by the secondary opens at a higher Jacobi constant than for the primary star). The work from Sutherland and Fabrycky (2015) also shows that the trends seen herein hold for moderate eccentricity binaries where the CR3BP is inapplicable. We illustrate how changes in C_J correspond with planetary encounter in Figure 4.6, where we show the distance from the barycenter and the Jacobi constant for a system drawn from the JT08 distribution. In this figure, the purple planet collides after undergoing interactions that change the Jacobi constant.

It has been suggested by Laughlin and Adams (1997) and Gonzalez (1997) that the collisions of planets with the host stars may provide atmospheric pollution, leading to a measurable metallicity increase. Although the planet-metallicity correlation is likely dominated by formation effects rather than pollution (Youdin and Shu, 2002), the effect might still be measurable (Mack et al., 2014). Thus, if circumbinary disks and circumstellar disks have similar planet formation efficiencies, we can speculate that planet-hosting close binaries might show a deficit in pollution signatures as compared to single stars due to the sharp reduction in collisions.

In addition to the reduction of stellar collisions, we see a marked increase in ejections. Thus, if circumbinary systems form over-packed, we might expect that a portion of the population of free floating planets, as suggested by Sumi et al. (2011), originate from binary systems. Veras and Raymond (2012) note that the free floating planet population cannot be explained by planet scattering in single star systems alone. The potentially large contribution of free floating planets from binaries is particularly important for microlensing, which is extremely prior-dependent for interpreting detections. However, known the free-floating planet population is mainly comprised of massive planets, which might be intrinsically rare around close binaries. Additionally, known CBP hosts, with their short periods, represent a small fraction of the total binary star population (Raghavan et al., 2010).

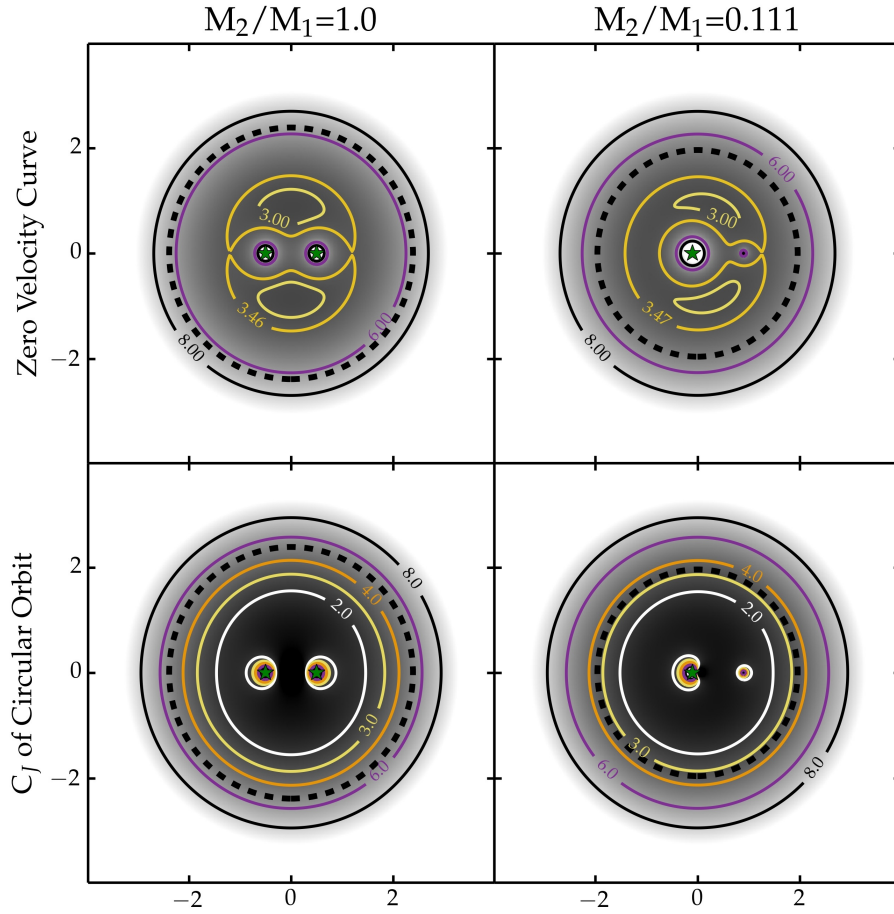


Figure 4.5: Zero velocity contours (top row) and the Jacobi constants for planets on circular orbits (bottom row) for two mass ratios. Both the gray-scale gradient and colored contours show the value of C_J and are scaled to the same range in all plots. The axes are dimensionless distances scaled to the binary semi-major axis. The dashed circle in each plot shows the Holman and Wiegert (1999) instability boundary. In the top panel, orbits cannot cross contours of the same color, thereby forbidding regions of phase space for a planet. For $C_J \lesssim 3.46$, a planet can collide with the binary; for any higher value of the Jacobi constant, scattering is the only interaction allowed. Comparison with the bottom row reveals that planets beginning on circular orbits exterior to the instability boundary have C_J too large to collide with either star, but may still penetrate the region in which orbits are unstable. We find that while planet-planet perturbations of course violate the CR3BP and change the value of C_J and thus the parameter space available to orbit, interactions in between encounters behave according to the present value of C_J . This leads to a much larger number of ejections and a smaller number stellar collisions compared to the single star case.

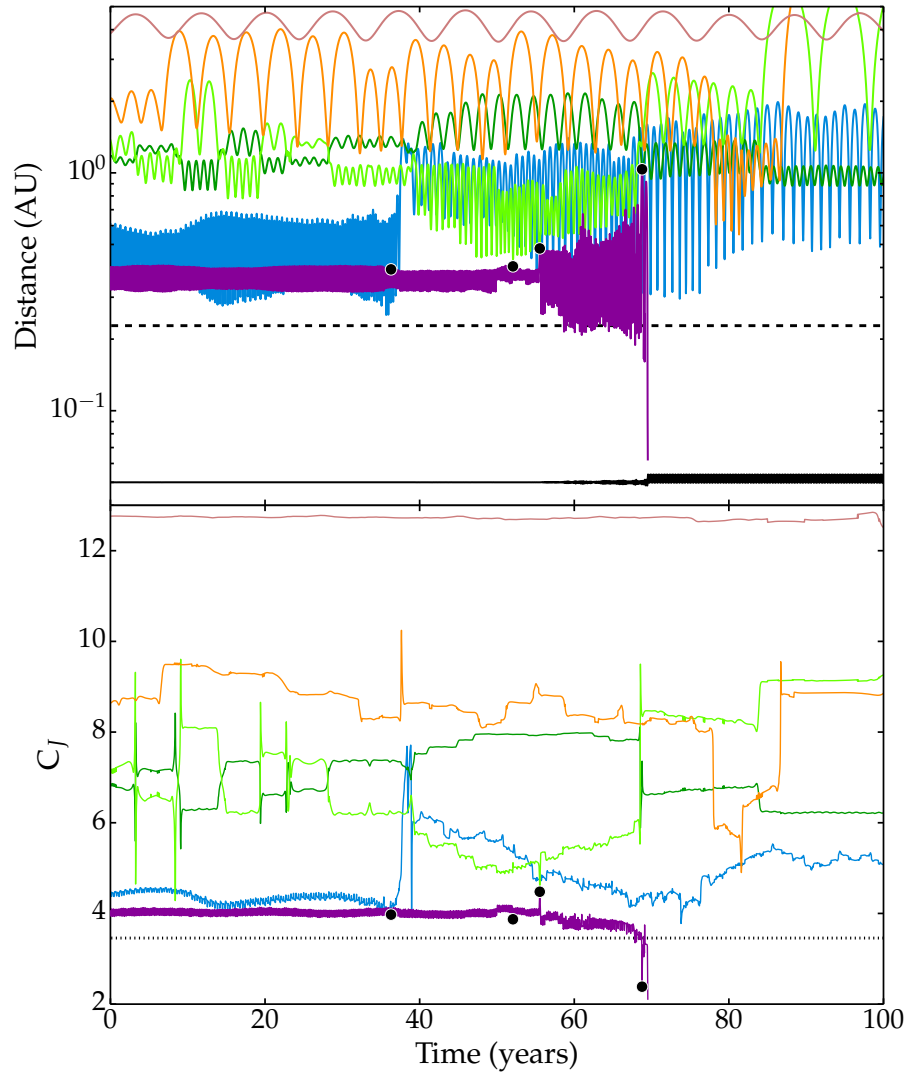


Figure 4.6: Distance from the barycenter (top) and instantaneous Jacobi constant (bottom) for six planets drawn from the JT08 distribution during the first 100 years of an integration. The solid black line in the top plot shows the behavior of the secondary star while the dashed line is the Holman and Wiegert (1999) instability boundary. In the bottom plot, the dotted line shows $C_J = 3.46$, where the zero velocity curves permit stellar collisions. The planet denoted by the purple line that begins at 0.33 AU collides with the star at 70 years. The black points show close encounters between the purple planet and other planets in the system. After these close encounters, C_J decreases such that the planet can first cross the instability region and then collide with the star. Every planet that collides with the binary has a similar evolution.

4.5.3 Extent of Binary Influence

We highlight the influence of the binary on planet populations in Figure 4.7, which shows the minimum recorded pericenter distance (relative to the system barycenter) q for ejected planets in the JT08, MMHR, and Mordasini planet populations. The histograms have been normalized to the total number of planets in the system so that the relative heights of the histograms are indicative of the total population of ejected planets. For all three populations, planets around a single star have closer pericenter passages, whereas the binary effectively removes planets once they approach the instability region (the dashed line). The planets in circumbinary systems are preferentially ejected if they pass within $10a_b$, or 1 AU.

Examining the four planet populations jointly, planets that come within 1 AU of the binary, regardless of initial semi-major axis, have a $\gtrsim 80\%$ chance of being removed from the system. Conversely, planets that never come within 1 AU have a 40–80% chance of *remaining* in the system, depending on the population. Dynamical evolution leads to 51% and 76% of planets crossing within 1 AU despite only 25% and 29% of planets initially being at separations closer than 1 AU for the JT08 and Mordasini, respectively. Thus, we find that the binary has a strong influence on the planet population within order $10a_b$. This explains why only the MMHR distribution, which populates this semi-major axis range heavily, shows significantly different final planet statistics between binary and single stars.

Although we have focused on very tight binaries in this study, our results are scalable to wider binaries than we have explored here because planet loss is dominated by ejections. Planetary and stellar radii set some absolute scale, but orbital periods and timescales may be rescaled. Although planet-planet collision rates decline at larger absolute semi-major axes, these collisions are a small impact on the overall population and would only be smaller when scaled.

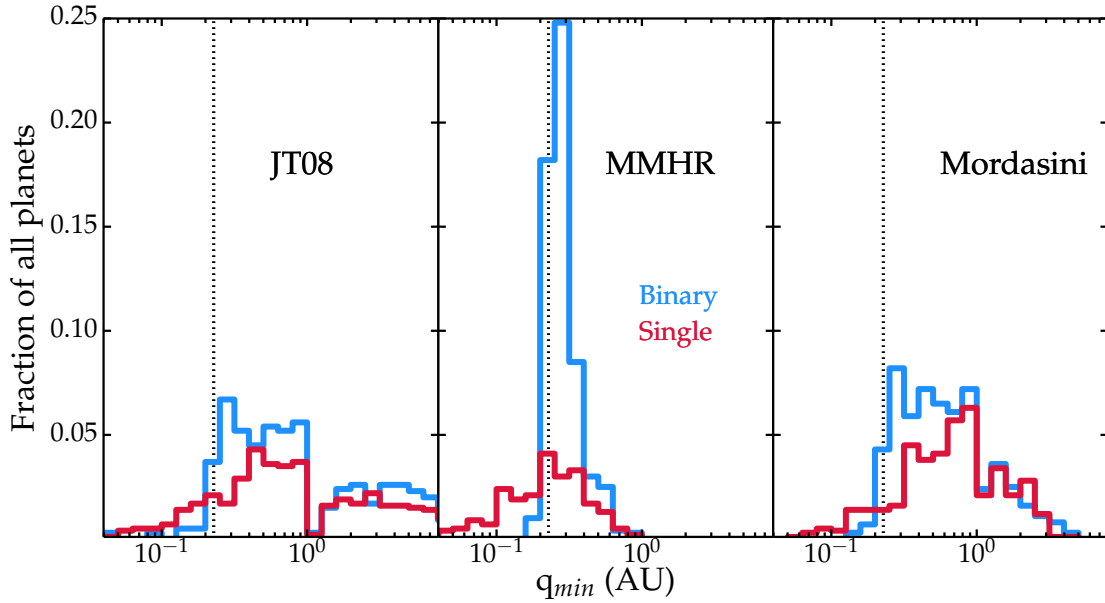


Figure 4.7: Ejected planets binned by minimum recorded pericenter distance for JT08, MMHR, and Mordasini populations. The red line shows planets around a single star and the blue line shows planets around a binary. The vertical dotted line depicts the Holman and Wiegert (1999) instability boundary. The histograms have been normalized to the full 1000 planet sample. While planets around a single star can get much closer to the star, many more close-in planets are removed from the system due to the binary. The circumbinary planets dominate ejections in all cases out to about ten times the binary semi-major axis.

4.5.4 Role of Giant Planets in Planet Multiplicity

Observed CBPs lack close-in large planets, as noted in Martin et al. (2015). While this could be a bias of small number statistics, we explore the possibility of it being a dynamical effect. We find that planet multiplicity is a strong function of the highest initial mass in the system, as is shown in Figure 4.8, but there is no statistical difference between planet populations around single stars and binary stars. Specifically looking at our numerical results for Mordasini and LM planetary systems around binaries, systems with Jupiter mass planets undergo very different evolution than their lower mass counterparts. We find that it is rare for systems beginning with a planet the mass of Jupiter or greater to have a multiplicity greater than five. Indeed, in the LM case especially, there appears to be a large break in the median highest initial mass in a system between systems containing four and five planets. Systems with four planets have a median highest mass of about $2 M_J$, while systems with five planets have a median mass of about $60 M_\oplus$, or about $3.5 M_{\text{Neptune}}$.

In Figure 4.9 we present the resultant orbital elements for the LM and Mordasini CBPs (in the same format as Figure 4.4) but split into systems having or lacking a Jupiter. In the Mordasini case, the resultant eccentricity and β distributions are statistically different for the high and low mass cases. The eccentricity of systems with a Jupiter mass planet is generally lower; both still peak at around 0.1, but the systems without a Jupiter have a small population of high eccentricity planets. The β distributions are also statistically different, with the high mass systems having a peak around 8 and the low mass systems having a peak around 15. This is consistent with the low mass systems being stable for Gyr timescales, if we apply the Smith and Lissauer (2009) results for single stars. The LM systems are where the greatest differences are seen. The eccentricities, semi-major axes, and β distributions are statistically dissimilar. The high mass systems tend to have smaller semi-major axes, eccentricities, and mutual separations. The β distribution peaks around 5 for the systems with massive planets and 30 for systems without. These characteristics all suggest that the absence of a high mass population of circumbinary planets is

not the result of different dynamical evolution. The increase in dynamical evolution in the presence of a giant planet was also seen by Hands and Alexander (2016).

Systems lacking giant planets are more widely spaced in mutual Hill radii. Because the outcome of planet-planet perturbations is controlled by the more massive body, systems without a massive planet have a larger probability of non-catastrophic planet-planet interactions. Thus, the systems can stay intact at high multiplicity. However, as will be discussed in Section 4.5.5, we find no correlation between intrinsic multiplicity and the number of transits seen in a system for the populations studied here. Therefore, the lack of observed giant planets stems from either small number statistics or formation.

4.5.5 Observables

In order to make a rough comparison with *Kepler* detections, we make a simplified calculation of the number of planets that would transit based on the following limiting assumptions. We assume that the systems are seen along $i = 90$ (edge on) for the binary systems. We also neglect planets’ orbital evolution over our assumed 5 year “mission lifetime” and limit ourselves to planets having at most a 2 year period. Martin and Triaud (2015) show that, given enough time, nearly all circumbinary planets are expected to transit due to precession effects, so these results are only valid for short duration monitoring. We find that 10–30% of systems have at least one transiting planet; only 1–5% show more than one transit. The number of systems showing a given number of transits is shown in Table 4.3. There is no correlation between observed multiplicity and intrinsic multiplicity. To provide a comparable sample around the single stars, we assume an equatorial line of sight and calculate transits. While this is an oversimplification, as stars are randomly oriented with respect to the observer, randomly choosing lines of sight would only decrease the number of observed transits and we want to compare transit rates for comparably-aligned systems. We find a slightly higher number of transits for the single star systems, but the planets around a single star can reside closer to the central star in a stable orbit and are therefore more likely to transit. Similarly, the number

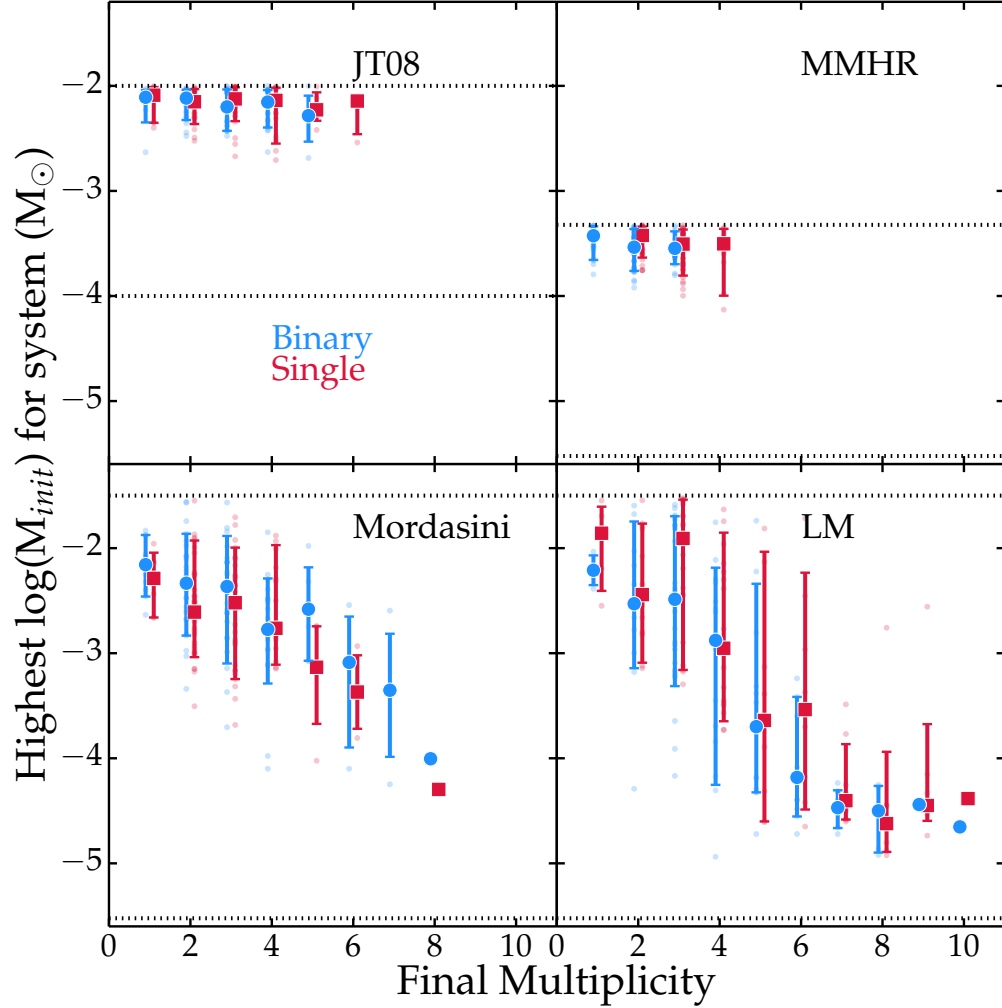


Figure 4.8: The highest initial mass in the system as a function of multiplicity for the four planet populations. The binary systems are in blue (shifted left) and the single star systems are in red (shifted right). The small points show the highest mass for an individual system, the symbols (circle for binary and square for single) show the median value of all systems at each multiplicity, and the error bars encompass the 10th-90th percentiles. The dashed lines show the highest and lowest initial masses for a population. The colored numbers (blue below and red above) show the number of systems that fall into each multiplicity bin. We can see that the presence of a Jupiter-mass planet appears to restrict the multiplicity to be less than about 5. However, the multiplicity of single and binary star systems is overall similar, so intrinsic differences in observed populations are likely due to formation and not scattering.

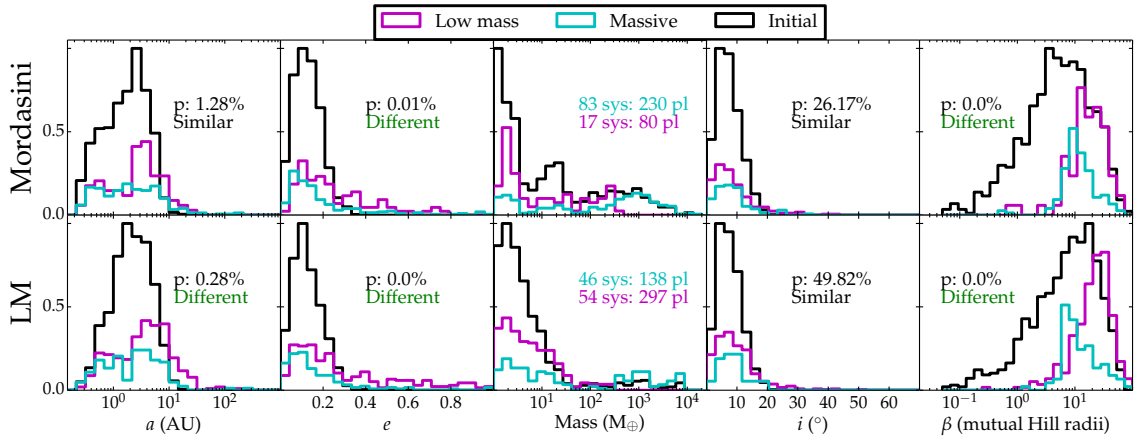


Figure 4.9: Orbital elements for LM and Mordasini circumbinary populations split by the presence of a massive planet, in the same format as in Figure 4.4. The black histogram shows the initial planet population, the magenta histogram shows the systems containing only planets less than $1 M_J$, and the cyan histogram shows the systems that have a Jupiter-mass planet or larger. All histograms have been normalized to the maximum of the initial distribution. The Anderson-Darling p-value comparing the low mass and high mass systems is shown. There are significant variations in the β distributions in particular, showing that the presence of a Jupiter strongly influences the evolution and structure of a planetary system.

Table 4.3: Number of transits: The number of systems showing transits. The first column shows the planet population. Each subsequent pair of columns (binary on the left and single star on the right) shows the number of systems with a given number of transits.

Dist.	0		1		2		3+	
	Binary	Single	Binary	Single	Binary	Single		
JT08	88	87	12	13	0	0	0	0
MMHR	81	66	15	30	4	4	0	0
Mordasini	75	71	24	28	1	1	0	0
LM	77	80	21	12	2	7	0	1

of transits is a function of the compactness of a planet population’s semi-major axis distribution. We find no correlations with the probability of a transit and planet mass, but the mass of transiting planets is roughly consistent with the mass of the initial distribution. This confirms that the dearth of giant planets on close-in orbits is not the result of different scattering behavior around binaries. The fraction of observed single planet systems to observed multi-planet systems is consistent with the known *Kepler* systems from Batalha et al. (2013).

Kepler-47 We also investigate the ability of our simulations to create a system like Kepler-47, which has three nearly unstable planets close to the central binary (binary period of 7.5 days and planet periods 49.5, 187, and 303 days (Welsh et al., 2015)). While not common, we find that both the LM and Mordasini populations finish the 10 Myr simulation with a handful of moderate multiplicity, tightly packed (both dynamically and physically) systems. However, the majority of three planet systems have average semi-major axes much larger than the true Kepler-47. Thus, Kepler-47 could be the remnant of a system sculpted by dynamical evolution but would require rather extreme initial conditions.

4.6 Conclusions

We have performed N-body simulations of planet-planet scattering around single and binary stars to tease out the influence of a central binary on the dynamical evolution of the system. Our modified version of the MERCURY code has been

released online. Our most important findings are as follows:

1. The average loss rate for planets is very similar between single star planetary systems and CBPs for a range of initial orbital distributions, though there is a weak dependence on the compactness of the initial semi-major axis distribution. Planets packed closer to the binary will be more perturbed.
2. The loss method between single star and binary systems is very different. Circumbinary systems always have far more ejections than the single star planetary systems, and both planet-planet and planet-star collisions are suppressed around binaries (planet-star collisions often by an order of magnitude). Using intuition based off the CR3BP, these reductions are expected because the orbital phase space in which planets are perturbed and rapidly ejected is much larger than the phase space allowing stellar collisions. We speculate that the reduction of collisions in circumbinary systems may lead to a measurably lower atmospheric metallicity in close binaries than in single stars or wide binaries.
3. There are few differences in the final orbital distributions of planets around single and binary stars. The final planet populations have characteristics that depend mostly on the initial populations, not on the central object. We see no evidence for a planet pileup around the binary instability boundary. We also find that systems similar to Kepler-47, while not common, are not prohibited by scattering.
4. Systems with a giant planet evolve differently than those without one. The highest multiplicity systems do not have massive planets. However, the presence of a giant planet has a similar impact on single and binary star systems.

We have shown that intrinsic differences in the populations of CBPs and exoplanets around single stars likely arise from differences in formation or disk-driven orbital evolution. We see no evidence that the lack of observed giant planets nor the pile-up of planets around the binary instability boundary can be attributed to

planet-planet and planet-star scattering. And yet, the binary does impact planets that come within roughly a factor of 10 of the binary semi-major axis. Planets born in-situ on close-in orbits are most likely to evolve differently around binary and single stars. However, this parameter space is where planet formation is most likely inhibited around binaries due to the excitation of the disk and planetesimal eccentricities close to the stars. If planet formation around binaries is very efficient, circumbinary systems might be responsible for a population of free floating planets. Thus, while dynamical evolution may not hold the key to creating intrinsic differences in circumbinary and single star planetary systems, it may provide the crucial observational evidence we need to understand these differences.

Acknowledgements

We sincerely appreciate the comments of our reviewer, Alexander James Mustill, and his work to improve this chapter. Our gratitude to Dimitri Veras and Renu Malhotra for their insightful and encouraging comments on an early draft. RAS is supported by the National Science Foundation under Grant No. AST-1410174 and Grant No. DGE-1143953. KMK is supported by the National Science Foundation under Grant No. AST-1410174. AS is supported by the European Union through ERC Grant No. 279973. The numerical simulations presented herein were run on the El Gato supercomputer, which is supported by the National Science Foundation under Grant No. 1228509.

CHAPTER 5

The Highly Variable Time Evolution of Star-forming Cores Identified with Dendrograms

This chapter has been submitted to MNRAS as Smullen, R. A., Kratter, K. M., Offner, S. S. R., and Lee, A. T. 2020

Abstract

We investigate the time evolution of dense cores identified in molecular cloud simulations using dendrograms, which are a common tool to identify hierarchical structure in simulations and observations of star formation. We develop an algorithm to link dendrogram structures through time using the three-dimensional density field from magnetohydrodynamical simulations, thus creating histories for all dense cores in the domain. We find that the population-wide *distributions* of core properties are relatively invariant in time, and quantities like the core mass function match with observations. Despite this consistency, an *individual* core may undergo large ($>40\%$), stochastic variations due to the redefinition of the dendrogram structure between timesteps. This variation occurs independent of environment and stellar content. We identify a population of short-lived (<200 kyr) overdensities masquerading as dense cores that may comprise $\sim 20\%$ of any time snapshot. Finally, we note the importance of considering the full history of cores when interpreting the origin of the initial mass function; we find that, especially for systems containing multiple stars, the core mass defined by a dendrogram leaf in a snapshot is typically less than the final system stellar mass. This work reinforces that there is no time-stable density contour that defines a star-forming core. The dendrogram itself can induce significant structure variation between timesteps due to small changes in the density field. Thus, one must use caution when comparing dendrograms of regions with dif-

ferent ages or environment properties because differences in dendrogram structure may not come solely from the physical evolution of dense cores.

5.1 Introduction

Understanding the early progression and end state of star formation is fundamental to many areas of astronomy, from modeling the formation of galaxies to studying the assembly of planetary systems. Stars form in dense molecular cores embedded within gravitationally contracting filamentary structures (André et al., 2010; Arzoumanian et al., 2013; Smith et al., 2014; Arzoumanian et al., 2019). On core scales, gravity sets the dominant dense core properties (Goodman et al., 2009; Lee et al., 2014b; Storm et al., 2016), while turbulence is thought to regulate the star formation efficiency and core formation, including properties like core rotation (Padoan et al., 2012; Chen and Ostriker, 2018). There is also a population of observed, pressure-confined cores that will likely not form stars if left untouched, although these objects may later collapse due to shock interactions (Seo et al., 2015; Keown et al., 2017; Kirk et al., 2017; Chen et al., 2019a). Despite an understanding of this broad process of star formation, there are still many open questions. These include the relationship between observed core masses and the initial mass function, the time evolution of dense core properties, the role of the physical environment in the star formation process, and the formation mechanisms of bound binary (or higher order multiple) systems, among others.

Previous works have attempted to answer some of these questions by looking at individual snapshots of observed regions or simulations, yet few have ever attempted to correlate the evolution of individual cores with the broad core property distributions reported in the literature. The interplay between the time evolution of individual cores and their contribution to distributions of core properties may be especially important when understanding the connection between the core mass function (CMF) and stellar initial mass function (IMF) (Offner et al., 2014, and references therein). There is still debate about whether the IMF directly inherits its

shape from the CMF (e.g., Padoan and Nordlund 2002; Hennebelle and Chabrier 2008; Hopkins 2013) or is independent of core masses (e.g., Bonnell et al., 2001; Bate et al., 2003; Clark et al., 2007). The IMF is frequently fit with the form of a power law at high masses and a log-normal distribution at lower masses as first demonstrated in Chabrier (2003). Subsequent work has suggested that the IMF is mostly independent of star-formation physics such as accretion rate and star formation inefficiency (Hennebelle, 2012; Cunningham et al., 2018), but may depend on local environmental properties like the global radiation field and local magnetic fields (Offner et al., 2009; Bate, 2009; Dib et al., 2017; Guszejnov et al., 2017; Lee et al., 2017; Cunningham et al., 2018; Ntormousi and Hennebelle, 2019). Thus, it is imperative to know how individual cores may contribute to the interplay between the CMF and IMF evolution.

A fundamental aspect to properly interpreting both simulation snapshots and observations of star-forming regions is understanding *what* overdensities are identified as cores. Core identification in both observed star-forming regions and simulations has been a topic of active investigation for decades. Beginning with the by-eye identification of structure in molecular clouds from Blitz and Stark (1986), the field has expanded in two dominant directions. The first direction is the singular identification of dense clumps, which started from the watershed segmentation algorithm of Williams et al. (1994). This developed into the CLUMPFIND algorithm that has been utilized extensively. Other core-finding methods that return singular clumps include the gradient-tracing scheme FellWalker (Berry, 2015), GaussClumps (Stutzki and Guesten, 1990), which fits Gaussians to all peaks in the data, and CUTEX (Molinari et al., 2011), which looks for curvature changes in the data, among others. The other method of core identification is using hierarchical structure methods. Early hierarchical structure methods such as the structure trees from Houlahan and Scalo (1992) then evolved into the commonly adopted dendrogram algorithm first presented in Rosolowsky et al. (2008). Dendrograms connect structures in star-forming regions from filaments to dense cores and allow a better understanding of the hierarchical nature of the star formation process (Goodman et al., 2009).

Each core identification algorithm comes with its own often subtle biases that must be understood in the context of the analysis performed (e.g., Li et al., 2019). For instance, GaussClumps and CUTEX only fit elliptical sources, but GaussClumps can easily handle overlapping sources (Stutzki and Guesten, 1990) and CUTEX works well with large background variations (Molinari et al., 2011). CLUMPFIND has been found to be sensitive to input parameters but is widely available (e.g., Berry, 2015). FellWalker clumps can sometimes have artificial splitting due to the cleaning process but tends to be more robust to noise (Berry, 2015). Dendrograms can be sensitive to the algorithm tuning choices but provide the best understanding of the physical environment surrounding cores (Rosolowsky et al., 2008). The above is not a comprehensive list of the benefits and drawbacks of core identification methods, but it serves to show that every algorithm in use will work better in some situations as compared to others.

Simulations have become a critical tool to interpret the necessarily-incomplete window provided by observations in star-forming regions, especially as simulations have grown in resolution and complexity. For instance, Mairs et al. (2014) note the importance of high resolution observations in recovering the full mass and detailed structure of star-forming cores. Observations at moderate resolution tend to miss mass and structure due to averaging errors (Offner et al., 2012; Mairs et al., 2014). Similarly, Beaumont et al. (2013) reach the important conclusion that position-position-velocity observations carry uncertainties of 40% in computed quantities when compared to a three-dimensional simulation. Effects like gas superposition along the line of sight, line opacity obscuring core structure, and mapping observational (PPV) space to physical (PPP) space contribute confusion to an accurate physical interpretation of cores from observations, because the line-of-sight structure of a core can be easily miscalculated (e.g., Ostriker et al., 2001; Ballesteros-Paredes and Low, 2002; Shetty et al., 2010; Beaumont et al., 2013).

In this chapter, we explore the time evolution of star-forming cores identified with dendrograms and work to understand the role of the dendrogram algorithm itself in the properties of identified cores. We begin by creating an algorithm to

link dendrogram structures through time, which we describe in Section 5.2. The robustness of this methodology depends on several tunable parameters, and we explore the effect of the three major parameters in Section 5.3. We present the time evolution of the identified cores, the distributions of core properties, and other results of note in Section 5.4, and we then explore the reasons for the variability we find in Section 5.5. Finally, Section 5.6 notes the implications of our findings, including the importance of full core histories and the limitations of the dendrogram algorithm. Section 5.7 summarizes our findings.

5.2 Methodology

In this work, we aim to trace the histories of cores in simulations of star formation to test the robustness of core parameters measured throughout a core’s lifetime. Here, we discuss the magnetohydrodynamic simulation used in this work, describe our method of core identification, and present our new core tracking method. We describe the fiducial choices for our core identification and linking methodology in this section and test the impact of variations in these choices in Section 5.3.

5.2.1 A Note on Nomenclature

The meaning of the word “core” is not well defined between works. Observationally-based definitions of cores, collected in Chen et al. (2019a) and references therein, include “dense cores”, which are regions that have a dominant thermal velocity and low virial α (virialized), “starless cores” that do not have a protostar and are not virialized, “prestellar cores” that do not have a protostar but are virialized, and “protostellar cores”, which do have protostars and are virialized. Cores can also be defined in simulations as the material that accretes onto a star particle (e.g., Bate et al., 2003), or the region of dense material at a single snapshot (e.g., Ntormousi and Hennebelle, 2019).

This chapter explores differences between algorithmic, physical, and phenomenological understandings of dense cores in star formation. Toward that goal, we use

the term *leaf* for a dense structure inside contours identified with a dendrogram, the term *overdensity* for a physical collection of dense gas in the simulations, and the term *core* for the loosely-defined, observationally motivated dense structures that may form stars.

5.2.2 Simulations

Our simulation initial conditions are identical to those of run W2T2 in Offner and Arce (2015). These conditions are intended to model a piece of a local, Gould Belt star-forming region like the Perseus molecular cloud. For our purposes, the simulation represents a prototypical turbulent molecular cloud that serves as a test-bed for our core identification and tracking method; the properties of the cloud itself have little bearing on our methodology as we are investigating trends in the evolution of core structure. We outline the initialization and parameters of the simulation below.

We run a magnetohydrodynamical (MHD) simulation of a $\sim 3800 M_{\odot}$ (7.5×10^{36} g) gas cloud using the ORION2 code (Klein, 1999; Krumholz et al., 2007; Li et al., 2012). ORION2 is a 3-dimensional adaptive mesh refinement (AMR) MHD grid code that includes physics such as self-gravity, ideal MHD (Li et al., 2012), and Lagrangian accreting sink particles (Krumholz et al., 2004; Lee et al., 2014a). Our simulations are initialized on a 256^3 base grid that corresponds to 5 pc on a side with periodic boundary conditions in all spatial dimensions. We expect little influence on core evolution from our choice of boundary condition as compared to a global molecular cloud simulation.

These simulations refine the spatial resolution based on the Jeans number J such that

$$J \equiv \frac{\Delta x_i}{\lambda_J} < 0.125, \quad (5.1)$$

where Δx_i is the cell size at the current level i and $\lambda_J = (\pi c_s^2 / G \rho)^{1/2}$ is the Jeans length (Truelove et al., 1997). When $J > 0.125$, finer cells with size Δx_i are added, thus resolving the Jeans wavelength with higher resolution. Our simulations

have 5 refinement levels over the base grid, which defines our minimum resolution as ~ 4034 AU per cell for the 256^3 grid at level 0 and the maximum resolution as ~ 126 AU per cell for the cells refined to level 5. These sizes are defined based on the mean gas density in the simulation of $\rho_0 = 5 \times 10^{-21} \text{ g cm}^{-3}$ (1300 cm^{-3}) and the mean sound speed of 18800 cm s^{-1} . In regions undergoing gravitational collapse, gas is removed from the grid and replaced with a sink particle if $J > 0.25$ on the finest level (Krumholz et al., 2004). Sinks accrete mass and momentum from gas within a radius of four cells at level 5 as well as interact gravitationally with the surrounding gas.

We generate the cloud initial conditions through a turbulent driving phase that proceeds without gravity, which produces self-consistent turbulent gas density and velocity distributions (e.g., Mac Low, 1999; Li et al., 2004; Offner et al., 2008). The simulation begins with a uniform density, uniform temperature of 10 K and a uniform magnetic field in the z direction, $B_z = 13.5 \mu\text{G}$, which corresponds to an initial thermal pressure to magnetic pressure ratio (plasma β) of $\beta = 8\pi\rho_0 c_s^2 / B_z^2 = 0.1$. Then the gas is stirred for two gas crossing times by perturbing the gas velocities with a random velocity distribution that corresponds to a flat distribution in Fourier space with wave numbers $k = 1 - 2$. At the end of the driving phase, the gas reaches a turbulent steady state with a turbulent power spectrum $P(k) \propto k^{-2}$ and $\beta = 0.02$ (Offner and Arce, 2015; Offner and Liu, 2018). Finally, self-gravity is turned on, and we evolve the simulation for approximately 70% of a global free-fall time ($t_{\text{ff}} = \sqrt{3\pi/32G\rho_0} \simeq 1.5 \text{ Myr}$).

We adopt a barotropic equation of state of the form $p = \rho c_{\text{iso}}^2 [1.0 + (\rho/\rho_c)^{\gamma-1}]$, where c_{iso} is the sound speed for 10 K gas, ρ_c is the critical density at which the gas transitions from isothermal to adiabatic and $\gamma = 5/3$ is the adiabatic index. We choose an effective critical density that is comparable to the Jeans density on the maximum AMR level, $\rho_c = 7 \times 10^{-15} \text{ g cm}^{-3}$. This value is smaller than the expected critical density for dense gas, $\rho_c \simeq 10^{-14} \text{ g cm}^{-3}$ (Masunaga et al., 1998), in order to produce some warming when the maximum gas densities are reached. This lower critical density acts to eliminate contiguous small scale fragmentation,

which would otherwise occur within isothermal filaments at high resolution (Kratte et al., 2010) and roughly approximates the influence of radiative feedback, which is expected to heat the gas once protostars form (Offner et al., 2009).

The time evolution of the dense gas is shown in Figure 5.1. The density thresholds used in this plot correspond to the densities of the AMR refinement thresholds (computed from Equation 5.1). The simulations end with about $70 M_{\odot}$ of mass in 25 sink particles. The fraction of mass in the densest gas shows more variability because of mass accretion onto the sink particles. Most of the dense cores are formed in one large filament that spans the majority of the volume.

5.2.3 Structure Identification

Dendrograms are a common tool used to identify dense structures in both simulations and observations of star-forming regions; many previous works have used them to find and identify properties of bound clumps and filaments (e.g., Rosolowsky et al., 2008; Goodman et al., 2009; Beaumont et al., 2013; Burkhart et al., 2013; Lee et al., 2014b; Seo et al., 2015; Storm et al., 2016; Friesen et al., 2016; Keown et al., 2017; Wong et al., 2017; Nayak et al., 2018; Chen et al., 2018). Dendrograms also provide a metric to quantify the structure of molecular cloud emission and associated physical properties (e.g., Boyden et al., 2016; Koch et al., 2017; Boyden et al., 2018; Koch et al., 2019). For example, Goodman et al. (2009) demonstrated that dendrograms produce more physically reasonable identifications of cores in 3D spectral line data compared to another previously popular algorithm, CLUMPFIND. As an additional benefit, dendrograms naturally identify nested features and therefore reflect the relationship between structures of different sizes in the data. Thus, we choose dendrograms as our structure identification algorithm to better quantify the interpretation of this widely adopted method. However, because of the fundamental similarities between all core identification methodologies—that cores are identified from peaks in quantities such as density or emission—the results of this work should be generally applicable across algorithms.

A dendrogram is a tree algorithm that identifies hierarchical structures in any

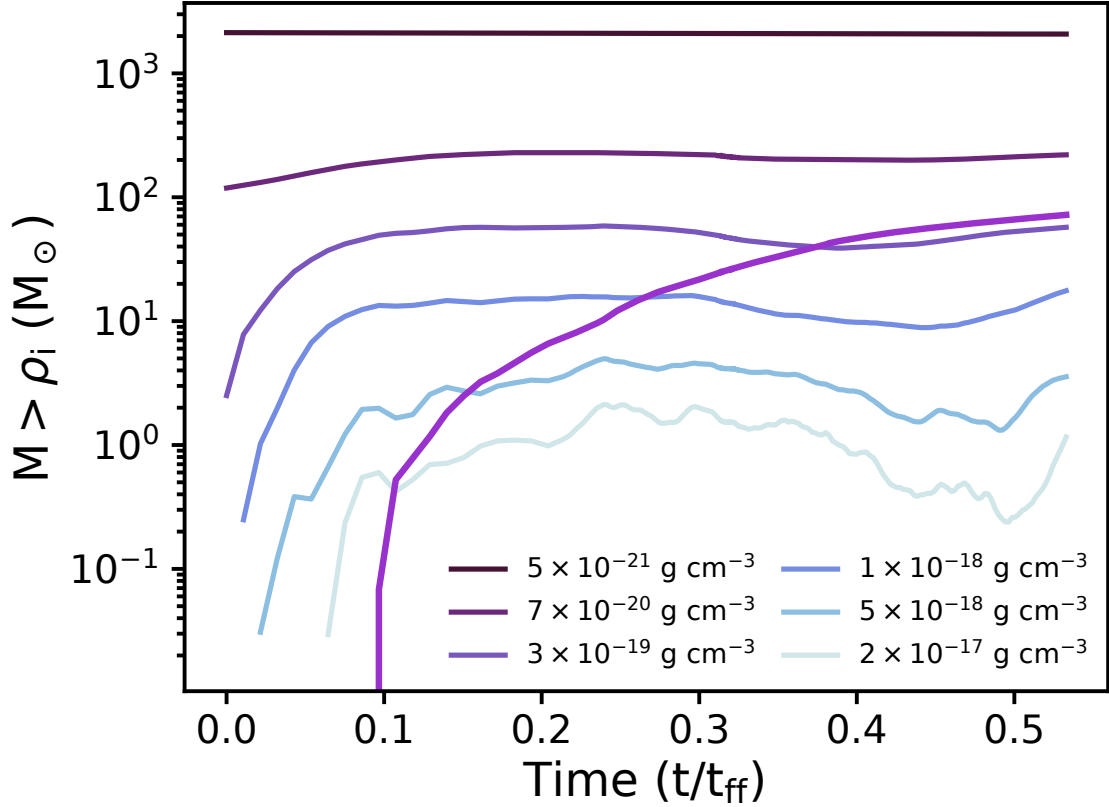


Figure 5.1: Time evolution of dense gas in our simulation. The blue colored lines indicate the total mass above a given density across time, while the purple line shows the mass of sink particles across time. The lowest density shown, $5 \times 10^{-21} \text{ g cm}^{-3}$, corresponds to a number density of approximately $1300 \text{ nH}_2 \text{ cm}^{-3}$, while the highest density of $2 \times 10^{-17} \text{ g cm}^{-3}$ corresponds to a molecular hydrogen density of $5 \times 10^6 \text{ cm}^{-3}$.

input quantity in a 2- or 3-dimensional grid. A dendrogram contains leaves (the most refined structure), trunks (the lowest level structure that may contain refined substructure), and branches (structures that connect leaves to other branches or trunks). The dendrogram initialization is commonly defined by three parameters: the background level cutoff that defines the base of the tree, the minimum difference (height) between two nested structures in the quantity being dendrogrammed required to create a new branch or leaf, and the minimum size of an identified structure. The dendrogram is built by first identifying the maximum value in the grid. The algorithm then iteratively searches adjoining cells and uses the size and density increase criteria to determine if a new branch or leaf needs to be created. The tree ends when the background cutoff value is reached. Neighboring leaves can be children of a single branch if they are both contained in the spatial bounds of the branch. A region can contain multiple unconnected trees if an area surrounding two structures is below the background cutoff. Note that dendrograms are inherently relative structures because they are computed based on the maximum value in a region. This work utilizes the **astrodendro** Python package.¹

We carefully consider how we optimize the three parameters (background cutoff, minimum density increase for new structure creation, and minimum structure size) that define how a dendrogram is built². The background cutoff will set the fraction of gas in the simulation included in the dendrogram and impact the total height of the tree (peak to minimum density, which will likely also impact the number of structures in a tree) and the number of branches that can be created. The minimum density increase to create new structure sets a height at which new branches and leaves are created: a smaller value allows smaller density increases to be considered as new structure, while a larger value makes the creation of new structure much more stringent. Finally, the minimum structure size influences the size and internal complexity of an identified core. Too large of a size means that we might group individual compact structures into one leaf, while too small of a size might over-

¹<http://www.dendrograms.org/>

²In the **astrodendro** package, these variables are named `min_value`, `min_delta`, and `min_npix`

resolve substructure in the star-forming cores we wish to study (e.g., lumps in a disk-like overdensity).

The background density threshold is a major limitation to the complexity of the dendrogram. A low background density threshold connects more of the cloud structure, including filaments, but these structures would not be readily observable in traditional tracers. On the other hand, a high density threshold might prematurely truncate low density structure. We use a fiducial density threshold of $\rho = 7 \times 10^{-20} \text{ g cm}^{-3}$ ($1.8 \times 10^4 \text{ cm}^{-3}$), which is the density needed to refine a cell from level 0 to level 1. The threshold density chosen herein roughly corresponds to the minimum density observed in ammonia emission ($n \gtrsim 10^4 \text{ cm}^{-3}$ or $\rho = 4 \times 10^{-20} \text{ g cm}^{-3}$), so the structures identified in our dendrograms would be observed in synthetic observations (Flower et al., 2006). This creates a dendrogram that contains only a few percent of the data by volume and consistently contains the same dense structures throughout the entire simulation time. As seen in Figure 5.1, our fiducial density encompasses a roughly constant mass (around $100 M_{\odot}$) over the length of the simulation. Variations of the background density cutoff are described in Section 5.3.1.

We next consider the density increase to create a new leaf. This parameter impacts the inclusion of low-density structures in our dendrograms. A small density increment produces many nested structures, and these new structures (typically intermediate branches) do not add to the understanding of either leaf structure or the hierarchy. A large density increment leads to very large leaves and begins to under-resolve the dense structures that best resemble dense cores by combining multiple overdensities into one leaf. We therefore chose a factor of 3 increase in density as the fiducial density contrast required to create a new leaf. This choice is further discussed in Section 5.3.2.

Finally, we set the fiducial minimum size of a structure to be 125 voxels (3-dimensional cells; at our fiducial grid size, one voxel is $(1000 \text{ AU})^3$). The minimum size of 125 voxels is large enough to encompass compact structures, such as protostellar disks, without being small enough to allow clumpy sub-structures to split

into multiple leaves. At our fiducial resolution, this leads to a *minimum* leaf size of about $(5000 \text{ AU})^3$, although most structures are substantially larger. For comparison, the dendrograms of Friesen et al. (2016), who investigate the size and mass of embedded clumps in the Serpens South protocluster, have a smallest effective radius of $\sim 0.02 \text{ pc}$ or $\sim 4100 \text{ AU}$. Typical observed core sizes from works such as Seo et al. (2015) and Keown et al. (2017) are 10^{-2} – 10^{-1} pc , so our minimum size resolves structures in our simulation that are similar to observed cores. The choice of the other two dendrogram initialization parameters can, in some instances, negate the utility of the minimum size. If the background density threshold is high and the density increase is large, small structures will be not be able to be resolved and every structure will exceed the minimum structure size. With our fiducial parameters, structure can approach the minimum size but the majority of leaves have volumes of a few hundred to a few thousand voxels (core sizes $\gtrsim 0.05 \text{ pc}$).

While dendrograms can be computed for any scalar quantity, we choose to compute dendrograms on the three-dimensional density grid. The large dynamic range of physical density in our simulations means that a logarithmic scaling better traces the physical structures. Therefore, to define structures in our simulations, we compute a dendrogram with periodic (wrapping) boundary conditions on the log of the density field at each simulation snapshot. The dendrogram routine can only search a uniform grid, so we must apply a covering grid to our AMR simulations. Covering grids interpolate the AMR data onto a fixed grid of size $256 \cdot 2^i$ in each dimension where 256 is the base size of the simulation and i is the level for which we want to create the grid. We define our dendrogram on a level 2 covering grid with each cell having a side length of $1.5 \times 10^{16} \text{ cm}$, or about $0.005 \text{ pc} \approx 1000 \text{ AU}$. Our choice of fiducial resolution is discussed in Section 5.3.3.

Our choice of parameters leads to dendrograms containing about 80 leaves in all but the earliest timesteps when gravitating structure has barely started to collapse. An example of the dendrogram computed with these fiducial parameters at an intermediate timestep ($40\% t_{\text{ff}}$) is shown in Figure 5.2. Many of the leaves ($> 50\%$) are isolated and not part of a larger structure that contains further refinement due to

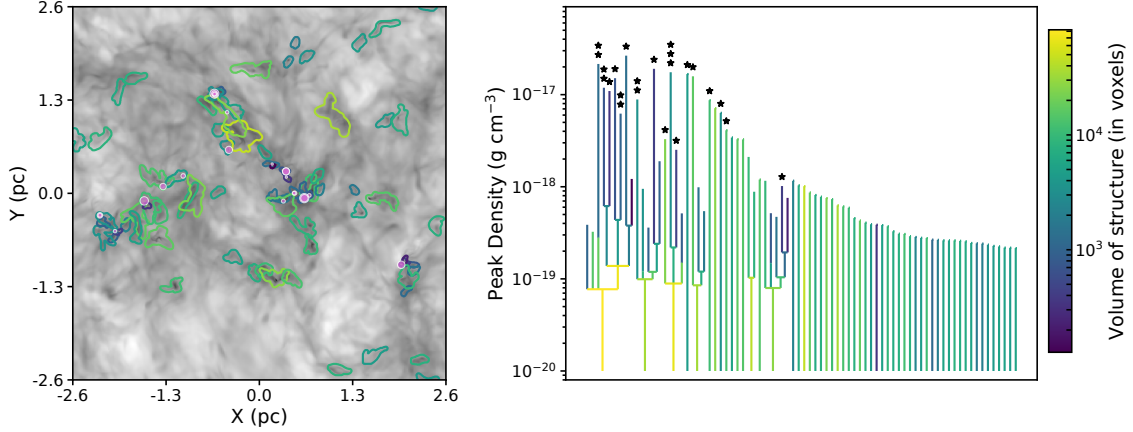


Figure 5.2: An example of the dendrogram computed with fiducial parameters at an intermediate timestep. The right panel shows the tree colored by the volume of the leaf. Black stars denote the presence of sink particles in the leaf. The x -axis has no physical meaning; the structures have been roughly sorted by peak density. The left panel shows the $x - y$ projection of the leaves. Pink circles denote the location of sink particles with sizes scaled by the mass of the sink.

our choice of background density cutoff; however, these leaves tend to be of relatively low-density, and most will likely not form stars as they are temporary structures (see further discussion in Section 5.4.4). Most leaves ($> 80\%$) do not form sink particles by the end of the simulation, and leaves containing one sink particle are about 2-3 times more common than leaves hosting multiple sink particles. Sink-hosting leaves can decrease in peak density after sink formation due to accretion of high-density gas onto the sink particle.

With the dendrogram defined, we output a catalog of important leaf parameters at each timestep (density, position, velocity, magnetic fields, etc.) using the full AMR grid that falls within the volume of the uniform-grid leaf surface. This catalog is then used to perform the linking algorithm defined in the next section.

5.2.4 Linking Structures Through Time

Once the 3-D structures are constructed for every timestep, we link them through time. We take a two step approach by first linking structures between consecutive timesteps and then by reconstructing a structure’s full path through time.

Pair-wise Linking

To match structures between timesteps, we use a geometric search that relies upon simulation outputs being frequent enough that structures do not move significantly (more than about half of their size) between outputs. Beginning with an individual leaf (l_a) at timestep t_a , we search for all leaves at timestep t_b where the center of mass of l_a is within the surface of a leaf at t_b . We then reverse the search such that we look for the center of mass of a time t_b leaf to be within the surface of a time t_a leaf. We do allow for an offset of the center of mass from the boundary of the leaf in two dimensions because of the possibility of dendrogram contours being defined differently between consecutive timesteps as discussed below. The choice of this offset is described in Section 5.3.4, but our fiducial value is set to 10 grid cells at level 2. A leaf at one timestep can be associated with multiple leaves at the next timestep, and we describe the consequences of this further below. This search is then continued between all consecutive pairs of timesteps (i.e., $t_a \leftrightarrow t_b$, $t_b \leftrightarrow t_c$, etc.).

There are four cases that result from the pair-wise linking as shown in Figure 5.3. Leaves can be uniquely identified with a single structure between $t_a \rightarrow t_b$ and $t_b \rightarrow t_a$. This is most common and leads to a single path between timesteps (panels “standard” and “offset”). However, multiple leaves can be found at one timestep that map back to a single leaf at the adjacent timestep. If the single leaf is at an earlier timestep and the multiple leaves are at a later timestep, this is a “split”. If the single leaf is at a later timestep and the multiple leaves are at an earlier timestep, this is a “merger”. In our simulations, splits and mergers are most frequently due to dendrogram leaf boundaries being drawn to encompass multiple nearby overdensities, not actual physical merging or fragmentation. Physical evolution can happen but is difficult to disentangle from the changes in dendrogram contours.

In the 170 output timesteps of our simulation, we link 11,000 leaf pairs; 10,500 of those are securely linked, meaning that we identify the same linked pair looking forward and backward. We find ~ 200 splits and mergers. About 60–70% of linked

pairs have no offset, and the average offset of the remaining linked pairs is about 10 cells (~ 0.05 pc).

We initially incorporated the velocity information, specifically the leaf center-of-mass velocity, (which includes the contribution from any sink particles that may be present in the leaf), into our algorithm to help inform the direction of motion to uniquely track a leaf through time and reduce the number of nearby, unassociated leaves linked. However, because of variability in the computation of dendrogram structures between timesteps, the leaf center of mass does not always move in predictable patterns. Therefore the addition of velocity information does not improve our linking. To demonstrate this issue, we present two examples of leaf behavior in Figure 5.4. The error bars in the upper panels have been doubled in length to be more visible. The left panels shows what a well-behaved leaf looks like: the leaf center of mass at the next time is within the position expected from the velocity. However, a significant number ($\gtrsim 25\%$) of our leaves have a history that look more like the right panels, where at certain times, the dendrogram contours are redrawn to include more material. This then changes the center of mass of the leaf and the expected position of the leaf center is wildly offset from the computed location of the center of mass. The leaf centers at consecutive timesteps are typically within the leaf contours, meaning that the less complicated geometric search discussed above is more reliable for our data. We do encounter a few pathological cases where a reconstruction cannot be performed in an automated way, such as when the leaf is shaped like a banana— the center of mass lies outside the leaf contour and is therefore computed to have a large offset to the leaf boundary at the next timestep.

Path Reconstruction

The last step to fully trace the histories of overdensities in our simulations is to transform the pairwise linking into a coherent path through time. We use the terminology “path” to denote a single set of related leaves through time and “path family” to denote a group of paths that were found to be related to a single starting leaf. For the analysis presented herein, we work backward in time (from the end

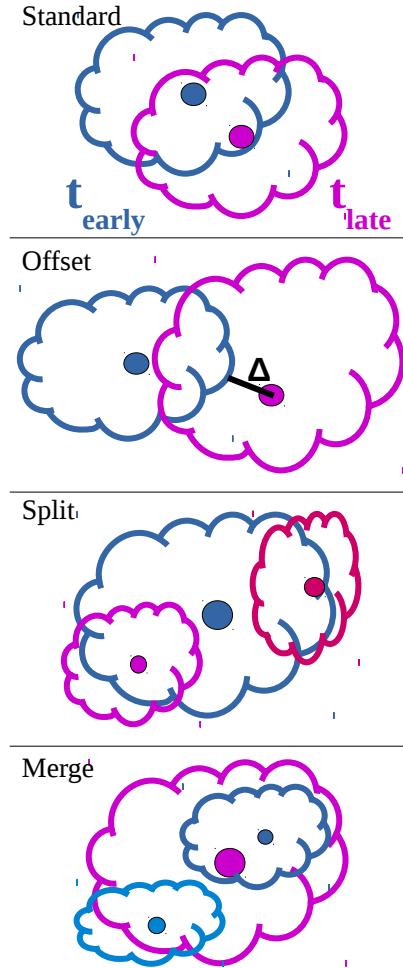


Figure 5.3: A cartoon of the cases that result from the pair-wise linking. Blue colors indicate earlier times and the purple colors indicate later times. The top is the “standard” linking where the center of mass at one timestep (filled circle) is found within the volume at the other timestep (open contour). The “offset” linking allows there to be a small offset (Δ) between the leaf center of mass and the leaf volume at consecutive timesteps, which typically arises from dendrogram contours being redrawn to include more material. “Splits” and “mergers” are cases in which a leaf at one timestep can be associated with more than one leaf at a consecutive time. Note that, while this cartoon is shown in 2-D, the linking in our data is done in 3-D.

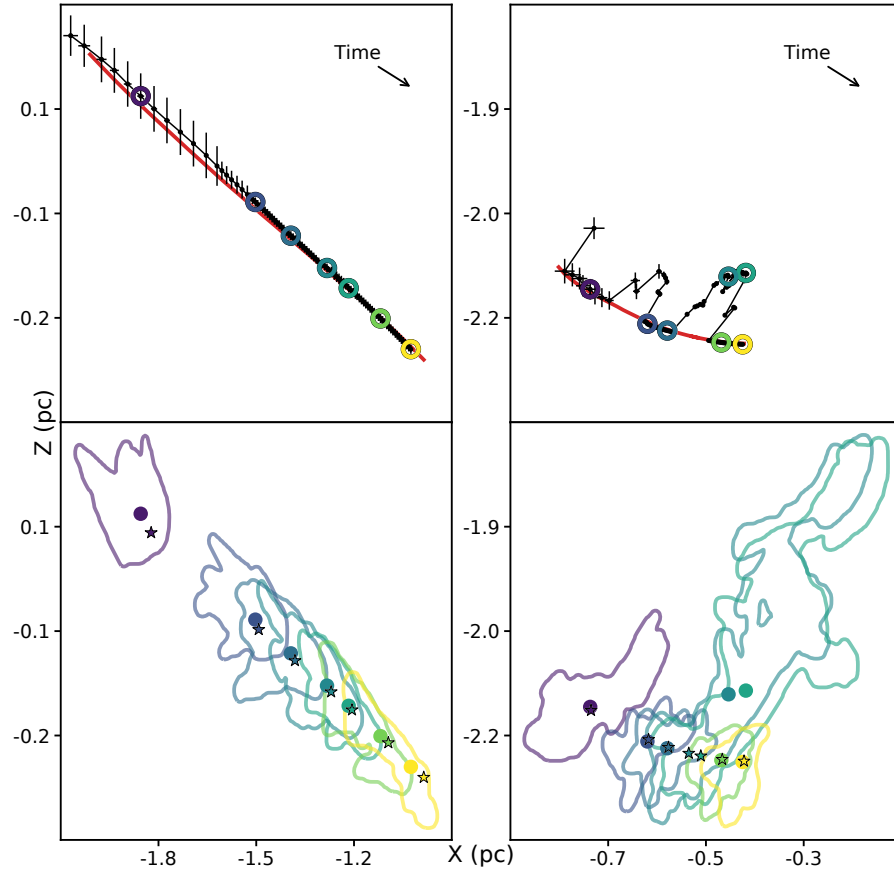


Figure 5.4: Two examples of leaf behavior illustrated by sink-hosting leaves. The left column shows an ideal behavior where the leaf structure evolves smoothly, while the right column shows a leaf that undergoes significant dendrogram structure variations in time. The upper panels show the $x - z$ positions of a leaf through time. The black line show the center of mass of the leaf through time, while the red line shows the position of the sink particle in the leaf. The error bars on the black line show the “expected” position of the leaf at the next timestep given the velocity of the center of mass of the leaf. The bottom panels show a selection of the projected leaf contours at the times indicated by colored points in the top panel. The solid circles denote the center of mass of the leaf and the star indicates the position of the sink particle. The lower right panel demonstrates a common barrier to velocity-based linking: the dendrogram leaf contours can change significantly between timesteps, offsetting the center of mass of the leaf from the expected position.

of the simulation to the start) because the most relevant structures to compare to observations are the compact overdensities found in well-evolved regions at later times in the integration. Because we use a fixed starting point in time, cores may be traced at different evolutionary stages.

we start by selecting a leaf (l_0) from the cohort of leaves at the final timestep (t_0). We search through the linked pairs $t_0 \leftrightarrow t_1$ to find the leaf at t_1 linked to l_0 . This found leaf is added to the path. We then check if the leaf at t_1 is associated with any other leaves at t_0 . We then iteratively repeat this process to search for matches to the earliest leaf in the path going backward in time.

For the cases where there are mergers (two or more leaves at an earlier time being associated with only one leaf at a later time), we add one of the leaves to the current path and then add new paths to the path family by copying the current path and appending the other merged leaf. Each path in the path family is then reconstructed independently.

For the cases where there are splits (two or more leaves at a later time being associated with only one leaf at an earlier time), we create a new path and recursively search in the opposite direction (from early times to late times) to find the path(s) associated with the new leaf.

Path families can have many component paths because each new split or merger effectively doubles the number of paths in a path family. While not always indicative of physical interactions, a large-number path family does indicate that the structure lives in a crowded area of the simulation volume.

5.3 Parameter Variations

All core identification algorithms include tunable parameters, and the dendrogram algorithm we adopt here is no exception. In observational studies, the parameters are chosen based on the noise, sensitivity and resolution of the data. When analyzing simulation data there is more flexibility in parameter choice. Consequently, we explore a variety of parameter values to assess the physical impact of our parameter

choices, including background cutoff density, density increment to create a new structure, grid resolution, and linking distance Δ . Thus, in this section, we explore how variations in these parameters impact our reconstructed path families. While the minimum leaf volume at constant resolution is also a tunable parameter, we find negligible impact on the final dendrogram structure when varying this quantity within reasonable limits.

5.3.1 Background cutoff

The background cutoff influences the tree complexity, leaf structure, and computational requirements of a dendrogram. Values near the mean density in the simulation ($5 \times 10^{-21} \text{ g cm}^{-3}$) include too much gas that never participates in the star formation process. Very large, low density structures affiliated with the filamentary structure are commonly identified as leaves. Values at high-density (level 2 refinement density or higher, or around $3 \times 10^{-19} \text{ g cm}^{-3} \sim 8 \times 10^4 \text{ cm}^{-3}$) exclude an extremely large portion of the gas ($\gtrsim 99\%$), including gas at early times that will eventually fall in to a dense core. The level 2 refinement density corresponds to a Jeans length of 0.08 pc, which is smaller than typically observed cores. The dendrogram would be less likely to resolve any structure larger than this, which includes most of the objects that resemble observed cores; instead, the algorithm would only identify small peaks in larger overdensities. For these reasons, and the physical arguments described in the previous section, we use the fiducial density of $7 \times 10^{-20} \text{ g cm}^{-3}$.

5.3.2 Density Increment

The contrast required to create a new structure in the dendrogram mainly impacts the low-density structure identified in the tree. We compare density increases of factors of 2, 3 (my fiducial choice), 4, 5, and 10 and find little difference between the leaves identified, although the trees themselves are quite different. We show the comparison of factors of 2, 3, and 5 in Figure 5.5. All high-density structure is contained in all trees; the major differences arise in the low-density structures.

Every sink particle lives in a nearly identical leaf, meaning that the important structures for star formation are not impacted greatly by our choices of density contrast parameter.

The trees computed with large density contrasts identify much less structure because overdensities must be much more significant to be added to the tree. This means that, in dense regions especially, two neighboring overdensities may be enclosed in one leaf. Small density contrasts can lead to very low density leaves being added to the tree. These leaves are insignificant temporary perturbations above the background cutoff and add a level of unnecessary “noise” to the linking process.

Burkhart et al. (2013) perform a similar analysis by varying the density increase required to create a new structure (δ in that work) and comparing the resulting dendrograms across a suite of MHD simulations. They find that dendrogram structure varies significantly with δ and can provide information about the relative importance of shocks, self-gravity, and super-Alfvénic turbulence.

5.3.3 Resolution

The size and shape of structures in the dendrogram are highly correlated with the resolution of the uniform grid used to compute the dendrogram. When all other parameters are kept fixed, an increase in resolution, unsurprisingly, allows for both more refined structures and physically smaller structures. The algorithm identifies more structures because each increase in the level of the uniform grid provides a factor of 8 increase in the number of cells, meaning that there is more flexibility to define compact structure. Physically smaller structures are identified because the minimum size of a structure is fixed at 125 cells; therefore, each increase in level decreases the minimum required physical volume of a structure by a factor of 8.

We compute our fiducial dendrogram at level 2. 1024^3 cells in the volume gives a 1000AU/cell resolution. We also tested level 3 (2048^3 cells; 500AU/cell) and level 4 (4096^3 cells; 250AU/cell) resolution. The memory required for producing a dendrogram at the full level 4 volume was prohibitive. We therefore use a subset of the volume of size $[2048, 2048, 1536]$ at level 4 (about 10% of the volume) that

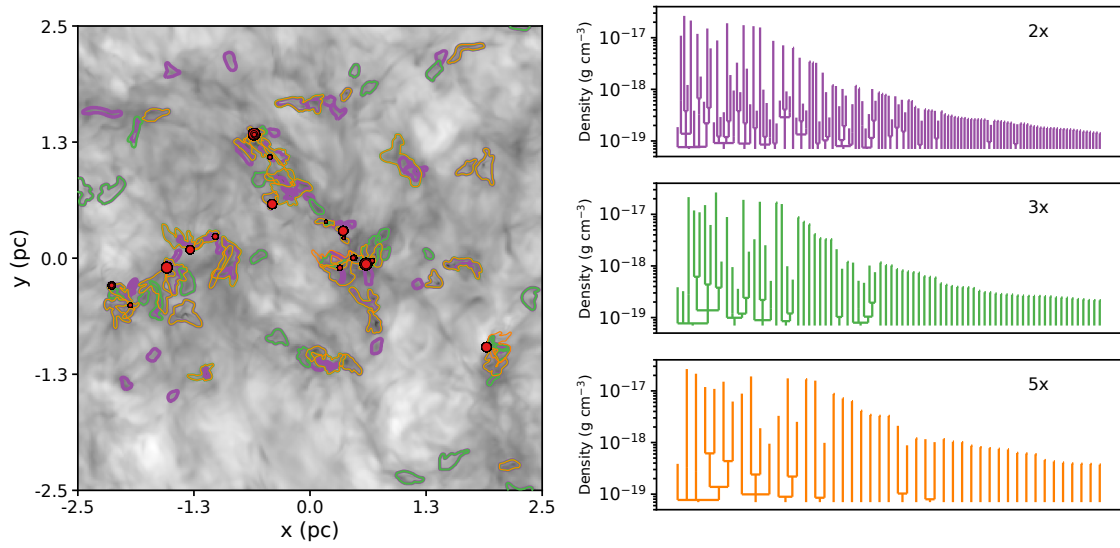


Figure 5.5: A comparison of dendrogram leaves given different density increments. On the left, the purple, green, and orange contours demarcate leaves from dendrograms with a 2x, 3x, and 5x density increase (contrast) required to create a new leaf, respectively. Contours are shown over a density projection of the simulation with darker colors indicating denser regions. Red circles show the locations of sink particles and are scaled by sink mass. The right panels show the full dendrograms for each density increment. The different trees trace out the same dense material, indicating that our results are relatively invariant of the choice of contrast.

contains 15 of our 24 sink particles and many of the structures identified at level 2. Other than resolution, we compute the dendrograms for each case using the same fiducial parameters as described above in Section 5.2.3. The comparison volume contains 40 level 2 leaves, 52 level 3 leaves, and 63 level 4 leaves.

The contours of leaves at the three levels are shown in Figure 5.6. As seen in the left panel, the contours at all levels broadly agree. Only in the densest regions do the leaf volumes differ significantly. The right panel shows one of these dense regions: a triple system in a complicated overdensity illustrates how differences in the resolution can change the leaf structure. The level 2 dendrogram encloses all triple members in one leaf. The level 3 dendrogram draws the central binary in one contour but excludes the tertiary component along the z -direction. The tertiary’s local overdensity is not large enough to create an independent leaf. The level 4 dendrogram assigns all the small overdensities in the greater disk-like overdensity to their own leaves.

Figure 5.6 suggests that level 4 is too sensitive to substructure: the overdensity of one physically bound system is often split into sub-structures such that we lose information about the bound core. It is not possible to compute important system quantities such as gravitational potential or virial parameter without having the full bound structure contained in a single leaf.

Next, we assess the utility of the level 3 dendrogram. Ideally, we want to minimize large changes in the density contours while including all important structure (or sink particles) in a given overdensity. To this end, we compare the derived leaf parameters between leaves tracing the same physical structure at level 2 and level 3 in Figure 5.7. The correlation in mass, peak density, and velocity dispersion is very good (typically within a factor of 3) despite the fact that there is a factor of 8 difference in the minimum volume. Outliers below the one-to-one correlation in all panels except velocity dispersion arise from the population of small, low-density leaves that are identified as independent structures at level 3. These small overdensities are typically included as part of a larger level 2 leaf at the lower resolution, but the low density of the structures means that the mass-weighted

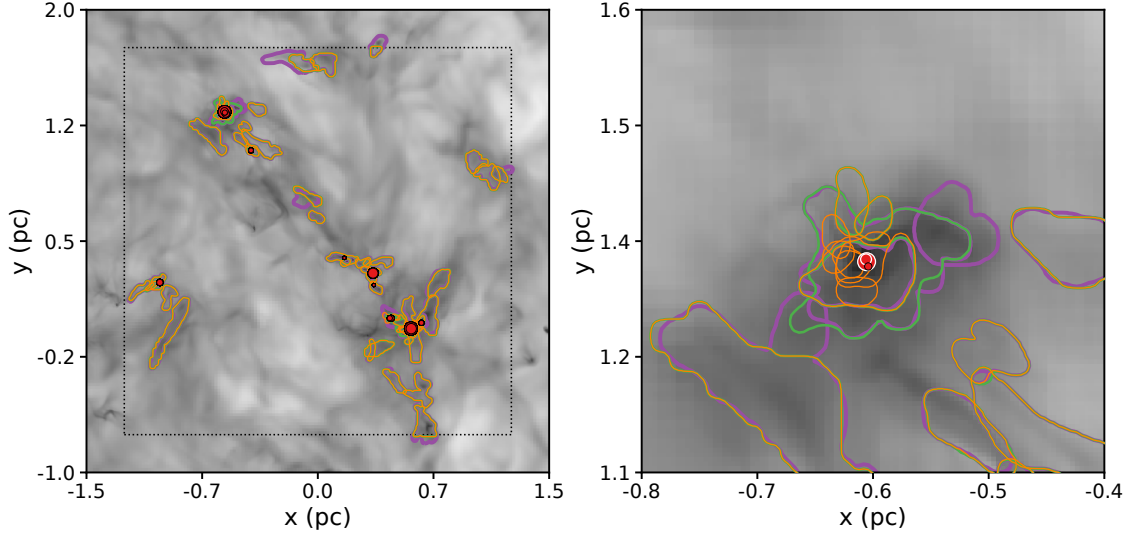


Figure 5.6: Contours of leaves from trees computed on uniform grids at AMR levels 2 (the fiducial choice in this work), 3, and 4 in purple, green, and orange, respectively. The contours are shown over a density projection of the simulation with darker colors indicating denser regions. Red circles show the locations of sink particles and are scaled in size relative to their mass. The black dashed line in the left panel indicates the extent of the comparison volume. As is seen in the left panel, the contours at all levels broadly agree. The right panel reveals that only in the densest regions do the leaf volumes differ significantly. This region contains an overdensity that surrounds a bound triple system. The sink particles outlined in white comprise the central binary ($5 M_{\odot}$ and $2 M_{\odot}$), while the small circle outlined in black is the tertiary companion ($0.8 M_{\odot}$). The tertiary is separated from the central binary by a few thousand AU.

parameters such as velocity dispersion are mostly agnostic about their inclusion. Leaves above the one-to-one line in the same panels come from ambiguities in the correlation of leaves across resolution, but they constitute a small fraction of the total number of leaves shown. Patterns of points forming lines in any of the panels are indicative of time evolution. Thus, we conclude that the difference in leaves identified at level 2 and level 3 does not impact our understanding of dense core evolution.

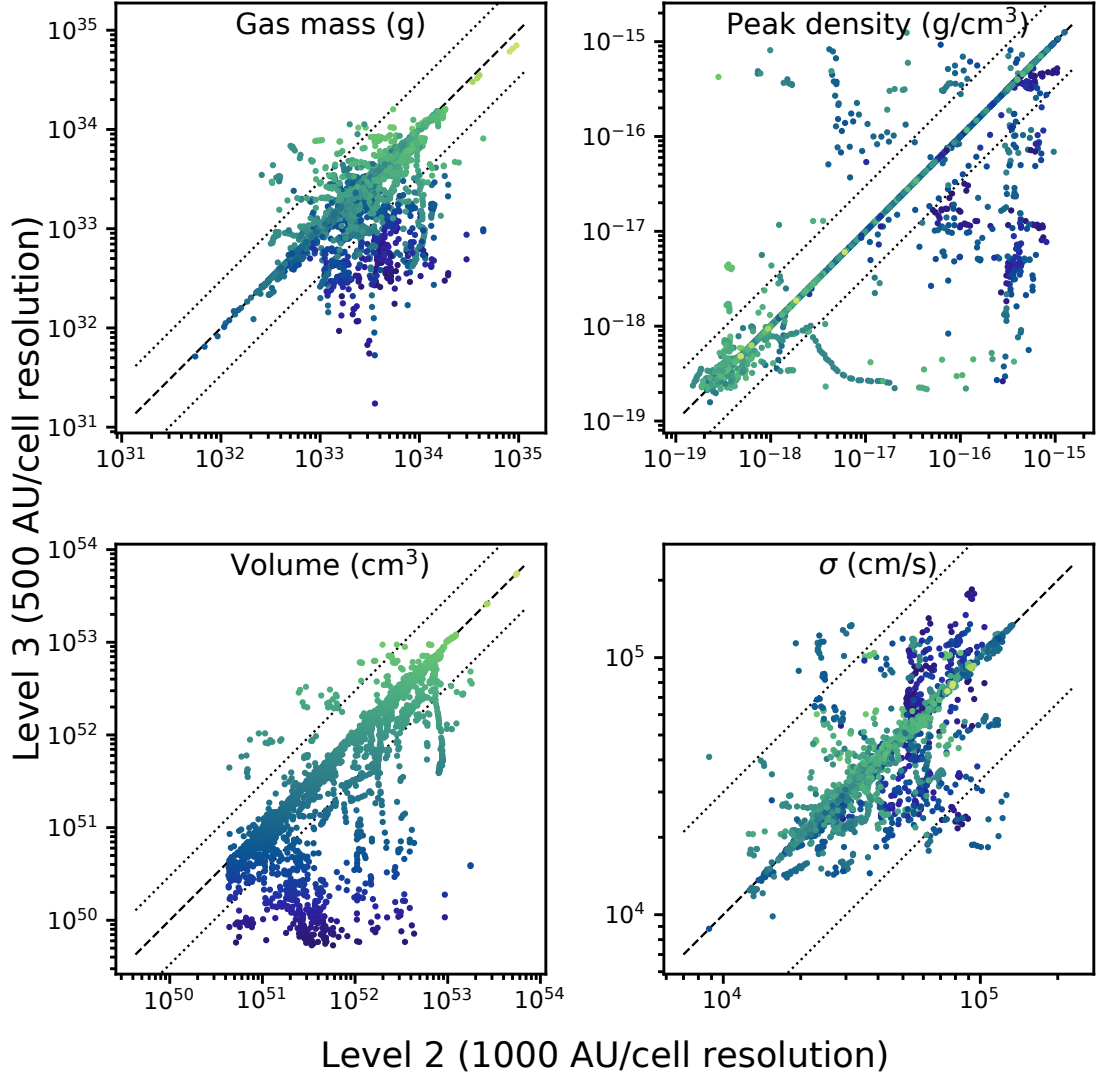


Figure 5.7: A comparison of derived leaf parameters between correlated leaves at level 2 and level 3. The panels show gas mass, peak density, volume, and velocity dispersion. Points are colored by the volume at level 3. The horizontal axis shows the values of leaves computed on level 2 and the vertical axis shows the value for the corresponding leaf computed at level 3. The black dashed line shows the one-to-one correlation, while the dotted lines show a factor of three difference. The correlation in mass, peak density, and velocity dispersion is very good despite the fact that there is a factor of 8 difference in the minimum leaf volume.

5.3.4 Linking Distance

While the aforementioned parameters control the construction of the dendrogram at each time snapshot, the linking distance is the crucial parameter that controls the history of structures (Δ in the “offset” panel in Figure 5.3). The linking distance is the distance between the center of mass of a leaf at one timestep and the surface of the leaf to which it has been linked. Linking distance will simultaneously impact the number of paths in a family and the number of timesteps traced in an individual path. Typical leaf sizes are of order 0.2 pc, so we test linking distances of 0 cells (no offset; a leaf center is within the contour at the neighboring time), 10 cells ($\sim 10^4$ AU; about a typical leaf radius), 100 cells ($\sim 10^5$ AU; about 10 leaf radii), and 200 cells ($\sim 2 \times 10^5$ AU). Our goal is to robustly identify leaves with common histories without permitting too many uncertain connections while, at the same time, allowing for variations in dendrogram leaf contours.

We present the results of our investigation in Figure 5.8. There are minimal variations between the 100 cell and 200 cell linking distances, so we only present the 100 cell results in the figure. For most path families, specifically those of isolated leaves, linking distance does not make a difference in the number of paths reconstructed. The smaller two linking distances, on average, create smaller numbers of paths in the family. Some of this is due to large variations in dendrogram contours between timesteps; the changes in the leaf boundaries can be larger than the linking distance. Linking distance does have a much stronger impact on the length of a path history, however. Larger linking distances typically lead to longer paths, while a linking distance of 0 can sometimes artificially truncate a path.

The linking distance becomes an important consideration for leaves in dense environments, which is also where the majority of sink particles reside, including the many bound multiple systems. In these environments, leaves can exhibit significant variation in structure between timesteps, and therefore a very small linking distance will result in frequent premature truncation of paths. However, because of the proximity to many dense structures, it is easy to link two nearby, but not physically

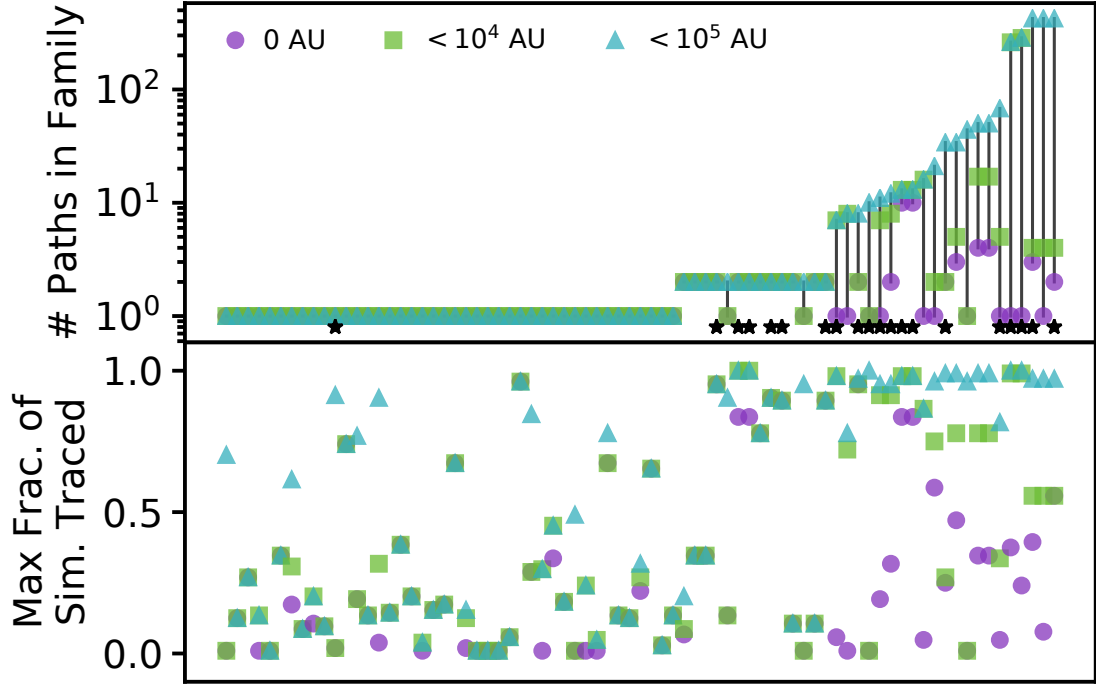


Figure 5.8: Comparison of different linking distances. The colored shapes represent different linking distances. The top panel shows the number of paths in a family (the unique combinations of leaf histories identified for a single starting leaf). The horizontal axis is arbitrary and simply serves to order the leaves. Vertical lines connect the the path families for a single leaf at different linking distances. Black stars along the bottom indicate the presence of at least one sink particle in a leaf. The bottom panel shows the maximum fraction of the total simulation time traced by a path family; ordering matches the top panel. The choice of linking distance is most significant in dense environments where there are many leaves in close proximity.

interacting, structures, leading to a large increase in the number of paths in a family.

We adopt 10 grid cells as our fiducial linking distance because it allows some variation in the dendrogram leaf contours without leading to linking with many nearby, unassociated leaves. We are still able to identify paths through a substantial fraction of the simulation time, but we don't reach the extremely numerous, and less physically meaningful, path families found with larger linking distances.

5.4 Results: Core Properties and Evolution

We have identified dense core analogs using dendrograms at multiple simulation outputs and reconstructed the time evolution of these leaves. We now study the broad distributions of leaf properties (such as is frequently done in other work, both observational and computational) and the time evolution of individual leaves in our simulations. We summarize our findings below.

5.4.1 Core Property Distributions vs. Individual Core History

We study both the distribution and individual evolution of the large sample of leaves in our simulation. Every parameter distribution we investigate is relatively constant in time. However, the individual evolution of a leaf can be quite variable. We present an example of this dichotomy in Figure 5.9. The mass distribution does not vary significantly in time; major variations are only seen at the earliest times when structure is beginning to collapse due to self-gravity. The bottom panel reveals that a leaf may have a computed gas mass that can span upwards of an order of magnitude in time, and the typical evolution does not smoothly vary from time to time. Note that in these (and all future figures), time is measured relative to the beginning of the simulation.

To better understand the relative variability in core evolution, we use a parameter called the coefficient of variation (CV), which is defined as the standard deviation of a parameter (σ) divided by the mean (μ) of that parameter. This quantity allows us to directly compare leaf properties of varied units and physical scales and has units of percent. For our analysis, we consider paths that are tracked for more than 15 kyr and compute the standard deviation of the total path. Because of the rapid evolution in both volume and density of leaves at early times due to the introduction of gravitationally collapsing structure, we exclude the earliest $\sim 30\%$ of the simulation from our computation of the CV.

Table 5.1 presents the minimum, mean, and maximum variation of 16 different parameters: total mass, gas mass, leaf volume, leaf size, mean density, oblateness,

virial parameter, the Mach number of gas in the core, the Mach number of the core in the simulation volume, the Alfvén Mach number of the core, the angular momentum magnitude, the variation in the angular momentum orientation, the magnetic field magnitude, the variation in the magnetic field orientation, and plasma β . While there are few substantial trends to remark upon for individual quantities, for completeness, we report CVs for the entire ensemble of parameters studied in our analysis. We have separated the paths into three bins in each section. Under each bin is the number of individual paths that fall into the bin. The final line in each table section is Δ , which is the spread in CV (maximum CV minus minimum CV) for the collection of quantities and is designed to show the variation in variability for each bin.

Size of Path Family

We first split our full contingent of paths by the number of paths in a family. Paths with $n = 1$ are isolated; they typically show the least variation. However, these paths are, on average, shorter than paths in other bins that can lead to suppressed variation. Paths with $n \geq 10$ are typically in very dense environments and are therefore most susceptible to being linked to multiple nearby leaves. This can cause variations to be artificially high as physically unassociated cores (overdensities that don't physically interact in space) are linked in the same path; the large CV of volume in the non-isolated paths hints that leaf contour changes (arising from structures bouncing above and below the structure refinement threshold due to minute changes in the local density field) may cause the large CVs in other parameters.

Number of Sinks

We then group paths by the number of sinks in the leaf at the final timestep. Paths with $n = 0$ are starless overdensities. The starless paths with low CVs are typically short-lived, low-density leaves. The paths containing multiple sink particles are frequently part of large path families in dense regions where physically independent

overdensities are identified as related due to a temporary co-location or dendrogram contour changes that cause multiply-linked leaves.

Length of Path

Finally, we divide the ensemble of paths by their length. The shortest paths ($< 75\text{kyr}$) are frequently temporary overdensities and therefore have little physical evolution over the time they are traced as indicated by the low CVs. However, there are also short paths with high variability that belong to a large path family. The longest paths (lifetimes greater than 250kyr) have little correlation with the size of the path family or the presence of stars, so the CVs in the final bin span a large range.

General Trends

The path histories we trace have significant variation— frequently upwards of 40% in CV. In all three methods of dividing paths presented in the table, the average CV increases from left to right, meaning that shorter lived, isolated, starless cores tend to have less variability. However, the maximum CV does not show the same trend, indicating that any given path can vary significantly.

It is also important to note that a low variability in one parameter does not indicate low variability in all parameters. This is demonstrated with the parameter Δ at the bottom of each section. This quantity shows the maximum difference in the CV of the 16 parameters for each leaf, or the maximum variation in the variation of our computed properties. The average Δ in all cases is over 50%, meaning that the majority of paths have little correlation in the amount of variability in different quantities. Thus, the computed properties of observed overdensities identified with dendrograms may not correlate well with the physical evolution of the bound core itself.

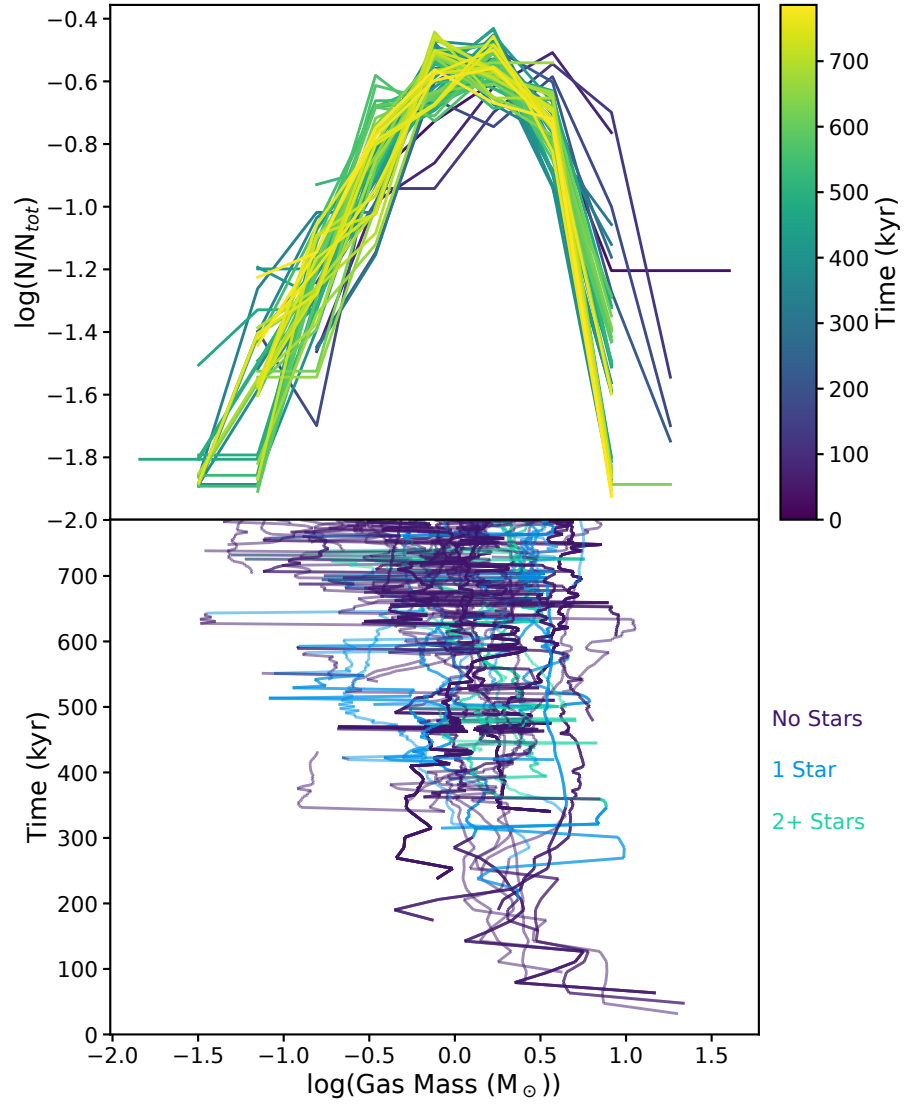


Figure 5.9: Core mass distribution vs. individual core evolution. The top panel shows the distribution of gas mass in the cores across time. The bottom panel shows the gas mass evolution of a subset of reconstructed paths through time; dark purple lines show leaves without sinks particles, blue lines show leaves with a single sink particle, and green lines show leaves with multiple sink particles. While the broad distribution of gas mass is nearly invariant in time, any individual leaf may have large variations in its reconstructed history.

Table 5.1: Coefficient of variance range for different core properties. The CV is defined as the standard deviation divided by the mean of a quantity.

Number of paths in a family									
Quantity	$n = 1$ (34)			$1 < n < 10$ (89)			$n \geq 10$ (790)		
	Min (%)	Mean (%)	Max (%)	Min (%)	Mean (%)	Max (%)	Min (%)	Mean (%)	Max (%)
Total mass	9	27	53	12	55	213	9	42	153
Gas mass	9	27	53	10	57	279	13	52	144
Volume	1	17	61	10	68	266	18	67	152
Size	1	31	277	4	52	246	6	27	243
Mean density	2	17	96	3	56	196	12	67	244
Oblateness	1	26	89	16	43	92	15	38	74
Virial α	3	27	75	8	49	214	14	41	254
Internal \mathcal{M}	1	10	34	4	24	65	4	22	49
Total \mathcal{M}	0	6	20	2	11	40	5	13	28
Alfven \mathcal{M}	2	11	30	6	32	104	11	30	72
$ \vec{j} $	3	38	154	18	77	242	10	80	189
$(\text{Max}(\vec{j})-\text{Min}(\vec{j}))/\text{Mean}(\vec{j})$	0	25	64	5	27	53	11	31	61
$ \vec{B} $	1	12	56	1	27	54	4	24	60
$(\text{Max}(\vec{B})-\text{Min}(\vec{B}))/\text{Mean}(\vec{B})$	1	17	45	6	29	71	10	31	48
Plasma β	2	16	67	6	51	156	14	43	140
Δ	19	59	272	31	110	270	36	94	262
Number of sinks at final timestep									
Quantity	$n = 0$ (520)			$n = 1$ (85)			$n > 1$ (308)		
	Min (%)	Mean (%)	Max (%)	Min (%)	Mean (%)	Max (%)	Min (%)	Mean (%)	Max (%)
Total mass	9	54	213	9	44	213	21	25	110
Gas mass	9	54	279	11	51	207	24	48	157
Volume	1	61	266	7	53	190	28	77	196
Size	1	39	277	6	29	246	13	14	31
Mean density	2	53	185	17	61	196	18	83	244
Oblateness	1	36	89	29	51	92	15	38	59
Virial α	3	49	141	9	44	96	15	28	254
Internal \mathcal{M}	1	26	55	5	19	61	4	15	65
Total \mathcal{M}	0	14	25	3	11	28	6	11	40
Alfven \mathcal{M}	2	19	104	8	28	72	15	47	57
$ \vec{j} $	3	64	189	10	56	242	21	109	185
$(\text{Max}(\vec{j})-\text{Min}(\vec{j}))/\text{Mean}(\vec{j})$	0	28	64	8	30	61	22	35	53
$ \vec{B} $	1	20	56	11	22	43	8	33	60
$(\text{Max}(\vec{B})-\text{Min}(\vec{B}))/\text{Mean}(\vec{B})$	1	26	71	12	32	50	13	37	45
Plasma β	2	37	79	3	38	154	14	53	156
Δ	19	90	272	45	85	241	53	105	262
Length of path history									
Quantity	$t < 75\text{kyr}$ (35)			$75\text{kyr} < t < 250\text{kyr}$ (21)			$t > 250\text{kyr}$ (857)		
	Min (%)	Mean (%)	Max (%)	Min (%)	Mean (%)	Max (%)	Min (%)	Mean (%)	Max (%)
Total mass	9	54	213	10	42	81	9	43	153
Gas mass	9	62	279	10	41	81	11	51	144
Volume	1	60	266	2	36	102	5	67	152
Size	1	29	217	6	44	171	6	29	277
Mean density	2	35	196	3	37	110	5	65	244
Oblateness	1	31	62	9	41	92	10	38	76
Virial α	3	35	254	14	47	141	8	42	144
Internal \mathcal{M}	1	14	50	5	14	32	2	22	65
Total \mathcal{M}	0	6	18	1	9	17	2	13	40
Alfven \mathcal{M}	2	27	104	4	17	38	7	30	72
$ \vec{j} $	3	52	232	5	59	154	10	80	242
$(\text{Max}(\vec{j})-\text{Min}(\vec{j}))/\text{Mean}(\vec{j})$	0	24	52	8	22	64	7	31	61
$ \vec{B} $	1	17	48	5	15	45	4	25	60
$(\text{Max}(\vec{B})-\text{Min}(\vec{B}))/\text{Mean}(\vec{B})$	1	25	71	7	22	43	8	30	50
Plasma β	2	36	154	3	26	67	15	43	156
Δ	19	85	270	31	80	166	34	95	272

5.4.2 Isolated, Starless Cores

Naively, we might expect the long-lived, isolated, starless cores in our simulations to show the least variation. Observed lower density cores can have lifetimes of upwards of 1 Myr, which suggests that these cores should vary slowly over their lifetime if they are free from external influence (André et al., 2014). Thus, we analyze these isolated cores separately; Table 5.2 shows the coefficient of variance for the 18 isolated (one path in the family), long lived ($t > 75\text{kyr}$), starless leaves. While some vary by only a few percent, other paths have variability of $\text{CV} > 40\%$ for the 15 parameters in the table. This indicates that these leaves have large computed variability, in contrast to our naive expectation. The individual leaf evolution tracks are shown in Figure 5.10, where we plot mean density, mass, volume, and virial parameter. Most leaves show fairly large stochastic variations in individual quantities on short timescales. These variations are commonly due to changes in the physical structures included in the dendrogram leaf rather than significant physical evolution. However, a few of our leaves (namely, those plotted in purple), show relatively quiescent evolution over their full lifetime, which are akin to the structures identified in Chen et al. (2019a). These quiescent cores will contribute to the statistics of core property distributions while not participating in the star formation process, thereby confusing the mapping of the core mass function to the initial mass function of stars (e.g. Offner et al., 2014).

5.4.3 Virial Evolution of Cores

Despite the wide variability in the time evolution of other core properties identified with dendrograms, the virial evolution of leaves does trend in the expected direction of lower virial numbers with time as seen in the lower panel of Figure 5.11. This fits the classic view of star formation where a magnetized core undergoing global gravitational contraction will eventually become supercritical and collapse to form a star (Mouschovias and Spitzer, 1976). However, our core tracking algorithm does not find strong evidence that a leaf with low virial α will form a star as shown in Fig-

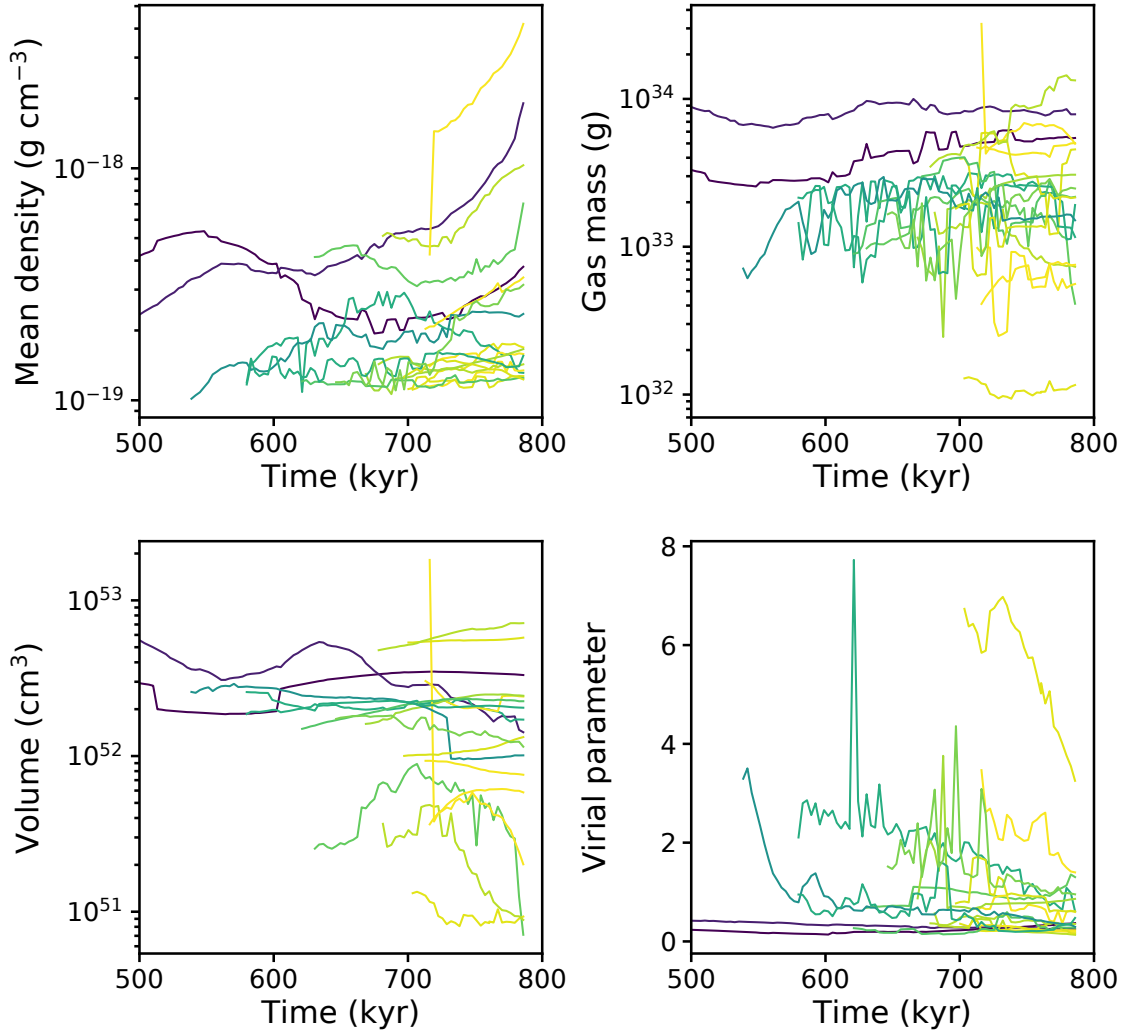


Figure 5.10: Individual core evolution for the long-lived, isolated, starless cores in our simulation. We show mean density, gas mass, volume, and virial parameter in the four panels. Most cores show stochastic variation on the order of a factor of a few over the course of their lifetimes.

Table 5.2: Coefficient of variance range for isolated, long-lived, starless cores

Quantity	Min (%)	Mean (%)	Max (%)
Total mass	10	30	53
Gas mass	10	30	53
Volume	2	18	61
Size	6	45	277
Mean density	3	17	54
Oblateness	9	33	89
Virial α	14	35	75
Internal \mathcal{M}	2	12	27
Total \mathcal{M}	1	8	20
Alfven \mathcal{M}	4	15	30
$ \vec{j} $	5	48	154
$(\text{Max}(\vec{j})-\text{Min}(\vec{j}))/\text{Mean}(\vec{j})$	8	28	64
$ \vec{B} $	5	14	56
$(\text{Max}(\vec{B})-\text{Min}(\vec{B}))/\text{Mean}(\vec{B})$	7	21	45
Plasma β	6	21	67

ure 5.11. Note that we are using the simplified gravitational α (which is frequently used in observations, e.g., Kirk et al., 2017) and not computing the full virial α that includes boundary terms. Most leaves ($> 70\%$), especially those hosting sink particles, do finish the simulations with $\alpha < 2$. However, a substantial population of the long-lived, starless leaves have $\alpha < 2$ as well. Many of these low- α leaves persist for longer than a local free-fall time (a few hundred kyr) without forming a star. Thus, virial α is not necessarily the best predictor of future star formation; other physics, such as pressure or magnetic support, are important factors in the global evolution of a core.

5.4.4 Short-lived Overdensities

We observe a population of short-lived, low-density peaks arising from turbulent flows that contribute a level of “noise” to the interpretation of long-term core evolution, since they do not go on to collapse and form protostars. These overdensities account for about 25% of path families identified when tracing paths forward

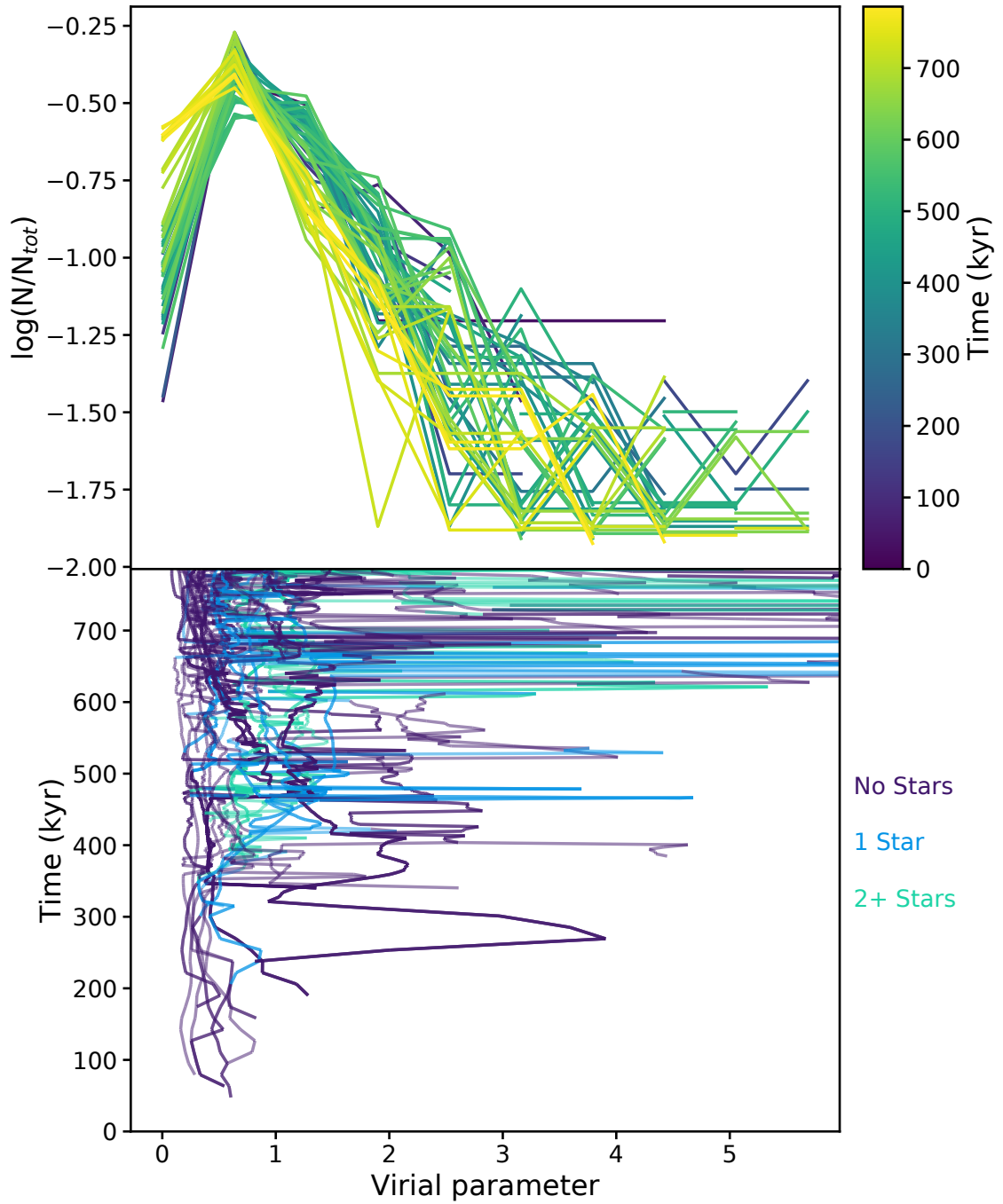


Figure 5.11: Core property distribution vs. individual core evolution of the virial parameter. The top panel shows the distribution of the virial parameter of the cores across time. The bottom panel shows the virial evolution of a subset of reconstructed paths through time. Coloring is the same as Figure 5.9.

from an intermediate timestep. We identify this temporary population of “imposter cores” as having lifetimes less than 200 kyr and densities less than $1 \times 10^{-18} \text{ g cm}^{-3}$ ($2.5 \times 10^5 \text{ cm}^{-3}$), as can be seen in Figure 5.12. The majority of isolated paths occupy a much lower density and shorter lifetime than the general path population. Most of the paths in the low-density and short lifetime region also show the trend that the maximum density (which is typically also less than $10^{-18} \text{ g cm}^{-3}$) is higher than the last identified density (the ending density of the path), suggesting that these leaves are physically temporary overdensities that decay below the threshold density required to be identified in the dendrogram. The free-fall time of these overdensities is about 100 kyr; because the free-fall time is roughly equivalent to the overdensity lifetime, these objects are not dominated by gravitational collapse.

The presence of this substantial population of imposter cores could introduce a bias in the instantaneous core mass function. These overdensities have gas masses of order one solar mass and sizes of roughly a tenth of a parsec, which is similar to masses and sizes of observed cores and may therefore masquerade as pre-star-forming cores. Thus, at any given time, roughly 15-25% of cores identified in a region may be from this temporary population. We performed a two-sample Kolmogorov-Smirnov test on the computed core properties of imposter cores compared to all other cores at the same time: we could not distinguish differences in the distributions of any parameter except density. For instance, gas mass and virial parameter both have a p-value of 3% and K-S statistic of 0.4; if the p-value is high (our preferred cutoff is more than 1%) and the K-S statistic is low (our preferred cutoff is less than 0.6), we cannot claim that the two samples are drawn from different populations. Indeed, p-values for our computed parameters except for density are typically above 3-5% and K-S statistics are typically less than 0.5. Thus, imposter cores are not easily separated from any other population of cores, so they will complicate the correlation of core and stellar properties. These temporary overdensities are explored in more detail in Chen et al. (2020).

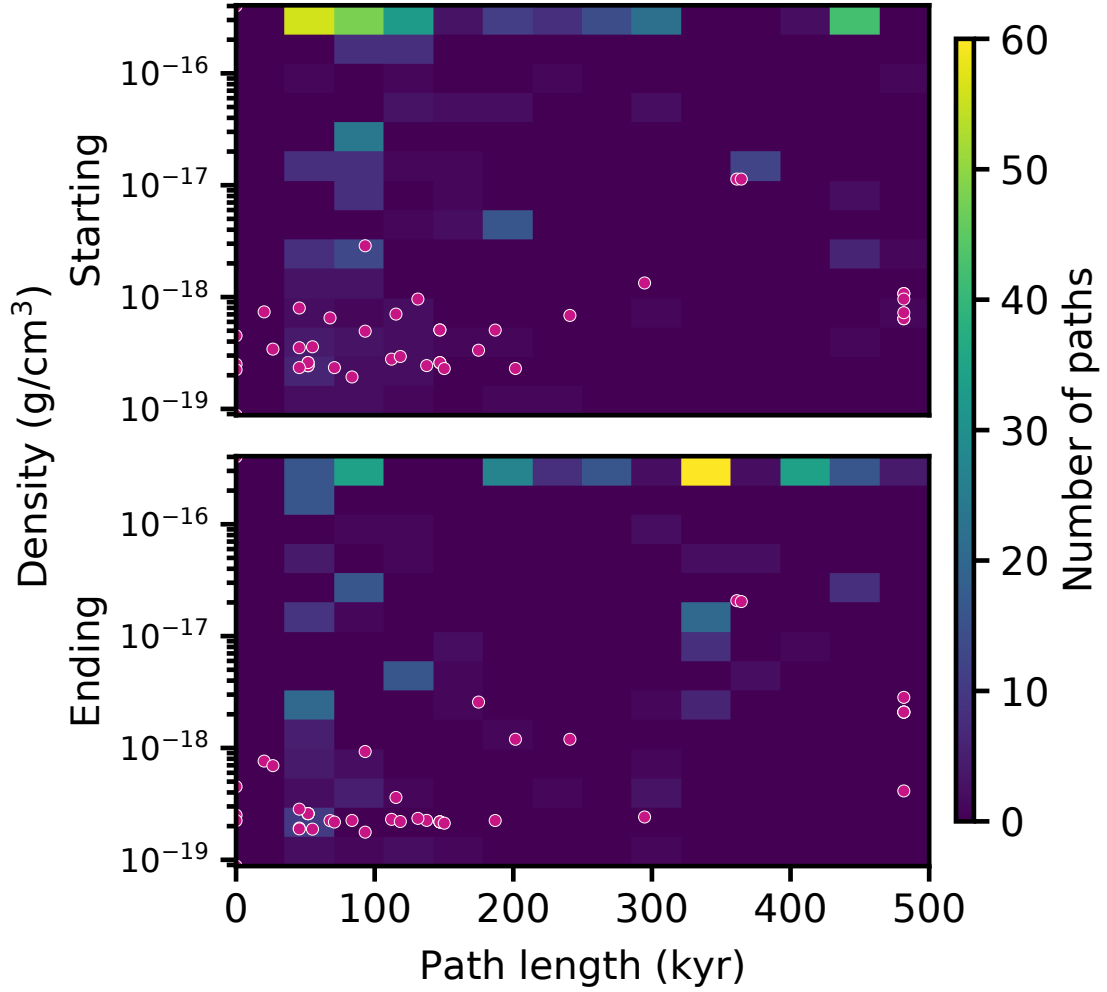


Figure 5.12: Starting and ending densities of isolated objects. The background histogram shows the starting and ending peak densities of all paths (top and bottom, respectively) plotted against the length of the path. The purple points denote isolated paths. There is a substantial population of low-density leaves with lifetimes less than 150 kyr (25% of all path families) that are temporary, non-gravitating overdensities that disperse and fall below the dendrogram floor.

5.4.5 Core Mass Function

We measure the core mass function (CMF) of our simulation. We show our CMF through time in Figure 5.13 together with mass functions from the literature. We compute the total core mass, which includes mass from both gas and sink particles. We compare our CMF to the fiducial CMF from Guszejnov and Hopkins (2015), the observed CMF from Alves et al. (2007), the initial mass function (IMF) inferred from observations from Chabrier (2003), and a log normal distribution. The CMF in our simulation agrees well with the observed CMF of the Pipe dark cloud from Alves et al. (2007) and with other observational CMFs not plotted here such as those observed in Perseus, Serpens and Ophiuchus from Enoch et al. (2008), Aquila from André et al. (2010) and Könyves et al. (2015), and Vela C from Massi et al. (2019). We also find a good agreement with a Chabrier (2003) system IMF scaled by a factor of 6. We do not, however, create the population of low mass cores of the Guszejnov and Hopkins (2015) model. We also do not create the population of low mass sinks particles seen by other simulations such as Bate (2012) despite our ability to create sink particles with masses much less than $1 M_{\odot}$ (although this is expected due to the coarse spatial resolution).

As is seen in the figure, our CMF is relatively invariant through time. Our peak mass is constant at around $1.4 M_{\odot}$ with a range from about $0.3 - 10 M_{\odot}$. There is a small apparent bias towards higher masses at earlier times, which is a byproduct of low number statistics and the lack of significantly refined structure in our simulations shortly after gravity is turned on. The constant nature of the CMF is likely due to two effects. The dendrogram introduces new leaves when temporary overdensities are significant enough to warrant leaf creation, leading to the transient population of low-mass “cores” discussed above that balances the small physical growth of persistent cores and the algorithmic fragmentation of more massive leaves into smaller structures. The trend of nearly constant CMF across time in a singular environment is seen in other simulations, such as Cunningham et al. (2018), where cores mass distributions do not show significant mass evolution after formation. As described

above, any given leaf can occupy a wide range of the total mass space as we track it through time, but the ensemble of leaves maintains a constant distribution in time. Thus, the CMF derived from a dendrogram population does not necessarily correlate with the final IMF of the region; the stochastic nature of leaf mass evolution makes it very difficult to compute a relationship between a core mass at any snapshot and the resultant stellar mass.

We compare the CMF derived from the leaf gas mass to the CMF derived from more observationally-motivated core definitions including the leaves that eventually form stars (equivalent to prestellar and protostellar cores), leaves with $\alpha < 2$, and leaves that are Jeans unstable for their mean density. All of these different populations produce quantitatively similar results, as shown in Figure 5.14. The CMFs all have peaks slightly higher than $1 M_{\odot}$, a spread of about two orders of magnitude, and are invariant in time. We therefore conclude that any structures not involved in the traditional star-formation process (e.g., transient overdensities) have little impact on the derived CMF. Computing the CMF based on different properties in observations also produce similarly invariant CMFs (e.g. Sokol et al., 2019).

The highly variable masses of identified leaves through time means that we cannot infer the IMF by looking at a population of cores identified with dendrograms at a given time snapshot. While there may be an underlying physical evolution of star-forming cores, the instantaneous properties of a region identified by a dendrogram cannot be assured to correlate with that evolution. we reiterate that our goal in this work is not to measure CMFs in detail but to (a) show that our results are comparable to observations and (b) illustrate that the apparent similarities between observed CMFs and IMFs may not derive from a simplistic evolution of the former to the latter.

5.5 Results: Insights from Methodology

It is imperative to understand the impact of the dendrogram algorithm on cores identified in both simulations and observations due to the algorithm’s wide pop-

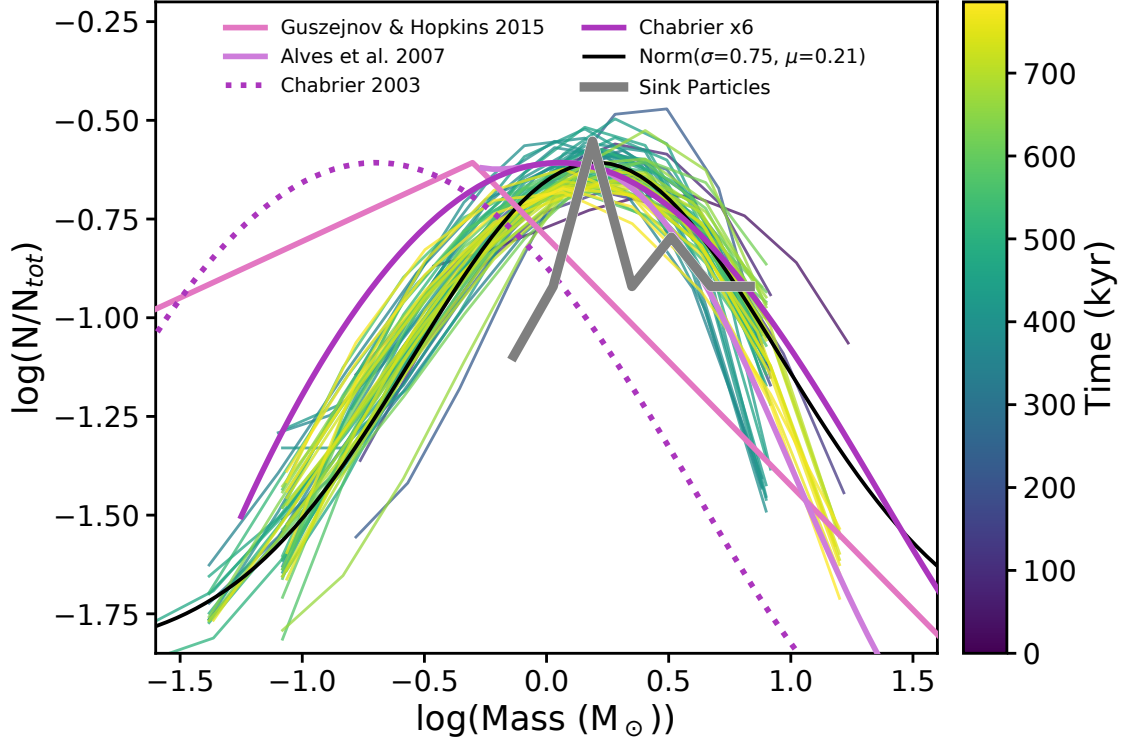


Figure 5.13: The core mass function (CMF) across time in our simulations. The purple to yellow color scale show our normalized core masses for a selection of timesteps. We plot the total core mass, which includes mass from both gas and sink particles. The mass function of our sink particles (which are equivalent to a protostar and compact disk) is shown in the thick gray line. We also show the fiducial CMF from Guszejnov and Hopkins (2015), the observed CMF from Alves et al. (2007), and the initial mass function (IMF) inferred from observations from Chabrier (2003). We plot a log normal in black.

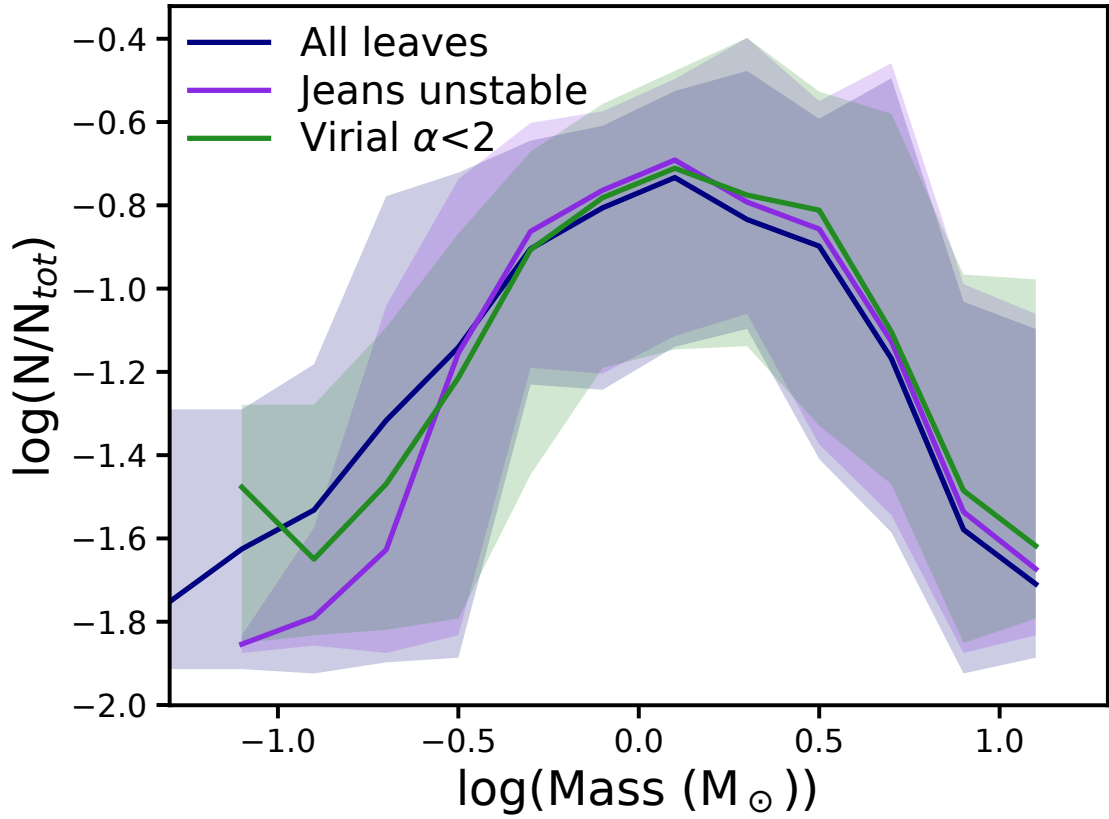


Figure 5.14: The core mass function for different core definitions. Solid lines show an average CMF across time, while the shaded regions show the minimum and maximum bins across time. Blue shows the CMF of all leaves in the simulation (which is what is shown in Figure 5.13). The other colors show core selections that might be more physically motivated: purple shows cores that have masses greater than the local Jeans mass, and green shows cores that have virial $\alpha < 2$. All mean CMFs overlap except at the lowest mass end, where some of the low mass cores don't satisfy the stricter Jeans or Virial criteria.

ularity in the literature. In this section, we discuss the insights into the use of dendrograms gained from this work.

We have used dendrograms to identify dense structures in our simulations of a star-forming region, but we have also demonstrated a limitation of dendrograms: because dendrograms identify *relative* variations in structure, leaf structure may vary significantly between timesteps due to small variations in the local density structures. Dendrograms are built beginning from the maximum value, so any variations in that maximum may cascade into substantial changes in the resultant dendrogram architecture.

An example of this phenomenon is shown in Figure 5.15. The left and right columns depict neighboring timesteps. Despite very little physical evolution between timesteps (a $\sim 5\%$ change in the peak density), the dendrogram identifies leaf structure quite differently. This translates to a nearly order of magnitude variation in the volume of the sink-hosting leaf and substantial variation in the computed properties of the leaf.

The two leaves in the right panel that are part of the sink-hosting sub-tree (the two left-most leaves in the dendrogram) are not physically interacting over the course of the simulation. They are simply nearby overdensities. However, because of the variations in the dendrogram structure, our algorithm identifies these two leaves as belonging to the same path family. Thus, one of the major failings of tracking overdensities identified via dendrogram through a simulation to study core evolution is that it becomes difficult to disentangle physical evolution from “algorithmic” artifacts. In other words, there is no easy, automated way to differentiate between physical structure change and dendrogram structure change.

The change in consecutive dendrograms arises because of small variation in the relative properties of structures (typically intermediate density structure). Figure 5.16 aims to illustrate the issue. Structures 1, 2, and 3 are shown at two consecutive times. The physical properties of the structures (peak and width, in this cartoon) don’t change between the top (earlier time) and bottom (later time). However, their relative locations with respect to one another do change. The struc-

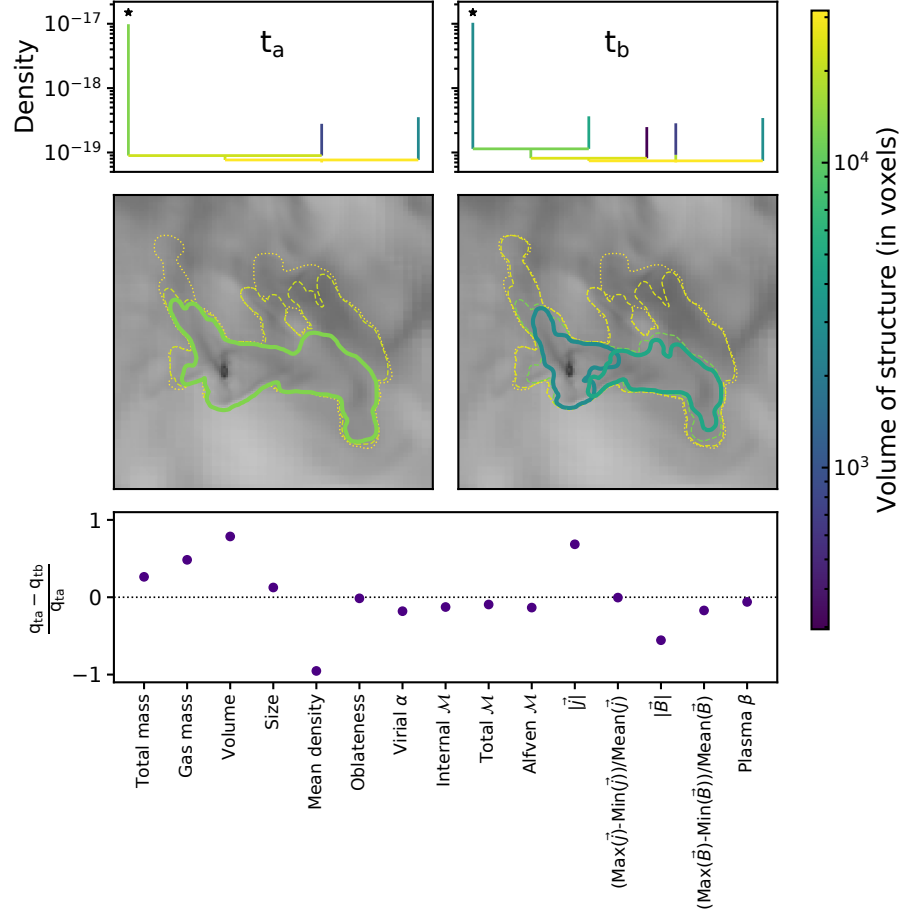


Figure 5.15: The dendrograms of a small volume in consecutive timesteps. The left and right columns depict different timesteps. The upper panels show the dendrogram structure colored by leaf volume. The starred leaf in each panel is the leaf containing the dominant overdensity in the middle panels. The middle panels show the leaf contours over a grayscale density projection of the simulation. Dotted contours show the trunk, dashed contours show branches, and solid contours show leaves. Despite very little physical evolution between timesteps, the dendrogram identifies different tree structure, leading to significantly different leaf morphologies. The bottom panel shows the impact of the different leaf structure on computed leaf properties for the leaf starred in the upper panels. Critical quantities such as mass show significant differences between the two times that can only be attributed to the redefinition of the leaf contours.

tures have moved closer to one another and therefore the saddle point between them has become shallower. This causes the nodes (horizontal lines) to be at different heights at the two different times. At the earlier time, the node is low enough that both structures 2 and 3 exceed the density increase criterion (indicated by the pink vertical lines), while at the later times, the node is at a high enough density that the individual density peaks are not significant enough to allow substructure to be identified.

To further explain the example presented from this work, the second leaf in the right panel of Figure 5.15 is just above the density refinement criterion at its physical location in that timestep. However, the peak density in that region drops by 4% in the left panel, which then leads to the overdensity not being quite “peaky” enough to satisfy the density refinement when compared with the maximum peak. This is not a problem unique to our density refinement criterion: any density refinement chosen will exhibit these artifacts to some degree due to the relative nature of dendrogram structure identification. Even observationally, these issues may be seen: differences in resolution or noise levels in observations of the same region may lead to changes in the computed hierarchy. Any variation between consecutive observations in the region around a peak dendrogram can lead to variations in the contour drawn by the dendrogram.

5.6 Discussion

5.6.1 Interpreting the IMF from the CMF

One natural question we can ask in this work is how the instantaneous core masses correlate with the stars they form, which can provocatively be described as translating a CMF into an IMF. We plot this in Figure 5.17, where we show the total sink mass at the end against the initial masses of leaves that merge into the final overdensity. First, there is a wide array of scatter in the initial leaf masses that doesn’t correlate well with the final sink mass; some of this scatter may result from the lack of feedback in our simulations, which is expected to create overmassive sink parti-

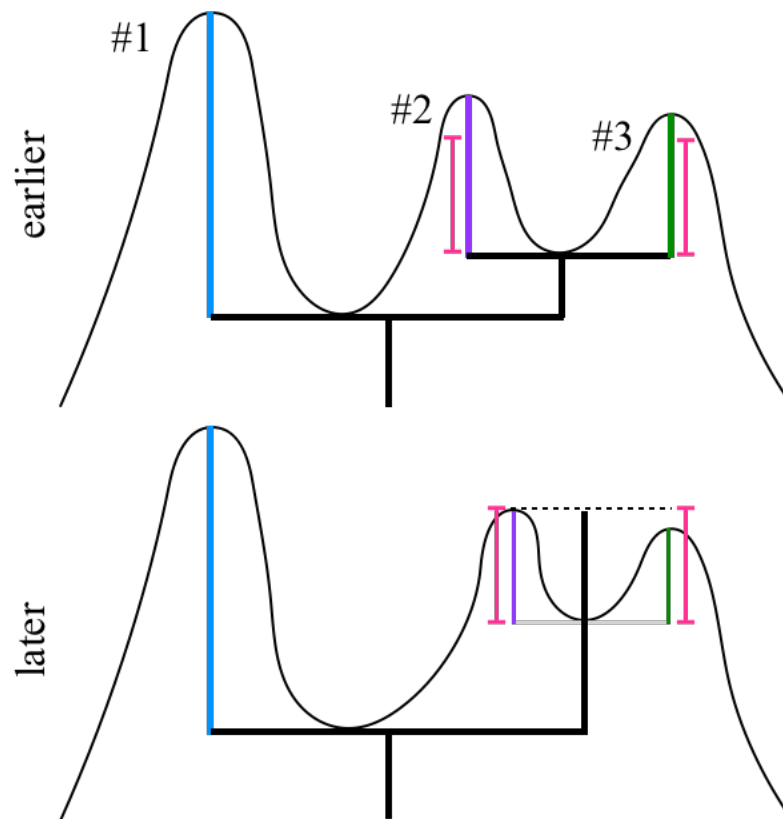


Figure 5.16: Cartoon explanation of the origin of algorithmic structure variation in time. Structures 1 (blue), 2 (purple), and 3 (green) are shown at two consecutive times. The physical properties of the structures (peak and width) don't change between the top (earlier time) and bottom (later time). However, their relative locations with respect to one another do change: structures 2 and 3 move closer to one another, thereby increasing the density of the saddle point between them. This causes the nodes (horizontal black lines) to be at different heights at the two different times. At the earlier time, both structures 2 and 3 exceed the density increase criterion (indicated by the pink vertical lines), while at the later times, the individual density peaks of 2 and 3 are not significant enough to allow for substructure to be identified.

cles, and some may arise from the fact that a protostar can accrete from outside the initially bound gas core. This observation is consistent with other works for low to intermediate-mass stars such as Smith et al. (2009) and Mairs et al. (2014). Second, the *sum* of all component leaf masses seems to be a very important consideration, especially when considering the growth of systems containing multiples.

The young, typically singular, sink particles fall above the 1:1 correlation in Figure 5.17, indicating that the nascent overdensity is the primary reservoir of gas that accretes onto the protostar by the final snapshot of the simulation. Older sinks and systems containing multiple sinks frequently have individual leaf masses below the 1:1 line. Because protostellar outflow feedback is expected to reduce stellar masses by at least a factor of three compared to the case without feedback (Offner et al., 2014; Offner and Chaban, 2017), we also indicate the 3:1 sink:leaf mass ratio with a dot-dashed line. For the most massive multiple systems, the component leaves (which constitute the idealistic “gas reservoir” for the protostars) still do not lie above the aforementioned feedback relation, but the sum of the leaf masses puts these systems into a comparable space as other systems. For instance, if the expected reduction in mass due to feedback was included, the rightmost system in Figure 5.17 would likely have a total sink mass of $\sim 5 M_{\odot}$ and a combined leaf (core/reservoir) mass of $\sim 6 M_{\odot}$; however, all component leaves for that system that would be measured in a CMF have masses $\lesssim 3 M_{\odot}$. The leaves would then appear to contain sufficient mass to form the stars, but we caution that this, and even the simple 3:1 relationship, is an oversimplification of the nature of protostellar feedback and its cumulative effect on the surrounding gas.

It is important to note that the systems containing multiple stars do not form from multiple leaves containing single stars merging together; rather, the bound multiple forms in one leaf, and the subsequent accretion of gas overdensities may help trigger the formation of new stars. This result is similar to that seen in Padoan et al. (2019), who see little correlation between core mass (or even extended mass around a core) and stellar mass for high-mass stars. This observation supports binary formation models such as turbulent fragmentation in a single core (e.g.,

Offner et al., 2010) or disk fragmentation (e.g., Kratter et al., 2010) as opposed to dynamical capture (e.g., Bate et al., 2003).

5.6.2 Other Ways to Identify Cores

There are a few ways one may attempt to overcome the limitations of core identification and comparison using density dendrograms. We discuss the advantages and limitations of these ideas.

One could try to overcome the impositions of the dendrogram algorithm itself. Custom merging strategies are possible in `astrodendro`; a “pruning” strategy will allow peaks near the density refinement criterion to remain more stable and thereby overcome some of the relative structure variation shown in Section 5.5. However, this solution is subject to human bias due to the addition of another tunable parameter. It is unclear how to create a custom merger strategy in a way that is agnostic to the human-desired structure without introducing more bias.

In principle, one could also create contours at absolute density levels instead of relying on a relative measure. By using an absolute density contour, the leaf structure should slowly vary from timestep to timestep and may therefore better identify bound cores. One could then create a hierarchical structure tree that is similar to a dendrogram, but the nature of hierarchy would be more difficult to determine due to the fact that many density peaks would be broken into a single nested hierarchy. Additionally, this type of hierarchy would destroy the physical utility of dendrograms in studying the relation of physical structures in a region and again relies on an arbitrary density threshold, which we advocate against.

Core identification in simulations might also be better done in 2-D synthetic observation space instead of 3-D density grids because there will be fewer variations in integrated intensity between timesteps. However, this method is best suited to isolated cores and may suffer from false over-densities in emission created by chance alignments (e.g., Beaumont et al., 2014).

Finally, density may not even be the best tracer of star-forming cores as cores are highly dynamic and will not be defined by the same density contour across time. It

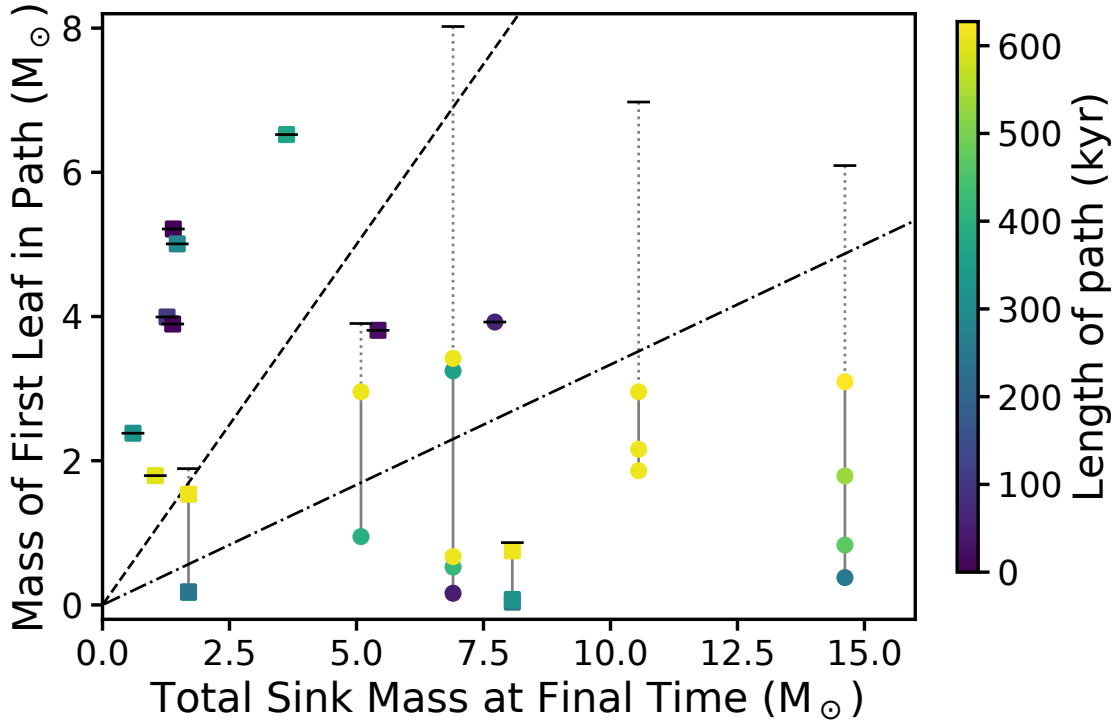


Figure 5.17: Sink mass at the final time plotted against leaf mass. Squares show leaves containing one star at the final time, while circles show leaves containing multiple stars. Points are colored by the length of the path, and we have truncated the paths to have an earliest age of 250 kyr after the gravity turned on. Systems that consist of multiple paths are connected by a vertical line. The sum of the leaf masses is indicated by the horizontal marker. The dashed line shows the 1:1 correlation, while the dot-dashed line shows the trend if the sink mass is reduced by the factor of ~ 3 arising from the lack of protostellar feedback in the simulations. For instance, the rightmost system (currently at $15 M_{\odot}$) would likely have a mass of about $5 M_{\odot}$ if feedback was included in these simulations. Additionally, the inherent variability in leaf snapshots can cause a clearly unphysical mass budget for a protostellar system.

is likely that a more physically motivated property such as virial parameter, velocity dispersion, or gravitational potential could be a better quantity with which to build hierarchical structures (see, for instance Mao et al., 2019). These properties should be less variable across time and should therefore provide a more stable core identification. However, these quantities are more difficult to measure observationally and will make comparisons between simulations and observations harder.

In simulations, one can also include tracer particles that will trace the evolution of gas in a core identification-independent way. However, interpreting that evolution is non-trivial. Smith et al. (2009) and others find that a non-negligible fraction of tracer particles in a bound gas clump will accrete onto a sink particle outside of that bound clump. Indeed, they find that most of the mass in a sink particle can be accreted from outside its nascent core. Thus, the meaning of a core in this context becomes even less apparent, as the star may contain gas from all around the molecular cloud.

One could employ alternate core identification algorithms used in the field. All of these other methods (CLUMPFIND, FellWalker, GaussClumps, etc.), would suffer similar issues because they all fundamentally rely on the relative positions and heights of peaks to determine structure. Different algorithms might have different sensitivity to the less dense material surrounding density peaks, but all algorithms have some way to combine peaks that are thought to not be independent. In a simple test in which we identified structures in two consecutive timesteps with dendrograms, CLUMPFIND, FellWalker, and Reinhold, all core identification algorithms produced structures that broadly followed the 1:1 trend in volume, but all algorithms had \sim order of magnitude deviations in volume for at least a few structures. The dendrogram and FellWalker algorithms had the least dispersion along the 1:1 relation in this test, but the substantial redefinition of “core” boundaries was still observed.

Each of the methods discussed above would likely identify the same dense gas structures, but the variations in core identification would still likely lead to changes in computed core properties between methodologies. Further work is needed to

explore the full impact and limitations of these different structure identification methods in the time domain. However, this work suggests that there is no unique way to define a core in both simulations and observations using existing methods.

5.6.3 Implications of Core Identification

This work shows that there is no time-stable density contour with which to define cores. Because of the dynamic nature of core evolution, a single set of dendrogram parameters will not trace unique core parameters across the entire lifetime of core formation. Additionally, we show that a substantial change in the cloud properties (due to time evolution in this case) are required to see changes in the observed CMF: over $> 70\%$ of our simulation snapshots show the same CMF, despite order unity variations in individual cores. Changes in the distribution occur at early times. In the context of our simulations, this is because gravity has had less time to overcome the turbulence in the gas. In real systems, this would correspond to the time when the cloud itself was only weakly bound. This trend suggests that variations in the CMF only coarsely trace the time evolution of a star forming region. Thus variations in the CMF from one star forming region to should not be attributed solely to differences in age. Finally, computing a dendrogram in density or intensity on an observed region introduces an inherent uncertainty in the physical importance of structures identified. Dendrograms have many tunable parameters, so disentangling physical structure from algorithmically imposed structure in an automated fashion is a non-trivial endeavor.

The large variability in the computed core boundaries will likely be less dramatic in observational space due to the integration of the signal along a line of sight. The lower density material around the edges of our identified leaves will not contribute as much signal, so structures will appear more compact around only the densest part of the core. However, as Beaumont et al. (2013) and citations therein show, simulation projections and observation are highly subject to projection effects, such as non-physical cores being identified due to a large column of low-density material. Thus, neither physical nor observational spaces have cores that can be robustly and

uniquely defined across all time.

5.7 Conclusions

In this work, we have presented an algorithm that links dendrogram leaves through time in order to study the evolution of dense cores in MHD simulations. We aim to understand not only the evolution of the star-forming gas reservoir in our simulations, but also the manner in which the use of the dendrogram algorithm may bias interpretation of core properties and evolution. Ideally, the parameters used for identifying and linking cores are set by the underlying physics. As is shown in this work, we ultimately conclude that there is no robust set of density-based parameters that can trace coherent cores through time. Additionally, we find the following:

1. The distributions of core properties, such as mass, are relatively invariant in time. The CMF matches well with observed CMF distributions such as Alves et al. (2007) and shifted IMFs such as Chabrier (2003). Most property distributions do not show significant trends over long timescales.
2. Individual core histories show large variability ($> 40\%$) on short timescales (< 100 kyr) that arise from changes in the leaf boundaries. This non-monotonic variability persists across environment (isolated or crowded) and stellar content. Additionally, a leaf history that shows low variability in one parameter will not necessarily show low variability in all parameters. There are no obvious regular trends in time with the exception of virial parameter (which tends to decrease to $\alpha < 2$ as the cores reach the end of the simulation). There is some evidence for long-term evolution in of individual paths traced in other properties that may correspond to physical evolution, but the shorter stochastic variability makes these trends difficult to quantify.
3. The variability exhibited in our analysis of individual core evolution is at least partially attributable to the dendrogram algorithm itself. Small changes in the

relative structure of the density between timesteps can propagate to incredibly large changes in the computed boundaries of structures. In extreme cases, volumes can change by an order of magnitude between timesteps, leading to nearly 100% variability in computed core properties. The sensitivity of the dendrogram to small changes in physical conditions raises concerns about hierarchies identified in both simulations and observations. For instance, changes in noise or resolution may lead to different hierarchies in the same region.

4. we find a population of short-lived overdensities in each timestep that may serve as a substantial source of “noise” for core property distributions in observations. The overdensities tend to have lower density ($< 10^{-18}$) and lifetimes less than 200 kyr, and they account for 15 – 25% of identified leaves every timestep. These overdensities have other properties, such as mass and size, that are comparable to other cores in the simulation that go on to form stars.
5. Assessing the full history of cores (including events like mergers) may be important for interpreting the IMF. We find that, especially for massive multiple star systems, the sum of all initial leaves associated with the multiple is typically required to agree with CMF-IMF scaling assumptions even when inefficiency produced by feedback is taken into account.
6. There is no time-stable density contour that defines a star-forming core. The dynamic nature of core formation and evolution means that dendrograms will not trace the same structures across time in a reliable way. Thus, we urge caution when comparing dendrograms of different ages or environments because differences in the dendrogram may come from the algorithm itself instead of physical changes.

In summary, cores identified with dendrograms are subject to algorithmic limitations that impact the physical interpretation of “observed” core boundaries. And yet, understanding the full time evolution of star-forming cores is critical to understanding the end results of star formation, such as interpreting the relationship

(or lack thereof) between the CMF and IMF. We have shown the need for caution when extrapolating instantaneous observations of star-forming cores either forward or backward in time, as cores can have substantial variability both intrinsically and observationally.

Acknowledgements

We are grateful for the helpful suggestions of our anonymous referee. We also thank others, including Jaime Pineda and Alyssa Goodman, for insightful discussions during the course of this work. RAS acknowledges support from the National Science Foundation under Grant No. DGE-1143953. ATL, SSRO, and KMK acknowledge support from NASA grant NNX15AT05G. KMK additionally acknowledges support from NASA grant 80NSSC18K0726 and RCSA award ID 26077. SSRO and HHC acknowledge support from a Cottrell Scholar Award from Research Corporation and NSF Career Grant AST-1650486. The analysis presented herein utilized HPC resources supported by the University of Arizona TRIF, UITS, and RDI and maintained by the UA Research Technologies department. This research made use of `astrodendro`, a Python package to compute dendrograms of astronomical data, and the software package `yt` from Turk et al. (2010).

CHAPTER 6

Summary and Future Directions

6.1 Summary

In this dissertation, I have conducted an exploration of the formation and early evolution of binaries and their environments at different scales using a wide variety of numerical techniques and analyses. Here, I present a summary of the four chapters and their main science conclusions.

Debris in the Pluto-Charon Binary

In Chapter 2, I use N-body simulations of a debris disk around the Pluto-Charon binary to probe the observational consequences of debris resulting from the Charon-forming impact. I first show that the current circumbinary moons of the Pluto-Charon binary, Styx, Nix, Kerberos, and Hydra, are at locations that are dynamically unstable during any model of Charon’s tidal evolution that requires eccentricities above $e \gtrsim 0.05$. This indicates that (a) Charon’s evolution to its current location requires a tidal evolution model that has little to no eccentricity evolution, (b) the circumbinary moons formed or were captured after the current orbit of the Pluto-Charon binary was achieved, or (c) the moons experienced (gas) damping after the tidal evolution. Next, I show that the predominant loss mechanisms for debris around a newly-formed Pluto-Charon are collisions with Charon or ejections from the Pluto-Charon system into the Solar System. Collisions with Charon are more common than collisions with Pluto (despite Pluto being the much larger body) because particles will interact with the secondary (less massive) component of a binary through the second Lagrange point before they can interact with the primary. Collisions with Charon dominate the debris loss mechanisms in the inner part of the debris disk, while ejections dominate loss in the outer part of the disk. I calculate

that there could be hundreds of small craters on Charon’s surface due to impacting debris; however, Singer et al. (2016) find a paucity of small craters on Charon, suggesting that (a) violent tidal heating could have resurfaced Charon or eroded craters such that they are not observable today, or (b) the debris disk extent or composition led to a lack of impactors. I also follow the ejection of debris into the Solar System. While most debris was ejected from the Solar System altogether, a substantial fraction of the debris that remained stayed in the 3:2 resonance with Pluto-Charon and may be observable as a Pluto-Charon disk collisional family. This population could contain up to a few 10s of bodies that would be identifiable through their similar composition and low relative velocity dispersion. This work predicts signatures of the Charon-forming collision that will be important to understanding the collisional histories in the Solar System and the formation of large planetesimal binaries.

Classification of Kuiper Belt Populations

Chapter 3 further explores the dynamical characteristics of Kuiper Belt populations by creating a machine learning classifier to sort observed KBOs into the four Gladman et al. (2008) dynamical populations based on short (100 kyr) numerical integrations of their orbits. This work is a critical first step in preparing for the near future in astronomical survey science (such as the VRO’s LSST). The number of observed KBOs is expected to increase by at least an order of magnitude, and therefore, traditional classification methodologies that require substantial human intervention will be quickly buried under too much data. Machine learning provides an avenue for fast, automated, and high accuracy classification. The machine learning classifier best suited to the currently observed KBO catalog is a regression tree classifier; I achieve a $\sim 98\%$ classification accuracy, and $> 80\%$ of objects have a $> 3\sigma$ probability of class membership. This method is robust to errors in measurement (97% accuracy in classification for samples drawn from the observed errors of a KBO) and new data (92% accuracy in classification for the Wasserman et al. 2020 DECam KBOs not included in our fiducial catalog). Misclassified objects typically fall into three categories: objects lacking statistical representation in the data (such

as mixed-argument resonant KBOs), objects with intermittent dynamical behavior (for instance, switching between resonant and classical characteristics on \sim Myr timescales), and objects that undergo late-time dynamical scattering. The last two reasons for misclassification illuminate a fundamental ambiguity of the KBO classification methodology: timescale is just as critical a factor in the classification as other, more obvious characteristics, such as libration in resonance. This work creates a foundation for revising the entire methodology of Kuiper Belt classification used today.

Circumbinary Planet Dynamics

Chapter 4 studies the influence of a tight central binary on the post-disk evolution of planetary systems. Using a large suite of 10 Myr N-body simulations for four different planetary populations around both single and binary stars, I found that the resultant multiplicity of planetary systems after dynamical evolution doesn't change with the presence of a binary. Indeed, the final system architectures around single and binary stars are typically similar with only a small preference for slightly more inclined and eccentric systems around single stars. The presence of a binary mainly influences the speed and mechanism of planetary loss. Planet-star collisions are reduced by over an order of magnitude around binaries, and planet-planet collisions are reduced by a factor of ~ 2 , with the difference in the binary population ending as ejections. This effect can be intuitively explained by the CR3BP: planets have large enough C_J that they cannot cross the zero velocity surface to interact directly with the stars without first experiencing strong scattering from the Holman and Wiegert (1999) binary instability boundary. Thus, most planets that scatter close into the stars are rapidly ejected unless they have an interaction with another planet that changes the value of C_J shortly before they reach the inner system. Contrarily, around a single star, scattering is a more extended process that requires multiple close encounters to lead to collisions or ejections. I find that the main driver behind the dynamical architecture of the final systems is the presence of a massive planet. In my simulations, final multiplicity is a strong function of the highest planet mass, and

the orbital properties, such as semi-major axis, eccentricity, and dynamical spacing, are statistically different in systems hosting a giant planet. This work shows that there is little influence from a central binary on the final architectures of planetary systems, but rather that a central binary has a strong impact on loss mechanism.

Variability in Star-forming Cores

Finally, in Chapter 5, I explore the time evolution of star-forming cores identified with the dendrogram hierarchical structure identification methodology in a large magnetohydrodynamical simulation. All structure identification algorithms common in the literature use local maxima in a quantity such as intensity or density to identify similar regions based on the local structure around the peak. The dendrogram is unique in that it traces multiple levels of structure in a region, from dense cores (called leaves) to the more filamentary structure that connects cores (called branches and trunks). In this work, I create an algorithm to connect dendrogram leaves between time outputs to investigate the interplay between physical evolution in the star-forming region and variation in physical quantities induced by the structure identification. I find that, while the *distributions* of core properties are statistically invariant over the course of our simulation ($\sim 750 \text{ kyr} \approx 0.55 t_{\text{ff}}$ for the global region), *individual* cores can show variability upwards of 40%. The variability I observe is mostly attributable to the structure identification algorithm. Because of the relative nature of structure identification, small changes in the local density environment around a peak can cause large variations in the contours of identified cores. In one case, a less than 5% change in peak density led to a 400% change in volume. Because of this, I argue that there is no time-invariant density contour in the star formation process, and therefore, one must be cautious to not over-interpret physical evolution from observed cores. This work raises a significant concern in observations of star-forming regions: how much does the structure identification algorithm impact the core properties derived from observations? Observations already have biases in understanding intrinsic structure due to effects like line-of-sight integration, and my work shows that significant additional bias could be introduced by core identification

algorithms.

6.2 Future Directions

As in any research program, the work presented herein has raised more questions than it answered. In this section, I elaborate on two research avenues that will be valuable in the near future to adapt to upcoming observational upgrades in the astronomical community.

Kuiper Belt Classification

As noted in Chapter 3, there are improvements that should be made to the machine learning classifier before this type of method is ready for use in something like a LSST pipeline. The major improvement to this work is to create a synthetic catalog of KBOs to use as the input training set for the machine learning classifier. This has several benefits:

1. A synthetic catalog can compensate for the low number statistics of rare KBOs, such as the mixed eccentricity-inclination resonances of which order 10 are known today.
2. Time dependent objects, such as intermittent librators, will be better characterized such that the features passed to the classifier may be able to predict future behavior not observed in the short integration.
3. As yet unobserved KBOs, such as exotic resonant objects or distant classicals, can be included to ensure accurate classification if these objects ever are observed.
4. A very large number (\sim millions) of synthetic KBOs can be run to uniformly cover the desired parameter space without observational bias, and the classifier only needs to be trained once instead of being regularly updated with new observations.

In addition, because of the increased statistical power of a larger catalog, more classes could be introduced. This would allow, for instance, resonant objects to be classified directly as 3:2 or 2:1, or for classical objects to be split into cold and hot classical KBOs. Finally, with a more thorough and accurate classifier, human intervention in classification could be even more substantially reduced, thereby allowing more time for science pursuits.

Star-Forming Core Identification

Chapter 5 leaves open many questions that are critical for proper interpretation of star formation simulations and observations. In the near future, both computational and observational investigations of star formation will grow in size and detail. Thus, it is imperative to understand both the physical and observational consequences of star formation so that correct conclusions are drawn.

Structure Identification Across Different Simulations

There are a wide variety of simulation types and initial conditions that are publicly available. Thus, it is advisable to apply the same structure identification methodology to the broad ensemble of available data to understand the influence of a core-finding algorithm on the broad collection of physics represented in the simulations. Are there systematic differences that are attributable to physics? Do the conclusions of Chapter 5 hold across different regions?

Structure-independent Core Identification

Chapter 5 calls into question the use of modern structure identification algorithms: the algorithmic structure is difficult to disentangle from physical structure. However, there are methods that make no assumption about the physical structure of a region: machine learning provides an ideal direction to investigate to get a differently biased understanding of core evolution. Using a deep learning technique called a convolutional neural network that can take an image (or three dimensional array), one should be able to find core-like structures without relying upon density contours or intensity gradients. Additional machine learning techniques like

the tracking-detection method allow for core trajectory tracing while allowing for variable speed, changing boundaries, and intermittent phenomena like obscuration. These types of machine learning techniques will be widely applicable across astronomy: for instance, they could be used to track dense knots in galactic outflows (Schneider et al., 2018) or understand the evolving morphologies of supernovae ejecta (Wongwathanarat et al., 2015).

REFERENCES

- Abbott, B. P., R. Abbott, T. D. Abbott, F. Acernese, K. Ackley, C. Adams, T. Adams, P. Addesso, R. X. Adhikari, V. B. Adya, C. Affeldt, M. Afrough, B. Agarwal, M. Agathos, K. Agatsuma, N. Aggarwal, O. D. Aguiar, L. Aiello, A. Ain, P. Ajith, B. Allen, G. Allen, A. Allocca, P. A. Altin, A. Amato, A. Ananyeva, S. B. Anderson, W. G. Anderson, S. V. Angelova, S. Antier, S. Appert, K. Arai, M. C. Araya, J. S. Areeda, N. Arnaud, K. G. Arun, S. Ascenzi, G. Ashton, M. Ast, S. M. Aston, P. Astone, D. V. Atallah, P. Aufmuth, C. Aulbert, K. AultONeal, C. Austin, A. Avila-Alvarez, S. Babak, P. Bacon, M. K. M. Bader, S. Bae, M. Bailes, P. T. Baker, F. Baldaccini, G. Ballardin, S. W. Ballmer, S. Banagiri, J. C. Barayoga, S. E. Barclay, B. C. Barish, D. Barker, K. Barkett, F. Barone, B. Barr, L. Barsotti, M. Barsuglia, D. Barta, S. D. Barthelmy, J. Bartlett, I. Bartos, R. Bassiri, A. Basti, J. C. Batch, M. Bawaj, J. C. Bayley, M. Bazzan, B. Bécsy, C. Beer, M. Bejger, I. Belahcene, A. S. Bell, B. K. Berger, G. Bergmann, S. Bernuzzi, J. J. Bero, C. P. L. Berry, D. Bersanetti, A. Bertolini, J. Betzwieser, S. Bhagwat, R. Bhandare, I. A. Bilenko, G. Billingsley, C. R. Billman, J. Birch, R. Birney, O. Birnholtz, S. Biscans, S. Biscoveanu, A. Bisht, M. Bitossi, C. Biwer, M. A. Bizouard, J. K. Blackburn, J. Blackman, C. D. Blair, D. G. Blair, R. M. Blair, S. Bloemen, O. Bock, N. Bode, M. Boer, G. Bogaert, A. Bohe, F. Bondu, E. Bonilla, R. Bonnand, B. A. Boom, R. Bork, V. Boschi, S. Bose, K. Bossie, Y. Bouffanais, A. Bozzi, C. Bradaschia, P. R. Brady, M. Branchesi, J. E. Brau, T. Briant, A. Brillet, M. Brinkmann, V. Brisson, P. Brockill, J. E. Broida, A. F. Brooks, D. A. Brown, D. D. Brown, S. Brunett, C. C. Buchanan, A. Buikema, T. Bulik, H. J. Bulten, A. Buonanno, D. Buskulic, C. Buy, R. L. Byer, M. Cabero, L. Cadonati, G. Cagnoli, C. Cahillane, J. Calderón Bustillo, T. A. Callister, E. Calloni, J. B. Camp, M. Canepa, P. Canizares, K. C. Cannon, H. Cao, J. Cao, C. D. Capano, E. Capocasa, F. Carbognani, S. Caride, M. F. Carney, G. Carullo, J. Casanueva Diaz, C. Casentini, S. Caudill, M. Cavaglià, F. Cavalier, R. Cavalieri, G. Cella, C. B. Cepeda, P. Cerdá-Durán, G. Cerretani, E. Cesarini, S. J. Chamberlin, M. Chan, S. Chao, P. Charlton, E. Chase, E. Chassande-Mottin, D. Chatterjee, K. Chatziioannou, B. D. Cheeseboro, H. Y. Chen, X. Chen, Y. Chen, H.-P. Cheng, H. Chia, A. Chincarini, A. Chiummo, T. Chmiel, H. S. Cho, M. Cho, J. H. Chow, N. Christensen, Q. Chu, A. J. K. Chua, S. Chua, A. K. W. Chung, S. Chung, G. Ciani, R. Ciolfi, C. E. Cirelli, A. Cirone, F. Clara, J. A. Clark, P. Clearwater, F. Cleva, C. Cocchieri, E. Coccia, P.-F. Cohadon, D. Cohen, A. Colla, C. G. Collette, L. R. Cominsky, M. Constancio, L. Conti, S. J. Cooper, P. Corban, T. R. Corbitt, I. Cordero-Carrión, K. R. Corley, N. Cornish, A. Corsi, S. Cortese, C. A.

Costa, M. W. Coughlin, S. B. Coughlin, J.-P. Coulon, S. T. Countryman, P. Couvares, P. B. Covas, E. E. Cowan, D. M. Coward, M. J. Cowart, D. C. Coyne, R. Coyne, J. D. E. Creighton, T. D. Creighton, J. Cripe, S. G. Crowder, T. J. Cullen, A. Cumming, L. Cunningham, E. Cuoco, T. Dal Canton, G. Dálya, S. L. Danilishin, S. D'Antonio, K. Danzmann, A. Dasgupta, C. F. Da Silva Costa, V. Dattilo, I. Dave, M. Davier, D. Davis, E. J. Daw, B. Day, S. De, D. DeBra, J. Degallaix, M. De Laurentis, S. Deléglise, W. Del Pozzo, N. Demos, T. Denker, T. Dent, R. De Pietri, V. Dergachev, R. De Rosa, R. T. DeRosa, C. De Rossi, R. DeSalvo, O. de Varona, J. Devenson, S. Dhurandhar, M. C. Díaz, T. Dietrich, L. Di Fiore, M. Di Giovanni, T. Di Girolamo, A. Di Lieto, S. Di Pace, I. Di Palma, F. Di Renzo, Z. Doctor, V. Dolique, F. Donovan, K. L. Dooley, S. Doravari, I. Dorrington, R. Douglas, M. Dovalé Álvarez, T. P. Downes, M. Drago, C. Dreisigacker, J. C. Driggers, Z. Du, M. Ducrot, R. Dudi, P. Dupej, S. E. Dwyer, T. B. Edo, M. C. Edwards, A. Effler, H.-B. Eggenstein, P. Ehrens, J. Eichholz, S. S. Eikenberry, R. A. Eisenstein, R. C. Essick, D. Estevez, Z. B. Etienne, T. Etzel, M. Evans, T. M. Evans, M. Factourovich, V. Fafone, H. Fair, S. Fairhurst, X. Fan, S. Farinon, B. Farr, W. M. Farr, E. J. Fauchon-Jones, M. Favata, M. Fays, C. Fee, H. Fehrmann, J. Feicht, M. M. Fejer, A. Fernandez-Galiana, I. Ferrante, E. C. Ferreira, F. Ferrini, F. Fidecaro, D. Finstad, I. Fiori, D. Fiorucci, M. Fishbach, R. P. Fisher, M. Fitz-Axen, R. Flaminio, M. Fletcher, H. Fong, J. A. Font, P. W. F. Forsyth, S. S. Forsyth, J.-D. Fournier, S. Frasca, F. Frasconi, Z. Frei, A. Freise, R. Frey, V. Frey, E. M. Fries, P. Fritschel, V. V. Frolov, P. Fulda, M. Fyffe, H. Gabbard, B. U. Gadre, S. M. Gaebel, J. R. Gair, L. Gammaitoni, M. R. Ganija, S. G. Gaonkar, C. Garcia-Quiros, F. Garufi, B. Gateley, S. Gaudio, G. Gaur, V. Gayathri, N. Gehrels, G. Gemme, E. Genin, A. Gennai, D. George, J. George, L. Gergely, V. Germain, S. Ghonge, A. Ghosh, A. Ghosh, S. Ghosh, J. A. Giaime, K. D. Giardina, A. Giazotto, K. Gill, L. Glover, E. Goetz, R. Goetz, S. Gomes, B. Goncharov, G. González, J. M. Gonzalez Castro, A. Gopakumar, M. L. Gorodetsky, S. E. Gossan, M. Gosselin, R. Gouaty, A. Grado, C. Graef, M. Granata, A. Grant, S. Gras, C. Gray, G. Greco, A. C. Green, E. M. Gretarsson, P. Groot, H. Grote, S. Grunewald, P. Gruning, G. M. Guidi, X. Guo, A. Gupta, M. K. Gupta, K. E. Gushwa, E. K. Gustafson, R. Gustafson, O. Halim, B. R. Hall, E. D. Hall, E. Z. Hamilton, G. Hammond, M. Haney, M. M. Hanke, J. Hanks, C. Hanna, M. D. Hannam, O. A. Hannuksela, J. Hanson, T. Hardwick, J. Harms, G. M. Harry, I. W. Harry, M. J. Hart, C.-J. Haster, K. Haughian, J. Healy, A. Heidmann, M. C. Heintze, H. Heitmann, P. Hello, G. Hemming, M. Hendry, I. S. Heng, J. Hennig, A. W. Heptonstall, M. Heurs, S. Hild, T. Hinderer, W. C. G. Ho, D. Hoak, D. Hofman, K. Holt, D. E. Holz, P. Hopkins, C. Horst, J. Hough, E. A. Houston, E. J. Howell, A. Hreibi, Y. M. Hu, E. A. Huerta, D. Huet, B. Hughey, S. Husa, S. H. Huttner, T. Huynh-Dinh, N. Indik, R. Inta, G. Intini, H. N. Isa, J.-M. Isac, M. Isi, B. R. Iyer, K. Izumi, T. Jacqmin, K. Jani, P. Jaranowski, S. Jawahar, F. Jiménez-Forteza, W. W. Johnson, N. K. Johnson-McDaniel, D. I.

Jones, R. Jones, R. J. G. Jonker, L. Ju, J. Junker, C. V. Kalaghatgi, V. Kalogera, B. Kamai, S. Kandhasamy, G. Kang, J. B. Kanner, S. J. Kapadia, S. Karki, K. S. Karvinen, M. Kasprzack, W. Kastaun, M. Katolik, E. Katsavounidis, W. Katzman, S. Kaufer, K. Kawabe, F. Kéfélian, D. Keitel, A. J. Kemball, R. Kennedy, C. Kent, J. S. Key, F. Y. Khalili, I. Khan, S. Khan, Z. Khan, E. A. Khazanov, N. Kijbunchoo, C. Kim, J. C. Kim, K. Kim, W. Kim, W. S. Kim, Y.-M. Kim, S. J. Kimbrell, E. J. King, P. J. King, M. Kinley-Hanlon, R. Kirchhoff, J. S. Kissel, L. Kleybolte, S. Klimenko, T. D. Knowles, P. Koch, S. M. Koehlenbeck, S. Koley, V. Kondrashov, A. Kontos, M. Korobko, W. Z. Korth, I. Kowalska, D. B. Kozak, C. Krämer, V. Kringel, B. Krishnan, A. Królak, G. Kuehn, P. Kumar, R. Kumar, S. Kumar, L. Kuo, A. Kutynia, S. Kwang, B. D. Lackey, K. H. Lai, M. Landry, R. N. Lang, J. Lange, B. Lantz, R. K. Lanza, S. L. Larson, A. Lartaux-Vollard, P. D. Lasky, M. Laxen, A. Lazzarini, C. Lazzaro, P. Leaci, S. Leavey, C. H. Lee, H. K. Lee, H. M. Lee, H. W. Lee, K. Lee, J. Lehmann, A. Lenon, E. Leon, M. Leonardi, N. Leroy, N. Letendre, Y. Levin, T. G. F. Li, S. D. Linker, T. B. Littenberg, J. Liu, X. Liu, R. K. L. Lo, N. A. Lockerbie, L. T. London, J. E. Lord, M. Lorenzini, V. Lorette, M. Lormand, G. Losurdo, J. D. Lough, C. O. Lousto, G. Lovelace, H. Lück, D. Lumaca, A. P. Lundgren, R. Lynch, Y. Ma, R. Macas, S. Macfoy, B. Machenschalk, M. MacInnis, D. M. Macleod, I. Magaña Hernandez, F. Magaña-Sandoval, L. Magaña Zertuche, R. M. Magee, E. Majorana, I. Maksimovic, N. Man, V. Mandic, V. Mangano, G. L. Mansell, M. Manske, M. Mantovani, F. Marchesoni, F. Marion, S. Márka, Z. Márka, C. Markakis, A. S. Markosyan, A. Markowitz, E. Maros, A. Marquina, P. Marsh, F. Martelli, L. Martellini, I. W. Martin, R. M. Martin, D. V. Martynov, J. N. Marx, K. Mason, E. Massera, A. Masserot, T. J. Massinger, M. Masso-Reid, S. Mastrogiovanni, A. Matas, F. Matichard, L. Matone, N. Mavalvala, N. Mazumder, R. McCarthy, D. E. McClelland, S. McCormick, L. McCuller, S. C. McGuire, G. McIntyre, J. McIver, D. J. McManus, L. McNeill, T. McRae, S. T. McWilliams, D. Meacher, G. D. Meadors, M. Mehmet, J. Meidam, E. Mejuto-Villa, A. Melatos, G. Mendell, R. A. Mercer, E. L. Merilh, M. Merzougui, S. Meshkov, C. Messenger, C. Messick, R. Metzдорff, P. M. Meyers, H. Miao, C. Michel, H. Middleton, E. E. Mikhailov, L. Milano, A. L. Miller, B. B. Miller, J. Miller, M. Millhouse, M. C. Milovich-Goff, O. Minazzoli, Y. Minenkov, J. Ming, C. Mishra, S. Mitra, V. P. Mitrofanov, G. Mitselmakher, R. Mittleman, D. Moffa, A. Moggi, K. Mogushi, M. Mohan, S. R. P. Mohapatra, I. Molina, M. Montani, C. J. Moore, D. Moraru, G. Moreno, S. Morisaki, S. R. Morriss, B. Mours, C. M. Mow-Lowry, G. Mueller, A. W. Muir, A. Mukherjee, D. Mukherjee, S. Mukherjee, N. Mukund, A. Mullavey, J. Munch, E. A. Muñiz, M. Muratore, P. G. Murray, A. Nagar, K. Napier, I. Nardecchia, L. Naticchioni, R. K. Nayak, J. Neilson, G. Nelemans, T. J. N. Nelson, M. Nery, A. Neunzert, L. Nevin, J. M. Newport, G. Newton, K. K. Y. Ng, P. Nguyen, T. T. Nguyen, D. Nichols, A. B. Nielsen, S. Nissanke, A. Nitz, A. Noack, F. Nocera, D. Nolting, C. North, L. K. Nuttall, J. Oberling, G. D. O'Dea, G. H. Ogin, J. J.

Oh, S. H. Oh, F. Ohme, M. A. Okada, M. Oliver, P. Oppermann, R. J. Oram, B. O'Reilly, R. Ormiston, L. F. Ortega, R. O'Shaughnessy, S. Ossokine, D. J. Ottaway, H. Overmier, B. J. Owen, A. E. Pace, J. Page, M. A. Page, A. Pai, S. A. Pai, J. R. Palamos, O. Palashov, C. Palomba, A. Pal-Singh, H. Pan, H.-W. Pan, B. Pang, P. T. H. Pang, C. Pankow, F. Pannarale, B. C. Pant, F. Paoletti, A. Paoli, M. A. Papa, A. Parida, W. Parker, D. Pascucci, A. Pasqualetti, R. Passaquieti, D. Passuello, M. Patil, B. Patricelli, B. L. Pearlstone, M. Pedraza, R. Pedurand, L. Pekowsky, A. Pele, S. Penn, C. J. Perez, A. Perreca, L. M. Perri, H. P. Pfeiffer, M. Phelps, O. J. Piccinni, M. Pichot, F. Piergiovanni, V. Pierro, G. Pillant, L. Pinard, I. M. Pinto, M. Pirello, M. Pitkin, M. Poe, R. Poggiani, P. Popolizio, E. K. Porter, A. Post, J. Powell, J. Prasad, J. W. W. Pratt, G. Pratten, V. Predoi, T. Prestegard, M. Prijatelj, M. Principe, S. Privitera, R. Prix, G. A. Prodi, L. G. Prokhorov, O. Puncken, M. Punturo, P. Puppo, M. Pürerer, H. Qi, V. Quetschke, E. A. Quintero, R. Quitzow-James, F. J. Raab, D. S. Rabeling, H. Radkins, P. Raffai, S. Raja, C. Rajan, B. Rajbhandari, M. Rakhmanov, K. E. Ramirez, A. Ramos-Buades, P. Rapagnani, V. Raymond, M. Razzano, J. Read, T. Regimbau, L. Rei, S. Reid, D. H. Reitze, W. Ren, S. D. Reyes, F. Ricci, P. M. Ricker, S. Rieger, K. Riles, M. Rizzo, N. A. Robertson, R. Robie, F. Robinet, A. Rocchi, L. Rolland, J. G. Rollins, V. J. Roma, J. D. Romano, R. Romano, C. L. Romel, J. H. Romie, D. Rosińska, M. P. Ross, S. Rowan, A. Rüdiger, P. Ruggi, G. Rutins, K. Ryan, S. Sachdev, T. Sadecki, L. Sadeghian, M. Sakellariadou, L. Salconi, M. Saleem, F. Salemi, A. Samajdar, L. Sammut, L. M. Sampson, E. J. Sanchez, L. E. Sanchez, N. Sanchis-Gual, V. Sandberg, J. R. Sanders, B. Sassolas, B. S. Sathyaprakash, P. R. Saulson, O. Sauter, R. L. Savage, A. Sawadsky, P. Schale, M. Scheel, J. Scheuer, J. Schmidt, P. Schmidt, R. Schnabel, R. M. S. Schofield, A. Schönbeck, E. Schreiber, D. Schuette, B. W. Schulte, B. F. Schutz, S. G. Schwalbe, J. Scott, S. M. Scott, E. Seidel, D. Sellers, A. S. Sengupta, D. Sentenac, V. Sequino, A. Sergeev, D. A. Shaddock, T. J. Shaffer, A. A. Shah, M. S. Shahriar, M. B. Shaner, L. Shao, B. Shapiro, P. Shawhan, A. Sheperd, D. H. Shoemaker, D. M. Shoemaker, K. Siellez, X. Siemens, M. Sieniawska, D. Sigg, A. D. Silva, L. P. Singer, A. Singh, A. Singhal, A. M. Sintes, B. J. J. Slagmolen, B. Smith, J. R. Smith, R. J. E. Smith, S. Somala, E. J. Son, J. A. Sonnenberg, B. Sorazu, F. Sorrentino, T. Souradeep, A. P. Spencer, A. K. Srivastava, K. Staats, A. Staley, M. Steinke, J. Steinlechner, S. Steinlechner, D. Steinmeyer, S. P. Stevenson, R. Stone, D. J. Stops, K. A. Strain, G. Stratta, S. E. Strigin, A. Strunk, R. Sturani, A. L. Stuver, T. Z. Summerscales, L. Sun, S. Sunil, J. Suresh, P. J. Sutton, B. L. Swinkels, M. J. Szczepańczyk, M. Tacca, S. C. Tait, C. Talbot, D. Talukder, D. B. Tanner, M. Tápai, A. Taracchini, J. D. Tasson, J. A. Taylor, R. Taylor, S. V. Tewari, T. Theeg, F. Thies, E. G. Thomas, M. Thomas, P. Thomas, K. A. Thorne, K. S. Thorne, E. Thrane, S. Tiwari, V. Tiwari, K. V. Tokmakov, K. Toland, M. Tonelli, Z. Tornasi, A. Torres-Forné, C. I. Torrie, D. Töyrä, F. Travasso, G. Traylor, J. Trinastic, M. C. Tringali, L. Trozzo,

- K. W. Tsang, M. Tse, R. Tso, L. Tsukada, D. Tsuna, D. Tuyenbayev, K. Ueno, D. Ugolini, C. S. Unnikrishnan, A. L. Urban, S. A. Usman, H. Vahlbruch, G. Vajente, G. Valdes, M. Vallisneri, N. van Bakel, M. van Beuzekom, J. F. J. van den Brand, C. Van Den Broeck, D. C. Vander-Hyde, L. van der Schaaf, J. V. van Heijningen, A. A. van Veggel, M. Vardaro, V. Varma, S. Vass, M. Vasúth, A. Vecchio, G. Vedovato, J. Veitch, P. J. Veitch, K. Venkateswara, G. Venugopalan, D. Verkindt, F. Vetrano, A. Viceré, A. D. Viets, S. Vinciguerra, D. J. Vine, J.-Y. Vinet, S. Vitale, T. Vo, H. Vocca, C. Vorvick, S. P. Vyatchanin, A. R. Wade, L. E. Wade, M. Wade, R. Walet, M. Walker, L. Wallace, S. Walsh, G. Wang, H. Wang, J. Z. Wang, W. H. Wang, Y. F. Wang, R. L. Ward, J. Warner, M. Was, J. Watchi, B. Weaver, L.-W. Wei, M. Weinert, A. J. Weinstein, R. Weiss, L. Wen, E. K. Wessel, P. Weßels, J. Westerweck, T. Westphal, K. Wette, J. T. Whelan, S. E. Whitcomb, B. F. Whiting, C. Whittle, D. Wilken, D. Williams, R. D. Williams, A. R. Williamson, J. L. Willis, B. Willke, M. H. Wimmer, W. Winkler, C. C. Wipf, H. Wittel, G. Woan, J. Woehler, J. Wofford, K. W. K. Wong, J. Worden, J. L. Wright, D. S. Wu, D. M. Wysocki, S. Xiao, H. Yamamoto, C. C. Yancey, L. Yang, M. J. Yap, M. Yazback, H. Yu, H. Yu, M. Yvert, A. Zadrozny, M. Zanolin, T. Zelenova, J.-P. Zendri, M. Zevin, L. Zhang, M. Zhang, T. Zhang, Y.-H. Zhang, C. Zhao, M. Zhou, Z. Zhou, S. J. Zhu, X. J. Zhu, A. B. Zimmerman, M. E. Zucker, J. Zweizig, LIGO Scientific Collaboration, and Virgo Collaboration (2017). GW170817: Observation of Gravitational Waves from a Binary Neutron Star Inspiral. *Physical Review Letters*, **119**, p. 161101. doi: 10.1103/PhysRevLett.119.161101.
- Adorf, H. M. and E. J. A. Meurs (1988). Supervised and Unsupervised Classification — the Case of Iras Point Sources. In Seitter, W. C., H. W. Duerbeck, and M. Tacke (eds.) *Large-Scale Structures in the Universe Observational and Analytical Methods*, Lecture Notes in Physics, pp. 315–322. Berlin, Heidelberg. ISBN 978-3-540-45938-5. doi: 10.1007/3-540-50135-5_86.
- ALMA Partnership, C. L. Brogan, L. M. Pérez, T. R. Hunter, W. R. F. Dent, A. S. Hales, R. E. Hills, S. Corder, E. B. Fomalont, C. Vlahakis, Y. Asaki, D. Barkats, A. Hirota, J. A. Hodge, C. M. V. Impellizzeri, R. Kneissl, E. Liuzzo, R. Lucas, N. Marcelino, S. Matsushita, K. Nakanishi, N. Phillips, A. M. S. Richards, I. Toledo, R. Aladro, D. Broguiere, J. R. Cortes, P. C. Cortes, D. Espada, F. Galarza, D. Garcia-Appadoo, L. Guzman-Ramirez, E. M. Humphreys, T. Jung, S. Kamenon, R. A. Laing, S. Leon, G. Marconi, A. Mignano, B. Nikolic, L.-A. Nyman, M. Radiszcz, A. Remijan, J. A. Rodón, T. Sawada, S. Takahashi, R. P. J. Tilanus, B. Vila Vilaro, L. C. Watson, T. Wiklind, E. Akiyama, E. Chapillon, I. de Gregorio-Monsalvo, J. Di Francesco, F. Gueth, A. Kawamura, C.-F. Lee, Q. Nguyen Luong, J. Mangum, V. Pietu, P. Sanhueza, K. Saigo, S. Takakuwa, C. Ubach, T. van Kempen, A. Wootten, A. Castro-Carrizo, H. Francke, J. Gal-

- lardo, J. Garcia, S. Gonzalez, T. Hill, T. Kaminski, Y. Kurono, H.-Y. Liu, C. Lopez, F. Morales, K. Plarre, G. Schieven, L. Testi, L. Videla, E. Villard, P. Andreani, J. E. Hibbard, and K. Tatematsu (2015). The 2014 ALMA Long Baseline Campaign: First Results from High Angular Resolution Observations toward the HL Tau Region. *The Astrophysical Journal Letters*, **808**, p. L3. doi: 10.1088/2041-8205/808/1/L3.
- Alves, J., M. Lombardi, and C. J. Lada (2007). The Mass Function of Dense Molecular Cores and the Origin of the IMF. *Astronomy & Astrophysics*, **462**(1), pp. L17–L21. doi: 10.1051/0004-6361:20066389.
- André, P., J. Di Francesco, D. Ward-Thompson, S.-I. Inutsuka, R. E. Pudritz, and J. E. Pineda (2014). From Filamentary Networks to Dense Cores in Molecular Clouds: Toward a New Paradigm for Star Formation. *Protostars and Planets VI*, p. 27. doi: 10.2458/azu_uapress_9780816531240-ch002.
- André, P., A. Men'shchikov, S. Bontemps, V. Könyves, F. Motte, N. Schneider, P. Didelon, V. Minier, P. Saraceno, D. Ward-Thompson, J. D. Francesco, G. White, S. Molinari, L. Testi, A. Abergel, M. Griffin, T. Henning, P. Royer, B. Merín, R. Vavrek, M. Attard, D. Arzoumanian, C. D. Wilson, P. Ade, H. Aussel, J.-P. Baluteau, M. Benedettini, J.-P. Bernard, J. a. D. L. Blommaert, L. Cambrésy, P. Cox, A. D. Giorgio, P. Hargrave, M. Hennemann, M. Huang, J. Kirk, O. Krause, R. Launhardt, S. Leeks, J. L. Pennece, J. Z. Li, P. G. Martin, A. Maury, G. Olofsson, A. Omont, N. Peretto, S. Pezzuto, T. Prusti, H. Roussel, D. Russeil, M. Sauvage, B. Sibthorpe, A. Sicilia-Aguilar, L. Spinoglio, C. Waelkens, A. Woodcraft, and A. Zavagno (2010). From Filamentary Clouds to Prestellar Cores to the Stellar IMF: Initial Highlights from the Herschel Gould Belt Survey. *Astronomy & Astrophysics*, **518**, p. L102. doi: 10.1051/0004-6361/201014666.
- Andrews, S. M., J. Huang, L. M. Pérez, A. Isella, C. P. Dullemond, N. T. Kurtovic, V. V. Guzmán, J. M. Carpenter, D. J. Wilner, S. Zhang, Z. Zhu, T. Birnstiel, X.-N. Bai, M. Benisty, A. M. Hughes, K. I. Öberg, and L. Ricci (2018). The Disk Substructures at High Angular Resolution Project (DSHARP). I. Motivation, Sample, Calibration, and Overview. *The Astrophysical Journal Letters*, **869**, p. L41. doi: 10.3847/2041-8213/aaf741.
- Arimatsu, K., K. Tsumura, F. Usui, Y. Shinnaka, K. Ichikawa, T. Ootsubo, T. Kotani, T. Wada, K. Nagase, and J. Watanabe (2019). A Kilometre-Sized Kuiper Belt Object Discovered by Stellar Occultation Using Amateur Telescopes. *Nature Astronomy*, **3**(4), pp. 301–306. doi: 10.1038/s41550-018-0685-8.
- Armstrong, D. J., H. P. Osborn, D. J. A. Brown, F. Faedi, Y. Gomez Maqueo Chew, D. V. Martin, D. Pollacco, and S. Udry (2014). On the Abundance of Circumbi-

- nary Planets. *Monthly Notices of the Royal Astronomical Society*, **444**(2), pp. 1873–1883. doi: 10.1093/mnras/stu1570.
- Arzoumanian, D., P. André, V. Könyves, P. Palmeirim, A. Roy, N. Schneider, M. Benedettini, P. Didelon, J. D. Francesco, J. Kirk, and B. Ladjelate (2019). Characterizing the Properties of Nearby Molecular Filaments Observed with Herschel. *Astronomy & Astrophysics*, **621**, p. A42. doi: 10.1051/0004-6361/201832725.
- Arzoumanian, D., P. André, N. Peretto, and V. Könyves (2013). Formation and Evolution of Interstellar Filaments - Hints from Velocity Dispersion Measurements. *Astronomy & Astrophysics*, **553**, p. A119. doi: 10.1051/0004-6361/201220822.
- Ballesteros-Paredes, J. and M.-M. M. Low (2002). Physical versus Observational Properties of Clouds in Turbulent Molecular Cloud Models. *The Astrophysical Journal*, **570**(2), p. 734. doi: 10.1086/339624.
- Bannister, M. T., B. J. Gladman, J. J. Kavelaars, J.-M. Petit, K. Volk, Y.-T. Chen, M. Alexandersen, S. D. J. Gwyn, M. E. Schwamb, E. Ashton, S. D. Benecchi, N. Cabral, R. I. Dawson, A. Delsanti, W. C. Fraser, M. Granvik, S. Greenstreet, A. Guilbert-Lepoutre, W.-H. Ip, M. Jakubik, R. L. Jones, N. A. Kaib, P. Lacerda, C. Van Laerhoven, S. Lawler, M. J. Lehner, H. W. Lin, P. S. Lykawka, M. Marsset, R. Murray-Clay, R. E. Pike, P. Rousselot, C. Shankman, A. Thirouin, P. Vernazza, and S.-Y. Wang (2018). OSSOS. VII. 800+ Trans-Neptunian Objects—the Complete Data Release. *Astrophysical Journal, Supplement Series*, **236**(1), p. 18. doi: 10.3847/1538-4365/aab77a.
- Batalha, N. M., J. F. Rowe, S. T. Bryson, T. Barclay, C. J. Burke, D. A. Caldwell, J. L. Christiansen, F. Mullally, S. E. Thompson, T. M. Brown, A. K. Dupree, D. C. Fabrycky, E. B. Ford, J. J. Fortney, R. L. Gilliland, H. Isaacson, D. W. Latham, G. W. Marcy, S. N. Quinn, D. Ragozzine, A. Shporer, W. J. Borucki, D. R. Ciardi, T. N. Gautier, M. R. Haas, J. M. Jenkins, D. G. Koch, J. J. Lissauer, W. Rapin, G. S. Basri, A. P. Boss, L. A. Buchhave, J. A. Carter, D. Charbonneau, J. Christensen-Dalsgaard, B. D. Clarke, W. D. Cochran, B.-O. Demory, J.-M. Desert, E. Devore, L. R. Doyle, G. A. Esquerdo, M. Everett, F. Fressin, J. C. Geary, F. R. Girouard, A. Gould, J. R. Hall, M. J. Holman, A. W. Howard, S. B. Howell, K. A. Ibrahim, K. Kinemuchi, H. Kjeldsen, T. C. Klaus, J. Li, P. W. Lucas, S. Meibom, R. L. Morris, A. Prša, E. V. Quintana, D. T. Sanderfer, D. Sasselov, S. E. Seader, J. C. Smith, J. H. Steffen, M. Still, M. C. Stumpe, J. C. Tarter, P. Tenenbaum, G. Torres, J. D. Twicken, K. Uddin, J. Van Cleve, L. M. Walkowicz, and W. F. Welsh (2013). Planetary Candidates Observed by Kepler III. Analysis of the First 16 Months of Data. *The Astrophysical Journal Supplement Series*, **204**(2), p. 24. doi: 10.1088/0067-0049/204/2/24.

- Bate, M. R. (2009). The Importance of Radiative Feedback for the Stellar Initial Mass Function. *Monthly Notices of the Royal Astronomical Society*, **392**(4), pp. 1363–1380. doi: 10.1111/j.1365-2966.2008.14165.x.
- Bate, M. R. (2012). Stellar, Brown Dwarf and Multiple Star Properties from a Radiation Hydrodynamical Simulation of Star Cluster Formation. *Monthly Notices of the Royal Astronomical Society*, **419**(4), pp. 3115–3146. doi: 10.1111/j.1365-2966.2011.19955.x.
- Bate, M. R., I. A. Bonnell, and V. Bromm (2003). The Formation of a Star Cluster: Predicting the Properties of Stars and Brown Dwarfs. *Monthly Notices of the Royal Astronomical Society*, **339**(3), pp. 577–599. doi: 10.1046/j.1365-8711.2003.06210.x.
- Beaumont, C. N., A. A. Goodman, S. Kendrew, J. P. Williams, and R. Simpson (2014). The Milky Way Project: Leveraging Citizen Science and Machine Learning to Detect Interstellar Bubbles. *The Astrophysical Journal Supplement Series*, **214**(1), p. 3. doi: 10.1088/0067-0049/214/1/3.
- Beaumont, C. N., S. S. R. Offner, R. Shetty, S. C. O. Glover, and A. A. Goodman (2013). Quantifying Observational Projection Effects Using Molecular Cloud Simulations. *The Astrophysical Journal*, **777**(2), p. 173. doi: 10.1088/0004-637X/777/2/173.
- Benner, L. A. and W. B. McKinnon (1995). Orbital Behavior of Captured Satellites: The Effect of Solar Gravity on Triton’s Post-Capture Orbit. *Icarus*, **114**(1), pp. 1–20. doi: 10.1006/icar.1995.1039.
- Bernstein, G. and B. Khushalani (2000). Orbit Fitting and Uncertainties for Kuiper Belt Objects. *Astronomical Journal*, **120**(6), pp. 3323–3332. doi: 10.1086/316868.
- Bernstein, G. M., D. E. Trilling, R. L. Allen, M. E. Brown, M. J. Holman, and R. Malhotra (2004). The Size Distribution of Trans-Neptunian Bodies. *The Astronomical Journal*, **128**(3), pp. 1364–1390. doi: 10.1086/422919.
- Berry, D. S. (2015). FellWalker—a Clump Identification Algorithm. *Astronomy and Computing*, **10**, pp. 22–31. doi: 10.1016/j.ascom.2014.11.004.
- Beust, H. (2003). Symplectic Integration of Hierarchical Stellar Systems. *Astronomy and Astrophysics*, **400**(3), pp. 1129–1144. doi: 10.1051/0004-6361:20030065.
- Blitz, L. and A. A. Stark (1986). Detection of Clump and Interclump Gas in the Rosette Molecular Cloud Complex. *The Astrophysical Journal Letters*, **300**, pp. L89–L93. doi: 10.1086/184609.

- Bonnell, I. A., M. R. Bate, C. J. Clarke, and J. E. Pringle (2001). Competitive Accretion in Embedded Stellar Clusters. *Monthly Notices of the Royal Astronomical Society*, **323**(4), pp. 785–794. doi: 10.1046/j.1365-8711.2001.04270.x.
- Boyden, R. D., E. W. Koch, E. W. Rosolowsky, and S. S. R. Offner (2016). An Exploration of the Statistical Signatures of Stellar Feedback. *The Astrophysical Journal*, **833**(2), p. 233. doi: 10.3847/1538-4357/833/2/233.
- Boyden, R. D., S. S. R. Offner, E. W. Koch, and E. W. Rosolowsky (2018). Assessing the Impact of Astrochemistry on Molecular Cloud Turbulence Statistics. *The Astrophysical Journal*, **860**(2), p. 157. doi: 10.3847/1538-4357/aac76d.
- Brasser, R., M. J. Duncan, H. F. Levison, M. E. Schwamb, and M. E. Brown (2012). Reassessing the Formation of the Inner Oort Cloud in an Embedded Star Cluster. *Icarus*, **217**(1), pp. 1–19. doi: 10.1016/j.icarus.2011.10.012.
- Bromley, B. C. and S. J. Kenyon (2015). Evolution of a Ring Around the Pluto–Charon Binary. *The Astrophysical Journal*, **809**(1), p. 88. doi: 10.1088/0004-637X/809/1/88.
- Brown, M. E., K. M. Barkume, D. Ragozzine, and E. L. Schaller (2007). A Collisional Family of Icy Objects in the Kuiper Belt. *Nature*, **446**(7133), pp. 294–296. doi: 10.1038/nature05619.
- Brown, M. E. and E. L. Schaller (2007). The Mass of Dwarf Planet Eris. *Science*, **316**(5831), pp. 1585–1585. doi: 10.1126/science.1139415.
- Brozovic, M., M. R. Showalter, R. A. Jacobson, M. W. Buie, M. Brozović, M. R. Showalter, R. A. Jacobson, and M. W. Buie (2015). The Orbits and Masses of Satellites of Pluto. *Icarus*, **246**, pp. 317–329. doi: 10.1016/j.icarus.2014.03.015.
- Burkhart, B., A. Lazarian, A. Goodman, and E. Rosolowsky (2013). Hierarchical Structure of Magnetohydrodynamic Turbulence in Position-Position-Velocity Space. *The Astrophysical Journal*, **770**(2), p. 141. doi: 10.1088/0004-637X/770/2/141.
- Canup, R. M. (2005). A Giant Impact Origin of Pluto-Charon. *Science (New York, N.Y.)*, **307**(5709), pp. 546–50. doi: 10.1126/science.1106818.
- Canup, R. M. (2011). On a Giant Impact Origin of Charon, Nix, and Hydra. *The Astronomical Journal*, **141**(2), p. 35. doi: 10.1088/0004-6256/141/2/35.
- Carruba, V., S. Aljbaae, R. C. Domingos, A. Lucchini, and P. Furlaneto (2020). Machine Learning Classification of New Asteroid Families Members. *Monthly Notices of the Royal Astronomical Society*. doi: 10.1093/mnras/staa1463.

- Chabrier, G. (2003). Galactic Stellar and Substellar Initial Mass Function*. *Publications of the Astronomical Society of the Pacific*, **115**(809), p. 763. doi: 10.1086/376392.
- Chambers, J. E. and F. Migliorini (1997). Mercury - A New Software Package for Orbital Integrations. *American Astronomical Society*, **29**.
- Chambers, J. E., E. V. Quintana, M. J. Duncan, and J. J. Lissauer (2002). Symplectic Integrator Algorithms for Modeling Planetary Accretion in Binary Star Systems. *The Astronomical Journal*, **123**(5), pp. 2884–2894. doi: 10.1086/340074.
- Chambers, J. E., G. Wetherill, and A. P. Boss (1996). The Stability of Multi-Planet Systems. *Icarus*, **119**(2), pp. 261–268. doi: 10.1006/icar.1996.0019.
- Charnoz, S. and C. Michaut (2015). Evolution of the Protolunar Disk: Dynamics, Cooling Timescale and Implantation of Volatiles onto the Earth. *Icarus*, **260**, pp. 440–463. doi: 10.1016/j.icarus.2015.07.018.
- Chatterjee, S., E. B. Ford, S. Matsumura, and F. A. Rasio (2008). Dynamical Outcomes of Planet-Planet Scattering. *The Astrophysical Journal*, **686**(1), pp. 580–602. doi: 10.1086/590227.
- Chen, C.-Y. and E. C. Ostriker (2018). Geometry, Kinematics, and Magnetization of Simulated Prestellar Cores. *The Astrophysical Journal*, **865**(1), p. 34. doi: 10.3847/1538-4357/aad905.
- Chen, H. H.-H., B. Burkhardt, A. Goodman, and D. C. Collins (2018). The Anatomy of the Column Density Probability Distribution Function (N-PDF). *The Astrophysical Journal*, **859**(2), p. 162. doi: 10.3847/1538-4357/aabaf6.
- Chen, H. H.-H., S. S. R. Offner, J. E. Pineda, A. A. Goodman, A. Burkert, A. Ginsburg, and S. Choudhury (2020). Core Formation, Coherence and Collapse: A New Core Evolution Paradigm Revealed by Machine Learning. *arXiv:2006.07325*.
- Chen, H. H.-H., J. E. Pineda, A. A. Goodman, A. Burkert, S. S. R. Offner, R. K. Friesen, P. C. Myers, F. Alves, H. G. Arce, P. Caselli, A. Chacón-Tanarro, M. C.-Y. Chen, J. D. Francesco, A. Ginsburg, J. Keown, H. Kirk, P. G. Martin, C. Matzner, A. Punanova, E. Redaelli, E. Rosolowsky, S. Scibelli, Y. Seo, Y. Shirley, and A. S. and (2019a). Droplets. I. Pressure-Dominated Coherent Structures in L1688 and B18. *The Astrophysical Journal*, **877**(2), p. 93. doi: 10.3847/1538-4357/ab1a40.
- Chen, Y.-T., B. Gladman, K. Volk, R. Murray-Clay, M. J. Lehner, J. J. Kavelaars, S.-Y. Wang, H.-W. Lin, P. S. Lykawka, M. Alexandersen, M. T. Bannister, S. M. Lawler, R. I. Dawson, S. Greenstreet, S. D. J. Gwyn, and J.-M. Petit (2019b).

- OSSOS. XVIII. Constraining Migration Models with the 2:1 Resonance Using the Outer Solar System Origins Survey. *Astronomical Journal*, **158**(5), p. 214. doi: 10.3847/1538-3881/ab480b.
- Cheng, W., M. H. Lee, and S. J. Peale (2014a). Complete Tidal Evolution of Pluto–Charon. *Icarus*, **233**, pp. 242–258. doi: 10.1016/j.icarus.2014.01.046.
- Cheng, W., S. J. Peale, and M. H. Lee (2014b). On the Origin of Pluto’s Small Satellites by Resonant Transport. *Icarus*, **241**, pp. 180–189. doi: 10.1016/j.icarus.2014.07.006.
- Chiang, E. and H. Choi (2008). The Warped Plane of the Classical Kuiper Belt. *Astronomical Journal*, **136**(1), pp. 350–357. doi: 10.1088/0004-6256/136/1/350.
- Chiang, E. I. and A. B. Jordan (2002). On the Plutinos and Twotinos of the Kuiper Belt. *The Astronomical Journal*, **124**(6), pp. 3430–3444. doi: 10.1086/344605.
- Chiang, E. I., A. B. Jordan, R. L. Millis, M. W. Buie, L. H. Wasserman, J. L. Elliot, S. D. Kern, D. E. Trilling, K. J. Meech, and R. M. Wagner (2003). Resonance Occupation in the Kuiper Belt: Case Examples of the 5:2 and Trojan Resonances. *The Astronomical Journal*, **126**(1), p. 430. doi: 10.1086/375207.
- Choudhary, A., J. F. Lindner, E. G. Holliday, S. T. Miller, S. Sinha, and W. L. Ditto (2019). Physics Enhanced Neural Networks Predict Order and Chaos. *arXiv:1912.01958 [physics]*.
- Clark, P. C., R. S. Klessen, and I. A. Bonnell (2007). Clump Lifetimes and the Initial Mass Function. *Monthly Notices of the Royal Astronomical Society*, **379**(1), pp. 57–62. doi: 10.1111/j.1365-2966.2007.11896.x.
- Cunningham, A. J., M. R. Krumholz, C. F. McKee, and R. I. Klein (2018). The Effects of Magnetic Fields and Protostellar Feedback on Low-Mass Cluster Formation. *Monthly Notices of the Royal Astronomical Society*, **476**(1), pp. 771–792. doi: 10.1093/mnras/sty154.
- De Souza Torres, K. and D. R. Anderson (2008). Symplectic Integrator Mercury: Bug Report.
- Demircan, O. and G. Kahraman (1991). Stellar Mass-Luminosity and Mass-Radius Relations. *Astrophysics and Space Science*, **181**(2), pp. 313–322. doi: 10.1007/BF00639097.
- Desch, S. J., J. C. Cook, T. Doggett, and S. B. Porter (2009). Thermal Evolution of Kuiper Belt Objects, with Implications for Cryovolcanism. *Icarus*, **202**(2), pp. 694–714. doi: 10.1016/j.icarus.2009.03.009.

- Dib, S., S. Schmeja, and S. Hony (2017). Massive Stars Reveal Variations of the Stellar Initial Mass Function in the Milky Way Stellar Clusters. *Monthly Notices of the Royal Astronomical Society*, **464**(2), pp. 1738–1752. doi: 10.1093/mnras/stw2465.
- Dobrovolskis, A. R. (1989). Dynamics of Pluto and Charon. *Geophysical Research Letters*, **16**(11), pp. 1217–1220. doi: 10.1029/GL016i011p01217.
- Dobrovolskis, A. R., S. J. Peale, and A. W. Harris (1997). Dynamics of the Pluto-Charon Binary. *Pluto and Charon. Edited by S. Alan Stern, and David J. Tholen; with the editorial assistance of A. S. Ruskin, M. L. Guerrieri and M. S. Matthews. Tucson: University of Arizona Press*, p. 159.
- Dones, L., R. Brasser, N. Kaib, and H. Rickman (2015). Origin and Evolution of the Cometary Reservoirs. *Space Science Reviews*, **197**(1-4), pp. 191–269. doi: 10.1007/s11214-015-0223-2.
- Doyle, L. R., J. A. Carter, D. C. Fabrycky, R. W. Slawson, S. B. Howell, J. N. Winn, J. A. Orosz, A. Prša, W. F. Welsh, S. N. Quinn, D. W. Latham, G. Torres, L. A. Buchhave, G. W. Marcy, J. J. Fortney, A. Shporer, E. B. Ford, J. J. Lissauer, D. Ragozzine, M. Rucker, N. M. Batalha, J. M. Jenkins, W. J. Borucki, D. G. Koch, C. K. Middelour, J. R. Hall, S. McCauliff, M. N. Fanelli, E. V. Quintana, M. J. Holman, D. A. Caldwell, M. Still, R. P. Stefanik, W. R. Brown, G. A. Esquerdo, S. Tang, G. Furesz, J. C. Geary, P. Berlind, M. L. Calkins, D. R. Short, J. H. Steffen, D. Sasselov, E. W. Dunham, W. D. Cochran, A. P. Boss, M. R. Haas, D. Buzasi, and D. A. Fischer (2011). Kepler-16: A Transiting Circumbinary Planet. *Science*, **333**(6049), pp. 1602–6. doi: 10.1126/science.1210923.
- Duchêne, G. and A. L. Kraus (2013). Stellar Multiplicity. *Annual Review of Astronomy and Astrophysics*, **51**(1), pp. 269–310. doi: 10.1146/annurev-astro-081710-102602.
- Dupuy, T. J., K. M. Kratter, A. L. Kraus, H. Isaacson, A. W. Mann, M. J. Ireland, A. W. Howard, and D. Huber (2016). Orbital Architectures of Planet-Hosting Binaries. I. Forming Five Small Planets in the Truncated Disk of Kepler-444A. *The Astrophysical Journal*, **817**(1), p. 80. doi: 10.3847/0004-637X/817/1/80.
- Elliot, J. L., S. D. Kern, K. B. Clancy, A. A. S. Gulbis, R. L. Millis, M. W. Buie, L. H. Wasserman, E. I. Chiang, A. B. Jordan, D. E. Trilling, and K. J. Meech (2005). The Deep Ecliptic Survey: A Search for Kuiper Belt Objects and Centaurs. II. Dynamical Classification, the Kuiper Belt Plane, and the Core Population. *Astronomical Journal*, **129**(2), pp. 1117–1162. doi: 10.1086/427395.
- Enoch, M. L., N. J. E. Li, A. I. Sargent, J. Glenn, E. Rosolowsky, and P. Myers (2008). The Mass Distribution and Lifetime of Prestellar Cores in Perseus,

- Serpens, and Ophiuchus. *The Astrophysical Journal*, **684**(2), p. 1240. doi: 10.1086/589963.
- Everhart, E. (1985). An Efficient Integrator That Uses Gauss-Radau Spacings. *Dynamics of Comets: Their Origin and Evolution*, **115**.
- Faber, P. and A. C. Quillen (2007). The Total Number of Giant Planets in Debris Discs with Central Clearings. *Monthly Notices of the Royal Astronomical Society*, **382**(4), pp. 1823–1828. doi: 10.1111/j.1365-2966.2007.12490.x.
- Fabrycky, D. C. and S. Tremaine (2007). Shrinking Binary and Planetary Orbits by Kozai Cycles with Tidal Friction. *The Astrophysical Journal*, **669**(2), pp. 1298–1315. doi: 10.1086/521702.
- Fang, J. and J.-L. Margot (2012a). Architecture of Planetary Systems Based on Kepler Data: Number of Planets and Coplanarity. *The Astrophysical Journal*, **761**(2), p. 92. doi: 10.1088/0004-637X/761/2/92.
- Fang, J. and J.-L. Margot (2012b). Predicting Planets in Kepler Multi-Planet Systems. *The Astrophysical Journal*, **751**(1), p. 23. doi: 10.1088/0004-637X/751/1/23.
- Fang, J. and J.-L. Margot (2013). Are Planetary Systems Filled to Capacity? A Study Based on Kepler Results. *The Astrophysical Journal*, **767**(2), p. 115. doi: 10.1088/0004-637X/767/2/115.
- Ferraz-Mello, S. (1994). Kirkwood Gaps and Resonant Groups. *Asteroids, Comets, Meteors 1993: Proceedings of the 160th Symposium of the International Astronomical Union*, **160**, p. 175.
- Flower, D. R., G. P. des Forêts, and C. M. Walmsley (2006). The Abundances of Nitrogen-Containing Molecules during Pre-Protostellar Collapse. *Astronomy & Astrophysics*, **456**(1), pp. 215–223. doi: 10.1051/0004-6361:20065375.
- Fraser, W. C., M. T. Bannister, R. E. Pike, M. Marsset, M. E. Schwamb, J. J. Kavelaars, P. Lacerda, D. Nesvorný, K. Volk, A. Delsanti, S. Benecchi, M. J. Lehner, K. Noll, B. Gladman, J.-M. Petit, S. Gwyn, Y.-T. Chen, S.-Y. Wang, M. Alexandersen, T. Burdullis, S. Sheppard, and C. Trujillo (2017). All Planetesimals Born Near the Kuiper Belt Formed as Binaries. *Nature Astronomy*, **1**(4), pp. 1–6. doi: 10.1038/s41550-017-0088.
- Fraser, W. C., M. E. Brown, A. Morbidelli, A. H. Parker, and K. Batygin (2014). The Absolute Magnitude Distribution of Kuiper Belt Objects. *The Astrophysical Journal*, **782**(2), p. 100. doi: 10.1088/0004-637X/782/2/100.

- Fressin, F., G. Torres, D. Charbonneau, S. T. Bryson, J. Christiansen, C. D. Dressing, J. M. Jenkins, L. M. Walkowicz, and N. M. Batalha (2013). The False Positive Rate of Kepler and the Occurrence of Planets. *The Astrophysical Journal*, **766**(2), p. 81. doi: 10.1088/0004-637X/766/2/81.
- Friesen, R. K., T. L. Bourke, J. D. Francesco, R. Gutermuth, and P. C. Myers (2016). The Fragmentation and Stability of Hierarchical Structure in Serpens South. *The Astrophysical Journal*, **833**(2), p. 204. doi: 10.3847/1538-4357/833/2/204.
- Gladman, B. (1993). Dynamics of Systems of Two Close Planets. *Icarus*, **106**(1), pp. 247–263. doi: 10.1006/icar.1993.1169.
- Gladman, B. and C. Chan (2006). Production of the Extended Scattered Disk by Rogue Planets. *Astrophysical Journal*, **643**(2), pp. L135–L138. doi: 10.1086/505214.
- Gladman, B., M. Holman, T. Grav, J. Kavelaars, P. Nicholson, K. Aksnes, and J. M. Petit (2002). Evidence for an Extended Scattered Disk. *Icarus*, **157**(2), pp. 269–279. doi: 10.1006/icar.2002.6860.
- Gladman, B., B. G. Marsden, and C. Vanlaerhoven (2008). Nomenclature in the Outer Solar System. In Barucci, M. A., Boehnhardt, H., Cruikshank, D. P., Morbidelli, A., & Dotson, R. (ed.) *The Solar System beyond Neptune*, pp. 43–57.
- Goldreich, P., N. W. Murray, P. Y. Longaretti, and D. Banfield (1989). Neptune’s Story. *Science*, **245**(4917).
- Gonzalez, G. (1997). The Stellar Metallicity–Giant Planet Connection. *Monthly Notices of the Royal Astronomical Society*, **285**(2), pp. 403–412. doi: 10.1093/mnras/285.2.403.
- Goodman, A. A., E. W. Rosolowsky, M. A. Borkin, J. B. Foster, M. Halle, J. Kauffmann, and J. E. Pineda (2009). A Role for Self-Gravity at Multiple Length Scales in the Process of Star Formation. *Nature*, **457**(7225), pp. 63–66. doi: 10.1038/nature07609.
- Götberg, Y., S. E. de Mink, M. McQuinn, E. Zapartas, J. H. Groh, and C. Norman (2020). Contribution from Stars Stripped in Binaries to Cosmic Reionization of Hydrogen and Helium. *Astronomy & Astrophysics*, **634**, p. A134. doi: 10.1051/0004-6361/201936669.
- Greenstreet, S., B. Gladman, and W. B. McKinnon (2015). Impact and Cratering Rates onto Pluto. *Icarus*, **258**, pp. 267–288. doi: 10.1016/j.icarus.2015.05.026.

- Grundy, W. M., K. S. Noll, H. G. Roe, M. W. Buie, S. B. Porter, A. H. Parker, D. Nesvorný, H. F. Levison, S. D. Benecchi, D. C. Stephens, and C. A. Trujillo (2019). Mutual Orbit Orientations of Transneptunian Binaries. *Icarus*, **334**, pp. 62–78. doi: 10.1016/j.icarus.2019.03.035.
- Guszejnov, D. and P. F. Hopkins (2015). Mapping the Core Mass Function to the Initial Mass Function. *Monthly Notices of the Royal Astronomical Society*, **450**(4), pp. 4137–4149. doi: 10.1093/mnras/stv872.
- Guszejnov, D., P. F. Hopkins, and M. R. Krumholz (2017). Protostellar Feedback in Turbulent Fragmentation: Consequences for Stellar Clustering and Multiplicity. *Monthly Notices of the Royal Astronomical Society*, **468**(4), pp. 4093–4106. doi: 10.1093/mnras/stx725.
- Hamers, A. S., H. B. Perets, and S. F. Portegies Zwart (2016). A Triple Origin for the Lack of Tight Coplanar Circumbinary Planets around Short-Period Binaries. *Monthly Notices of the Royal Astronomical Society*, **455**(3), pp. 3180–3200. doi: 10.1093/mnras/stv2447.
- Hands, T. O. and R. D. Alexander (2016). There Might Be Giants: Unseen Jupiter-Mass Planets as Sculptors of Tightly Packed Planetary Systems. *Monthly Notices of the Royal Astronomical Society*, **456**(4), pp. 4121–4127. doi: 10.1093/mnras/stv2897.
- Harris, R. J., S. M. Andrews, D. J. Wilner, and A. L. Kraus (2012). A Resolved Census of Millimeter Emission from Taurus Multiple Star Systems. *The Astrophysical Journal*, **751**(2), p. 115. doi: 10.1088/0004-637X/751/2/115.
- Hennebelle, P. (2012). Formation of Proto-Clusters and Star Formation within Clusters: Apparent Universality of the Initial Mass Function? *Astronomy & Astrophysics*, **545**, p. A147. doi: 10.1051/0004-6361/201219440.
- Hennebelle, P. and G. Chabrier (2008). Analytical Theory for the Initial Mass Function: CO Clumps and Prestellar Cores. *The Astrophysical Journal*, **684**(1), p. 395. doi: 10.1086/589916.
- Holman, M. J. and P. A. Wiegert (1999). Long-Term Stability of Planets in Binary Systems. *The Astronomical Journal*, **117**(1), pp. 621–628. doi: 10.1086/300695.
- Hopkins, P. F. (2013). Variations in the Stellar CMF and IMF: From Bottom to Top. *Monthly Notices of the Royal Astronomical Society*, **433**(1), pp. 170–177. doi: 10.1093/mnras/stt713.
- Houllahan, P. and J. Scalo (1992). Recognition and Characterization of Hierarchical Interstellar Structure. II - Structure Tree Statistics. *The Astrophysical Journal*, **393**, pp. 172–187. doi: 10.1086/171495.

Ivezić, Ž., S. M. Kahn, J. A. Tyson, B. Abel, E. Acosta, R. Allsman, D. Alonso, Y. AlSayyad, S. F. Anderson, J. Andrew, J. R. P. Angel, G. Z. Angeli, R. Ansari, P. Antilogus, C. Araujo, R. Armstrong, K. T. Arndt, P. Astier, É. Aubourg, N. Auza, T. S. Axelrod, D. J. Bard, J. D. Barr, A. Barrau, J. G. Bartlett, A. E. Bauer, B. J. Bauman, S. Baumont, E. Bechtol, K. Bechtol, A. C. Becker, J. Belda, C. Beldica, S. Bellavia, F. B. Bianco, R. Biswas, G. Blanc, J. Blazek, R. D. Blandford, J. S. Bloom, J. Bogart, T. W. Bond, M. T. Booth, A. W. Borgland, K. Borne, J. F. Bosch, D. Boutigny, C. A. Brackett, A. Bradshaw, W. N. Brandt, M. E. Brown, J. S. Bullock, P. Burchat, D. L. Burke, G. Cagnoli, D. Calabrese, S. Callahan, A. L. Callen, J. L. Carlin, E. L. Carlson, S. Chandrasekharan, G. Charles-Emerson, S. Chesley, E. C. Cheu, H.-F. Chiang, J. Chiang, C. Chirino, D. Chow, D. R. Ciardi, C. F. Claver, J. Cohen-Tanugi, J. J. Cockrum, R. Coles, A. J. Connolly, K. H. Cook, A. Cooray, K. R. Covey, C. Cribbs, W. Cui, R. Cutri, P. N. Daly, S. F. Daniel, F. Daruich, G. Daubard, G. Daues, W. Dawson, F. Delgado, A. Dellapenna, R. de Peyster, M. de Val-Borro, S. W. Digel, P. Doherty, R. Dubois, G. P. Dubois-Felsmann, J. Durech, F. Economou, T. Eifler, M. Eracleous, B. L. Emmons, A. F. Neto, H. Ferguson, E. Figueroa, M. Fisher-Levine, W. Focke, M. D. Foss, J. Frank, M. D. Freemon, E. Gangler, E. Gawiser, J. C. Geary, P. Gee, M. Geha, C. J. B. Gessner, R. R. Gibson, D. K. Gilmore, T. Glanzman, W. Glick, T. Goldina, D. A. Goldstein, I. Goodenow, M. L. Graham, W. J. Gressler, P. Gris, L. P. Guy, A. Guyonnet, G. Haller, R. Harris, P. A. Hascall, J. Haupt, F. Hernandez, S. Herrmann, E. Hileman, J. Hoblitt, J. A. Hodgson, C. Hogan, J. D. Howard, D. Huang, M. E. Huffer, P. Ingraham, W. R. Innes, S. H. Jacoby, B. Jain, F. Jammes, J. Jee, T. Jenness, G. Jernigan, D. Jevremović, K. Johns, A. S. Johnson, M. W. G. Johnson, R. L. Jones, C. Juramy-Gilles, M. Jurić, J. S. Kalirai, N. J. Kallivayalil, B. Kalmbach, J. P. Kantor, P. Karst, M. M. Kasliwal, H. Kelly, R. Kessler, V. Kinnison, D. Kirkby, L. Knox, I. V. Kotov, V. L. Krabbendam, K. S. Krughoff, P. Kubánek, J. Kuczewski, S. Kulkarni, J. Ku, N. R. Kurita, C. S. Lage, R. Lambert, T. Lange, J. B. Langton, L. L. Guillou, D. Levine, M. Liang, K.-T. Lim, C. J. Lintott, K. E. Long, M. Lopez, P. J. Lotz, R. H. Lupton, N. B. Lust, L. A. MacArthur, A. Mahabal, R. Mandelbaum, T. W. Markiewicz, D. S. Marsh, P. J. Marshall, S. Marshall, M. May, R. McKercher, M. McQueen, J. Meyers, M. Migliore, M. Miller, D. J. Mills, C. Miraval, J. Moeyens, F. E. Moolekamp, D. G. Monet, M. Moniez, S. Monke-witz, C. Montgomery, C. B. Morrison, F. Mueller, G. P. Muller, F. M. Arancibia, D. R. Neill, S. P. Newbry, J.-Y. Nief, A. Nomerotski, M. Nordby, P. O'Connor, J. Oliver, S. S. Olivier, K. Olsen, W. O'Mullane, S. Ortiz, S. Osier, R. E. Owen, R. Pain, P. E. Palecek, J. K. Parejko, J. B. Parsons, N. M. Pease, J. M. Peterson, J. R. Peterson, D. L. Petravick, M. E. L. Petrick, C. E. Petry, F. Pierfederici, S. Pietrowicz, R. Pike, P. A. Pinto, R. Plante, S. Plate, J. P. Plutchak, P. A. Price, M. Prouza, V. Radeka, J. Rajagopal, A. P. Rasmussen, N. Regnault, K. A. Reil, D. J. Reiss, M. A. Reuter, S. T. Ridgway, V. J. Riot, S. Ritz, S. Robin-

- son, W. Roby, A. Roodman, W. Rosing, C. Roucelle, M. R. Rumore, S. Russo, A. Saha, B. Sassolas, T. L. Schalk, P. Schellart, R. H. Schindler, S. Schmidt, D. P. Schneider, M. D. Schneider, W. Schoening, G. Schumacher, M. E. Schwamb, J. Sebag, B. Selvy, G. H. Sembroski, L. G. Seppala, A. Serio, E. Serrano, R. A. Shaw, I. Shipsey, J. Sick, N. Silvestri, C. T. Slater, J. A. Smith, R. C. Smith, S. Sobhani, C. Soldahl, L. Storrie-Lombardi, E. Stover, M. A. Strauss, R. A. Street, C. W. Stubbs, I. S. Sullivan, D. Sweeney, J. D. Swinbank, A. Szalay, P. Takacs, S. A. Tether, J. J. Thaler, J. G. Thayer, S. Thomas, A. J. Thornton, V. Thukral, J. Tice, D. E. Trilling, M. Turri, R. V. Berg, D. V. Berk, K. Vetter, F. Virieux, T. Vucina, W. Wahl, L. Walkowicz, B. Walsh, C. W. Walter, D. L. Wang, S.-Y. Wang, M. Warner, O. Wiecha, B. Willman, S. E. Winters, D. Wittman, S. C. Wolff, W. M. Wood-Vasey, X. Wu, B. Xin, P. Yoachim, and H. Zhan (2019). LSST: From Science Drivers to Reference Design and Anticipated Data Products. *The Astrophysical Journal*, **873**(2), p. 111. doi: 10.3847/1538-4357/ab042c.
- Jackson, B., R. Barnes, and R. Greenberg (2008). Tidal Heating of Terrestrial Extrasolar Planets and Implications for Their Habitability. *Monthly Notices of the Royal Astronomical Society*, **391**(1), pp. 237–245. doi: 10.1111/j.1365-2966.2008.13868.x.
- Jurić, M. and S. Tremaine (2008). Dynamical Origin of Extrasolar Planet Eccentricity Distribution. *The Astrophysical Journal*, **686**(1), pp. 603–620. doi: 10.1086/590047.
- Kaib, N. A., R. Roškar, and T. Quinn (2011). Sedna and the Oort Cloud Around a Migrating Sun. *Icarus*, **215**(2), pp. 491–507. doi: 10.1016/j.icarus.2011.07.037.
- Kenyon, S. J. and B. C. Bromley (2014). The Formation of Pluto’s Low-Mass Satellites. *The Astronomical Journal*, **147**(1), p. 8. doi: 10.1088/0004-6256/147/1/8.
- Keown, J., J. D. Francesco, H. Kirk, R. K. Friesen, J. E. Pineda, E. Rosolowsky, A. Ginsburg, S. S. R. Offner, P. Caselli, F. Alves, A. Chacón-Tanarro, A. Punanova, E. Redaelli, Y. M. Seo, C. D. Matzner, M. C.-Y. Chen, A. A. Goodman, H.-H. Chen, Y. Shirley, A. Singh, H. G. Arce, P. Martin, and P. C. Myers (2017). The Green Bank Ammonia Survey: Observations of Hierarchical Dense Gas Structures in Cepheus-L1251. *The Astrophysical Journal*, **850**(1), p. 3. doi: 10.3847/1538-4357/aa93ec.
- Kirk, H., R. K. Friesen, J. E. Pineda, E. Rosolowsky, S. S. R. Offner, C. D. Matzner, P. C. Myers, J. D. Francesco, P. Caselli, F. O. Alves, A. Chacón-Tanarro, H.-H. Chen, M. C.-Y. Chen, J. Keown, A. Punanova, Y. M. Seo, Y. Shirley, A. Ginsburg, C. Hall, A. Singh, H. G. Arce, A. A. Goodman, P. Martin, and E. Redaelli (2017).

- The Green Bank Ammonia Survey: Dense Cores Under Pressure in Orion A. *The Astrophysical Journal*, **846**(2), p. 144. doi: 10.3847/1538-4357/aa8631.
- Klein, R. I. (1999). Star Formation with 3-D Adaptive Mesh Refinement: The Collapse and Fragmentation of Molecular Clouds. *Journal of Computational and Applied Mathematics*, **109**(1), pp. 123–152. doi: 10.1016/S0377-0427(99)00156-9.
- Koch, E. W., E. W. Rosolowsky, R. D. Boyden, B. Burkhart, A. Ginsburg, J. L. Loeppky, and S. S. R. Offner (2019). TurbuStat: Turbulence Statistics in Python. *The Astronomical Journal*, **158**(1), p. 1. doi: 10.3847/1538-3881/ab1cc0.
- Koch, E. W., C. G. Ward, S. Offner, J. L. Loeppky, and E. W. Rosolowsky (2017). Identifying Tools for Comparing Simulations and Observations of Spectral-Line Data Cubes. *Monthly Notices of the Royal Astronomical Society*, **471**(2), pp. 1506–1530. doi: 10.1093/mnras/stx1671.
- Kochanek, C. S. (2009). Stellar Binary Companions to Supernova Progenitors. *The Astrophysical Journal*, **707**, pp. 1578–1587. doi: 10.1088/0004-637X/707/2/1578.
- Könyves, V., P. André, A. Men’shchikov, P. Palmeirim, D. Arzoumanian, N. Schneider, A. Roy, P. Didelon, A. Maury, Y. Shimajiri, J. D. Francesco, S. Bontemps, N. Peretto, M. Benedettini, J.-P. Bernard, D. Elia, M. J. Griffin, T. Hill, J. Kirk, B. Ladjelate, K. Marsh, P. G. Martin, F. Motte, Q. N. Luong, S. Pezzuto, H. Rousset, K. L. J. Rygl, S. I. Sadavoy, E. Schisano, L. Spinoglio, D. Ward-Thompson, and G. J. White (2015). A Census of Dense Cores in the Aquila Cloud Complex: SPIRE/PACS Observations from the Herschel Gould Belt Survey. *Astronomy & Astrophysics*, **584**, p. A91. doi: 10.1051/0004-6361/201525861.
- Kratter, K. M., R. A. Murray-Clay, and A. N. Youdin (2010). The Runts of the Litter: Why Planets Formed Through Gravitational Instability Can Only Be Failed Binary Stars. *The Astrophysical Journal*, **710**(2), pp. 1375–1386. doi: 10.1088/0004-637X/710/2/1375.
- Kratter, K. M. and H. B. Perets (2012). Star Hoppers: Planet Instability and Capture in Evolving Binary Systems. *The Astrophysical Journal*, **753**(1), p. 91. doi: 10.1088/0004-637X/753/1/91.
- Kratter, K. M. and A. Shannon (2014). Planet Packing in Circumbinary Systems. *Monthly Notices of the Royal Astronomical Society*, **437**(4), pp. 3727–3735. doi: 10.1093/mnras/stt2179.
- Kraus, A. L., M. J. Ireland, L. A. Hillenbrand, and F. Martinache (2011). The Role of Multiplicity in Disk Evolution and Planet Formation. *The Astrophysical Journal*, **745**(1), p. 19. doi: 10.1088/0004-637X/745/1/19.

- Krumholz, M. R., R. I. Klein, C. F. McKee, and J. Bolstad (2007). Equations and Algorithms for Mixed-Frame Flux-Limited Diffusion Radiation Hydrodynamics. *The Astrophysical Journal*, **667**(1), p. 626. doi: 10.1086/520791.
- Krumholz, M. R., C. F. McKee, and R. I. Klein (2004). Embedding Lagrangian Sink Particles in Eulerian Grids. *The Astrophysical Journal*, **611**(1), pp. 399–412. doi: 10.1086/421935.
- Lam, C. and D. Kipping (2018). A Machine Learns to Predict the Stability of Circumbinary Planets. *Monthly Notices of the Royal Astronomical Society*, **476**(4), pp. 5692–5697. doi: 10.1093/mnras/sty022.
- Laughlin, G. and F. C. Adams (1997). Possible Stellar Metallicity Enhancements from the Accretion of Planets. *The Astrophysical Journal*, **491**(1), pp. L51–L54. doi: 10.1086/311056.
- Lawler, S. M., R. E. Pike, N. Kaib, M. Alexandersen, M. T. Bannister, Y. T. Chen, B. Gladman, S. Gwyn, J. J. Kavelaars, J. M. Petit, and K. Volk (2019). OSSOS. XIII. Fossilized Resonant Dropouts Tentatively Confirm Neptunes Migration Was Grainy and Slow. *Astronomical Journal*, **157**(6), p. 253. doi: 10.3847/1538-3881/ab1c4c.
- Lee, A. T., A. J. Cunningham, C. F. McKee, and R. I. Klein (2014a). Bondi-Hoyle Accretion in an Isothermal Magnetized Plasma. *The Astrophysical Journal*, **783**(1), p. 50. doi: 10.1088/0004-637X/783/1/50.
- Lee, A. T., S. S. R. Offner, K. M. Kratter, R. A. Smullen, and P. S. Li (2019). The Formation and Evolution of Wide-Orbit Stellar Multiples In Magnetized Clouds. *The Astrophysical Journal*, **887**(2), p. 232. doi: 10.3847/1538-4357/ab584b.
- Lee, K. I., M. Fernández-López, S. Storm, L. W. Looney, L. G. Mundy, D. Segura-Cox, P. Teuben, E. Rosolowsky, H. G. Arce, E. C. Ostriker, Y. L. Shirley, W. Kwon, J. Kauffmann, J. J. Tobin, A. L. Plunkett, M. W. Pound, D. M. Salter, N. H. Volgenau, C.-Y. Chen, K. Tassis, A. Isella, R. M. Crutcher, C. F. Gammie, and L. Testi (2014b). Carma Large Area Star Formation Survey: Structure and Kinematics of Dense Gas in Serpens Main. *The Astrophysical Journal*, **797**(2), p. 76. doi: 10.1088/0004-637X/797/2/76.
- Lee, Y.-N., P. Hennebelle, and G. Chabrier (2017). Analytical Core Mass Function (CMF) from Filaments: Under Which Circumstances Can Filament Fragmentation Reproduce the CMF? *The Astrophysical Journal*, **847**(2), p. 114. doi: 10.3847/1538-4357/aa898f.

- Leinhardt, Z. M., R. A. Marcus, and S. T. Stewart (2010). The Formation of the Collisional Family Around the Dwarf Planet Haumea. *The Astrophysical Journal*, **714**(2), pp. 1789–1799. doi: 10.1088/0004-637X/714/2/1789.
- Leung, G. C. K. and M. H. Lee (2013). An Analytic Theory for the Orbits of Circumbinary Planets. *The Astrophysical Journal*, **763**(2), p. 107. doi: 10.1088/0004-637X/763/2/107.
- Levison, H. F. and M. J. Duncan (1994). The Long-Term Dynamical Behavior of Short-Period Comets. *Icarus*, **108**(1), pp. 18–36. doi: 10.1006/icar.1994.1039.
- Levison, H. F., A. Morbidelli, C. Van Laerhoven, R. Gomes, and K. Tsiganis (2008). Origin of the Structure of the Kuiper Belt during a Dynamical Instability in the Orbits of Uranus and Neptune. *Icarus*, **196**(1), pp. 258–273. doi: 10.1016/j.icarus.2007.11.035.
- Li, C., H.-c. Wang, Y.-w. Wu, Y.-h. Ma, and L.-h. Lin (2019). Assessing the Performance of Molecular Gas Clump Identification Algorithms. *arXiv e-prints*, p. arXiv:1910.07692.
- Li, P. S., D. F. Martin, R. I. Klein, and C. F. McKee (2012). A Stable, Accurate Methodology for High Mach Number, Strong Magnetic Field MHD Turbulence with Adaptive Mesh Refinement: Resolution and Refinement Studies. *The Astrophysical Journal*, **745**(2), p. 139. doi: 10.1088/0004-637X/745/2/139.
- Li, P. S., M. L. Norman, M.-M. M. Low, and F. Heitsch (2004). The Formation of Self-Gravitating Cores in Turbulent Magnetized Clouds. *The Astrophysical Journal*, **605**(2), pp. 800–818. doi: 10.1086/382652.
- Lissauer, J. J., D. C. Fabrycky, E. B. Ford, W. J. Borucki, F. Fressin, G. W. Marcy, J. A. Orosz, J. F. Rowe, G. Torres, W. F. Welsh, N. M. Batalha, S. T. Bryson, L. A. Buchhave, D. A. Caldwell, J. A. Carter, D. Charbonneau, J. L. Christiansen, W. D. Cochran, J.-M. Desert, E. W. Dunham, M. N. Fanelli, J. J. Fortney, T. N. Gautier, III, J. C. Geary, R. L. Gilliland, M. R. Haas, J. R. Hall, M. J. Holman, D. G. Koch, D. W. Latham, E. Lopez, S. McCauliff, N. Miller, R. C. Morehead, E. V. Quintana, D. Ragozzine, D. Sasselov, D. R. Short, and J. H. Steffen (2011a). A Closely Packed System of Low-Mass, Low-Density Planets Transiting Kepler-11. *Nature*, **470**, pp. 53–58. doi: 10.1038/nature09760.
- Lissauer, J. J., D. Ragozzine, D. C. Fabrycky, J. H. Steffen, E. B. Ford, J. M. Jenkins, A. Shporer, M. J. Holman, J. F. Rowe, E. V. Quintana, N. M. Batalha, W. J. Borucki, S. T. Bryson, D. A. Caldwell, J. A. Carter, D. R. Ciardi, E. W. Dunham, J. J. Fortney, T. N. Gautier, S. B. Howell, D. G. Koch, D. W. Latham, G. W. Marcy, R. C. Morehead, and D. Sasselov (2011b). Architecture and Dynamics

- of Kepler's Candidate Multiple Transiting Planet Systems. *The Astrophysical Journal Supplement Series*, **197**(1), p. 8. doi: 10.1088/0067-0049/197/1/8.
- Lithwick, Y. and Y. Wu (2008a). The Effect of Charon's Tidal Damping on the Orbits of Pluto's Three Moons. p. 12.
- Lithwick, Y. and Y. Wu (2008b). On the Origin of Pluto's Minor Moons, Nix and Hydra. p. 11.
- Long, F., G. J. Herczeg, D. Harsono, P. Pinilla, M. Tazzari, C. F. Manara, I. Pascucci, S. Cabrit, B. Nisini, D. Johnstone, S. Edwards, C. Salyk, F. Menard, G. Lodato, Y. Boehler, G. N. Mace, Y. Liu, G. D. Mulders, N. Hendler, E. Ragusa, W. J. Fischer, A. Banzatti, E. Rigliaco, G. van de Plas, G. Dipierro, M. Gully-Santiago, and R. Lopez-Valdivia (2019). Compact Disks in a High-Resolution ALMA Survey of Dust Structures in the Taurus Molecular Cloud. *The Astrophysical Journal*, **882**, p. 49. doi: 10.3847/1538-4357/ab2d2d.
- Luger, R., M. Sestovic, E. Kruse, S. L. Grimm, B.-O. Demory, E. Agol, E. Bolmont, D. Fabrycky, C. S. Fernandes, V. Van Grootel, A. Burgasser, M. Gillon, J. G. Ingalls, E. Jehin, S. N. Raymond, F. Selsis, A. H. M. J. Triaud, T. Barclay, G. Barentsen, S. B. Howell, L. Delrez, J. de Wit, D. Foreman-Mackey, D. L. Holdsworth, J. Leconte, S. Lederer, M. Turbet, Y. Almléaky, Z. Benkhaldoun, P. Magain, B. M. Morris, K. Heng, and D. Queloz (2017). A Seven-Planet Resonant Chain in TRAPPIST-1. *Nature Astronomy*, **1**(6), pp. 1–8. doi: 10.1038/s41550-017-0129.
- Lykawka, P. S. and T. Mukai (2007). Resonance Sticking in the Scattered Disk. *Icarus*, **192**(1), pp. 238–247. doi: 10.1016/j.icarus.2007.06.007.
- Mac Low, M.-M. (1999). The Energy Dissipation Rate of Supersonic, Magnetohydrodynamic Turbulence in Molecular Clouds. **524**(1), pp. 169–178. doi: 10.1086/307784.
- Machida, M. N., K. Tomisaka, T. Matsumoto, and S.-i. Inutsuka (2008). Formation Scenario for Wide and Close Binary Systems. *The Astrophysical Journal*, **677**, pp. 327–347. doi: 10.1086/529133.
- Mack, C. E., S. C. Schuler, K. G. Stassun, and J. Norris (2014). Detailed Abundances of Planet-Hosting Wide Binaries. I. Did Planet Formation Imprint Chemical Signatures in the Atmospheres of HD 20782/81? *The Astrophysical Journal*, **787**(2), p. 98. doi: 10.1088/0004-637X/787/2/98.
- Madau, P. and T. Fragos (2017). Radiation Backgrounds at Cosmic Dawn: X-Rays from Compact Binaries. *The Astrophysical Journal*, **840**(1), p. 39. doi: 10.3847/1538-4357/aa6af9.

- Mairs, S., D. Johnstone, S. S. R. Offner, and S. Schnee (2014). Synthetic Observations of the Evolution of Starless Cores in a Molecular Cloud Simulation: Comparisons with JCMT Data and Predictions for ALMA. *The Astrophysical Journal*, **783**(1), p. 60. doi: 10.1088/0004-637X/783/1/60.
- Malhotra, R. (1995a). The Origin of Pluto’s Orbit: Implications for the Solar System Beyond Neptune. *The Astronomical Journal*, **110**, p. 420. doi: 10.1086/117532.
- Malhotra, R. (1995b). The Origin of Pluto’s Peculiar Orbit. *Nature*, **365**(6449), pp. 819–821. doi: 10.1038/365819a0.
- Malhotra, R. (1996). The Phase Space Structure Near Neptune Resonances in the Kuiper Belt. *The Astronomical Journal*, **111**, p. 504. doi: 10.1086/117802.
- Malhotra, R. (2015). The Mass Distribution Function of Planets. *The Astrophysical Journal*, **808**(1), p. 71. doi: 10.1088/0004-637X/808/1/71.
- Malhotra, R. (2019). Resonant Kuiper Belt Objects: A Review. *Geoscience Letters*, **6**(1), p. 12. doi: 10.1186/s40562-019-0142-2.
- Mao, S. A., E. C. Ostriker, and C.-G. Kim (2019). Cloud Properties and Correlations with Star Formation in Numerical Simulations of the Three-Phase ISM. *arXiv:1911.05078*.
- Marcus, R. A., D. Ragozzine, R. A. Murray-Clay, and M. J. Holman (2011). Identifying Collisional Families in the Kuiper Belt. *The Astrophysical Journal*, **733**(1), p. 40. doi: 10.1088/0004-637X/733/1/40.
- Martin, D. V. (2017). Circumbinary Planets - II. When Transits Come and Go. *Monthly Notices of the Royal Astronomical Society*, **465**, pp. 3235–3253. doi: 10.1093/mnras/stw2851.
- Martin, D. V., T. Mazeh, and D. C. Fabrycky (2015). No Circumbinary Planets Transiting the Tightest Kepler Binaries – a Possible Fingerprint of a Third Star. *Monthly Notices of the Royal Astronomical Society*, **453**(4), pp. 3554–3567. doi: 10.1093/mnras/stv1870.
- Martin, D. V. and A. H. M. J. Triaud (2014). Planets Transiting Non-Eclipsing Binaries. *Astronomy & Astrophysics*, **570**, p. A91. doi: 10.1051/0004-6361/201323112.
- Martin, D. V. and A. H. M. J. Triaud (2015). Circumbinary Planets - Why They Are so Likely to Transit. *Monthly Notices of the Royal Astronomical Society*, **449**(1), pp. 781–793. doi: 10.1093/mnras/stv121.

- Martin, R. G., P. J. Armitage, and R. D. Alexander (2013). Formation of Circumbinary Planets in a Dead Zone. *The Astrophysical Journal*, **773**(1), p. 74. doi: 10.1088/0004-637X/773/1/74.
- Martin, R. G., C. Nixon, S. H. Lubow, P. J. Armitage, D. J. Price, S. Doğan, and A. King (2014). The Kozai-Lidov Mechanism in Hydrodynamical Disks. *The Astrophysical Journal*, **792**(2), p. L33. doi: 10.1088/2041-8205/792/2/L33.
- Marzari, F., P. Thebault, H. Scholl, G. Picogna, and C. Baruteau (2013). Influence of the Circumbinary Disk Gravity on Planetesimal Accumulation in the Kepler-16 System. *Astronomy & Astrophysics*, **553**, p. A71. doi: 10.1051/0004-6361/201220893.
- Massi, F., A. Weiss, D. Elia, T. Csengeri, E. Schisano, T. Giannini, T. Hill, D. Lorenzetti, K. Menten, L. Olmi, F. Schuller, F. Strafella, M. D. Luca, F. Motte, and F. Wyrowski (2019). Dense Cores and Star Formation in the Giant Molecular Cloud Vela C. *Astronomy & Astrophysics*, **628**, p. A110. doi: 10.1051/0004-6361/201935047.
- Masunaga, H., S. M. Miyama, and S.-i. Inutsuka (1998). A Radiation Hydrodynamic Model for Protostellar Collapse. I. The First Collapse. **495**(1), pp. 346–369. doi: 10.1086/305281.
- Mazeh, T. and J. Shaham (1979). The Orbital Evolution of Close Triple Systems - The Binary Eccentricity. *Astronomy and Astrophysics*, **77**, pp. 145–151.
- McKinnon, W. B. (1989). On the Origin of the Pluto-Charon Binary. *The Astrophysical Journal Letters*, **344**, pp. L41–L44. doi: 10.1086/185526.
- McKinnon, W. B., D. C. Richardson, J. C. Marohnic, J. T. Keane, W. M. Grundy, D. P. Hamilton, D. Nesvorný, O. M. Umurhan, T. R. Lauer, K. N. Singer, S. A. Stern, H. A. Weaver, J. R. Spencer, M. W. Buie, J. M. Moore, J. J. Kavelaars, C. M. Lisse, X. Mao, A. H. Parker, S. B. Porter, M. R. Showalter, C. B. Olkin, D. P. Cruikshank, H. A. Elliott, G. R. Gladstone, J. W. Parker, A. J. Verbiscer, L. A. Young, and New Horizons Science Team (2020). The Solar Nebula Origin of (486958) Arrokoth, a Primordial Contact Binary in the Kuiper Belt. *Science*, **367**(6481), p. aay6620. doi: 10.1126/science.aay6620.
- McLeod, M., N. Libeskind, O. Lahav, and Y. Hoffman (2017). Estimating the Mass of the Local Group Using Machine Learning Applied to Numerical Simulations. *Journal of Cosmology and Astroparticle Physics*, **2017**(12), pp. 034–034. doi: 10.1088/1475-7516/2017/12/034.

- Moe, M. and K. M. Kratter (2019). Impact of Binary Stars on Planet Statistics – I. Planet Occurrence Rates, Trends with Stellar Mass, and Wide Companions to Hot Jupiter Hosts. *arXiv e-prints*, **1912**, p. arXiv:1912.01699.
- Moe, M., K. M. Kratter, and C. Badenes (2019). The Close Binary Fraction of Solar-Type Stars Is Strongly Anticorrelated with Metallicity. *The Astrophysical Journal*, **875**, p. 61. doi: 10.3847/1538-4357/ab0d88.
- Moeckel, N. and D. Veras (2012). Exoplanets Bouncing between Binary Stars. *Monthly Notices of the Royal Astronomical Society*, **422**(1), pp. 831–840. doi: 10.1111/j.1365-2966.2012.20665.x.
- Molinari, S., E. Schisano, F. Faustini, M. Pestalozzi, A. M. di Giorgio, and S. Liu (2011). Source Extraction and Photometry for the Far-Infrared and Sub-Millimeter Continuum in the Presence of Complex Backgrounds. *Astronomy and Astrophysics*, **530**, p. A133. doi: 10.1051/0004-6361/201014752.
- Monteux, J., H. Amit, G. Choblet, B. Langlais, and G. Tobie (2015). Giant Impacts, Heterogeneous Mantle Heating and a Past Hemispheric Dynamo on Mars. *Physics of the Earth and Planetary Interiors*, **240**, pp. 114–124. doi: 10.1016/j.pepi.2014.12.005.
- Moore, J. M., E. Asphaug, M. J. Belton, B. Bierhaus, H. Breneman, S. M. Brooks, C. R. Chapman, F. C. Chuang, G. C. Collins, B. Giese, R. Greeley, J. W. Head, S. Kadel, K. P. Klaasen, J. E. Klemaszewski, K. P. Magee, J. Moreau, D. Morrison, G. Neukum, R. T. Pappalardo, C. B. Phillips, P. M. Schenk, D. A. Senske, R. J. Sullivan, E. P. Turtle, and K. K. Williams (2001). Impact Features on Europa: Results of the Galileo Europa Mission (GEM). *Icarus*, **151**(1), pp. 93–111. doi: 10.1006/icar.2000.6558.
- Moore, J. M., E. Asphaug, R. J. Sullivan, J. E. Klemaszewski, K. C. Bender, R. Greeley, P. E. Geissler, A. S. McEwen, E. P. Turtle, C. B. Phillips, B. Tufts, J. W. Head, R. T. Pappalardo, K. B. Jones, C. R. Chapman, M. J. Belton, R. L. Kirk, and D. Morrison (1998). Large Impact Features on Europa: Results of the Galileo Nominal Mission. *Icarus*, **135**(1), pp. 127–145. doi: 10.1006/icar.1998.5973.
- Moore, J. M., W. B. McKinnon, J. R. Spencer, A. D. Howard, P. M. Schenk, R. A. Beyer, F. Nimmo, K. N. Singer, O. M. Umurhan, O. L. White, S. A. Stern, K. Ennico, C. B. Olkin, H. A. Weaver, L. A. Young, R. P. Binzel, M. W. Buie, B. J. Buratti, A. F. Cheng, D. P. Cruikshank, W. M. Grundy, I. R. Linscott, H. J. Reitsema, D. C. Reuter, M. R. Showalter, V. J. Bray, C. L. Chavez, C. J. A. Howett, T. R. Lauer, C. M. Lisse, A. H. Parker, S. B. Porter, S. J. Robbins, K. Runyon, T. Stryk, H. B. Throop, C. C. C. Tsang, A. J. Verbiscer, A. M. Zangari, A. L. Chaikin, D. E. Wilhelms, and N. H. S. New Horizons Science Team

- (2016). The Geology of Pluto and Charon through the Eyes of New Horizons. *Science (New York, N.Y.)*, **351**(6279), pp. 1284–93. doi: 10.1126/science.aad7055.
- Morbidelli, A., H. F. Levison, and R. Gomes (2008). The Dynamical Structure of the Kuiper Belt and Its Primordial Origin. In Barucci, M. A., Boehnhardt, H., Cruikshank, D. P., Morbidelli, A., & Dotson, R. (ed.) *The Solar System beyond Neptune*, pp. 275–292.
- Morbidelli, A. and M. Moons (1993). Secular Resonances in Mean Motion Commensurabilities: The 2/1 and 3/2 Cases. *Icarus*, **102**(2), pp. 316–332. doi: 10.1006/icar.1993.1052.
- Mordasini, C., Y. Alibert, and W. Benz (2009a). Extrasolar Planet Population Synthesis I. Method, Formation Tracks, and Mass-Distance Distribution. *Astronomy and Astrophysics*, **501**(3), pp. 1139–1160. doi: 10.1051/0004-6361/200810301.
- Mordasini, C., Y. Alibert, W. Benz, and D. Naef (2009b). Extrasolar Planet Population Synthesis II: Statistical Comparison with Observation. *Astronomy & Astrophysics*, **501**(3), pp. 1161–1184. doi: 10.1051/0004-6361/200810697.
- Morrison, S. and R. Malhotra (2015). Planetary Chaotic Zone Clearing: Destinations and Timescales. *The Astrophysical Journal*, **799**(1), p. 41. doi: 10.1088/0004-637X/799/1/41.
- Morrison, S. J. and K. M. Kratter (2016). Orbital Stability of Multi-Planet Systems: Behavior at High Masses. *The Astrophysical Journal*, **823**(2), p. 118. doi: 10.3847/0004-637X/823/2/118.
- Morton, T. D. and J. Swift (2014). The Radius Distribution of Planets Around Cool Stars. *The Astrophysical Journal*, **791**(1), p. 10. doi: 10.1088/0004-637X/791/1/10.
- Mouschovias, T. C. and L. Spitzer (1976). Note on the Collapse of Magnetic Interstellar Clouds. *The Astrophysical Journal*, **210**, p. 326. doi: 10.1086/154835.
- Mudryk, L. R. and Y. Wu (2006). Resonance Overlap Is Responsible for Ejecting Planets in Binary Systems. *The Astrophysical Journal*, **639**(1), pp. 423–431. doi: 10.1086/499347.
- Muñoz, D. J. and D. Lai (2015). Survival of Planets Around Shrinking Stellar Binaries. *Proceedings of the National Academy of Sciences of the United States of America*, **112**(30), p. 10. doi: 10.1073/pnas.1505671112.
- Murray, C. D. and S. F. Dermott (1999). *Solar System Dynamics*. Cambridge, UK. ISBN 0-521-57597-4.

- Mustill, A. J., D. Veras, and E. Villaver (2014). Long-Term Evolution of Three-Planet Systems to the Post-Main Sequence and Beyond. *Monthly Notices of the Royal Astronomical Society*, **437**(2), pp. 1404–1419. doi: 10.1093/mnras/stt1973.
- Naoz, S., W. M. Farr, and F. A. Rasio (2012). On the Formation of Hot Jupiters in Stellar Binaries. *The Astrophysical Journal Letters*, **754**, p. L36. doi: 10.1088/2041-8205/754/2/L36.
- Nayak, O., M. Meixner, Y. Fukui, K. Tachihara, T. Onishi, K. Saigo, K. Tokuda, and R. Harada (2018). Molecular Cloud Structures and Massive Star Formation in N159. *The Astrophysical Journal*, **854**(2), p. 154. doi: 10.3847/1538-4357/aaab5f.
- Nesvorný, D. (2015). Evidence for Slow Migration of Neptune from the Inclination Distribution of Kuiper Belt Objects. *Astronomical Journal*, **150**(3), p. 73. doi: 10.1088/0004-6256/150/3/73.
- Nesvorný, D., R. Li, A. N. Youdin, J. B. Simon, and W. M. Grundy (2019a). Trans-Neptunian Binaries as Evidence for Planetesimal Formation by the Streaming Instability. *Nature Astronomy*, **3**, pp. 808–812. doi: 10.1038/s41550-019-0806-z.
- Nesvorný, D., R. Li, A. N. Youdin, J. B. Simon, and W. M. Grundy (2019b). Trans-Neptunian Binaries as Evidence for Planetesimal Formation by the Streaming Instability. *Nature Astronomy*, **3**(9), pp. 808–812. doi: 10.1038/s41550-019-0806-z.
- Neveu, M., S. J. Desch, E. Shock, and C. Glein (2015). Prerequisites for Explosive Cryovolcanism on Dwarf Planet-Class Kuiper Belt Objects. *Icarus*, **246**, pp. 48–64. doi: 10.1016/j.icarus.2014.03.043.
- Nord, B., A. J. Connolly, J. Kinney, J. Kubica, G. Narayan, J. E. G. Peek, C. Schafer, and E. J. Tollerud (2019). Algorithms and Statistical Models for Scientific Discovery in the Petabyte Era. **51**, p. 224.
- Ntormousi, E. and P. Hennebelle (2019). Core and Stellar Mass Functions in Massive Collapsing Filaments. *Astronomy & Astrophysics*, **625**, p. A82. doi: 10.1051/0004-6361/201834094.
- Offner, S. S. R. and H. G. Arce (2015). Impact of Winds from Intermediate-Mass Stars on Molecular Cloud Structure and Turbulence. **811**, p. 146. doi: 10.1088/0004-637X/811/2/146.
- Offner, S. S. R., J. Capodilupo, S. Schnee, and A. A. Goodman (2012). Observing Turbulent Fragmentation in Simulations: Predictions for CARMA and ALMA. *Monthly Notices of the Royal Astronomical Society: Letters*, **420**(1), pp. L53–L57. doi: 10.1111/j.1745-3933.2011.01194.x.

- Offner, S. S. R. and J. Chaban (2017). Impact of Protostellar Outflows on Turbulence and Star Formation Efficiency in Magnetized Dense Cores. *The Astrophysical Journal*, **847**(2), p. 104. doi: 10.3847/1538-4357/aa8996.
- Offner, S. S. R., P. C. Clark, P. Hennebelle, N. Bastian, M. R. Bate, P. F. Hopkins, E. Moraux, and A. P. Whitworth (2014). The Origin and Universality of the Stellar Initial Mass Function. *arXiv:1312.5326 [astro-ph]*. doi: 10.2458/azu_uapress_9780816531240-ch003.
- Offner, S. S. R., R. I. Klein, and C. F. McKee (2008). Driven and Decaying Turbulence Simulations of Low-Mass Star Formation: From Clumps to Cores to Protostars. *The Astrophysical Journal*, **686**(2), pp. 1174–1194. doi: 10.1086/590238.
- Offner, S. S. R., R. I. Klein, C. F. McKee, and M. R. Krumholz (2009). The Effects of Radiative Transfer on Low-Mass Star Formation. *Astrophysical Journal*, **703**(1), pp. 131–149. doi: 10.1088/0004-637X/703/1/131.
- Offner, S. S. R., K. M. Kratter, C. D. Matzner, M. R. Krumholz, and R. I. Klein (2010). The Formation of Low-Mass Binary Star Systems Via Turbulent Fragmentation. *The Astrophysical Journal*, **725**(2), pp. 1485–1494. doi: 10.1088/0004-637X/725/2/1485.
- Offner, S. S. R. and Y. Liu (2018). Turbulent Action at a Distance Due to Stellar Feedback in Magnetized Clouds. *Nature Astronomy*, **2**, pp. 896–900. doi: 10.1038/s41550-018-0566-1.
- Orosz, J. A., W. F. Welsh, J. A. Carter, D. C. Fabrycky, W. D. Cochran, M. Endl, E. B. Ford, N. Haghighipour, P. J. MacQueen, T. Mazeh, R. Sanchis-Ojeda, D. R. Short, G. Torres, E. Agol, L. A. Buchhave, L. R. Doyle, H. Isaacson, J. J. Lissauer, G. W. Marcy, A. Shporer, G. Windmiller, T. Barclay, A. P. Boss, B. D. Clarke, J. J. Fortney, J. C. Geary, M. J. Holman, D. Huber, J. M. Jenkins, K. Kinemuchi, E. Kruse, D. Ragozzine, D. Sasselov, M. Still, P. Tenenbaum, K. Uddin, J. N. Winn, D. G. Koch, and W. J. Borucki (2012). Kepler-47: A Transiting Circumbinary Multiplanet System. *Science (New York, N.Y.)*, **337**(6101), pp. 1511–4. doi: 10.1126/science.1228380.
- Orosz, J. A., W. F. Welsh, N. Haghighipour, B. Quarles, D. R. Short, S. M. Mills, S. Satyal, G. Torres, E. Agol, D. C. Fabrycky, D. Jontof-Hutter, G. Windmiller, T. W. A. Müller, T. C. Hinse, W. D. Cochran, M. Endl, E. B. Ford, T. Mazeh, and J. J. Lissauer (2019). Discovery of a Third Transiting Planet in the Kepler-47 Circumbinary System. *The Astronomical Journal*, **157**, p. 174. doi: 10.3847/1538-3881/ab0ca0.

- Ostriker, E. C., J. M. Stone, and C. F. Gammie (2001). Density, Velocity, and Magnetic Field Structure in Turbulent Molecular Cloud Models. *The Astrophysical Journal*, **546**(2), p. 980. doi: 10.1086/318290.
- Padoan, P., T. Haugbølle, and t. Nordlund (2012). A Simple Law of Star Formation. *The Astrophysical Journal*, **759**(2), p. L27. doi: 10.1088/2041-8205/759/2/L27.
- Padoan, P. and Å. Nordlund (2002). The Stellar Initial Mass Function from Turbulent Fragmentation. *The Astrophysical Journal*, **576**(2), p. 870. doi: 10.1086/341790.
- Padoan, P., L. Pan, M. Juvela, T. Haugbølle, and Å. Nordlund (2019). The Origin of Massive Stars: The Inertial-Inflow Model. *arXiv e-prints*, p. arXiv:1911.04465.
- Peale, S. J. (1999). Origin and Evolution of the Natural Satellites. *ANNUAL REVIEW OF ASTRONOMY AND ASTROPHYSICS*, **37**, pp. 533–602. doi: 10.1146/annurev.astro.37.1.533.
- Pedregosa, F., G. Varoquaux, A. Gramfort, V. Michel, B. Thirion, O. Grisel, M. Blondel, P. Prettenhofer, R. Weiss, V. Dubourg, J. Vanderplas, A. Passos, D. Cournapeau, M. Brucher, M. Perrot, and É. Duchesnay (2011). Scikit-Learn: Machine Learning in Python. *Journal of Machine Learning Research*, **12**(85), pp. 2825–2830. ISSN ISSN 1533-7928.
- Pierens, A. and R. P. Nelson (2008). On the Formation and Migration of Giant Planets in Circumbinary Discs. *Astronomy and Astrophysics*, **483**(2), pp. 633–642. doi: 10.1051/0004-6361:200809453.
- Pierens, A. and R. P. Nelson (2013). Migration and Gas Accretion Scenarios for the Kepler 16, 34, and 35 Circumbinary Planets. *Astronomy & Astrophysics*, **556**, p. A134. doi: 10.1051/0004-6361/201321777.
- Pike, R. E., W. C. Fraser, M. E. Schwamb, J. J. Kavelaars, M. Marsset, M. T. Bannister, M. J. Lehner, S.-Y. Wang, M. Alexandersen, Y.-T. Chen, B. J. Gladman, S. Gwyn, J.-M. Petit, and K. Volk (2017). Col-Ossos: Z-Band Photometry Reveals Three Distinct TNO Surface Types. *Astronomical Journal*, **154**(3), p. 101. doi: 10.3847/1538-3881/aa83b1.
- Pires dos Santos, P. M., A. Morbidelli, and D. Nesvorný (2012). Dynamical Capture in the Pluto–Charon System. *Celestial Mechanics and Dynamical Astronomy*, **114**(4), pp. 341–352. doi: 10.1007/s10569-012-9442-y.
- Porter, S. B., C. J. Bierson, O. Umurhan, R. A. Beyer, T. A. Lauer, M. W. Buie, A. H. Parker, M. Kinczyk, K. Runyon, W. M. Grundy, J. J. Kavelaars, A. M. Zangari, M. R. El-Maarry, D. T. Britt, J. M. Moore, A. J. Verbiscer, J. W.

- Parker, C. B. Olkin, H. A. Weaver, J. R. Spencer, S. A. Stern, and New Horizons GGI Team (2019). A Contact Binary in the Kuiper Belt: The Shape and Pole of (486958) 2014 MU69. **50**, p. 1611.
- Pu, B. and Y. Wu (2015). Spacing of Kepler Planets: Sculpting by Dynamical Instability. *The Astrophysical Journal*, **807**(1), p. 44. doi: 10.1088/0004-637X/807/1/44.
- Quarles, B., G. Li, V. Kostov, and N. Haghighipour (2020). Orbital Stability of Circumstellar Planets in Binary Systems. *The Astronomical Journal*, **159**(3), p. 80. doi: 10.3847/1538-3881/ab64fa.
- Raghavan, D., H. A. McAlister, T. J. Henry, D. W. Latham, G. W. Marcy, B. D. Mason, D. R. Gies, R. J. White, and T. A. ten Brummelaar (2010). A Survey of Stellar Families: Multiplicity of Solar-Type Stars. *The Astrophysical Journal Supplement Series*, **190**(1), pp. 1–42. doi: 10.1088/0067-0049/190/1/1.
- Ragozzine, D. and M. E. Brown (2007). Candidate Members and Age Estimate of the Family of Kuiper Belt Object 2003 EL61. *The Astronomical Journal*, **134**(6), pp. 2160–2167. doi: 10.1086/522334.
- Raymond, S. N., P. J. Armitage, and N. Gorelick (2010). Planet-Planet Scattering in Planetesimal Disks. II. Predictions for Outer Extrasolar Planetary Systems. *The Astrophysical Journal*, **711**(2), pp. 772–795. doi: 10.1088/0004-637X/711/2/772.
- Rein, H. and S.-F. Liu (2012). REBOUND: An Open-Source Multi-Purpose N - Body Code for Collisional Dynamics. *Astronomy & Astrophysics*, **537**, p. A128. doi: 10.1051/0004-6361/201118085.
- Rein, H. and D. S. Spiegel (2014). IAS15: A Fast, Adaptive, High-Order Integrator for Gravitational Dynamics, Accurate to Machine Precision over a Billion Orbits. *Monthly Notices of the Royal Astronomical Society*, **446**(2), pp. 1424–1437. doi: 10.1093/mnras/stu2164.
- Rodriguez, D. R., G. Duchêne, H. Tom, G. M. Kennedy, B. Matthews, J. Greaves, and H. Butner (2015). Stellar Multiplicity and Debris Discs: An Unbiased Sample. *Monthly Notices of the Royal Astronomical Society*, **449**(3), pp. 3160–3170. doi: 10.1093/mnras/stv483.
- Rosolowsky, E. W., J. E. Pineda, J. Kauffmann, and A. A. Goodman (2008). Structural Analysis of Molecular Clouds: Dendrograms. *The Astrophysical Journal*, **679**(2), p. 1338. doi: 10.1086/587685.
- Rubin, M. E., S. J. Desch, and M. Neveu (2014). The Effect of Rayleigh–Taylor Instabilities on the Thickness of Undifferentiated Crust on Kuiper Belt Objects. *Icarus*, **236**, pp. 122–135. doi: 10.1016/j.icarus.2014.03.047.

- Sana, H., S. E. de Mink, A. de Koter, N. Langer, C. J. Evans, M. Gieles, E. Gosset, R. G. Izzard, J.-B. Le Bouquin, and F. R. N. Schneider (2012). Binary Interaction Dominates the Evolution of Massive Stars. *Science*, **337**, p. 444. doi: 10.1126/science.1223344.
- Schlichting, H. E. and R. Sari (2009). The Creation of Haumea’s Collisional Family. *The Astrophysical Journal*, **700**(2), pp. 1242–1246. doi: 10.1088/0004-637X/700/2/1242.
- Schneider, E. E., B. E. Robertson, and T. A. Thompson (2018). Production of Cool Gas in Thermally Driven Outflows. *The Astrophysical Journal*, **862**(1), p. 56. doi: 10.3847/1538-4357/aacce1.
- Schwamb, M. E., H. Hsieh, M. T. Bannister, D. Bodewits, S. R. Chesley, W. C. Fraser, M. Granvik, R. L. Jones, M. Jurić, M. S. P. Kelley, D. Ragozzine, D. E. Trilling, and K. V. and (2019). A Software Roadmap for Solar System Science with the Large Synoptic Survey Telescope. *Research Notes of the AAS*, **3**(3), p. 51. doi: 10.3847/2515-5172/ab0e10.
- Schwamb, M. E., R. L. Jones, S. R. Chesley, A. Fitzsimmons, W. C. Fraser, M. J. Holman, H. Hsieh, D. Ragozzine, C. A. Thomas, D. E. Trilling, M. E. Brown, M. T. Bannister, D. Bodewits, M. de Val-Borro, D. Gerdes, M. Granvik, M. S. P. Kelley, M. M. Knight, R. L. Seaman, Q.-Z. Ye, and L. A. Young (2018). Large Synoptic Survey Telescope Solar System Science Roadmap. *arXiv:1802.01783 [astro-ph]*.
- Schwarz, R., B. Funk, R. Zechner, and Á. Bazsó (2016). New Prospects for Observing and Cataloguing Exoplanets in Well-Detached Binaries. *Monthly Notices of the Royal Astronomical Society*, **460**(4), pp. 3598–3609. doi: 10.1093/mnras/stw1218.
- Seo, Y. M., Y. L. Shirley, P. Goldsmith, D. Ward-Thompson, J. M. Kirk, M. Schmalzl, J.-E. Lee, R. Friesen, G. Langston, J. Masters, and R. W. Garwood (2015). An Ammonia Spectral Map of the L1495-B218 Filaments in the Taurus Molecular Cloud. I. Physical Properties of Filaments and Dense Cores. *The Astrophysical Journal*, **805**(2), p. 185. doi: 10.1088/0004-637X/805/2/185.
- Shankman, C., J. J. Kavelaars, B. Gladman, M. Alexandersen, N. Kaib, J.-M. Petit, M. T. Bannister, Y.-T. Chen, S. Gwyn, M. Jakubik, and K. Volk (2016). OSSOS II. a Sharp Transition in the Absolute Magnitude Distribution of the Kuiper Belt’s Scattering Population. *AJ*, **151**(2), p. 31. doi: 10.3847/0004-6256/151/2/31.
- Shetty, R., D. C. Collins, J. Kauffmann, A. A. Goodman, E. W. Rosolowsky, and M. L. Norman (2010). The Effect of Projection on Derived Mass-Size and Linewidth-Size Relationships. *The Astrophysical Journal*, **712**(2), pp. 1049–1056. doi: 10.1088/0004-637X/712/2/1049.

- Shikita, B., H. Koyama, and S. Yamada (2010). The Dynamics of Three-Planet Systems: An Approach from a Dynamical System. *The Astrophysical Journal*, **712**(2), pp. 819–832. doi: 10.1088/0004-637X/712/2/819.
- Showalter, M. R. and D. P. Hamilton (2015). Resonant Interactions and Chaotic Rotation of Pluto’s Small Moons. *Nature*, **522**(7554), pp. 45–49. doi: 10.1038/nature14469.
- Silsbee, K. and R. R. Rafikov (2015). Birth Locations of the Kepler Circumbinary Planets. *The Astrophysical Journal*, **808**(1), p. 58. doi: 10.1088/0004-637X/808/1/58.
- Sinclair, A. T. (1975). The Orbital Resonance amongst the Galilean Satellites of Jupiter. *Monthly Notices of the Royal Astronomical Society*, **171**, pp. 59–72. doi: 10.1093/mnras/171.1.59.
- Singer, K. N., W. B. McKinnon, S. J. Robbins, P. M. Schenk, S. Greenstreet, B. Gladman, A. H. Parker, S. A. Stern, V. J. Bray, H. A. Weaver, R. A. Beyer, L. A. Young, J. R. Spencer, J. M. Moore, C. B. Olkin, K. Ennico, R. P. Binzel, W. M. Grundy, New Horizons Geology, Geophysics Team, New Horizons Composition Team, New Horizons Mvic Team, and New Horizons Lorri Team (2016). Craters on Pluto and Charon — Surface Ages and Impactor Populations. *47th Lunar and Planetary Science Conference*.
- Smith, A. W. and J. J. Lissauer (2009). Orbital Stability of Systems of Closely-Spaced Planets. *Icarus*, **201**(1), pp. 381–394. doi: 10.1016/j.icarus.2008.12.027.
- Smith, R. J., P. C. Clark, and I. A. Bonnell (2009). Fragmentation in Molecular Clouds and Its Connection to the IMF. *Monthly Notices of the Royal Astronomical Society*, **396**(2), pp. 830–841. doi: 10.1111/j.1365-2966.2009.14794.x.
- Smith, R. J., S. C. O. Glover, and R. S. Klessen (2014). On the Nature of Star-Forming Filaments – I. Filament Morphologies. *Monthly Notices of the Royal Astronomical Society*, **445**(3), pp. 2900–2917. doi: 10.1093/mnras/stu1915.
- Smullen, R. A., K. M. Kratter, and A. Shannon (2016). Planet Scattering Around Binaries: Ejections, Not Collisions. *Monthly Notices of the Royal Astronomical Society*, **461**(2), pp. 1288–1301. doi: 10.1093/mnras/stw1347.
- Smullen, R. A. and K. Volk (2020). Machine Learning Classification of Kuiper Belt Populations. *MNRAS*. doi: 10.1093/mnras/staa1935.
- Sokol, A. D., R. A. Gutermuth, R. Pokhrel, A. I. Gómez-Ruiz, G. W. Wilson, S. S. R. Offner, M. Heyer, A. Luna, F. P. Schloerb, and D. Sánchez (2019). Early Science with the Large Millimetre Telescope: An LMT/AzTEC 1.1 Mm Survey of Dense

- Cores in the Monoceros R2 Giant Molecular Cloud. *Monthly Notices of the Royal Astronomical Society*, **483**(1), pp. 407–424. doi: 10.1093/mnras/sty3107.
- Spohn, T. and G. Schubert (1991). Thermal Equilibration of the Earth Following a Giant Impact. *Geophysical Journal International*, **107**(1), pp. 163–170. doi: 10.1111/j.1365-246X.1991.tb01164.x.
- Stern, S. A., F. Bagenal, K. Ennico, G. R. Gladstone, W. M. Grundy, W. B. McKinnon, J. M. Moore, C. B. Olkin, J. R. Spencer, H. A. Weaver, L. A. Young, T. Andert, J. Andrews, M. Banks, B. Bauer, J. Bauman, O. S. Barnouin, P. Bedini, K. Beisser, R. A. Beyer, S. Bhaskaran, R. P. Binzel, E. Birath, M. Bird, D. J. Bogan, A. Bowman, V. J. Bray, M. Brozović, C. Bryan, M. R. Buckley, M. W. Buie, B. J. Buratti, S. S. Bushman, A. Calloway, B. Carcich, A. F. Cheng, S. J. Conard, C. A. Conrad, J. C. Cook, D. P. Cruikshank, O. S. Custodio, C. M. Dalle Ore, C. Deboy, Z. J. Dischner, P. Dumont, A. M. Earle, H. A. Elliott, J. Ercol, C. M. Ernst, T. Finley, S. H. Flanigan, G. Fountain, M. J. Freeze, T. K. Greathouse, J. L. Green, Y. Guo, M. Hahn, D. P. Hamilton, S. A. Hamilton, J. Hanley, A. Harch, H. M. Hart, C. B. Hersman, A. Hill, M. E. Hill, D. P. Hinson, M. E. Holdridge, M. Horanyi, A. D. Howard, C. J. A. Howett, C. Jackman, R. A. Jacobson, D. E. Jennings, J. A. Kammer, H. K. Kang, D. E. Kaufmann, P. Kollmann, S. M. Krimigis, D. Kusnierkiewicz, T. R. Lauer, J. E. Lee, K. L. Lindstrom, I. R. Linscott, C. M. Lisse, A. W. Lunsford, V. A. Mallder, N. Martin, D. J. McComas, R. L. McNutt, D. Mehoke, T. Mehoke, E. D. Melin, M. J. Mutchler, D. Nelson, F. Nimmo, J. I. Nunez, A. Ocampo, W. M. Owen, M. Paetzold, B. Page, A. H. Parker, J. W. Parker, F. Pelletier, J. Peterson, N. Pinkine, M. Piquette, S. B. Porter, S. Protopapa, J. Redfern, H. J. Reitsema, D. C. Reuter, J. H. Roberts, S. J. Robbins, G. Rogers, D. Rose, K. Runyon, K. D. Retherford, M. G. Ryschkewitsch, P. M. Schenk, E. Schindhelm, B. Sepan, M. R. Showalter, K. N. Singer, M. Soluri, D. Stanbridge, A. J. Steffl, D. F. Strobel, T. Stryk, M. E. Summers, J. R. Szalay, M. B. Tapley, A. Taylor, H. W. Taylor, H. B. Throop, C. C. C. Tsang, G. L. Tyler, O. M. Umurhan, A. J. Verbiscer, M. H. Versteeg, M. Vincent, R. Webbert, S. Weidner, G. E. Weigle, O. L. White, K. Whittenburg, B. G. Williams, K. Williams, S. Williams, W. W. Woods, A. M. Zangari, and E. Zirnstein (2015). The Pluto System: Initial Results from Its Exploration by New Horizons. *Science (New York, N.Y.)*, **350**(6258), p. aad1815. doi: 10.1126/science.aad1815.
- Stern, S. A., W. M. Grundy, W. B. McKinnon, H. A. Weaver, and L. A. Young (2018). The Pluto System After New Horizons. *Annual Review of Astronomy and Astrophysics*, **56**(1), pp. 357–392. doi: 10.1146/annurev-astro-081817-051935.
- Stern, S. A., H. A. Weaver, J. R. Spencer, C. B. Olkin, G. R. Gladstone, W. M. Grundy, J. M. Moore, D. P. Cruikshank, H. A. Elliott, W. B. McKinnon, J. W.

- Parker, A. J. Verbiscer, L. A. Young, D. A. Aguilar, J. M. Albers, T. Andert, J. P. Andrews, F. Bagenal, M. E. Banks, B. A. Bauer, J. A. Bauman, K. E. Bechtold, C. B. Beddingfield, N. Behrooz, K. B. Beisser, S. D. Benecchi, E. Bernardoni, R. A. Beyer, S. Bhaskaran, C. J. Bierson, R. P. Binzel, E. M. Birath, M. K. Bird, D. R. Boone, A. F. Bowman, V. J. Bray, D. T. Britt, L. E. Brown, M. R. Buckley, M. W. Buie, B. J. Buratti, L. M. Burke, S. S. Bushman, B. Carcich, A. L. Chaikin, C. L. Chavez, A. F. Cheng, E. J. Colwell, S. J. Conard, M. P. Conner, C. A. Conrad, J. C. Cook, S. B. Cooper, O. S. Custodio, C. M. Dalle Ore, C. C. Deboy, P. Dharmavaram, R. D. Dhingra, G. F. Dunn, A. M. Earle, A. F. Egan, J. Eisig, M. R. El-Maarry, C. Engelbrecht, B. L. Enke, C. J. Ercol, E. D. Fattig, C. L. Ferrell, T. J. Finley, J. Firer, J. Fischetti, W. M. Folkner, M. N. Fosbury, G. H. Fountain, J. M. Freeze, L. Gabasova, L. S. Glaze, J. L. Green, G. A. Griffith, Y. Guo, M. Hahn, D. W. Hals, D. P. Hamilton, S. A. Hamilton, J. J. Hanley, A. Harch, K. A. Harmon, H. M. Hart, J. Hayes, C. B. Hersman, M. E. Hill, T. A. Hill, J. D. Hofgartner, M. E. Holdridge, M. Horányi, A. Hosadurga, A. D. Howard, C. J. A. Howett, S. E. Jaskulek, D. E. Jennings, J. R. Jensen, M. R. Jones, H. K. Kang, D. J. Katz, D. E. Kaufmann, J. J. Kavelaars, J. T. Keane, G. P. Keleher, M. Kinczyk, M. C. Kochte, P. Kollmann, S. M. Krimigis, G. L. Kruizinga, D. Y. Kusnierkiewicz, M. S. Lahr, T. R. Lauer, G. B. Lawrence, J. E. Lee, E. J. Lessac-Chenen, I. R. Linscott, C. M. Lisse, A. W. Lunsford, D. M. Mages, V. A. Mallder, N. P. Martin, B. H. May, D. J. McComas, R. L. McNutt, D. S. Mehoke, T. S. Mehoke, D. S. Nelson, H. D. Nguyen, J. I. Núñez, A. C. Ocampo, W. M. Owen, G. K. Oxtun, A. H. Parker, M. Pätzold, J. Y. Pelgrift, F. J. Pelletier, J. P. Pineau, M. R. Piquette, S. B. Porter, S. Protopapa, E. Quirico, J. A. Redfern, A. L. Regiec, H. J. Reitsema, D. C. Reuter, D. C. Richardson, J. E. Riedel, M. A. Ritterbush, S. J. Robbins, D. J. Rodgers, G. D. Rogers, D. M. Rose, P. E. Rosendall, K. D. Runyon, M. G. Ryschkewitsch, M. M. Saina, M. J. Salinas, P. M. Schenk, J. R. Scherrer, W. R. Schlei, B. Schmitt, D. J. Schultz, D. C. Schurr, F. Scipioni, R. L. Sepan, R. G. Shelton, M. R. Showalter, M. Simon, K. N. Singer, E. W. Stahlheber, D. R. Stanbridge, J. A. Stansberry, A. J. Steffl, D. F. Strobel, M. M. Stothoff, T. Stryk, J. R. Stuart, M. E. Summers, M. B. Tapley, A. Taylor, H. W. Taylor, R. M. Tedford, H. B. Throop, L. S. Turner, O. M. Umurhan, J. Van Eck, D. Velez, M. H. Versteeg, M. A. Vincent, R. W. Webbert, S. E. Weidner, G. E. Weigle, J. R. Wendel, O. L. White, K. E. Whittenburg, B. G. Williams, K. E. Williams, S. P. Williams, H. L. Winters, A. M. Zangari, and T. H. Zurbuchen (2019). Initial Results from the New Horizons Exploration of 2014 MU69, a Small Kuiper Belt Object. *Science*, **364**, p. aaw9771. doi: 10.1126/science.aaw9771.
- Storm, S., L. G. Mundy, K. I. Lee, M. Fernández-López, L. W. Looney, P. Teuben, H. G. Arce, E. W. Rosolowsky, A. M. Meisner, A. Isella, J. Kauffmann, Y. L. Shirley, W. Kwon, A. L. Plunkett, M. W. Pound, D. M. Segura-Cox, K. Tassis,

- J. J. Tobin, N. H. Volgenau, R. M. Crutcher, and L. Testi (2016). Carma Large Area Star Formation Survey: Dense Gas in the Young L1451 Region of Perseus. *The Astrophysical Journal*, **830**(2), p. 127. doi: 10.3847/0004-637X/830/2/127.
- Storrie-Lombardi, M. C., O. Lahav, L. Sodr , and L. J. Storrie-Lombardi (1992). Morphological Classification of Galaxies by Artificial Neural Networks. *Monthly Notices of the Royal Astronomical Society*, **259**(1), pp. 8P–12P. doi: 10.1093/mnras/259.1.8P.
- Stutzki, J. and R. Guesten (1990). High Spatial Resolution Isotopic CO and CS Observations of M17 SW - the Clumpy Structure of the Molecular Cloud Core. *The Astrophysical Journal*, **356**, pp. 513–533. doi: 10.1086/168859.
- Sumi, T., K. Kamiya, D. P. Bennett, I. A. Bond, F. Abe, C. S. Botzler, A. Fukui, K. Furusawa, J. B. Hearnshaw, Y. Itow, P. M. Kilmartin, A. Korpela, W. Lin, C. H. Ling, K. Masuda, Y. Matsubara, N. Miyake, M. Motomura, Y. Muraki, M. Nagaya, S. Nakamura, K. Ohnishi, T. Okumura, Y. C. Perrott, N. Rattenbury, T. Saito, T. Sako, D. J. Sullivan, W. L. Sweatman, P. J. Tristram, A. Udalski, M. K. Szymański, M. Kubiak, G. Pietrzyński, R. Poleski, I. Soszyński, L. Wyrzykowski, K. Ulaczyk, and Microlensing Observations in Astrophysics (MOA) Collaboration (2011). Unbound or Distant Planetary Mass Population Detected by Gravitational Microlensing. *Nature*, **473**(7347), pp. 349–52. doi: 10.1038/nature10092.
- Sutherland, A. P. and D. C. Fabrycky (2015). On the Fate of Unstable Circumbinary Planets: Tatooine’s Close Encounters with a Death Star. *The Astrophysical Journal*, **818**(1), p. 7. doi: 10.3847/0004-637X/818/1/6.
- Sutherland, A. P. and K. M. Kratter (2019). Instabilities in Multiplanet Circumbinary Systems. *Monthly Notices of the Royal Astronomical Society*, **487**(3), pp. 3288–3304. doi: 10.1093/mnras/stz1503.
- Szebehely, V. and R. McKenzie (1981). Stability of Outer Planetary Systems. *Celestial Mechanics*, **23**(1), pp. 3–7. doi: 10.1007/BF01228541.
- Tabachnik, S. and S. Tremaine (2002). Maximum-Likelihood Method for Estimating the Mass and Period Distributions of Extrasolar Planets. *Monthly Notices of the Royal Astronomical Society*, **335**(1), pp. 151–158. doi: 10.1046/j.1365-8711.2002.05610.x.
- Tamayo, D., A. Silburt, D. Valencia, K. Menou, M. Ali-Dib, C. Petrovich, C. X. Huang, H. Rein, C. van Laerhoven, A. Paradise, A. Obertas, and N. Murray (2016). A Machine Learns to Predict the Stability of Tightly Packed Planetary Systems. *The Astrophysical Journal*, **832**(2), p. L22. doi: 10.3847/2041-8205/832/2/L22.

- Tobin, J. J., L. W. Looney, Z.-Y. Li, C. J. Chandler, M. M. Dunham, D. Segura-Cox, S. I. Sadavoy, C. Melis, R. J. Harris, K. Kratter, and L. Perez (2016). The VLA Nascent Disk and Multiplicity Survey of Perseus Protostars (VANDAM). II. Multiplicity of Protostars in the Perseus Molecular Cloud. *The Astrophysical Journal*, **818**, p. 73. doi: 10.3847/0004-637X/818/1/73.
- Tonks, W. B. and H. J. Melosh (1993). Magma Ocean Formation Due to Giant Impacts. *Journal of Geophysical Research*, **98**(E3), p. 5319. doi: 10.1029/92JE02726.
- Trilling, D. E. (2016). The Surface Age of Sputnik Planum, Pluto, Must Be Less than 10 Million Years. *PLOS ONE*, **11**(1), p. e0147386. doi: 10.1371/journal.pone.0147386.
- Truelove, J. K., R. I. Klein, C. F. McKee, J. H. H. II, L. H. Howell, and J. A. Greenough (1997). The Jeans Condition: A New Constraint on Spatial Resolution in Simulations of Isothermal Self-Gravitational Hydrodynamics. *The Astrophysical Journal*, **489**(2), pp. L179–L183. doi: 10.1086/310975.
- Tsiganis, K., R. Gomes, A. Morbidelli, and H. F. Levison (2005). Origin of the Orbital Architecture of the Giant Planets of the Solar System. *Nature*, **435**(7041), pp. 459–61.
- Turk, M. J., B. D. Smith, J. S. Oishi, S. Skory, S. W. Skillman, T. Abel, and M. L. Norman (2010). A Multi-Code Analysis Toolkit for Astrophysical Simulation Data. *The Astrophysical Journal Supplement, Volume 192, Issue 1, article id. 9, 16 pp. (2011).*, **192**. doi: 10.1088/0067-0049/192/1/9.
- Van Eylen, V. and S. Albrecht (2015). Eccentricity from Transit Photometry: Small Planets in Kepler Multi-Planet Systems Have Low Eccentricities. *The Astrophysical Journal*, **808**(2), p. 126. doi: 10.1088/0004-637X/808/2/126.
- Veras, D. and B. T. Gansicke (2014). Detectable Close-in Planets around White Dwarfs through Late Unpacking. *Monthly Notices of the Royal Astronomical Society*, **447**(2), pp. 1049–1058. doi: 10.1093/mnras/stu2475.
- Veras, D. and S. N. Raymond (2012). Planet-Planet Scattering Alone Cannot Explain the Free-Floating Planet Population. *Monthly Notices of the Royal Astronomical Society: Letters*, **421**(1), pp. L117–L121. doi: 10.1111/j.1745-3933.2012.01218.x.
- Volk, K., R. Murray-Clay, B. Gladman, S. Lawler, M. T. Bannister, J. J. Kavelaars, J.-M. Petit, S. Gwyn, M. Alexandersen, Y.-T. Chen, P. S. Lykawka, W. Ip, and H. W. Lin (2017). OSSOS III—Resonant Trans-Neptunian Populations: Constraints from the First Quarter of the Outer Solar System Origins Survey. *The Astronomical Journal*, **152**(1), p. 23. doi: 10.3847/0004-6256/152/1/23.

- Wagner, K., R. Dong, P. Sheehan, D. Apai, M. Kasper, M. McClure, K. M. Morzinski, L. Close, J. Males, P. Hinz, S. P. Quanz, and J. Fung (2018). The Orbit of the Companion to HD 100453A: Binary-Driven Spiral Arms in a Protoplanetary Disk. *The Astrophysical Journal*, **854**(2), p. 130. doi: 10.3847/1538-4357/aaa767.
- Walsh, K. J. and H. F. Levison (2015). Formation and Evolution of Pluto’s Small Satellites. *The Astronomical Journal*, **150**(1), p. 11. doi: 10.1088/0004-6256/150/1/11.
- Ward, W. R. and R. M. Canup (2006). Forced Resonant Migration of Pluto’s Outer Satellites by Charon. *Science (New York, N.Y.)*, **313**(5790), pp. 1107–9. doi: 10.1126/science.1127293.
- Wasserman, H. L., D. E. Trilling, J. R. Lovering, R. L. Millis, R. A. Crudo, M. W. Buie, S. D. Kern, J. L. Elliot, S. Sheppard, C. Trujillo, P. H. Bernardinelli, G. Bernstein, and S. M. (2020). 131 New Distant Objects. *Minor Planet Electronic Circulars*, **2020-C88**.
- Weiss, L. M. and G. W. Marcy (2014). The Mass-Radius Relation for 65 Exoplanets Smaller Than 4 Earth Radii. *The Astrophysical Journal*, **783**(1), p. L6. doi: 10.1088/2041-8205/783/1/L6.
- Welsh, W. F., J. A. Orosz, J. A. Carter, and D. C. Fabrycky (2014). Recent Kepler Results On Circumbinary Planets. *Proceedings of the International Astronomical Union*, **8**(S293), pp. 125–132. doi: 10.1017/S1743921313012684.
- Welsh, W. F., J. A. Orosz, D. R. Short, W. D. Cochran, M. Endl, E. Brugamyer, N. Haghighipour, L. A. Buchhave, L. R. Doyle, D. C. Fabrycky, T. C. Hinse, S. R. Kane, V. Kostov, T. Mazeh, S. M. Mills, T. W. A. Müller, B. Quarles, S. N. Quinn, D. Ragozzine, A. Shporer, J. H. Steffen, L. Tal-Or, G. Torres, G. Windmiller, and W. J. Borucki (2015). Kepler 453 b—the 10th Kepler Transiting Circumbinary Planet. *The Astrophysical Journal*, **809**(1), p. 26. doi: 10.1088/0004-637X/809/1/26.
- Williams, J. P., E. J. de Geus, and L. Blitz (1994). Determining Structure in Molecular Clouds. *The Astrophysical Journal*, **428**, pp. 693–712. doi: 10.1086/174279.
- Wolfgang, A. and G. Laughlin (2012). The Effect of Population-Wide Mass-to-Radius Relationships on the Interpretation of Kepler and Harps Super-Earth Occurrence Rates. *The Astrophysical Journal*, **750**(2), p. 148. doi: 10.1088/0004-637X/750/2/148.
- Wong, T., A. Hughes, K. Tokuda, R. Indebetouw, J.-P. Bernard, T. Onishi, E. Wojciechowski, J. B. Bandurski, A. Kawamura, J. Roman-Duval, Y. Cao, C.-H. R.

- Chen, Y.-h. Chu, C. Cui, Y. Fukui, L. Montier, E. Muller, J. Ott, D. Paradis, J. L. Pineda, E. Rosolowsky, and M. Sewi\lo (2017). ALMA Observations of a Quiescent Molecular Cloud in the Large Magellanic Cloud. *The Astrophysical Journal*, **850**(2), p. 139. doi: 10.3847/1538-4357/aa9333.
- Wongwathanarat, A., E. Müller, and H.-T. Janka (2015). Three-Dimensional Simulations of Core-Collapse Supernovae: From Shock Revival to Shock Breakout. *Astronomy & Astrophysics*, **577**, p. A48. doi: 10.1051/0004-6361/201425025.
- Woo, J. M. Y. and M. H. Lee (2018). On the Early In Situ Formation of Pluto’s Small Satellites. *The Astronomical Journal*, **155**(4), p. 175. doi: 10.3847/1538-3881/aab367.
- Youdin, A. N., K. M. Kratter, and S. J. Kenyon (2012). Circumbinary Chaos: Using Pluto’s Newest Moon to Constrain the Masses of Nix and Hydra. *The Astrophysical Journal*, **755**(1), p. 17. doi: 10.1088/0004-637X/755/1/17.
- Youdin, A. N. and F. H. Shu (2002). Planetesimal Formation by Gravitational Instability. *The Astrophysical Journal*, **580**(1), pp. 494–505. doi: 10.1086/343109.
- Young, L. A., F. Braga-Ribas, and R. E. Johnson (2020). Volatiles Evolution and Atmospheres of Trans-Neptunian Objects. *The Trans-Neptunian Solar System*, pp. 127–151. doi: 10.1016/B978-0-12-816490-7.00006-0.
- Yu, T. Y. M., R. Murray-Clay, and K. Volk (2018). Trans-Neptunian Objects Transiently Stuck in Neptunes Mean-Motion Resonances: Numerical Simulations of the Current Population. *Astronomical Journal*, **156**(1), p. 33. doi: 10.3847/1538-3881/aac6cd.